Wrocław University of Technology
Centre of Advanced Materials and Nanotechnology

Materials Science-Poland

1st Polish Conference on Nanotechnology
NANO 2007
Wrocław, 26–28 April 2007

Vol. 26 • No. 1 • 2008

Oficyna Wydawnicza Politechniki Wrocławskiej

Materials Science is an interdisciplinary journal devoted to experimental and theoretical research into the synthesis, structure, properties and applications of materials.

Among the materials of interest are:

- glasses and ceramics
- sol-gel materials
- photoactive materials (including materials for nonlinear optics)
- laser materials
- photonic crystals
- semiconductor micro- and nanostructures
- piezo-, pyro- and ferroelectric materials
- high-T_c superconductors
- magnetic materials
- molecular materials (including polymers) for use in electronics and photonics
- novel solid phases
- other novel and unconventional materials

The broad spectrum of the areas of interest reflects the interdisciplinary nature of materials research. Papers covering the modelling of materials, their synthesis and characterisation, physicochemical aspects of their fabrication, properties and applications are welcome. In addition to regular papers, the journal features issues containing conference papers, as well as special issues on key topics in materials science.

Materials Science is published under the auspices of the Centre of Advanced Materials and Nanotechnology of the Wrocław University of Technology, in collaboration with the Institute of Low Temperatures and Structural Research of the Polish Academy of Sciences and the Wrocław University of Economics.

All accepted papers are placed on the Web page of the journal and are available at the address: http://MaterialsScience.pwr.wroc.pl

Materials Science is abstracted/indexed in: Chemical Abstracts, Materials Science Citation Index, Science Citation Index Expanded.

Editor-in-Chief

Juliusz Sworakowski

Institute of Physical and Theoretical Chemistry
Wrocław University of Technology
Wybrzeże Wyspiańskiego 27
50-370 Wrocław, Poland
sworakowski@pwr.wroc.pl

Associate Editors

Wiesław Stręk

Institute of Low Temperature
and Structure Research
Polish Academy of Sciences
P. O. Box 1410
50-950 Wrocław 2, Poland
strek@int.pan.wroc.pl

Jerzy Hanuza

Department of Bioorganic Chemistry
Faculty of Industry and Economics
Wrocław University of Economics
Komandorska 118/120
53-345 Wrocław, Poland
hanuza@credit.ae.wroc.pl

Scientific Secretary

Jan Felba

Faculty of Microsystem Electronics and Photonics
Wrocław University of Technology
Wybrzeże Wyspiańskiego 27
50-370 Wrocław, Poland
jan.felba@pwr.wroc.pl

Advisory Editorial Board

Ludwig J. Balk, Wuppertal, Germany
Frédéric Bernard, Dijon, France
Mikhaylo S. Brodyn, Kyiv, Ukraine
Alexander Bulinski, Ottawa, Canada
Roberto M. Faria, São Carlos, Brazil
Reimund Gerhard-Multhaupt, Potsdam, Germany
Paweł Hawrylak, Ottawa, Canada
Andrzej Kłonkowski, Gdańsk, Poland
Seiji Kojima, Tsukuba, Japan
Shin-ya Koshihara, Tokyo, Japan
Krzysztof J. Kurzydłowski, Warsaw, Poland
Janina Legendziewicz, Wrocław, Poland
Benedykt Licznerski, Wrocław, Poland
Jerzy Lis, Cracow, Poland
Tadeusz Luty, Wrocław, Poland
Joop H. van der Maas, Utrecht, The Netherlands
Bolesław Mazurek, Wrocław, Poland
Jan Misiewicz, Wrocław, Poland
Jerzy Mroziński, Wrocław, Poland
Robert W. Munn, Manchester, U.K.
Krzysztof Nauka, Palo Alto, CA, U.S.A.
Stanislav Nešpůrek, Prague, Czech Republic
Marek Samoć, Canberra, Australia
Jan Stankowski, Poznań, Poland
Jacek Ulański, Łódź, Poland
Vladislav Zolin, Moscow, Russia

The Journal is supported by the State Committee for Scientific Research

Editorial Office
Jan Wojna

Printed in Poland

© Copyright by Oficyna Wydawnicza Politechniki Wrocławskiej, Wrocław 2008

Drukarnia Oficyny Wydawniczej Politechniki Wrocławskiej
Zam. nr 334/2008.

Contents

A. Jakubowski, L. Łukasiak, CMOS evolution. Development limits 5

T. Błachowicz, Isotropic effects in exchange-biased ferromagnetic/antiferromagnetic bilayers 21

B. Boratyński, W. Kordalski, B. Ściana, M. Panek, I. Zborowska-Lindert, A new drain insulation design in GaAs SD-MAGFET 27

W. Kordalski, B. Boratyński, M. Panek, Properties and estimated parameters of a submicrometer HSDMAGFET 33

K. Gutowski, R.P. Sarzała, Computer simulation of tuned and detuned GaInNAsSb QW VCSELs for long-wavelength applications 45

K. Skrobas, R. Zdyb, M. Kisiel, M. Jałochowski, Band structure of In chains on Si(335)–Au 55

S. Kochowski, M. Szydłowski, R. Paszkiewicz, B. Paszkiewicz, Analysis of electrical equivalent circuit of metal–insulator–semiconductor structure based on admittance measurements 63

B. Ściana, D. Radziewicz, D. Pucicki, M. Tłaczała, G. Sęk, P. Poloczek, J. Misiewicz, J. Kováč, R. Srnanek, A. Christofi, Technology and properties of GaAs doping superlattices 71

J. Prażmowska, R. Korbutowicz, R. Paszkiewicz, A. Szyszka, A. Podhorodecki, J. Misiewicz, M. Tłaczała, Influence of the deposition parameters of nucleation layer on the properties of thick gallium nitride layers 79

M. Wośko, B. Paszkiewicz, A. Szyszka, W. Macherzyński, D. Radziewicz, B. Ściana, R. Paszkiewicz, M. Tłaczała, G. Sęk, P. Poloczek, M. Motyka, J. Misiewicz, A(III)B(V) detectors with graded active region 87

J. Bodzenta, Nanoscale heat transport 95

A. Bachmatiuk, R. J. Kaleńczuk, M. H. Rümmeli, T. Gemming, E. Borowiak-Palen, Preparation of ultra-large-scale catalysts for catalytic vapour deposition of carbon nanotubes 105

D. Kaczmarek, E. L. Prociow, J. Domaradzki, A. Borkowska, W. Mielcarek, D. Wojcieszak, Influence of substrate type and its placement on structural properties of TiO_2 thin films prepared by the high energy reactive magnetron sputtering method 113

E. Czerwosz, P. Dłużewski, J. Kęczkowska, M. Kozłowski, M.Suchańska, H. Wronka, Palladium nanocrystals and their properties 119

B. Cichy, W. Stręk, J. Dziuban, A. Górecka-Drzazga, Application of multiwall carbon nanotubes to microfluidic systems 127

M. Cwil, P. Firek, P. Konarski, A. Werbowy, SIMS depth profiling of thin boron nitride insulating films 135

J. Domaradzki, D. Kaczmarek, E. L. Prociow, A. Borkowska, T. Berlicki, K. Sieradzka, Optical and electrical properties of TiO_2 doped with Tb and Pd 143

B. Gągorowska, B. Kucharska, M. Duś-Sitek, A. Tokarz, Comparative X-ray investigation of Ni/Cu systems heated in the 250–350 °C temperature range 149

Ł. Gelczuk, M. Dąbrowska-Szata, J. Serafińczuk, A. Masalska, E. Łusakowska, P. Dłużewski, Anisotropic strain relaxation and surface morphology related to asymmetry in the formation of misfit dislocations in InGaAs/GaAs heterostructures 157

M. Hasiak, M. Miglierini, J. Kaleta, J. Zbroszczyk, H. Fukunaga, Microstructure and magnetic properties of nanocrystalline Fe-based alloys 167

M. Kramkowska, A. Szyszka, B. Ściana, I. Zubel, Submicron suspended structures based on A(III)B(V) epitaxial layers 173

B. Kucharska, Structure of 310S steel-based Fe–Cr–Ni coatings 181
S. Lis, R. Dylewicz, J. Myśliwiec, A. Miniewicz, S. Patela, Application of flowable oxides in photonics 189
A. Raźniak, P. Tomczyk, Application of microelectrodes for investigation of the oxygen electrode reaction in selected solid electrolytes 195
J. Serafińczuk, J. Kozłowski, Determination of indium and nitrogen content in four-compound epitaxial layers of $In_xGa_{1-x}As_{1-y}N_y$ deposited on GaAs substrate 207
P. Strzyżewski, M. J. Sadowski, R. Nietubyć, K. Rogacki, T. Paryjczak, J. Rogowski, Fabrication of thin metallic films by arc discharges under ultra-high vacuum conditions 213
A. Szyszka, B. Paszkiewicz, R. Paszkiewicz, M. Tłaczała, Influence of the columnar structure of heteroepitaxial nitride layers on the transport of electrons 221
K. Walczak, I. Nowak, Novel nanoporous organic-inorganic hybrid materials containing niobium 229
A. Feliczak, I. Nowak, Rational design of NbMSU-X type nanoporous materials with desired textural properties 237
M. J. Woźniak, J. Ryszkowska, T. Szymborski, G. Chen, T. Tateishi, K. J. Kurzydłowski, Application of phase imaging and force modulation mode for description of dispersion of carbon nanotubes in polyol matrix 245

Instructions for Authors

1. Submission of Manuscripts

Manuscripts can be sent by e-mail or by conventional mail. Submission of a manuscript to *Materials Science-Poland* implies that it is not being considered for publication elsewhere, and the authors have a necessary authorisation to publish the material contained in the paper.

1.1. First Submission

1.1.1. By Electronic Mail

Authors are encouraged to submit electronic versions of the manuscript to the e-mail address of the journal (*vide infra*). A single PDF file containing text, references, figures, tables etc. should be sent. When the size of such a file exceeds acceptable limits, the manuscript can be split into a few files (this should be clearly indicated in the covering letter). **Files in the DOC or RTF formats will be accepted only exceptionally.**

1.1.2. By Conventional Mail

The manuscripts can also be submitted by conventional mail. Authors are requested to send a CD with a PDF file containing a complete manuscript (text, references, tables, figures, etc.). The disk, accompanied by a covering letter, should be mailed to the Editor-in-Chief at his address given below.

1.2. Final Submission

After the manuscript has received preliminary acceptance, the authors will be requested to send the following material:

– A PDF file containing the complete manuscript (text, literature, tables, figures, etc). The file should be carefully checked as it will serve as a hard copy in case of doubts.

– A DOC or RTF file containing the text, references, tables and figure captions. The content of the file should be identical with that of the hard copy, and should exactly match the version seen and accepted be the referee(s).

– File(s) in appropriate formats containing figures. **Please consult Section 2.5 of this document.**

The files should be preferentially sent by e-mail, to the address of the Journal (*vide infra*), or by conventional mail, on a CD, to the Editor-in-Chief.

– **Additionally, the corresponding author is requested to send a copyright transfer form. The form should be copied from the web page of the Journal, filled out, signed and mailed to the Editor-in-Chief via conventional mail.**

2.4. Equations

Equations referred to in the text should be numbered consecutively at the right hand margin with Arabic numerals in parentheses.

2.5. Figures

All artwork will be reproduced in black and white. All figures should be numbered with Arabic numerals, have descriptive captions, and be mentioned in the text. An approximate position for each figure should be indicated in the text. The required formats of the drawings (plots, schemes of technological processes) must be vector files such as XLS, OPJ, cdr (Excel, Origin, CorelDraw) which may also be exported as EPS, EMF or WMF files. **Drawings submitted in tiff or jpg formats (bitmaps, raster graphics) even if exported as EPS, EMF or WMF files, will not be accepted.** `11 are acceptable only in the case of photographs (samples, laboratory equipment, etc.). The photographs (only in grayscale) should have the resolution not lower than 300 dpi (estimated for the size in which they are expected to be reproduced).

The figures may be embedded in the text or their approximate positions should be indicated. **In any case, they should also be attached separately as original files.** The list of figure captions should follow the list of references at the end of the text

2.6. Tables

Tables should be numbered consecutively with Arabic numerals. Each table should be given a descriptive caption. If the tables are grouped at the end of the main text, then an approximate position of each table should be indicated in the text. The tables should be planned so as their final widths do not exceed 13 cm.

Electronic versions of the manuscripts should be sent to:

MatSci@pwr.wroc.pl

Material sent by conventional mail should be addressed to:

Professor Juliusz Sworakowski
Politechnika Wroclawska
I-30
Wybrzeże Wyspiańskiego 27
50-370 Wrocław
Poland

Web page of Materials Science-Poland: www.MaterialsScience.pwr.wroc.pl

2. Organisation of the Manuscript

The hard copy of the manuscript, submitted as a PDF file, should contain the material that can be reproduced in the A4 or letter size format, double spaced with ample margins throughout. All pages of the manuscript should be numbered consecutively, including references, figure captions and tables.

2.1. The First Page

The first page should be organised as follows:

Title of the paper

J.A. White[1], T.J. Brown[2*], M. Green[2**]
[1]Affiliation 1
[2]Affiliation 2
E-mail (only the corresponding author)

Abstract

An abstract of no more than 200 words

Key words

3 to 5 keywords, separated by semicolons (;)

* (**)Footnote(s)

2.2. Headings, Sub-headings

These should be placed in the main text as appropriate. The authors are encouraged to conform to the standard sequence of sections (e.g., Introduction; Experimental; Results; Discussion; Conclusions; etc.)

2.3. References

In the main text, references should be numbered consecutively by Arabic numerals in square brackets (e.g., [1]; [3, 4]; [7–11]). **Each reference should contain names of all authors**. The list of references should follow the main text and should be of the following format:

For a paper in a journal:

[1] KITAMURA T., YOKOYAMA M., J. Appl. Phys., 69 (1991), 821.

For a book:

[2] SWALIN R.A., *Thermodynamics of Solids*, Wiley, New York, 1962.

For a chapter in a book:

[3] WILD U.P., RENN A., *Spectral Hole-Burning*, [in:] H. Dürr and H. Bouas-Laurent (Eds.), *Photochromism. Molecules and Systems*, Elsevier, Amsterdam, 1990, p. 930.
Journal abbreviations should be in accordance with the standards of *Chemical Abstracts*.

Materials Science-Poland, Vol. 26, No. 1, 2008

CMOS evolution. Development limits

A. JAKUBOWSKI*, L. ŁUKASIAK

Institute of Microelectronics and Optoelectronics, Warsaw University of Technology,
ul. Koszykowa 75, 00-662 Warsaw, Poland

Evolution of complementary metal oxide semiconductor (CMOS) technology is presented from the very first MOS transistors to state-of-the-art structures. Difficulties of scaling are discussed together with ways to overcome them. New options for silicon microelectronics (SOI technology and strain engineering) are described. Finally, fundamental limitations to progress in semiconductor devices are considered.

Key words: *CMOS; scaling; silicon microelectronics; silicon on insulator;SOI; strained silicon*

1. Introduction

Global amount of information doubles every year. If the current growth trend is maintained till 2020, this amount will be doubling every two weeks. While it is not the intention of the authors to discuss advantages or disadvantages of this state of affairs, we believe that one of the most important factors that led to such unprecedented growth is semiconductor electronics. We admit that the need for communications and data processing appeared long before the invention of transistor or even before the beginnings of electronics. It should be noted, however, that the development of semiconductor devices plays an extremely important role in information technology.

The slide rule (the majority of the readers have probably never had a chance to use it) was invented in the first half of the 17th century and was widely used for over 300 years. It was even used to design the first microprocessor (Intel 4004). Today's microprocessors have incomparable computing power thanks to the development of silicon microelectronics. It was found many years ago that the temporal behaviour of this development is exponential which is widely known as Moore's law [1]. To be more accurate, the development of practically any area of human activity follows the so called logistic curve. In the beginning, the rate of progress is slow, then thanks to several discoveries an innovations it gains momentum and becomes exponential, finally it slows down due to the lack of knowledge, technical and economic limitations or, possibly, due to a change of interests until an unprecedented breakthrough takes the development to a higher level and the whole process is repeated again (Fig. 1).

*Corresponding author, e-mail: L.Lukasiak@imio.pw.edu.pl

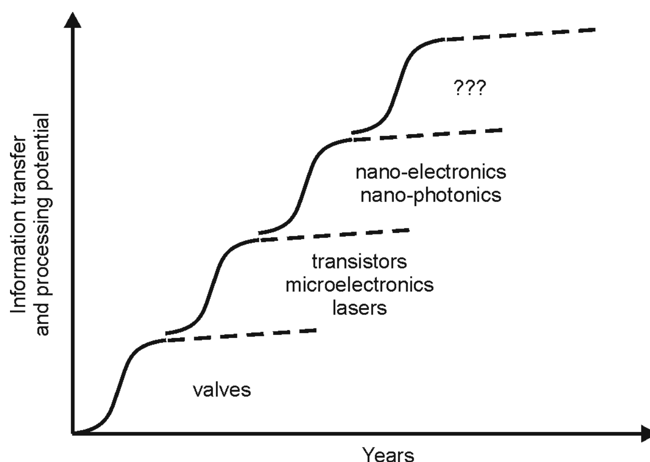

Fig. 1. Development of electronics

To illustrate the rate of exponential development, let us take dynamic random access memory (DRAM) as an example. Its capacity in 1970 was 1 kb, today it is 2 Gb. If we could find a way to multiply our financial means equally fast, during 37 years we would move from $1000 to 2 billion dollars! Obviously, budget planning in each of these two cases is an altogether different matter. With exponential development, a given quantity needs a specific time period to double its value (or to halve it). These periods are listed in Table 1 for several important microelectronics parameters.

Table 1. Examples of exponential development of silicon microelectronics [2]

Parameter	Trend	Period required to double/halve [years]
Average transistor price	decrease	1.6
Price of 1bit of DRAM	decrease	1.5
DRAM feature size	decrease	5.4
Processor performance (MIPS)	increase	2
Microprocessor clock frequency	increase	3
Total bits shipped	increase	1.1
Total transistors shipped	increase	1.5
DRAM capacity	increase	1.6

2. Evolution of MOSFET

Even though microelectronics started with germanium-based devices, silicon soon became its material of choice. This is because it is widely available and much cheaper than other semiconductor materials (see Table 2), it is easily passivated through oxida-

tion and has very good electrical properties. Recently it was found that silicon also has excellent mechanical properties, hence it has found application in microsystems.

Table 2. Prices of semiconductor substrates

Parameter	Material		
	Si	GaAs	InP
Wafer diameter*	12″	6″	4″
Wafer price [a.u.]	1	4	10
Price of 1 mm^2 [a.u.]	1	16	90

*Wafer diameters reflect the state-of-the-art in mass production in 2006.

A vast majority of integrated circuits are produced in CMOS technology. This technology is based on a pair of complementary MOSFETs (n-channel transistor and p-channel transistor). A schematic cross-section of a modern MOSFET is shown in Fig. 2.

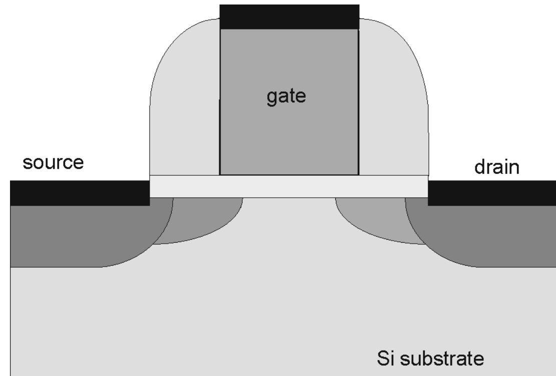

Fig. 2. A cross-section of a modern MOSFET

The principle of operation of this device is rather simple. If a sufficiently high positive voltage is applied to the gate, electrons are attracted to the semiconductor surface and a conductive channel is formed between source and drain making current flow possible. Gate voltage necessary to form the channel is called the threshold voltage V_T. According to the simplest theory of MOSFET, its most important parameters, that is drain current $I_{D\mathrm{sat}}$ and transconductance in saturation $g_{m\mathrm{sat}}$, may be described in the following way:

$$I_{D\mathrm{sat}} = \frac{W}{2L}\mu_{\mathrm{eff}} C_{\mathrm{diel}} \left(V_{GS} - V_T\right)^2 \tag{1}$$

$$g_{m\mathrm{sat}} = \frac{\partial I_{D\mathrm{sat}}}{\partial V_{GS}} = \frac{W}{L}\mu_{\mathrm{eff}} C_{\mathrm{diel}} \left(V_{GS} - V_T\right) \tag{2}$$

where: W, L are channel width and length, respectively, μ_{eff} is effective carrier mobility in the channel, C_{diel} – gate-dielectric capacitance per unit area, and V_{GS} stands for gate-to-source voltage.

To complete the description of MOSFET operation, a formula for cut-off frequency f_T is needed:

$$f_T = \mu_{\text{eff}} \frac{V_{GS} - V_T}{L^2} \tag{3}$$

In view of the above equations, the most obvious way to increase all these parameters would be to reduce channel length. If L is reduced 5 times it would be expected that the current will be five times higher at the same supply voltage, therefore a reduction of this voltage could be envisaged. The reduction of channel length upon time is shown in Fig. 3. It should be noticed that L decreased almost 3 orders of magnitude in approximately 30 years.

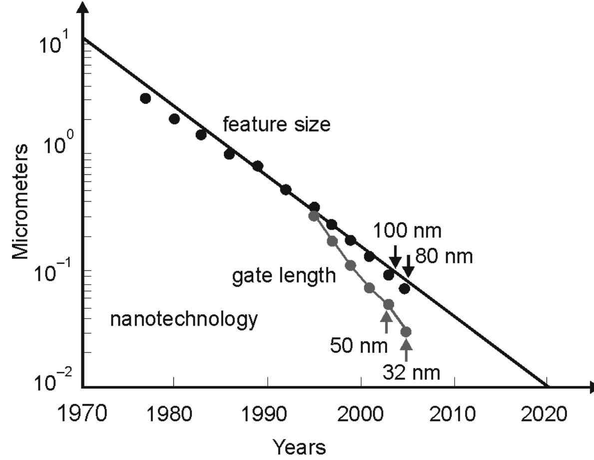

Fig. 3. Miniaturization of a semiconductor devices with time

This trend may be approximately described as:

$$L = 10\exp\left[-0.14\left(\text{year} - 1970\right)\right] \quad [\mu\text{m}] \tag{4}$$

In practice, however, reducing the channel length is not simple. Already in early seventies, when channel length of 1 μm was considered very short, it was found that drain field penetrates into the channel region which should normally be controlled by the gate, leading to lower threshold voltage values, especially at high drain voltages. Extensive studies indicated that to minimize this undesirable effect, the reduction of horizontal dimensions must be accompanied by an appropriate reduction of vertical ones (gate dielectric thickness and junction depth), increased doping and lowered supply voltage [3]. In fact, the evolution of MOSFET is a battle against so called

short-channel effects (SCE). A detailed history of MOSFET was presented in [4]. Here only a brief outline is given. Innovations implemented in MOSFET architecture are schematically illustrated in Fig. 4. The concept of a MOS structure was invented by Lilienfeld [5] in the late twenties. A great technological step towards today's MOSFETs was development of the silicon surface stabilization method by means of oxidation [6]. The first silicon MOSFET was presented in [7]. Not much later the concept of a CMOS inverter was invented [8]. Early MOSFETs had aluminum gate (Fig. 4a). Development of poly-Si gate [9] led to a self-aligned device (Fig. 4b), where the gate itself constitutes a mask for source and drain diffusion. In this way parasitic gate-to-source and gate-to-drain capacitances associated with gate overlap could be controlled.

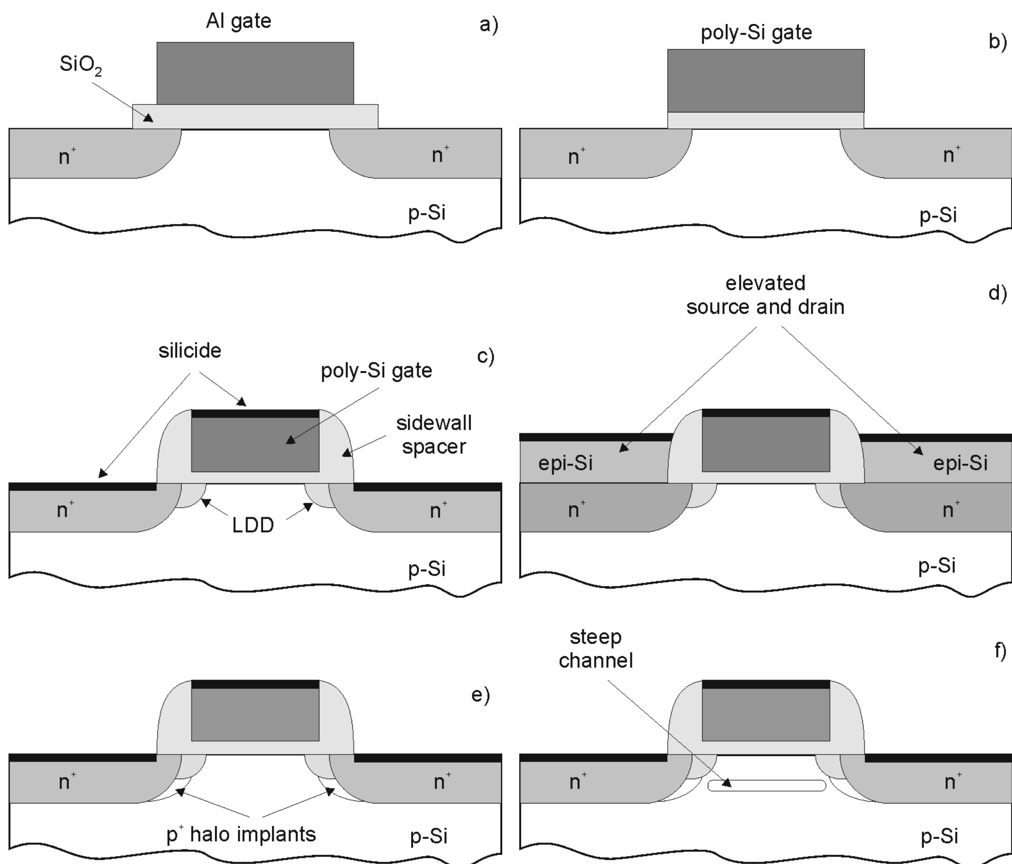

Fig. 4. Changes in MOSFET architecture: a) Al gate, b) self-aligned poly-Si gate, c) LDD structure with a silicided gate, source and drain, d) raised source and drain, e) halo implants, f) steep retrograde doping profile in the channel

As mentioned before, the main problem that appeared with the reduction of channel length was the short-channel effects (SCE). These undesirable phenomena are

caused by the fact that gate control over the channel is reduced by the influence of the drain potential (charge sharing). The most obvious result of this situation is that threshold voltage becomes dependent on channel length. One of the first models describing length-dependent threshold voltage was presented in [10]. Another short channel effect (the so called drain-induced barrier lowering DIBL [11]) is associated with interaction between source-channel barrier and drain potential. In long-channel devices this barrier is controlled by the gate. As the channel length is decreased, the drain potential affects the barrier, making threshold voltage dependent also on drain bias. Finally, as source and drain get closer, the risk of punch-through increases. Attempts made to minimize short channel effects concentrated on three different regions of the transistor, that is the source/drain, gate stack and channel.

2.1. Source/drain engineering

Control of SCE requires the reduction of source/drain junction depth [12]. This, however, increases the resistance of those regions, especially since doping concentration cannot exceed solid solubility limits. The first attempt to cope with this problem was lightly doped drain (LDD) together with spacer technology [13] (Fig. 4c). The shallow, lightly doped part of the drain served to reduce the maximum electric field. The deeper heavily doped part minimized the resistance. The spacer helped to control gate overlap holding parasitic capacitance in check. A further reduction of S/D resistance may be obtained through silicidation (Fig. 4c). Another way to reduce the parasitic resistance is to use elevated sources and drains (Fig. 4d) where the thickness of S/D regions is increased by selective Si epitaxy [14]. An ultimate solution to the problem might be the Schottky barrier S/D [15].

2.2. Channel engineering

Channel engineering is mostly intended to control threshold voltage and prevent punch-through. Increasing channel doping reduces the width of the depletion region thus minimizing SCE, it has however a deleterious effect on the mobility (e.g., [16]). Halo (pocket) implants were introduced [17] to control short channel effects by reducing the width of the depletion region and to increase device resistance to punch-through (Fig. 4e). A super-steep retrograde doping profile [18] in the channel serves for a better control of threshold voltage while keeping mobility high due to low surface doping (Fig. 4f).

2.3. Gate stack engineering

The structure of a gate stack is schematically shown in Fig. 5. Even highly doped, the poly-Si gate electrode represents a certain resistance. Deposition of a refractory metal silicide (the so called polycide) on top of the gate [19] helps alleviate this problem

(Fig. 4c). Gates made entirely of such silicides were also considered (e.g., [20, 21]). Self-aligned silicidation (salicidation) [22] made it possible to form silicide in selected regions (gate and S/D) without lithographic patterning. Another problem with poly-Si gates is depletion near the gate dielectric. Heavy doping reduces this effect but still in the on-state the equivalent gate oxide thickness (EOT) is increased by 0.4–0.5 nm. Slightly better results are obtained using poly-SiGe. It seems that metal gates will be the ultimate solution to this problem.

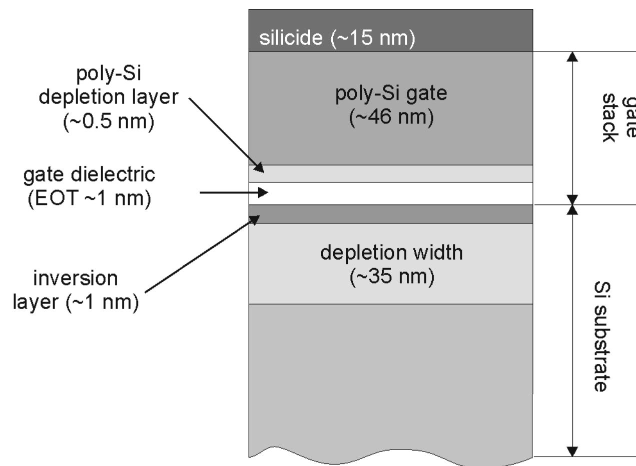

Fig. 5. Gate-stack structure

As seen from Eqs. (1) and (2), the reduction of gate-oxide thickness (increasing C_{diel}) results in higher current and transconductance. This is because the gate has better control of the channel. Changes of gate-oxide thickness over the years are shown in Fig. 6.

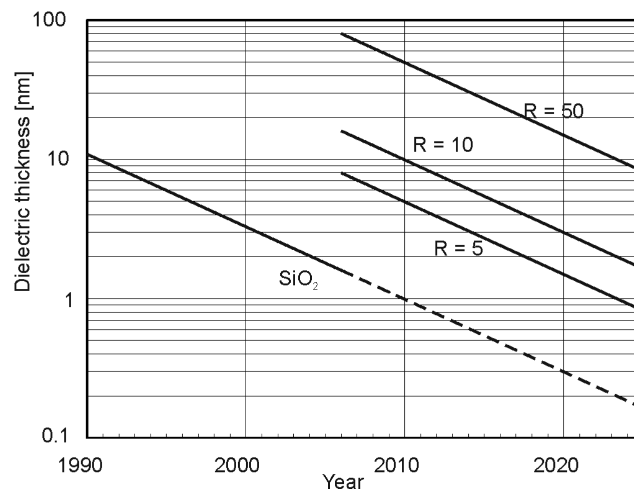

Fig. 6. Temporal evolution of the gate-oxide thickness

In an approximate way this trend may be described as:

$$t_{ox} = 120 \exp\left[-0.12\left(\text{year} - 1970\right)\right] \quad \text{[nm]} \tag{5}$$

As a result of decreased thickness, gate leakage current obviously grows, increasing power consumption of the entire chip, which is an undesirable effect for battery-powered mobile systems. It is estimated that gate leakage current increases approximately 30 times every technology generation, as opposed to 3–5 times increase of channel leakage current [23]. Apart from leakage current, the reduction of gate-oxide thickness increases the susceptibility of the device to boron penetration from the poly-Si gate into the channel. Replacing silicon dioxide with oxynitride (SiO_xN_y) is the most widely used solution to this problem (e.g., [24]). Eventually, however, oxynitride will have to give in to high-*k* dielectrics. If we assume that *R* is the ratio of the electric permittivity to that of SiO_2, then the layer of this dielectric may be *R* times thicker than SiO_2 and still produce the same capacitance at much lower leakage. The thickness of hypothetical materials with various values of *R* is plotted versus time in Fig. 6. Unfortunately, materials that might replace SiO_2 in the future have to meet several other requirements, such as resistance to thermal processing, low density of interface traps, sufficiently wide bandgap, etc. It seems that the gate dielectric will have to consist of two layers: a very thin buffer layer of SiO_2 to maintain high quality of the dielectric –semiconductor interface and a layer of high-*k* dielectric (Fig. 7). In the latter case, HfO_2 is believed to be the most promising candidate.

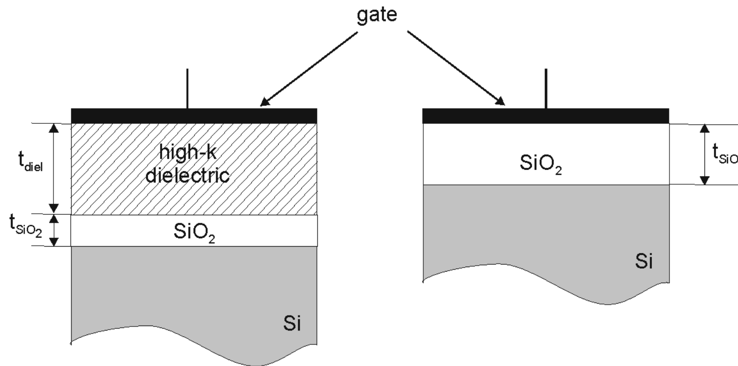

Fig. 7. Dual gate dielectric structure (left) compared to the standard structure (right)

2.4. Other scaling problems

Transport models used to describe semiconductor devices are usually developed with the assumption that device dimensions are much larger than the carrier free path. If this assumption is not justified, one has to deal with ballistic transport [25]. Moreover, progressing miniaturization causes device active regions to become ever smaller, therefore the number of dopant atoms in these regions decreases, too (Table 3). Thus

statistical fluctuations of doping concentration will become a challenge for process repeatability.

Table 3. Decreasing number of dopant atoms in the active region of a MOSFET

Parameter	Yesterday	Today	Tomorrow
Doping concentration [cm^{-3}]	10^{16}	10^{18}	10^{19}
Channel length [μm]	10	0.1	0.01
Channel width [μm]	10	0.25	0.01
Depletion width [μm]	0.3	0.03	0.002 (SOI)
Number of dopant atoms in the depletion region	3×10^{15}	750	2

3. Future progress

For the past 40 years the progress in silicon microelectronics was achieved mainly through miniaturization of both horizontal and vertical dimensions of the transistor. It seems, however, that this trend has to be accompanied by additional innovations to ensure the same rate of progress. It is believed [26] that there are four directions to follow: increasing inversion charge at constant voltage drive (i), improving carrier transport (ii), choosing ‘scaling-friendly’ device architectures to obtain shorter channels (iii) and reducing parasitic resistance and capacitance (iv).

3.1. Silicon on insulator

Silicon-on-insulator (SOI) technology [27] is the first step in the directions (i), (iii) and (iv). In this technology, the active region of a MOSFET is separated from the bulk

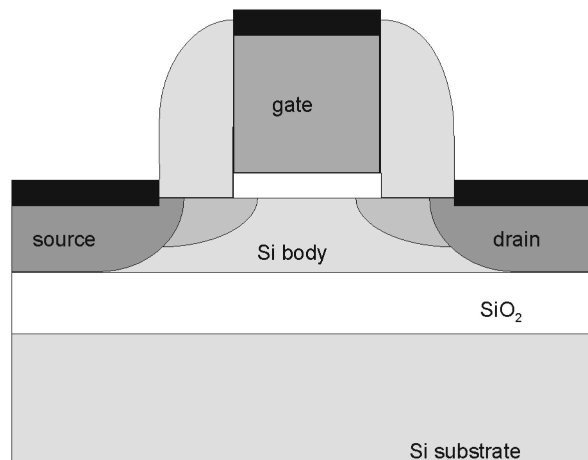

Fig. 8. Cross-section of a SOI MOSFET

silicon by a layer of buried oxide (BOX). A cross-section of a SOI device is shown in Fig. 8. The advantage of SOI is the ease of electrical insulation of a device from the rest of the integrated circuit, which increases packing density. Moreover, the areas of source and drain junctions are significantly reduced, thus decreasing parasitic capacitances. Finally, the depletion width is limited by the Si body thickness; therefore it is widely believed that SOI helps to reduce short channel effects (SCE) unless source-to-drain coupling through channel and BOX cannot be neglected. Properties of SOI devices are improved with the reduction of body thickness. It is believed that fully depleted ultra-thin-body SOI (FD UTB SOI) is one of the best scaling solutions. Due to excellent gate control of the channel, these devices may be undoped or very lightly doped. In this way, mobility is not degraded and threshold voltage is less dependent on the fluctuations of doping concentration [28].

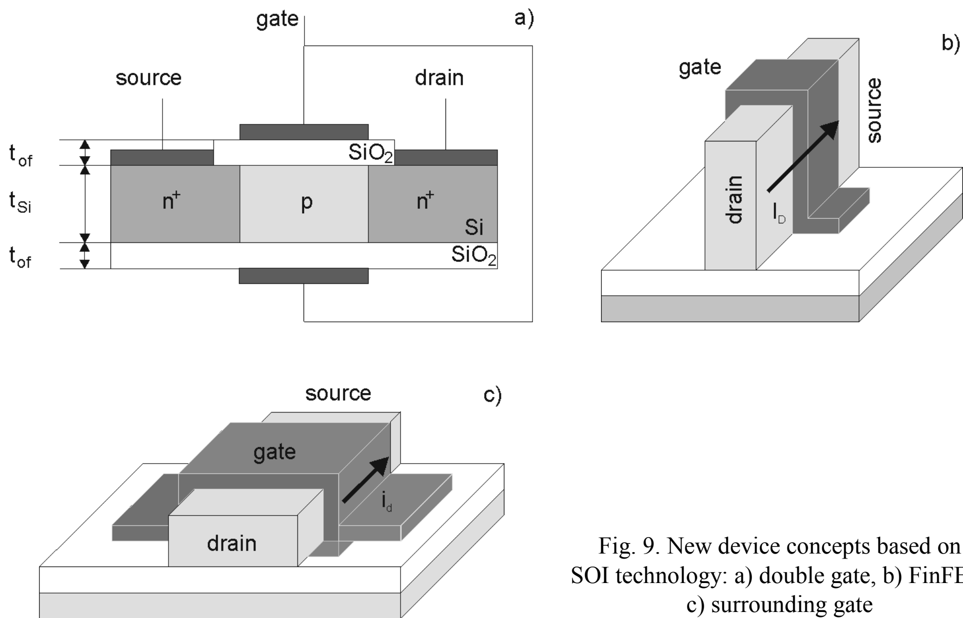

Fig. 9. New device concepts based on SOI technology: a) double gate, b) FinFET, c) surrounding gate

Another advantage of SOI is that it facilitates development of new device concepts. The first of those is the double-gate transistor (DG) shown schematically in Fig. 9a. Due to the presence of two gates, the influence of the longitudinal field induced by drain bias on the source-end of the channel is reduced [29], thus decreasing SCE. On the other hand, fabrication of these devices is not easy, especially alignment of the gates to one another and self-alignment of source and drain regions to both gates. These technological problems are considerably eased with a FinFET (Fig. 9b). A natural step forward is a transistor with a surrounding gate (e.g., [30]), presented in Fig. 9c. The ultimate surrounding-gate transistor is shown in Fig. 10. The geometry of a silicon nanowire makes gate control of the channel the highest possible.

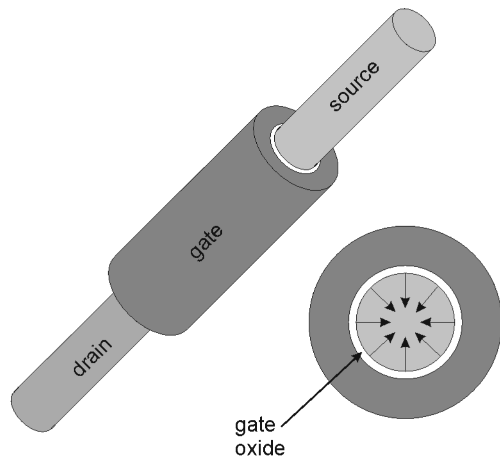

Fig. 10. Ultimate surrounding gate MOSFET

Due to undoped channels, the gate current is greatly reduced in FD UTB SOI and FinFETs [23] but the source-to-drain current in the off-state is not minimized easily. In Figs. 11a and 11b predictions of both these currents over the years are shown [31].

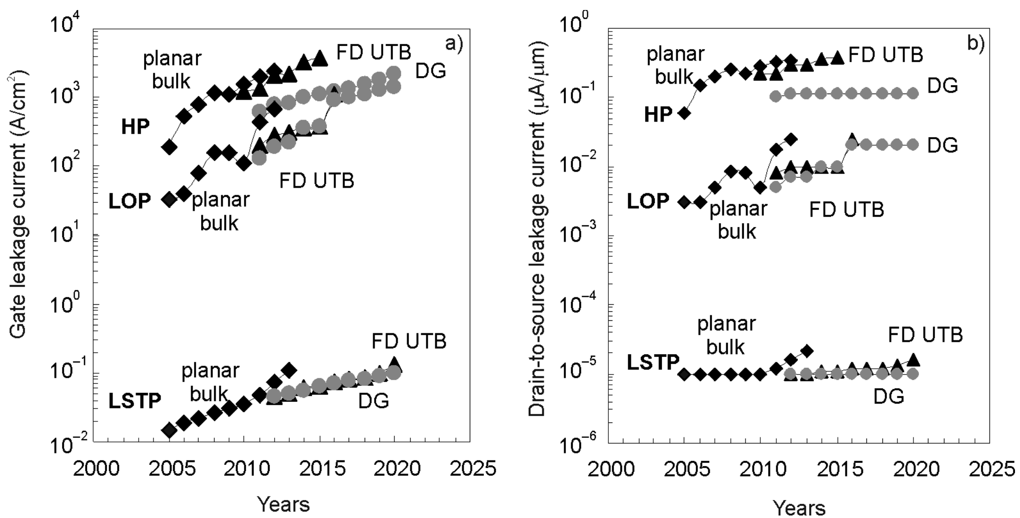

Fig. 11. Prediction [31] of gate leakage current (a) and source-to-drain current (b) for three application types: HP – high performance, LOP – low operation power, LSTP – low standby power

Unfortunately, as all human inventions, SOI technology is not perfect. One of its biggest problems is self-heating. Thermal conductivity of the buried oxide (1.4 $W \cdot m^{-1} \cdot K^{-1}$) is almost a hundred times lower than that of bulk Si (120 $W \cdot m^{-1} \cdot K^{-1}$). As a result, the mobility is lowered. Scaling of Si body thickness degrades thermal conductivity even further [23].

3.2. Stress engineering

While SOI technology is certainly a big step forward towards better devices, it does nothing to enhance transport properties. Carrier transport may be improved either using a high-mobility material in the channel (e.g. Ge, GaAs, etc.) or changing the properties of silicon by means of stress. Stress is introduced in the device using either a global technique (across the entire substrate) or a local one (based on epitaxial layers or high-stress cappings) [32]. The global approach consists, in, e.g., depositing a thin layer of silicon on a relaxed SiGe substrate (Fig. 12).

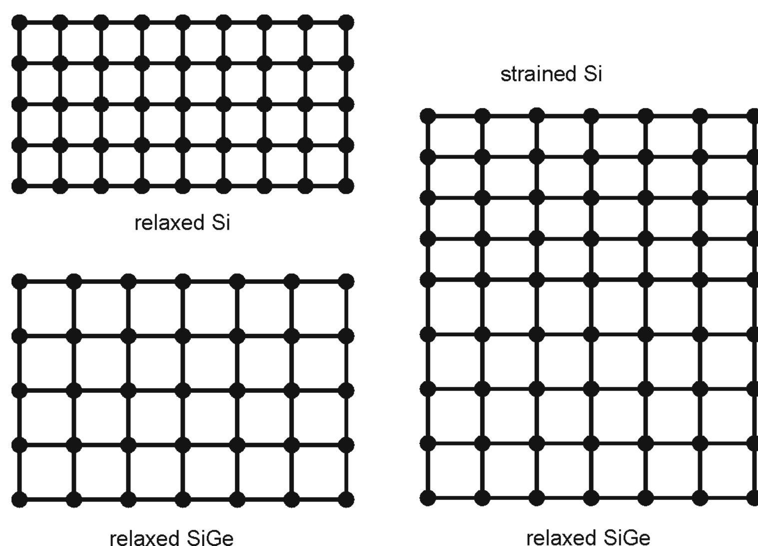

Fig. 12. Strained silicon on SiGe

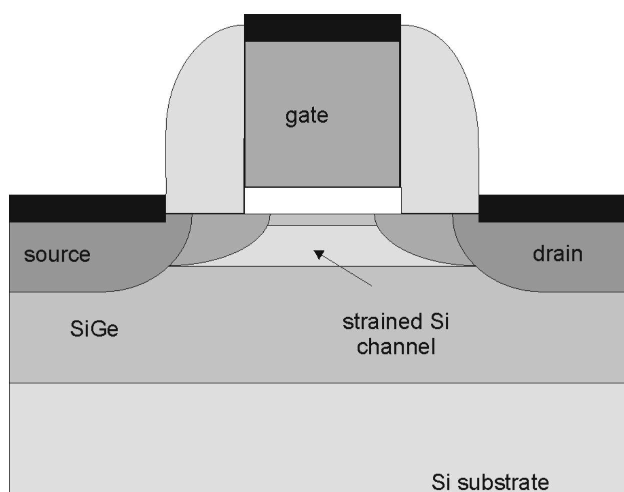

Fig. 13. MOSFET with a strained-silicon channel

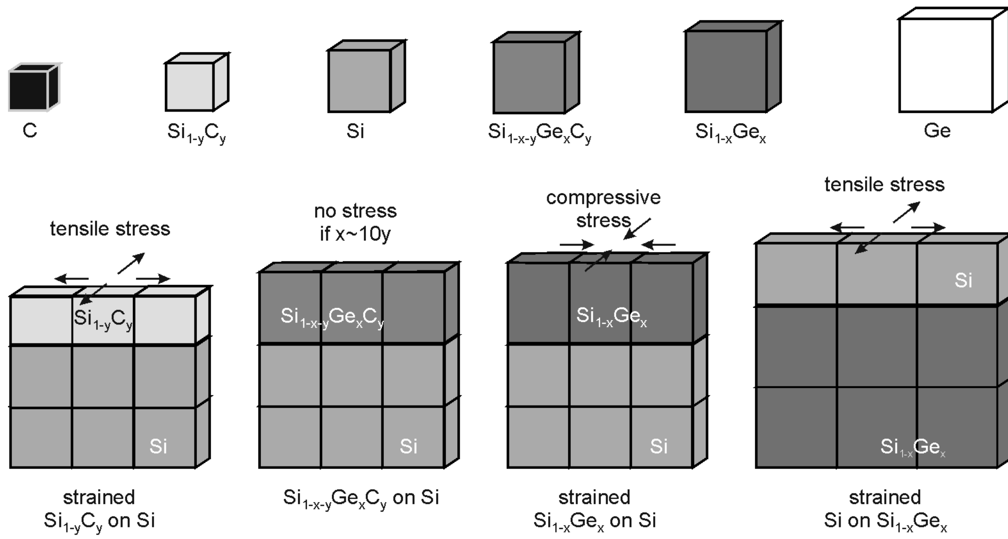

Fig. 14. Stress engineering – material combinations

Due to a lattice mismatch between SiGe and Si, the obtained silicon layer is strained improving electron mobility. A cross-section of a transistor with strained Si channel obtained by means of a global technique is shown in Fig. 13. Other material combinations that may be used for stress engineering are shown in Fig. 14. Local techniques include source and drain stressors (filling etched parts of source and drain with epitaxial SiGe for n-channel or SiC for p-channel devices) and deposition of highly tensile (Si_3N_4) or compressive (SiN) capping layers over complete devices. These techniques may also be combined to further improve transport properties.

4. Fundamental limitations

Fundamental limitations are often studied using a classical example of an ultimate laptop with the mass of 1 kg and volume of 1 dm^3 [33]. An elementary logic operation performed during time period Δt requires an average energy expense E determined from Heisenberg's uncertainty principle:

$$E \geq \frac{\pi\hbar}{2\Delta t} \tag{6}$$

As a result, a system with an average energy E may perform no more than $2E/\pi/\hbar$ logic operations during Δt. If, therefore, a 1-kg laptop has the energy of:

$$E = mc^2 = 8.9874 \times 10^{16} \text{ J} \tag{7}$$

it is capable of performing no more than 5.4×10^{50} operations per second. This simple calculation (its result is independent of computer architecture) indicates that we have

more than 200 years to go before this limitation kicks in, assuming that the current development rate (described by Moore's law) will be maintained in the future. It should be remembered though that modern computers contain many parts the mass of which cannot be transformed into data-processing energy. If we remember that energy determines velocity and entropy determines capacity (memory), another calculation leads to the conclusion that our ultimate laptop may contain up to approximately 2×10^{31} bits of memory. Other conclusions resulting from this analysis are less optimistic. The dissipated power and temperature of our computer are at the level of a huge nuclear explosion [33].

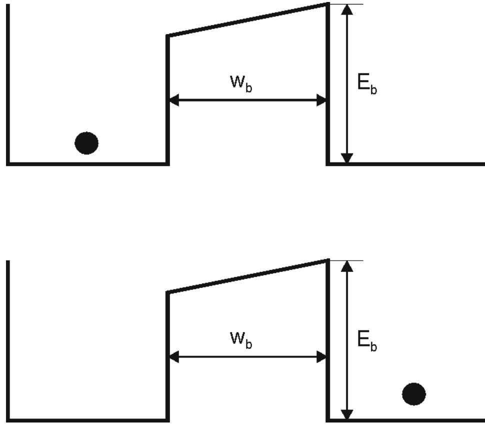

Fig. 15. Schematic illustration of a potential barrier in a switching device

Here is another simple analysis. Let us imagine that a bit of information is a charge carrier in a potential well. This well is separated from another one by a potential barrier E_b (Fig. 15). The classical probability of a carrier passing over the barrier is:

$$P = \exp\left(-\frac{E_b}{kT}\right) \tag{8}$$

According to the Shannon–von Neumann–Landauer expression, for both states to be distinguishable ($P < 1/2$) the barrier height must be at least:

$$E_b > kT\ln 2 \tag{9}$$

Let us assume that energy $E_b = 10kT$ is necessary to ensure that both states may be distinguished. If we use the uncertainty principle again, the time necessary to perform a logic operation is $\Delta t = 4\times10^{-15}$ s. If we assume further that our hypothetical switching device has the size of 5 nm×5 nm (considering recent progress in CMOS technology, such an assumption does not seem to be overly optimistic), the number of such devices packed in the area of 1 cm^2 is $N = 4\times10^{12}$. The power density is therefore:

$$P \approx N\times\frac{10kT}{\tau} \approx 4\times10^{7}\ \text{W/cm}^2 \tag{10}$$

It seems that heat removal will be the main scaling problem in the future. It will be more or less equally critical for any devices based on electron transport intended for digital logic [34]. Thus CMOS technology is still worth some effort. Moving beyond the above mentioned limitations requires considering of completely different physical principles of device operation.

5. Summary

Further scaling of silicon devices will most likely require new materials (e.g. strained silicon), and new device concepts (multi-gate structures enabled by SOI technology). We are confident that CMOS will overcome the difficulties it is facing. During the past 40 years the end of silicon microelectronics had been announced many times and never happened. Silicon technology needs enhancement, though (Fig. 16).

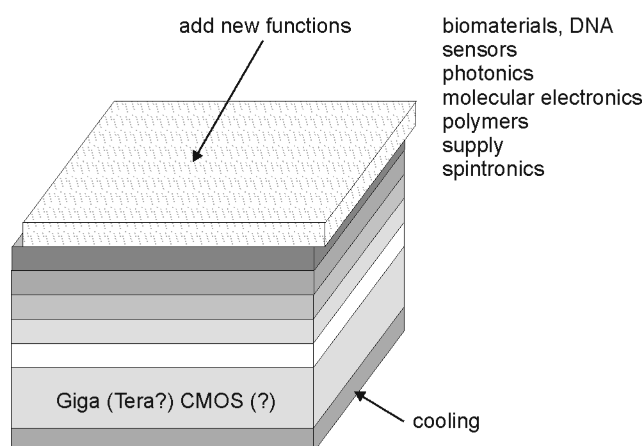

Fig. 16. Integration of silicon microelectronics with other technological solutions

It would be useful to integrate with new technological solutions (or new materials) to improve the functionality of the end product, e.g. silicon micromechanics, cooling systems, optical connections, molecular electronics or even spintronics.

References

[1] MOORE G.E., *Progress in digital integrated electronics*, IEEE Int. Dev. Meeting, Dig., 1975, p. 103
[2] KURZWEIL R., *The Singularity Is Near*, Penguin Books, 2005.
[3] DENNARD R.H., GAENSSLEN F.H., YU H.-N., RIDEOUT V.L., BASOUS E., LEBLANC A.R., IEEE J. Solid-State Circuits, 9 (1974), 256.
[4] SAH C.-T., Proc. IEEE, 76 (1988), 1280.
[5] LILIENFELD J.E., *Device for controlling electric current*, U.S. Patent 1 900 018. Application filed Mar. 28, 1928, granted Mar. 7, 1933.

[6] ATALLA M.M., TANENBAUM M., SHEIBNER E.J., Bell Syst. Tech. J., 38 (1959), 123.
[7] KAHNG D., ATALLA M.M., *Silicon–silicon dioxide field induced surface devices*, Proc. IRE-AIEE Solid-State Device Research Conference, Carnegie Institute of Technology, Pittsburgh, U.S.A., 1960.
[8] WANLASS F.M., SAH C.T., *Nanowatt logic using field-effect metal-oxide semiconductor triodes*, [in:] Technical Digest of the IEEE, Int. Solid-State Circuit Conf., 20.02.1963, pp. 32–33.
[9] KERWIN R.E., KLEIN D.L., SARACE J.C., *Method for making MIS structures*, U.S. Patent 3 475 234, filed Mar. 27, 1967, issued Oct. 28, 1969.
[10] YAU L.D., Solid State Electron., 17 (1974), 1059.
[11] TROUTMAN R.R., IEEE Trans. Electron. Dev., 26 (1979), 461.
[12] BREWS J.R., FICHTNER W., NICOLLIAN E.H., SZE S.N., IEEE Electron Dev. Lett., 1 (1980), 2.
[13] HUNTER W.R., HOLLOWAY T.C., CHATTERJEE P.K., TASCH A.F., IEDM Tech. Dig. (1980), 764.
[14] WONG S.S., BRADBURY D.R., CHEN D.C., CHIU K.Y., IEDM Tech. Dig. (1984), 634.
[15] MOCHIZUKI T., WISE K.D., IEEE Electron Dev. Lett., 5 (1984), 108.
[16] GHANI T., MISTRY K., PACKAN P., THOMPSON S., STETTLER M., TYAGI S., BOHR M., *Scaling challenges and device design requirements for high performance sub-50 nm gate length planar CMOS transistors*, Symp. VLSI Technology Dig. Tech. Papers, 2000, pp. 174–175.
[17] OGURA S., CODELLA C.F., ROVEDO N., SHEPARD J.F., RISEMAN J., IEDM Tech. Dig. (1982), 718.
[18] TIAN H., HULFACHOR R.B., ELLIS-MONAGHAN J.J., KIM K.W., LITTLEJOHN M.A., HAUSER J.R., MASNARI N.A., , IEEE Trans. Electron Dev., 41 (1994), 1880.
[19] CROWDER B.L., ZIRINSKI S., IEEE Trans. Electron Dev., 26 (1979), 369.
[20] MOHIZUKI T., SHIBATA K., INOUE T., OBUCHI K., KASHIWOGI M., ECS Extended Abstracts, 72-2 (1977), 331.
[21] SARASWAT K.C., MOHAMMEDI F., MEINDL J.D., IEDM Tech. Dig. (1979), 462.
[22] TING C.Y., IYER S.S., OSBURN C.M., HU G.IJ., SCHWEIGHART A.M., *The use of $TiSi_2$ in a self-aligned silicide technology*, ECS Extended Abstracts, 82-2 (1982), 254.
[23] CHUANG C.-T., BERNSTEIN K., JOSHI R.V., PURI R., KIM K., NOWAK E.J., LUDWIG T., ALLER I., IEEE Circuits Dev. Mag., Jan./Feb. 2004, 6.
[24] ZEITZOFF P.M., CHUNG J.E., IEEE Circuits Dev. Mag., Jan/Feb 2005, 4.
[25] LUNDSTROM M., GUO J., *Nanoscale Transistors – Device Physics, Modeling and Simulation, Springer*, New York, 2005.
[26] WONG H.-S.P., Solid State Electron., 49 (2005), 755.
[27] COLLINGE J.-P., *Silicon-on-Insulator Technology: Materials to VLSI*, Kluwer, Boston, 2004.
[28] SKOTNICKI T., HUTCHBY J.A., KING T.-J., WONG H.-S.P., BOEUF F., IEEE Circuits Dev. Mag., Jan./Feb. 2005, p. 16.
[29] NOWAK E.J., ALLER I., LUDWIG T., KIM K., JOSHI R.V., CHUANG C.-T., BERNSTEIN K., PURI R., Turning silicon on its edge, IEEE Circuits Dev. Mag., Jan/Feb 2004, p. 20.
[30] COLINGE J.-P., Solid State Electron., 48 (2004), 897.
[31] *International Technology Roadmap for Semiconductors*, Semiconductor Industry Association, 2006.
[32] MOHTA N., THOMPSON S.E., Mobility enhancement, IEEE Circuits Dev. Mag., Sept/Oct, 2005, p. 18.
[33] LLOYD S., Nature, 406 (2000), 1047.
[34] ZHIRNOV V.V., CAVIN R.K., HUTCHBY J.A., BOURIANOFF G.I., Proc. IEEE, 91 (2003), 1934.

Received 28 April 2007

Materials Science-Poland, Vol. 26, No. 1, 2008

Isotropic effects in exchange-biased ferromagnetic /antiferromagnetic bilayers

T. BŁACHOWICZ*

Department of Electron Technology, Institute of Physics, Silesian University of Technology, ul. Krzywoustego 2, 44-100 Gliwice, Poland

Novel, direction-independent (rotatable) spin-wave frequency modifications in a ferromagnetic layer biased by an antiferromagnetic film, revealed recently with Brillouin light scattering, have been analyzed. Physical conditions needed for the rotatable behaviour observations in epitaxial layers have been presented. The omni-rotatable down-shift, being a function of a spin-wave frequency, was distinguished from the up-shift of spin-wave frequencies induced by the exchange-bias. Additionally, the rotatable anisotropy constant was estimated from the available BLS results.

Key words: magnetoelectronics; exchange bias; rotatable anisotropy; Brillouin light scattering

1. Introduction

Different types of magnetoelectronic devices based on thin-film technology require a proper adjustment of structural, energetic and electronic parameters of materials. A fundamental functionality of these devices results from magnetic anisotropy fields, influencing the static and dynamic behaviour of magnetization. Among many types of magnetic anisotropies employed in magnetoelectronics, magnetocrystalline anisotropies and shape anisotropies are of special, practical importance.

Noteworthy, for the special case of a ferromagnetic (FM) film deposited onto an antiferromagnetic (AFM) layer, two new anisotropy fields can be induced. They may be subdivided into directional (unidirectional) and non-directional (rotatable) ones. In the former case, a ferromagnetic hysteresis loop is shifted along an externally applied magnetic field direction, thus a magnetic response is sensitive to different magnetic fields intensities enabling an adjustment of the ferromagnetic material performance. This effect is nowadays applied in spin-valves [1–3]. In the non-directional case, ferromagnetic spins are disturbed uniformly what results in a drop of the FM spins energy. The rotatable behaviour was discovered by McMichael et al. [4] in polycrystal-

*Corresponding author, e-mail: tomasz.blachowicz@polsl.pl

line exchange-biased materials using a ferromagnetic resonance (FMR), and recently by Błachowicz et al. [5], in epitaxial exchange-biased Co/CoO bilayers with the use of Brillouin light scattering (BLS). Within these BLS studies the up-shift of spin-wave frequencies was observed.

It should be pointed out that while the hysteresis-loop shifts represent a static aspect of the exchange-bias phenomenon, the rotatable effects revealed in the GHz range of frequencies through FMR or BLS experiments represent a dynamical part of the exchange-bias effect [6]. In this sense, a classical definition of the exchange-bias emphasizing the directional FM hysteresis loop shift, provided by Meiklejohn and Bean [7], addresses the static aspect of this phenomenon.

In this paper, BLS experimental conditions needed for rotatable effects observations are reported. Also, the epitaxial CoO(110) 20 nm/Co(110) 6 nm system [5], where there is no evidence for the out-of-plane magnetocrystalline anisotropies, is analyzed from the rotatable anisotropy point of view. Additionally, a rotatable anisotropy constant for this sample has been determined from BLS experimental results.

2. Experimental requirements

Both FMR and BLS methods are similar in principle, being perturbative methods. Samples are measured in the presence of an externally applied magnetic field at saturation and the magnetization vector, kept in a given direction, is disturbed from a local equilibrium state; this gives an access to the measured spin-wave frequencies. In the BLS experiments, a surface spin-wave frequency propagating in a given in-plane direction is measured. This wave is known as the Damon–Eshbach (DE) mode [9]. The DE mode frequency is dependent on all external and internal magnetic fields.

The BLS measurements are usually made using a Sandercock tandem 3-pass spectrometer [10], and an Ar^+ ion single-mode laser in the back-scattering geometry. The external magnetic field ($B < 1$ T) is applied in the sample plane in order to induce spin waves propagating on its surface. Measurements are carried out above and below the Néel temperature of the antiferromagnetic (AFM) layer. In a typical situation, low temperature measurements (~140 K) are easy to perform [5]. Additionally, a series of in-plane measurements for various sample orientations is needed; a sample is usually rotated in-plane, in the range of 0–360°, in order to detect magnetic surface anisotropies. More details about the BLS experiments can be found elsewhere [8].

However, in order to measure rotatable effects using BLS method, the sample has to reveal only in-plane magnetic anisotropies. The reason is that for samples with out-of-plane anisotropies, distinction between perpendicular contributions and rotatable anisotropies is not possible as both the contributions can be angle-independent. A good candidate meeting above criteria is a sample grown epitaxially on the MgO(110) substrate in a UHV MBE chamber. The sequence of layers was MgO(110)/CoO(20 nm)/Co(6 nm). The Co layer had the fcc structure with no evidence for out-of plane contributions. The CoO/Co sample structural details are described in Ref. 5.

3. Analysis of BLS results revealing a rotatable anisotropy

One of the main goals of the BLS experiments with a magnetoelectronic material is to determine anisotropy constants. A numerical fitting procedure is usually applied to the measured spin-wave frequencies ω_{DE} according to the following formula of the DE mode [9]

$$\frac{\omega_{DE}^2}{\gamma} = \left(\left[\frac{1}{M_s}\frac{\partial^2 E_{\text{ani}}}{\partial\theta^2} + \frac{2A}{M_s}q^2 + 4\pi M_s f\left(1-\frac{1}{2}q_{\text{II}}d\right) + H_{\text{ext}}\cos(\phi-\phi_H) + H_{\text{rot}} \right] \right.$$
$$\times\left[\frac{1}{M_s}\frac{\partial^2 E_{\text{ani}}}{\partial\phi^2} + \frac{2A}{M_s}q^2 + 4\pi M_s f\frac{1}{2}q_{\text{II}}d\sin^2(\phi-\phi_q) + H_{\text{ext}}\cos(\phi-\phi_H) + H_{\text{rot}} \right] \quad (1)$$
$$\left. -\left(\frac{1}{M_s}\frac{\partial^2 E_{\text{ani}}}{\partial\theta\partial\phi} \right)^2 \right)$$

where γ is the gyromagnetic ratio, M_s is the magnetization at saturation, E_{ani} is the free energy density, A is the exchange stiffness constant, q^2 is the squared wave-vector of a spin wave, f is the demagnetization factor which controls the balance between the shape anisotropy and out-of-plane anisotropy contributions, q_{II} is the in-plane component of a spin-wave wave-vector, H is the externally applied magnetic field intensity, H_{rot} is the isotropic (rotatable) field, $(\phi - \phi_H)$ is the angle between external magnetic field vector $\vec{H}$ and the magnetization $\vec{M}$, and $(\phi-\phi_q)$ is the angle between the $\vec{q}$ wave-vector and the magnetization $\vec{M}$. The constant values in Eq. (1) are: $\gamma = (1/2)\gamma_e g$, $\gamma_e = -1.759\times10^7$ Hz/Oe being the free electron gyromagnetic ratio. For the Co case, another set of physical constants can be applied: $g = 2.2$ – the spectroscopic splitting factor, $A = 3\times10^{-11}$ J/m, and $4\pi M_s = 17.8$ kOe ($M_s = 1.42\times10^6$ A/m).

For a simplified case (simplified Eq. (1)), with the lack of the out-of-plane and magnetoelastic anisotropies, the following formula for the spin-wave frequency can be employed (see discussion in [5]):

$$\frac{\omega_{DE}^2}{\gamma} = \left[\frac{2A}{M_s}q^2 + 4\pi M_s\left(1-\frac{1}{2}q_{\text{II}}d\right) + H_{\text{ext}}\cos(\phi-\phi_H) + H_{\text{rot}} \right]$$
$$\times\left[\frac{1}{M_s}\frac{\partial^2 E_{\text{ani}}}{\partial\phi^2} + \frac{2A}{M_s}q^2 + 4\pi M_s\frac{1}{2}q_{\text{II}}d\sin^2(\phi-\phi_q) + H_{\text{ext}}\cos(\phi-\phi_H) + H_{\text{rot}} \right] \quad (2)$$

As results from Eqs. (1), (2), measured spin-wave frequencies depend on several local fields acting on the magnetization. For example, looking at the second main factor in Eq. (2), we can easily recognize the following fields (from left to right): the anisotropy-energy field (the magnetocrystalline energy and the exchange-bias), the

quantum effective exchange-energy field, the demagnetization energy field, the Zeeman energy field, and finally the rotatable anisotropy field which can be described by the following angle-independent expression

$$H_{\mathrm{rot}} = \frac{1}{M_s} K_{\mathrm{rot}} \tag{3}$$

where K_{rot} is the rotatable anisotropy constant.

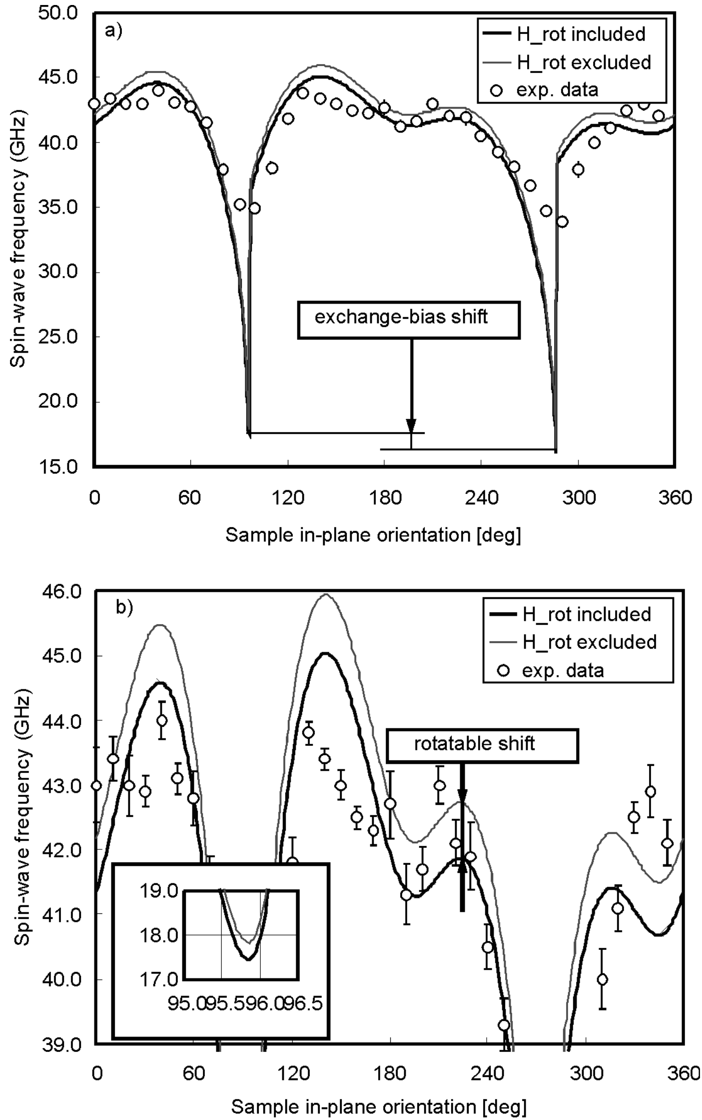

Fig. 1. Spin-wave frequencies as a function of an in-plane sample orientation: a) general view, b) zoomed view. The overall rotatable frequency shift is negative

In order to calculate the magnetocrystalline and exchange-bias contributions to the observed frequency behaviour (Eqs. (1), (2)), the following expression for the free energy density can be applied

$$F_{ani}(\phi) = K^{(4)}\cos^2(\phi)\sin^2(\phi) + K^{(2)}\cos^2(\phi) + K_{eb}\cos(\phi - \phi_{eb}) \qquad (4)$$

where $K^{(4)}$ and $K^{(2)}$ are the effective 4-fold and 2-fold symmetry anisotropy constants, respectively, ϕ is the sample orientation angle measured in respect to the sample edge, and ϕ_{eb} is the easy-direction of the exchange-bias (unidirectional) anisotropy field.

In Figure 1, measured spin-wave frequencies as functions of sample in-plane orientations have been shown with fittings to experimental data using Eqs. (2), (3), with the rotatable contribution (thick line), and without the rotatable contribution H_{rot} (thin line). Fig. 1b shows zoomed details giving some insight into a frequency dependence of the rotatable anisotropy. It is evident that the rotatable shift is larger for higher spin-wave frequencies.

Table 1. Anisotropy constants of the MgO(110)/CoO/Co sample obtained from the BLS measurements at 140 K

$K^{(4)}$(×10^4 J/m^3)	$K^{(2)}$(×10^4 J/m^3)	K_{eb}(×10^4 J/m^3)	K_{rot}(×10^4 J/m^3)
–16.4	–32.5	8.1	–14.1

Values of $K^{(4)}$, $K^{(2)}$, K_{eb} constants taken from [5].

In Table 1, the fitted anisotropy constants are given. The obtained negative value of K_{rot} constant is equivalent to down-shift of frequencies visible in Fig 1. A similar down-shift of frequencies was observed in the FMR experiments [4, 6]. We can also notice that the use of the H_{rot} term improves matching between experimental data and theory.

4. Conclusions

The results of the rotatable effects, obtained for the sample grown epitaxially – revealing in-plane anisotropies only – have shown that the rotatable anisotropy follows spin-wave frequencies for various sample orientations. The rotatable frequency down-shift is maximized (~0.9 GHz) in directions where the largest spin-wave frequencies were obtained (45 GHz at 140º position). On the other hand, a lower value of the rotatable shift (~0.4GHz) was obtained at about 96º position for the 17.5 GHz spin wave frequency (see inset in Fig. 1b).

The overall rotatable spin-wave frequency down-shift is a relatively small quantity, of the order of 2% in comparison to the measured spin-wave frequencies. The observed exchange-bias, readout from the dependences between spin-wave frequen-

cies and the sample in-plane orientations (Fig. 1), was a larger quantity. The difference between the frequencies at 96º and 186º positions equalled to 1.5 GHz. However, it is difficult to claim at this stage of investigations, if it is a rule that the exchange-bias shift dominates over the rotatable shift.

The current results address the issue of time-scales used in BLS and FMR experiments, what was first emphasized by McMichael et al. [6]. They claimed that during a typical BLS data collection, which runs in minutes or hours, the magnetocrystalline anisotropies, exchange-bias, and the shape anisotropies are stable as samples are kept at saturation. However, the precession time-period of the magnetization vector, involved in a wave-like movement (a spin-wave), is of the order of 10^{-10} s (GHz range). Thus at these time scales, the processional movement of magnetization can lose the contact with static, e.g. magnetocrystalline contributions, exerting an additional dynamical torque onto the AFM interface antiferromagnetic spins. Additionally, these antiferromagnetic spins have to overcome energy barriers associated with antiferromagnetic partial domain-walls. This is why we should expect a reduction of the FM spins energy. We also expect that when the precession time-scales are shorter (spin-frequencies are higher), the subsequent angle-independent rotatable-behaviour should be more intense.

References

[1] KAKA S., NIBARGER J. P., RUSSEK S. E., STUTZKE N. A., BURKETT S. L., J. Appl. Phys., 93 (2003), 7539.

[2] MOYERMAN S., ECKERT J. C., BORCHERS J. A., PERDUE K. L., DOUCET M., SPARKS P. D., CAREY M. J., J. Appl. Phys., 99 (2006), 08R505.

[3] VAN DIJKEN S., CROFTON M., CZAPKIEWICZ M., ZOLADZ M., STOBIECKI T., J. Appl. Phys., 99 (2006), 083901.

[4] MCMICHAEL R. D., STILES M. D., CHEN P. J., EGELHOFF W. F., J. Appl. Phys., 83 (1998), 7037.

[5] BLACHOWICZ T., TILLMANNS A., FRAUNE M., GHADIMI R., BESCHOTEN B., GÜNTHERODT G., Phys. Rev. B, 75 (2007), 054425.

[6] MCMICHAEL R. D., LEE C. G., STILES M. D., SERPA F. G., CHEN P. J., EGELHOFF W. F., J. Appl. Phys., 87 (2000), 6406.

[7] MEIKLEJOHN W.H., BEAN C.P., Phys. Rev., 105 (1957), 904.

[8] BLACHOWICZ T., GRIMSDITCH M. H., [in:] *Inelastic Scattering Technique – Brillouin, Encyclopedia of Condensed Matter Physics*, G. Bassani, G. Liedl, P. Wyder (Eds.), Elsevier, UK, 2005, p. 199.

[9] ESHBACH R., DAMON R. W., Phys. Rev., 118 (1960), 1208.

[10] MOCK R., HILLEBRANDS B., SANDERCOCK R., J. Phys. E: Sci. Instrum., 20 (1987), 656.

Received 28 April 2007
Revised 16 February 2008

Materials Science-Poland, Vol. 26, No. 1, 2008

A new drain insulation design in GaAs SD-MAGFET

B. BORATYŃSKI[1*], W. KORDALSKI[2], B. ŚCIANA[1], M. PANEK[1], I. ZBOROWSKA-LINDERT[1]

[1]Faculty of Microsystems Electronics and Photonics,
Wrocław University of Technology, ul. Janiszewskiego 11/17, 50-370 Wrocław

[2]Faculty of Electronics, Telecommunications and Informatics,
Gdańsk University of Technology, ul. Narutowicza 11/12, 80-952 Gdańsk

A new design of a split-drain MAGFET type magnetic sensor based on GaAs MESFET device with a sandwich-like drain configuration has been investigated. An excellent performance of the sensor, namely its high sensitivity and spatial resolution to magnetic field could be obtained as a result of an extremely short (200 nm) distance between the transistor drains realized using a unique epitaxial layer structure. A proper sequence of the AlGaAs/GaAs/AlAs/GaAs epitaxial layers grown by MOCVD technique followed by selective etching process has been proposed and realized. Structural parameters of the layers were studied. Electrical performance of the insulated drain structure was evaluated by measurements of the leakage current that was less than 10 nA for 2 V drain voltage bias difference.

Key words*: MAGFET; GaAs MESFET; epitaxial growth*

1. Introduction

Split-drain magnetic field sensitive field-effect-transistors (SD-MAGFET) are widely known magnetic field sensors [1]. Usually they are based on Si MOSFET devices with two or three split-drain contacts separated vertically, i.e., by an insulating layer perpendicular to the sensor surface. MAGFET sensors are also fabricated in GaAs technology and are based on HEMT type or resistor type [2] structures with high mobility 2DEG (2-dimensional electron gas).

Independently of the used technology, SD MAGFET sensors are based on the Hall effect and the resulting current difference between the two drains in the presence of a magnetic field. The sensitivity of a two-drain device is defined as

$$S = \frac{I_{d2} - I_{d1}}{\left(I_{d2} + I_{d1}\right)\left|B\right|}$$

[*]Corresponding author, e-mail: Boguslaw.Boratynski@pwr.wroc.pl

where ($I_{d2} - I_{d1}$) is the measured output signal, i.e., the drain current imbalance, directly proportional to the carrier mobility and the channel length. On the other hand, the differential current signal is inversely proportional to the separation distance between the drains. Locating the drain regions as close to each other as possible would increase the sensitivity as well as spatial resolution of a magnetic field, especially for small cross section area MAGFETs.

In this view, a new design approach for GaAs based MAGFET, where the drains are located one on top of the other (horizontally split-drains) separated by an electrically insulating layer, has been proposed [3]. The device structure is made of several epitaxial layers and subsequently etched mesas. A unique performance advantage of the device is its high sensitivity and spatial resolution due to extremely short distance between the drains, of the order of 200 nm (thickness of the epitaxial layer). Such a small drain separation is obtained using a GaAs/AlAs epitaxial structure that gives an efficient carrier collection and at the same time provides electrical insulation between the drain regions. A schematic view of the proposed split-drain MAGFET structure, in this particular case with two gate electrodes for a better current control, is shown in Fig. 1.

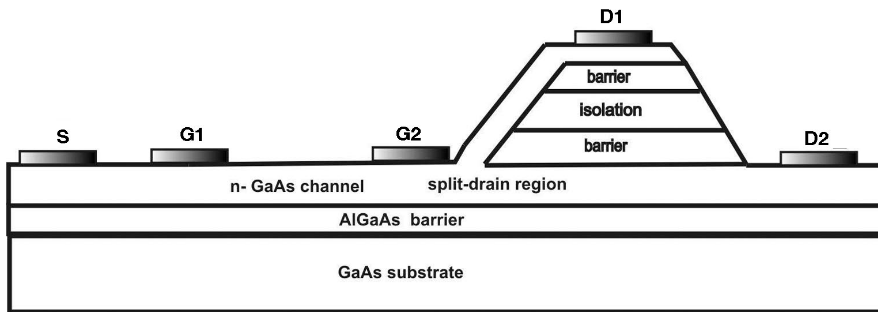

Fig. 1. Schematic view of a MAGFET structure (drawing not to scale)

In this work, a proper growth of the epitaxial layer sequence and subsequent layer selective etching processes have been investigated. The study is focused on the drain insulation region. The electrical performance of the structure is characterized by capacitance–voltage and current–voltage measurements.

2. Fabrication

Epitaxial structures of MAGFET sensors were grown by atmospheric pressure metal organic vapour phase epitaxy (APMOVPE) with an AIX200 R&D horizontal reactor. The following epilayers were grown on (100) – oriented semi-insulating (SI) GaAs substrate (layer thickness and carrier concentration are given):

- Undoped (UD) buffer heterostucture: GaAs (0.5 μm)/ $Al_{0.3}Ga_{0.7}As$ (0.5 μm).
- Two silicon-doped GaAs epilayers: n-GaAs (0.2 μm, $n \approx 2\times10^{17}$ cm^{-3})–n^{+}GaAs (0.2 μm, $n \approx 3\times10^{18}$ cm^{-3}), created a channel and a contact layer (drain D2) of the MAGFET.

• A sequence of three layers formed an insulation between two drains:
– a zinc-doped p^+-GaAs layer (20 nm, $p \approx 1\times10^{19}$ cm^{-3}),
– an undoped (UD) AlAs (0.2 μm),
– a zinc-doped p^+-GaAs layer (20 nm, $p \approx 1\times10^{19}$ cm^{-3}).
• Two silicon-doped GaAs epilayers: n-GaAs (0.1 μm, $n \approx 2\times10^{17}$ cm^{-3})–n^+GaAs (0.1 μm, $n \approx 3\times10^{18}$ cm^{-3}), created a channel and a contact layer (drain D1) of the MAGFET.

The growth process was carried out at 670 °C except of the AlAs epilayer grown at a higher temperature (760 °C) to improve its structural properties. Trimethylgallium (TMGa), trimethylaluminium (TMAl), arsine (AsH_3: 10% mixture in H_2), diethylzinc (DEZn) and silan (SiH_4: 20 ppm mixture in H_2) were used as the growth and dopant precursors. High purity hydrogen was employed as a carrier gas.

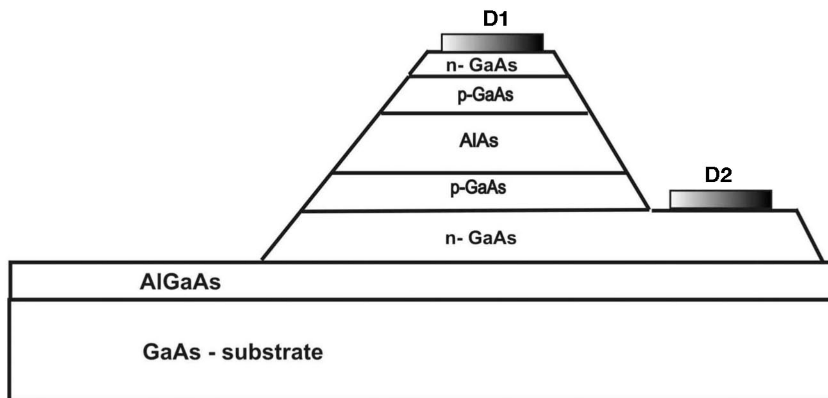

Fig. 2. The investigated insulated drain structure

Mesa type delineations of the structures were performed by several selective wet chemical etching steps in buffered hydrofluoric acid and citric acid, for AlAs and GaAs layers, respectively. The total height of the etched mesas was 0.9 μm and the diameter of the mesa structure was 150 μm. Ohmic contacts were obtained in a standard procedure using AuGe/Ni/Au metalization and alloying at 450 °C. A complete test structure is shown in Fig. 2.

3. Structural and electrical properties

Structural and electrical properties of the obtained MAGFET heterostructures were estimated using a Philips high resolution materials research diffractometer (HRMRD) with a four-crystal Bartels monochromator, a Bons/Hart analyser and a Bio-Rad PN 4300 electrochemical capacitance–voltage (EC–V) profiler. The rocking curves measurements (Fig. 3) allowed evaluation of the compositions and thicknesses of the epilayers. The angle distance between the reflexes from the GaAs sub-

strate and from AlGaAs (or AlAs) gives information about the aluminium content in the layer. The value $x = 0.34$ was estimated for the $Al_xGa_{1-x}As$ buffer. The presence of the Pendellösung fringes indicates good structural quality of the structure and gives information about the thickness of all epilayers except for GaAs buffer.

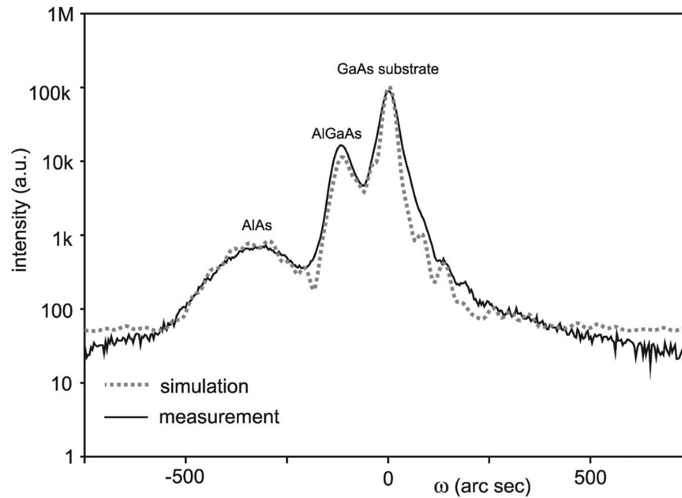

Fig. 3. Rocking curves of the MAGFET sensor structure for the (004) reflection (line – measurement, dots – simulation)

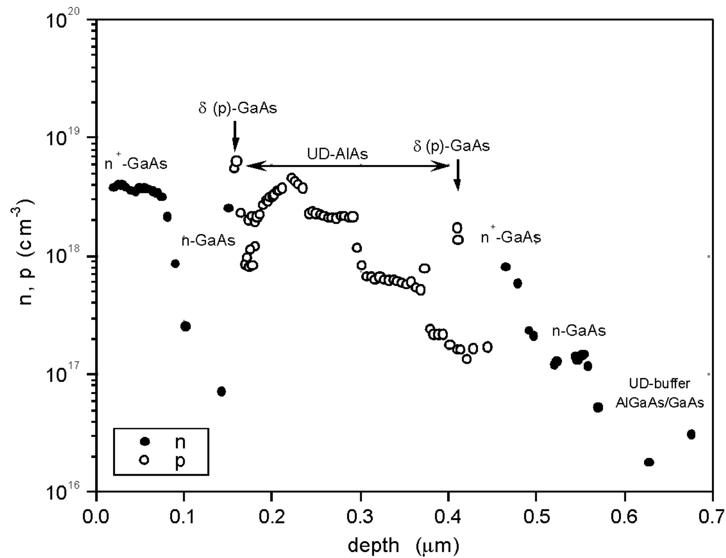

Fig. 4. EC-V profile of the MAGFET sensor structure

Carrier concentration in the doped layers of the MAGFET was determined by EC–V measurements. The method uses a capacitance–voltage analysis of a reverse

biased electrolyte–semiconductor Schottky junction. The obtained EC–V profile is shown in Fig. 4. The carrier concentration in every layer was readable. Determination of the carrier concentration in the undoped AlAs layer was difficult due to the etching problems.

4. Current-voltage characteristics

An important feature of the split-drain sensor is the electrical insulation between the drains. The current from the transistor source is distributed into two drain currents that should be of equal value in the absence of a magnetic field. A balance of the drain currents could also be obtained by changing the voltage bias of one drain with respect to the other. To accomplish the equilibrium condition, the drain regions should be electrically insulated. Current–voltage characteristics of the structure have been recorded sensing the current between drains and between source and drains. A typical characteristic of the voltage dependent leakage current in the isolated mesa is presented in Fig. 5.

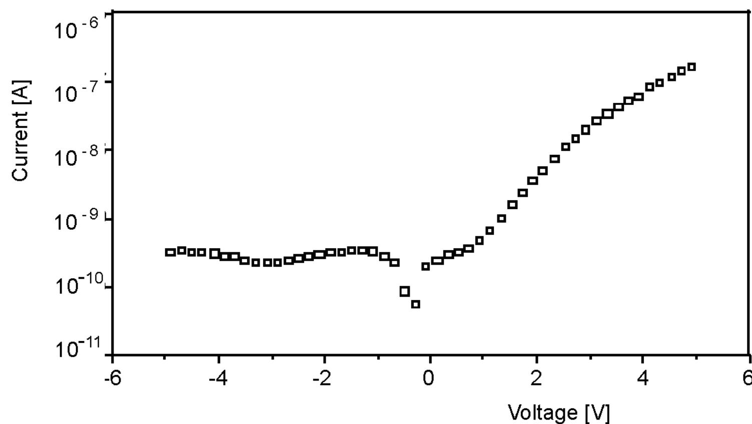

Fig. 5. Current-voltage dependence of the drain insulation structure

Up to 2 V of voltage bias difference between the drains, the current is not larger then 10 nA and a noticeable current rise-up is observed for the bias larger then 3 V. However, from the simulation results not included here, it appears that equilibrium condition for the drain currents may require drain bias difference of just about 1V. This would cause not more than 1 nA of the parasitic current between the drain regions.

5. Conclusions

A novel concept of the drain separation design in a split-drain GaAs MAGFET sensor based on epitaxial layer growth has been tested. A proper choice of GaAs/AlAs/GaAs

epitaxial sequence provided good electrical insulation between drain regions. The measured leakage current between drain regions was in the range of nA for up to 2 V drain voltage bias difference. This technique may increase magnetic field sensitivity of the MAGFET sensors.

Acknowledgements

This work was supported by the Ministry of Higher Education and Science, Grant No. 3 T11B 066 30.

References

[1] BALTES H., POPOVIC R., *Integrated Semiconductor Magnetic Field Sensor*, Proc. IEEE, 74 (1986), 1107.
[2] SUGIYAMA Y., SOGA H., TACANO M., BALTES H., IEEE Trans. Electron Dev., 36 (1989),1639.
[3] KORDALSKI W., BORATYŃSKI B., ZBOROWSKA-LINDERT I., PANEK M., ŚCIANA B., TŁACZAŁA M., *MAGFET-type magnetic field sensor*, Patent Application: PL 381793 of 20 Feb. 2007.

Received 28 April 2007
Revised 16 February 2008

Materials Science-Poland, Vol. 26, No. 1, 2008

Properties and estimated parameters of a submicrometer HSDMAGFET

W. KORDALSKI[1*], B. BORATYŃSKI[2], M. PANEK[3]

[1]Faculty of Electronics, Telecommunications and Informatics, Gdańsk University of Technology, ul. Narutowicza 11/12, 80-952 Gdańsk, Poland

[2]Faculty of Microsystem Electronics and Photonics, Wrocław University of Technology, ul. Janiszewskiego 11/17, 50-372 Wrocław, Poland

Main features and predicted values of key parameters of a novel magnetic field sensitive semiconductor device, horizontally-split-drain magnetic field sensitive field effect transistor (HSDMAGFET) which can be used to measure or detect steady or variable magnetic fields have been presented. Operating principle of the transistor is based on one of the galvanomagnetic phenomena and the gradual channel detachment effect (GCDE). The predicted relative sensitivity of the sensor can reach as high value as 100 [%/T]. Furthermore, due to its original structure, the spatial resolution of the MAGFET is extremely high, which makes this device particularly useful in reading magnetically encoded data or magnetic pattern recognition. Besides, a novel device related to the HSDMAGFET, namely, horizontally-split-drain current controlled field effect transistor (HSDCCFET) has been presented.

Key words: *magnetic field effect transistor (MAGFET); magnetic field measurement; magnetic pattern recognition*

1. Introduction

Density of magnetically recorded information on disk storage devices, magnetic field patterns, transaction cards, etc. has increased over the years, therefore development of magnetic field sensors and systems reading magnetically encoded data requires a continued improvement in magnetic field sensitive field effect transistor (MAGFET) performance [1–3]. Spatial and magnetic resolutions of MAGFETs are parameters of crucial importance [1, 2].

To meet requirements for key parameters of a magnetotransistor, a novel structure, horizontally-split-drain magnetic field sensitive field effect transistor (HSDMAGFET) has

[*]Corresponding author, e-mail: kord@ue.eti.pg.gda.pl

been proposed. It is pointed out that the expected high performance of the sensor could be improved when the vertical dimensions of the drain separation structure would be in the nanometer range. The structure, operating principle of the novel magnetotransistor, and its spatial resolution have been described. Magnetic sensitivity of the transistor has been predicted, and a novel device related to the HSDMAGFET, namely, horizontally-split-drain current controlled field effect transistor (HSDCCFET) has been presented.

2. MAGFET structure and its spatial resolution

The basic structure of the horizontally-split-drain magnetic field sensitive field effect transistor with n-type channel [4] is shown in Fig. 1. The device is a two-drain and two-gate enhancement-mode MOS type transistor in which the drain regions are placed one under the other and isolated from each other with a horizontal insulator

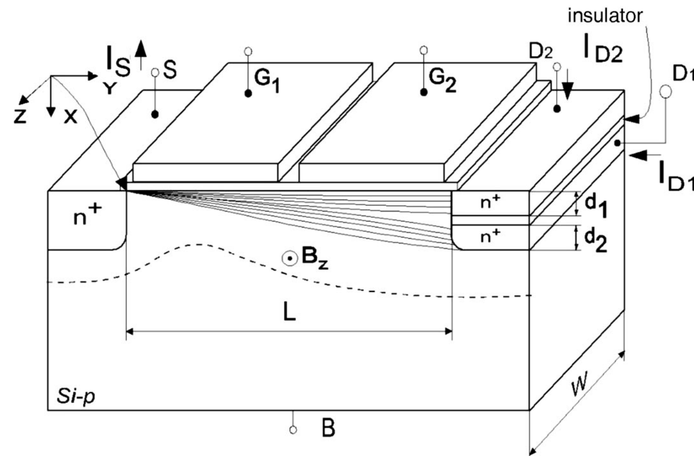

Fig. 1. Basic structure of the novel transistor [4]

layer. Positive voltages of the gates G_1 and G_2, V_{GS1} and V_{GS2}, induce an n-type channel in the transistor, and positive drain voltages, V_{DS1} and V_{DS2}, cause electrons to flow from the source S to the drains D_1 and D_2. The source current splitting electron streams flowing in the drains D_1 and D_2 is a consequence of a two-dimensional nature of kinetic processes in the transistor. Two-dimensional carrier flow is especially revealed when the magnitude of the drain-source voltages is higher than that of V_{GS}. Under this condition, the direction (the sense) of the transverse component of the electric field acting on the semiconductor surface in the vicinity of the drain is opposite to that of the source, which leads to repelling the negatively charged electrons from the semiconductor surface. Thus trajectories of mobile channel carriers are deflected downwards. This phenomenon can be called gradual channel detachment effect (GCDE). In turn, GCDE and non-uniformly distributed current of the carriers in the channel region

cause the channel of the transistor to spread out by diffusion – channel thickness modulation effect (CTME) takes place. Thus, these phenomena lead to gradually thicken and move away the electron stream from the semiconductor surface as values of the drain voltages are increasing. The effects stem from self-diffusion of mobile carriers and two-dimensional electric field distribution in the transistor channel (cf. e.g., [5, 6]). The GCDE and CTME are illustrated in Fig. 1 and clearly presented in Figs. 2 and 3 where the simulated electron concentration distributions in the transistor channel region are shown.

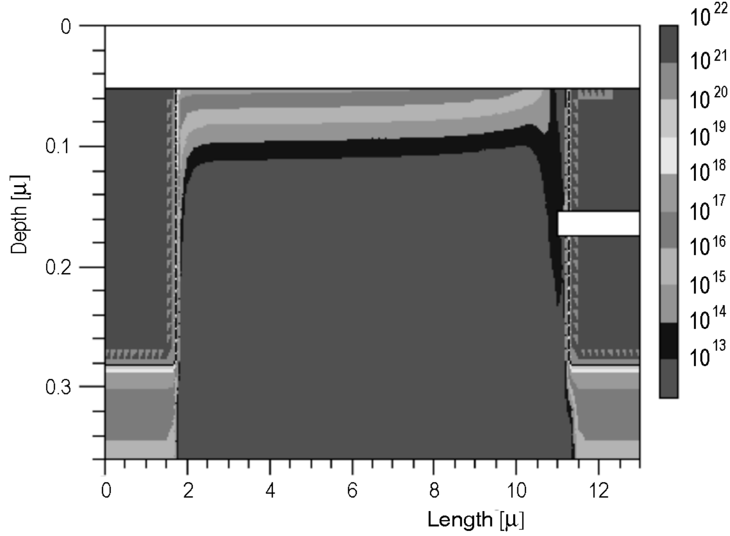

Fig. 2. Simulated electron concentration [cm^{-3}] distribution in an HSDMAGFET; $V_{DS1} = V_{DS2} = 9.2$ V, $V_{GS} = 1$ V, $B_z = 0$ T, $t_i = 20$ nm

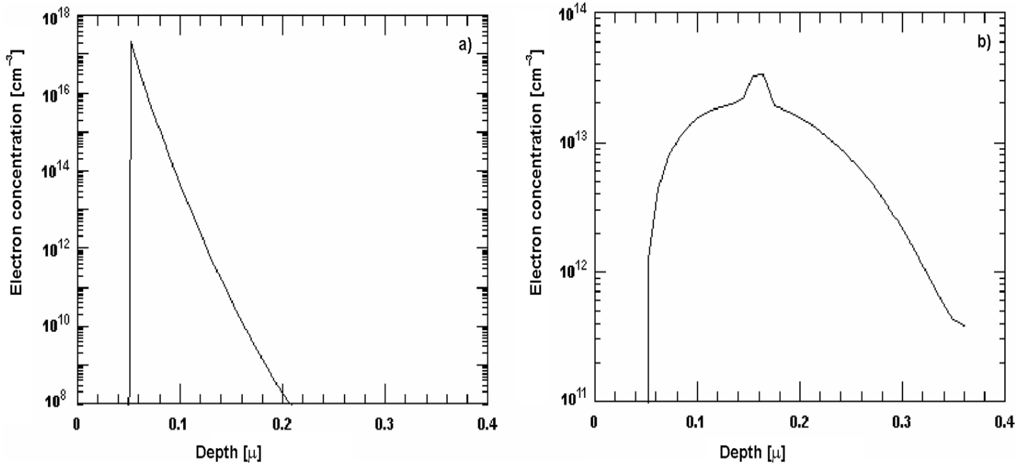

Fig. 3. Simulated electron concentration profiles for two cross sections made at abscissas $X_1 = 4000$ nm (a), and $X_2 = 11\,000$ nm (b) of the transistor channel of the HSDMAGFET shown in Fig. 2

A two-dimensional picture of the electron distribution in an HSDMAGFET with only one gate presented in Fig. 2 is obtained with the use of PISCES IIB program under the following biasing conditions: drain-to-source voltages $V_{DS1} = V_{DS2} = 9.2$ V, gate-to-source voltage $V_{GS} = 1$ V, the external magnetic induction z-component $B_z = 0$ T; thickness of the splitting insulator layer is equal to 20 nm. Figure 3 depicts more precisely simulated electron concentration profiles for two cross sections made at the abscissas $X_1 = 4$ µm and $X_2 = 11$ µm of the transistor channel of the HSDMAGFET shown in Fig. 2. For that specific bias of 9.2V at both drains, the drain currents I_{D1} and I_{D2} are equal to each other.

Referring to Figs. 1–3, we can assume the charge carriers in the channel to flow in the form of thin current layers while the Gauss law and the current continuity equation are fulfilled within each layer. Thicknesses of the drain regions, d_1 and d_2, and the splitting insulator layer t_i are assumed to be as small as possible and practically in the range of tens of nanometers.

The basic equation for the terminal currents of the device reads:

$$I_S = I_{D1} + I_{D2} \tag{1}$$

where I_S is the current injected into the channel through the source potential barrier, and I_{D1} and I_{D2} are currents flowing into the drains D_1 and D_2, respectively. Potential of the gate G_1 with respect to the source, V_{GS1}, determines the magnitude of I_S, and potential of the gate G_2, V_{GS2}, affects the ratio of current partition I_{D1}/I_{D2}. Thus the balance between drain currents can be achieved by changing the voltage V_{GS2}.

If we place the HSDMAFET in an external magnetic field, the Lorentz force acts on electrons moving in the channel [3]. Consequently, the magnetic induction z-component B_z (Fig. 1) causes the current layers in the channel region to deflect up or down, depending on the direction of B_z. This leads to an asymmetry in the terminal drain currents, which is a measure of the magnetic field strength. An imbalance between the drain currents, defined as $\Delta I = I_{D1} - I_{D2}$, is a function of the transistor channel width W, channel length L, biasing voltages V_{GS1}, V_{GS2}, V_{DS1}, V_{DS2}, and magnetic induction $\boldsymbol{B}$, which can be expressed as [7]

$$\Delta I = I_{D1} - I_{D2} = f(W, L, V_{GS1}, V_{GS2}, V_{DS1}, V_{DS2}, B_z) \tag{2}$$

As to the structure and principle of operation, the novel MAGFET is very similar to Popovic and Baltes's SDMAGFET, [3, 8] presented in Fig. 4. The SDMAGFET also comprises two drains, but they are placed side by side and vertically insulated, cf. Figs. 1 and 4. In Popovic's and Baltes's sensor, the x-component B_x of the magnetic field deflects current lines in the plane yz and finally an imbalance between I_{D1} and I_{D2} occurs, so the SDMAGFET is a sensor of the perpendicular-to-gate component of the magnetic field.

Magnetic field sensitivity and spatial resolution are basic parameters for an HSDMAGFET. The sensitivity of the magnetic field sensor is evaluated in the next section but spatial resolution of the device can be determined by taking into account

the arguments given in this section. Namely, referring to Fig. 1, one can see that an external magnetic induction z-component B_z uniformly distributed in the rectangular parallelepiped LWX_{ch} is needed for a proper operation of the HSDMAGFET, with L, W, and X_{ch} being, respectively, the channel length, the channel (transistor) width, and

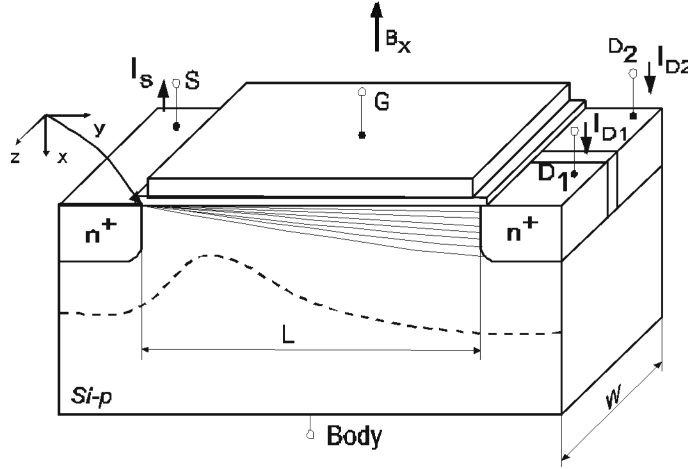

Fig. 4. A split-drain MAGFET structure after [3], [7], [8]

the channel thickness at the transistor drains. The channel thickness X_{ch} is close to an effective channel thickness d_{eff} that is defined in the next section and illustrated in Fig. 5, however, X_{ch} is always greater than d_{eff}, and is of the order of several hundreds of nanometers (d_{eff} depends on profile doping, depths of the drains, and thickness of the splitting insulator layer). The geometrical resolution of the HSDMAGFET in xy-plane is determined by LX_{ch}, and can be very high, making the device very suitable for reading high-density magnetically-encoded data (in the case of a standard SDMAG-FET this parameter equals LW, which is a much worse result).

3. Sensitivity of the HSDMAGFET

The relative magnetic sensitivity S [%/T] of the split-drain devices at small magnetic induction is defined as follows [3]:

$$S = \left| I_S^{-1} \frac{\partial \left(I_{D1} - I_{D2} \right)}{\partial B_z} \right|_{B_z = 0} \tag{3}$$

i.e., the partial derivative of the relative current imbalance with respect to the magnetic induction, taken at zero induction, which, for small B_z, can be replaced by [7, 9]

$$S = \left| \frac{I_{D1} - I_{D2}}{(I_{D1} + I_{D2})B_z} \right| \tag{4}$$

Due to horizontally split drain design requirements, manufacturing the device needs a modified CMOS technology. The experimental research in this direction has not been undertaken so far. However, based on results of the work [9], we are able to estimate the predicted magnetic sensitivity of the device.

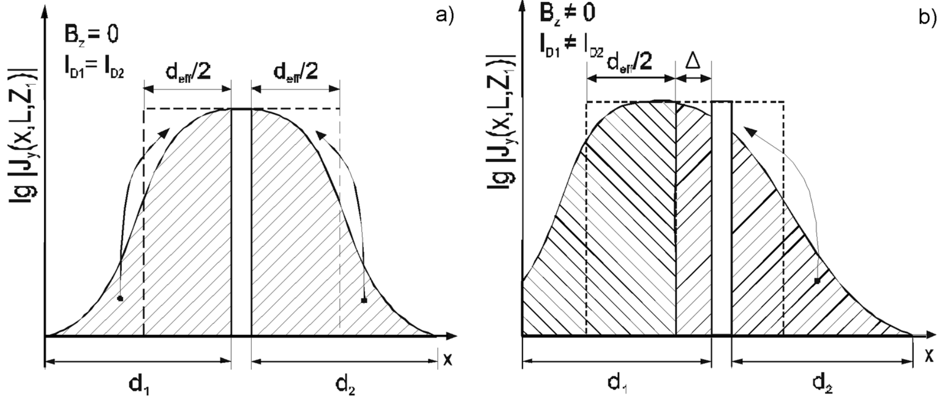

Fig. 5. An idealized current density distribution in a near-drain cross section of the channel of an HSDMAGFET operating in the saturation region of the output characteristics: a) $B_z = 0$, b) $B_z \neq 0$. The arrows show a method of calculating the effective near-drain channel thickness d_{eff}, where d_1 and d_2 are the thicknesses of the drains D_1 and D_2, respectively

Let us consider an idealized picture of the current density y-component distribution $J_y(x,L,z)$ in a near-drain cross section of an HSDMAGFET shown in Fig. 5a. In general, channel direct current I_{ch} through an arbitrary surface A perpendicular to the drawing plane in the transistor channel region can be expressed by

$$I_{ch} = -q \iint_A n(x,y)\, \mathbf{v}(x,y) dA \tag{5}$$

where q is the electronic charge, $n(x,z)$ – electron density distribution in xz-plane (Fig. 1), and $\mathbf{v}(x,z)$ – the velocity vector of electrons in the channel. Particularly, referring to Fig. 5a

$$I_{D1} = -W \int_0^{d_1} J_y(x,L) dx \tag{6}$$

and

$$I_{D2} = -W \int_{d_1+t_i}^{d_1+t_i+d_2} J_y(x,L) dx \tag{7}$$

Assuming that the velocity y-component $v_y(x,L)$ of current carriers (electrons) in appropriate regions of the plane $y = L$ is independent of x and equal to v_y (the longer the channel, the more adequate is the assumption), we can rewrite Eqs. (6) and (7) in the form:

$$I_{D1} = q v_y W \int_0^{d_1} n(x,L)\,dx \tag{8}$$

$$I_{D2} = q v_y W \int_{d_1+t_i}^{d_1+t_i+d_2} n(x,L)\,dx \tag{9}$$

Introducing an average current density in the neighbourhood of the splitting insulator, J_i, see Fig. 5(a),

$$J_i = \frac{J_y\left(d_1,L\right)+J_y\left(d_1+t_i,L\right)}{2} \tag{10}$$

we can define an effective channel thickness at the HSDMAGFET drain, d_{eff}, as

$$d_{\mathrm{eff}} = \frac{\int_0^{d_1} J_y(x,L)dx + \int_{d_1+t_i}^{d_1+t_i+d_2} J_y(x,L)dx}{J_i} \tag{11}$$

Assuming again that velocity y-component $v_y(x,L)$ of current carriers in appropriate regions of the plane $y = L$ is independent of x, Eqs. (10) and (11) can be written in the form:

$$J_i = \frac{q v_y\left(n\left(d_1,L\right)+n\left(d_1+t_i,L\right)\right)}{2} \tag{12}$$

$$d_{eff} = \frac{2\left(\int_0^{d_1} n(x,L)dx + \int_{d_1+t_i}^{d_1+t_i+d_2} n(x,L)dx\right)}{n\left(d_1,L\right)+n\left(d_1+t_i,L\right)} \tag{13}$$

As an external magnetic field acts on the HSDMAGFET, the Lorentz force causes the current layers in the channel region to deflect up or down (Fig. 1), depending on the direction of B_z. Introducing after [9] an effective current line deflection Δ, measured at the MAGFET drains (Fig. 5b), and defined as [9]

$$\Delta = L\,\mu_n \left|B_z\right| \tag{14}$$

where μ_n is the electron mobility in the channel, we can calculate the drain current imbalance, $\Delta I = I_{D1} - I_{D2}$ produced by magnetic field z-component B_z:

$$\left|\Delta I\right| = \left|I_{D1} - I_{D2}\right| = \frac{2\,L\,\mu_n\,B_z}{d_{\mathrm{eff}}}\left(\,I_{D1} + I_{D2}\,\right) \tag{15}$$

Inserting Eq. (15) into Eq. (4) and making use of Eqs. (12) and (13) lead to the relative sensitivity S [%/T] of the HSDMAGFET

$$S = \frac{2\,\mu_n\,L}{d_{\mathrm{eff}}} \tag{16}$$

or, alternatively,

$$S = \frac{\mu_n\,L\left[\,n\left(d_1, L\right) + n\left(d_1 + t_i, L\right)\,\right]}{\int\limits_0^{d_1} n(x,L)\,dx + \int\limits_{d_1+t_i}^{d_1+t_i+d_2} n(x,L)\,dx} \tag{17}$$

The mobility μ_n in Eqs. (14)–(17) is an electric field dependent parameter and its dependence on the longitudinal electric field component in the channel can be described as follows [10]:

$$\mu_n = \frac{\mu_{n0}}{\left[1 + \left(\dfrac{E_0}{E_C}\right)^B\right]^{\frac{1}{B}}}, \qquad E_0 = \frac{V_{DS}}{L} \tag{18}$$

where μ_{n0}, E_C, and B are low-field mobility, characteristic electric field, and a parameter ($1 \le B \le 5$), respectively.

From Eq. (17) it follows that the relative sensitivity S reaches its maximum value when the current carrier concentration at the cross-section plane for $y = L$ gets its maximum in the neighbourhood of the splitting insulator. This result converges well with the experimental results obtained for standard SDMAGFETs [7, 9].

Based on the theoretical analysis outlined in this section, and also on the results of numerical simulation (Fig 3b), we can estimate the expected sensitivity of the proposed HSDMAGFET. Taking some additional realistic data: μ_{n0} = 1000 cm^2·V^{-1}·s^{-1}, E_C = 10^3 V·cm^{-1}, B = 2, L = 10 μm, V_{DS} = 9.2 V, the calculated sensitivity value can reach 100 %/T, that is 50 times more than the experimental value 2–3 %/T obtained for a standard SDMAGFET [3, 7–9]. Again, examination of Eq. (17) allows us to speculate that even higher values of the sensitivity could be obtained for a more advanced design of the HSDMAGFET. Such a design should provide possibility for the drain current balance, $I_{D1} = I_{D2}$, at very low drain bias voltage V_{DS}, i.e., in the linear region of operation where the mobility value lowering is negligible.

4. A novel device related to the HSDMAGFET

Unlike the known SDMAGFET, the HSDMAGFET put forward in this work is sensitive to the *z*-component of the magnetic field enabling us to develop new types of semiconductor devices. An interesting example is discussed in this chapter.

A novel semiconductor device related to the HSDMAGFET, horizontally-split -drain current controlled field effect transistor (HSDCCFET) with two control electrodes has been proposed [11]. For the sake of brevity, the device can be called a CCFET. Operating principle of the proposed transistor is based on one of the galvanomagnetic phenomena, the Biot–Savart–Laplace law and the gradual channel detachment effect (GCDE).

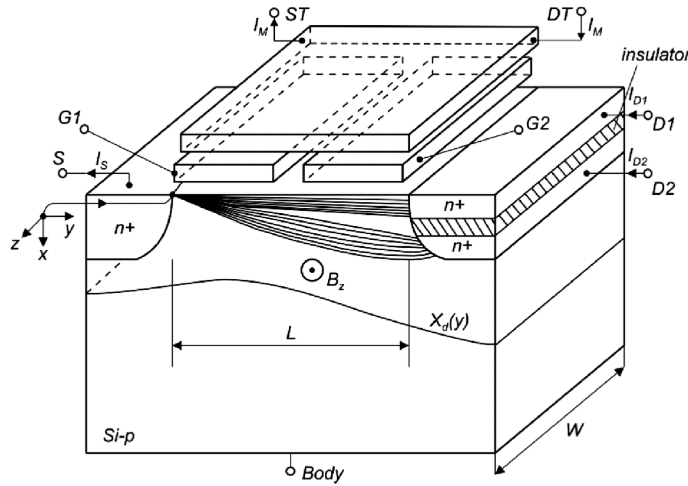

Fig. 6. Basic structure of the new current-controlled field effect transistor (CCFET)

If a dc current I_M flows between the terminals *DT* and *ST* of a conducting layer insulated from the transistor gates (Fig. 6), a magnetic field B_z is induced. According to the Biot–Savart–Laplace law, the magnetic induction B_z at any arbitrary point in the transistor channel is directly proportional to the current I_M. The magnetic field leads to an asymmetry in the terminal drain currents, which is a measure of the magnitude of the current I_M. An imbalance between the drain currents, defined as $\Delta I = I_{D1} - I_{D2}$, is a function of the transistor channel width *W*, channel length *L*, biasing voltages V_{GS1}, V_{GS2}, V_{DS1}, V_{DS2}, and the current I_M which can be expressed as [1, 3, 7–9]:

$$\Delta I = I_{D1} - I_{D2} = f(W, L, V_{GS1}, V_{GS2}, V_{DS1}, V_{DS2}, I_M) \tag{19}$$

Thus we can say that the novel transistor is a sensor of the current I_M which can flow in an arbitrary loop or branch of the integrated circuit (IC). In other words, the transistor is able to convert the current I_M flowing through an arbitrarily chosen connecting path in the IC into the difference between the drain currents, I_{D1} - I_{D2}. Like

a MOSFET, the CCFET has three primary regions of operation: cutoff, linear, and saturation. What is more interesting, the transistor is powerless-controlled, i.e., there is no voltage drop between the terminals *DT* and *ST*.

A p-channel version of the CCFET can be fabricated by reversing the polarities of the n- and p-type regions in Fig. 6. The direction of currents in the p-channel is opposite to that of the n-channel device, and the polarities of the operating bias voltages are reversed. The circuit symbols for n- and p-channel CCFETs are proposed in Fig. 7.

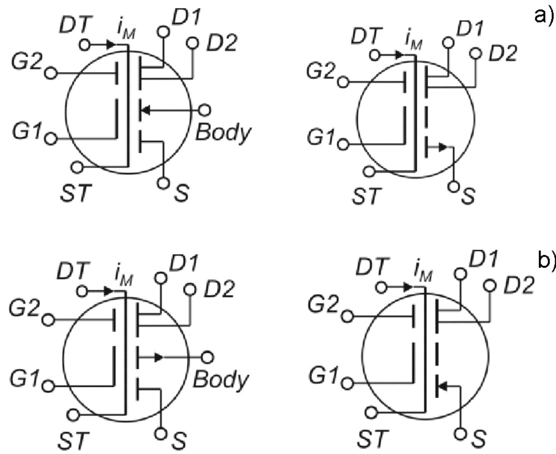

Fig. 7. Circuit symbols of the current-controlled field effect transistor (CCFET): a) for an n-channel device, b) for a p-channel device

In general, the device presented in this section can be applied as a magnetic field sensor and as an element of building blocks of integrated circuits (ICs). Selected basic circuit applications of the CCFET discussed in [11] include a current-controlled amplifier, operational current amplifier, and voltage–current multiplier cell.

An important feature of the device is that it can be controlled by the voltage V_{GS1} and the current I_M. Due to the principle of operation, power absorbed at input terminals *DT-ST* (Fig. 6) equals zero, hence the current I_M, or a fraction of it, can control a large number of such devices. Since a connecting path drawing the current I_M, isolated from the transistor structure, can be at an arbitrary potential, we can say that the CCFET can realize a function of a potential-free current detector (PFCD) or a potential-free current amplifier (PFCA). This feature of the device enables designers to eliminate transformers in IC design.

5. Conclusions

A novel MAGFET sensor structure with horizontally split drains has been put forward. Using analytical and numerical simulation approach, it was shown that predicted magnetic sensitivity of the sensor can reachthe value, to date unmatched, of

100 %/T. Therefore, HSDMAGFETs are very interesting for applications in magnetometry and reading high density magnetically encoded data. Also, a novel semiconductor device based on the HSDMAGFET concept, viz., horizontally-split-drain current controlled field effect transistor (HSDCCFET) with two control electrodes has been discussed. The new FET structure seems to be very promising for applications as a part of basic building blocks of integrated circuits. However, in both presented devices a modification of the standard CMOS technology is needed and remains crucial for the wider development of various magnetic field sensors based on the HSDMAGFET. One of possible further research directions is switching to III-V semiconductors and MAGFET sensors based on MESFET devices which benefits in higher carrier mobilities and possibility of epitaxial nano-layers bandgap engineering.

Acknowledgements

This work has been supported by the Ministry of Science and Higher Education, Grant No. 3 T11B 066 30.

References

[1] LI Z., SUN X., IEEE Electron Dev. Lett., 24 (2003), 652.
[2] O N., NATHAN A., IEDM Tech. Dig., 167–170 (1995).
[3] BALTES H., POPOVIC R., Proc. IEEE, 74 (1986), 1107.
[4] KORDALSKI W., POLOWCZYK M., *A transistor as a magnetic field sensor*, Proc. of the Metrology Congress, Wrocław, 6-9 Sept., 2004, Vol. II, pp. 347-350.
[5] SELBERHERR S., *Analysis and Simulation of Semiconductor Devices*, Springer, Wien, 1984.
[6] YAMAGUCHI K., IEEE Trans. Electron Dev., ED-26 (1979), 1068.
[7] KLUGE J.W.A., LANGHEINRICH W.A., IEEE Trans. Electron Dev., ED-46 (1999), 89.
[8] POPOVIC R., BALTES H., IEEE J. Solid-State Circuits, SC-18 (1983), 426.
[9] RODRIGUEZ-TORRES R., GUTIERREZ-DOMINGUEZ E.A., KLIMA R., SELBERHERR S., IEEE Trans. Electron Dev., ED-51 (2004), 2237.
[10] SZE S.M., *Physics of Semiconductor Devices*, Wiley, New York, 1981.
[11] KORDALSKI W., *A Current-Controlled FET*," Gdańsk University of Technology, Faculty of ETI Annals, 14 (2007), 635.

Received 28 April 2007
Revised 16 February 2008

Materials Science-Poland, Vol. 26, No. 1, 2008

Computer simulation of tuned and detuned GaInNAsSb QW VCSELs for long-wavelength applications

K. GUTOWSKI, R. P. SARZAŁA*

Laboratory of Computer Physics, Institute of Physics, Technical University of Łódź, ul. Wólczańska 219, 93-005 Łódź, Poland

$Ga_{0.62}In_{0.38}N_{0.023}As_{0.95}Sb_{0.027}/GaN_{0.025}As_{0.975}$ quantum wells (QWs) used in standard GaAs-based GaInNAsSb/GaNAs vertical-cavity surface-emitting diode lasers (VCSELs) exhibit at room temperature (RT) the highest optical gain for the 1422 nm wavelength. Its RT continuous-wave threshold current for the 5 μm device is as low as only 0.68 mA. An increase in the QW active region temperature by about 100 K has been found to be followed by a shift of the gain spectrum of the above QW to the 1500 nm range. Therefore, a comprehensive computer simulation has been used to verify a possibility to highly detune GaAs-based GaInNAsSb/GaNAs VCSELs from the wavelength of 1422 nm to 1500 nm, closer to the wavelength used in the third generation of the fibre optical communication. Such a temperature-enhanced RT CW lasing operation of the 1500 nm VCSEL, with an active region identical to that of the 1422 nm one and the cavity properly re-designed for the 1500 nm wavelength, has been found to be reached at the threshold current as many as 17 times higher than that of the 1422 nm VCSEL.

Key words: *GaInNAsSb diode laser; 1.5 μm VCSELs; threshold laser simulation*

1. Introduction

Since discovering by Kondow et al. [1] unusual properties of GaInNAs, many research centres started investigations to manufacture diode lasers based on this material and exhibiting high performance in the 1.3 μm emission range. It has been later discovered that an addition of Sb not only enables producing quantum wells of higher quality without phase segregation and too many defects but it is also built-in into the chemical compound creating a new five-element GaInNAsSb compound [2–4] of even lower band-gap than GaInNAs [5]. This technology is still very immature and its properties are still not completely known. Therefore 1.5 μm RT continuous wave (CW) vertical cavity surface emitting diode lasers (VCSELs) have not been reported until now.

*Corresponding author, e-mail: rpsarzal@p.lodz.pl

The main goal of this work was to investigate properties of tuned and highly detuned GaInNAsSb VCSELs. Physical aspects of both a shift of the gain spectrum enhanced by an intentionally introduced active region temperature increase and a detuning of the VCSEL lasing emission following a cavity redesigning, from the 1422 nm radiation, corresponding to the room-temperature (RT) maximal optical gain of the GaInNAsSb QW, to the desired 1500 nm radiation have been analysed. The analysis is based on a modified version of the comprehensive three-dimensional optical-electrical-thermal-gain fully self-consistent VCSEL model which has been successfully used in our earlier simulations [6–9].

2. The model

Many VCSEL models have been reported in the literature. Their comparative analysis has been given by Osiński and Nakwaski [10] but none of them has been devoted to an advanced modelling of GaInNAsSb/GaNAs VCSELs. Recently, a comprehensive three-dimensional (3D) optical-electrical-thermal-gain self-consistent model of GaAs-based VCSELs has been developed to investigate their threshold RT operation. Both pulse and CW RT operations are considered. The model consists of four interrelated parts:

- The optical model describes, for successive radiation modes, their wavelengths and distributions of their optical fields within the resonator. The model is based on the effective frequency method [11]. The lasing threshold is determined from the condition of the real propagation constant.
- The finite-element (FE) electrical model characterizes both the current spreading (including carrier drift and diffusion processes) within the device volume between the top and the bottom contacts, the injection of both electrons and holes into the active region, their radial diffusion within it and their over-barrier leakage.
- The FE thermal model gives details of heat generation (non-radiative recombination, reabsorption of radiation as well as volume and barrier Joule heating) and its spreading from heat sources towards a heat sink and within it.
- The gain model, based on the Fermi golden rule, yields information about the optical gain spectra.

One of the important features of this well-conducted self-consistent approach is that it allows an integration of various physical phenomena, crucial for its RT CW operation, within a VCSEL device. The above means that all important, usually non-linear, interactions between individual physical phenomena are taken into account using the self-consistent algorithm of calculations shown in Fig. 1. More details about the simulation model may be found elsewhere (cf. [5]). General rules of the advanced modelling of a VCSEL operation have also been formulated by Osiński and Nakwaski [10].

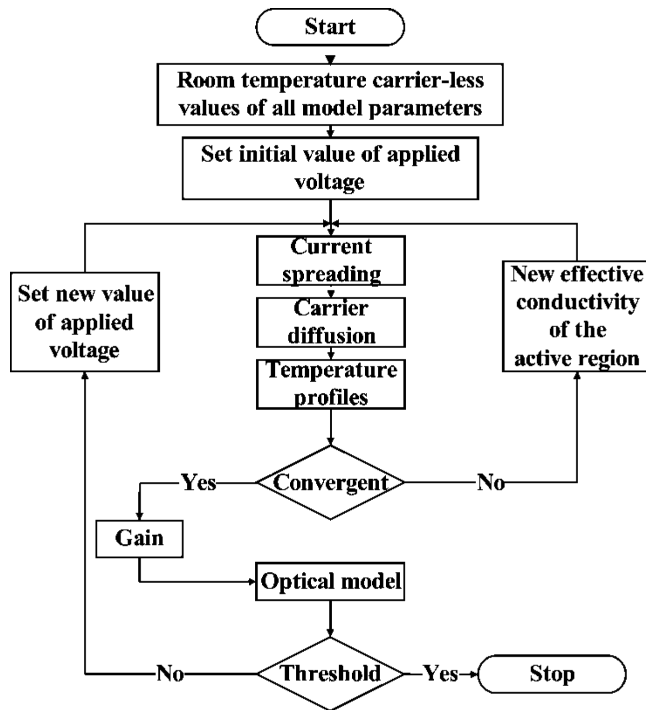

Fig. 1. Flow chart of the self-consistent calculation algorithm used in the modelling

3. The GaInNAsSb VCSEL structure

Let us consider the GaAs-based oxide-confined VCSEL configuration shown schematically in Fig. 2. Its active region is identical with that proposed by Goddard et al. [12]. Its modern double-intracavity-contact structure enables application of no-intentionally-doped distributed-Bragg-reflector (DBR) resonator mirrors which reduce optical absorption within them. The active region is a single 7.8 nm $Ga_{0.62}In_{0.38}N_{0.023}As_{0.95}Sb_{0.027}$ quantum well (QW) sandwiched by 22 nm $GaN_{0.025}As_{0.975}$ barriers.

To reduce the threshold current, the shortest possible (for the VCSEL configuration under consideration) 1.5λ cavity is assumed. 28 pairs of quarter-wave $Al_{0.8}Ga_{0.2}As$/GaAs layers and 34 pairs of AlAs/GaAs layers are used for the upper and bottom, DBRs respectively.The 15 nm central oxide aperture of the 5 μm diameter is created within the p-type spacer to create both electrical and optical radial confinements. The spacer parts neighbouring the active region are assumed not to be intentionally doped, whereas their parts important for radial current spreading from annular contacts towards centrally located active region are highly doped to enhance uniformity of carrier injection. The laser crystal is attached to the copper heat sink of a form of a cylinder of the 5 mm in diameter and 5 mm high.

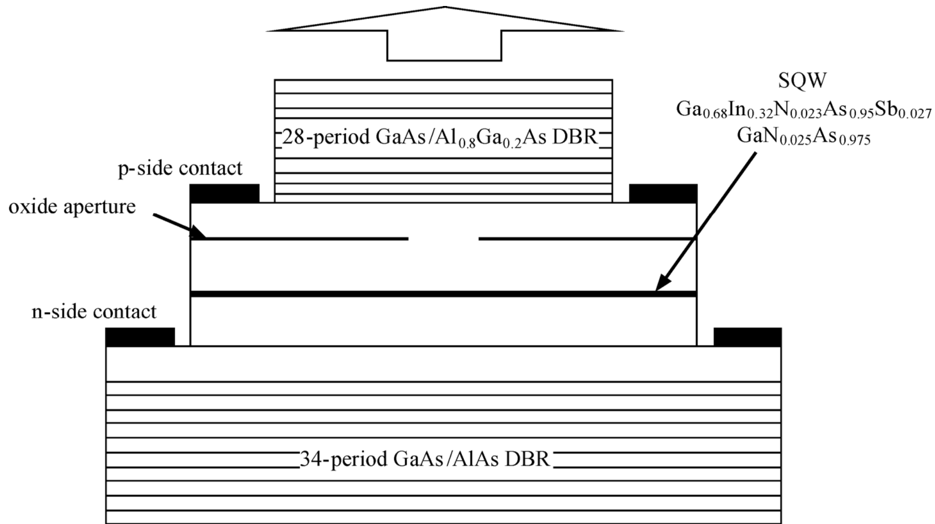

Fig. 2. The double-intracavity-contact GaAs-based oxide-confined GaInNAsSb/GaNAs quantum well vertical-cavity surface-emitting diode laser (VCSEL) structure

For a typical active region carrier concentration of 5×10^{18} cm^{-3}, the $Ga_{0.62}In_{0.38}N_{0.023}As_{0.95}Sb_{0.027}/GaN_{0.025}As_{0.975}$ QW active region has been found to exhibit the highest RT optical gain for the 1422 nm wavelength. Therefore, the reference VCSEL cavity has been designed for the same wavelength. To analyse a possibility to reach emission at longer wavelengths, the VCSEL cavity detuned for the 1500 nm emission has been additionally considered. For the both VCSEL designs, layer thicknesses are listed in Table 1.

Table 1. Layer thicknesses (in nm) in the 1422 nm and 1500 nm GaInNAsSb/GaNAs VCSELs

Layer	1422 nm VCSEL	1500 nm VCSEL
GaAs in bottom DBR	34×104.9	34×110.9
AlAs in bottom DBR	34×122.6	34×129.3
n-GaAs spacer (10^{18} cm^{-3})	100.0	100.0
n-GaAs spacer (10^{16} cm^{-3})	83.2	95.3
$GaN_{0.025}As_{0.975}$ barrier	22.0	22.0
$Ga_{0.62}In_{0.38}N_{0.023}As_{0.95}Sb_{0.027}$ QW	7.8	7.8
p-GaAs (10^{17} cm^{-3})	177.7	190.6
Al_xO_y	15.0	15.0
p-GaAs (2×10^{18} cm^{-3})	204.3	216.8
GaAs in upper DBR	28×104.9	28×110.9
$Al_{0.8}Ga_{0.2}$As in upper DBR	28×118.9	28×125.8

4. Results

Radial profiles of the threshold current density j_{th} and the active region temperature T_A of the 1422 nm VCSEL operating at 300 K are shown in Fig. 3.

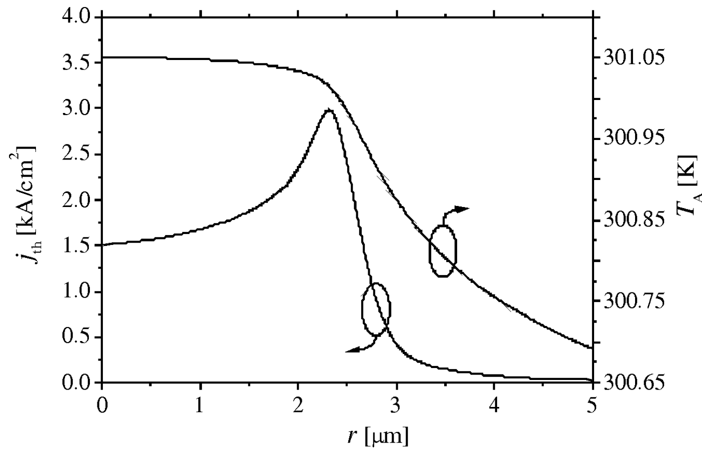

Fig. 3. Radial profiles of the threshold current density j_{th} and the active region temperature T_A of the 5 μm VCSEL emitting the 1422 nm radiation at 300 K

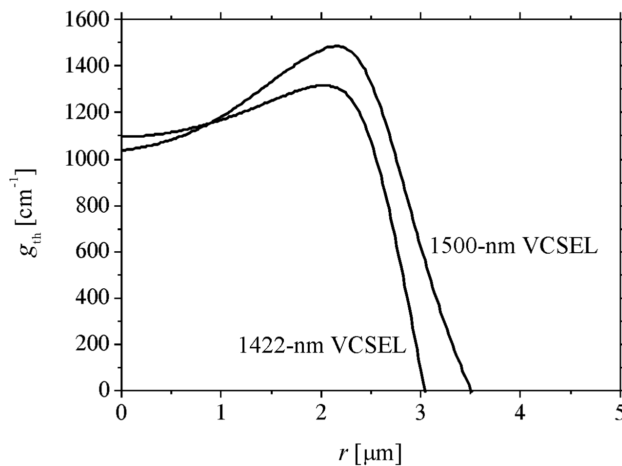

Fig. 4. RT radial profiles of the active region threshold optical gain g_{th} for the 5 μm VCSEL emitting the 1422 nm radiation and the 5 μm VCSEL emitting the1500 nm radiation

As one can see, current injection into the active region is in this case rather nonuniform with the current density close to the active region edge twice higher than that at the active region centre. This profile will be exchanged into somewhat less nonuniform threshold carrier concentration profile $n_{th}(r)$ because of radial diffusion of

carriers within the active region before their recombination but the continually non-uniform radial gain profile (Fig. 4), roughly proportional to n_{th}, will be still unprofitable for the desired fundamental LP_{01} mode. Active region temperature is the highest at its centre and is rather slowly reduced within it and somewhat more speedily beyond it. Because of thermal focusing, it partially compensates the anti-guiding effect associated with the gain profile. Threshold operation parameters of the 5 μm VCSEL under consideration emitting 1422 nm radiation at 300 K are listed in Table 2.

Table 2. RT threshold operation parameters of the 5 μm VCSEL emitting the 1422 nm radiation and the 5 μm VCSEL emitting the 1500 nm radiation

I_{th} [mA]	$j_{th,max}$ [kA/cm^2]	$g_{th,max}$ [cm^{-1}]	$n_{th,max}$ [10^{18} cm^{-3}]	$T_{A,max}$ [K]	λ [nm]
5 μm VCSEL emitting the 1422 nm radiation					
0.68	3.04	1315	5.21	301.1	1422
5 μm VCSEL emitting the1500 nm radiation					
11.59	70.78	1487	17.25	393.7	1509

For the 1422 nm VCSEL, the relation of the threshold-current versus the maximum active region temperature is shown in Fig. 5. The lasing threshold has been found to strongly depend on temperature, which means that this VCSEL construction is very sensitive to changes of temperature. Accordingly, the characteristic temperature T_0 describing the above changes is equal to only 67.4 K for temperature increases not exceeding 55 K over the room temperature (RT = 300 K), whereas, for analogous GaInAs/GaAs VCSELs, it is as high as 160–200 K [9].

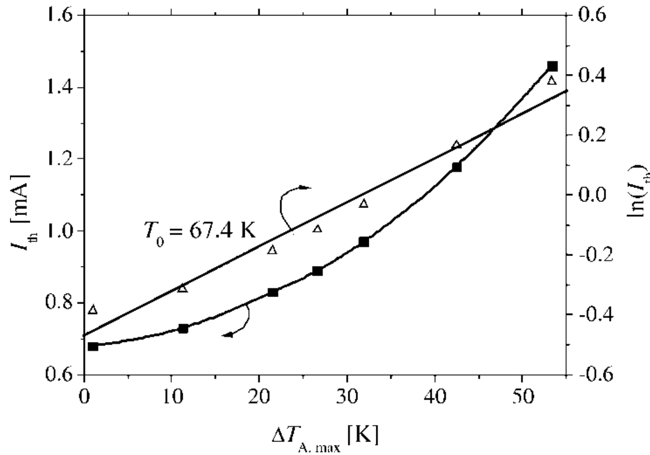

Fig. 5. Threshold current I_{th} of the 1422 nm VCSEL as a function of the maximum active region temperature increase $\Delta T_{A,max}$ over 300 K (RT)

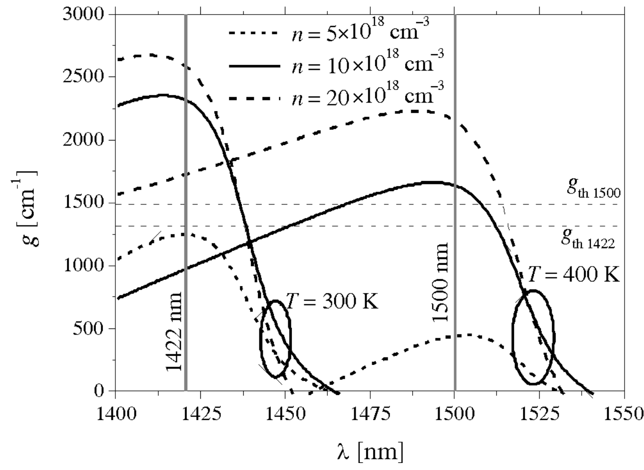

Fig. 6. The $Ga_{0.62}In_{0.32}N_{0.023}As_{0.950}Sb_{0.027}/GaN_{0.025}As_{0.975}$ quantum well gain spectra at 300 K and at 400 K for various active region carrier concentrations. Lasing thresholds for 1422 nm and 1500 nm are indicated

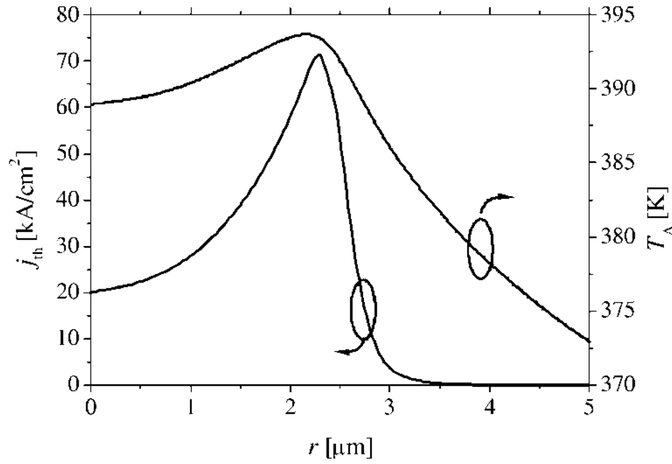

Fig. 7. Radial profiles of the threshold current density j_{th} and the active region temperature T_A of the 5 μm VCSEL emitting the 1509 nm radiation at 300 K

At RT, optical gain in the QW under consideration is limited to wavelengths shorter than 1465 nm even for very high carrier concentrations (Fig. 6). Then pulse currents of even very high amplitudes do not enable reaching the 1500 nm emission but at 400 K, QW gain spectra are found to be shifted to longer wavelengths and their maxima correspond to wavelengths close to 1500 nm. Because of heat generation close to the active region, such a temperature increase may be ensured by very high continuous wave (CW) operation currents. Then the threshold current at RT for the temperature enhanced 1500 nm emission

of the VCSEL, with the same active region of diameter $\phi = 5$ μm but with the properly re-designed cavity (Table 1) will be as high as 11.59 mA (Table 2), which is as high as over 17 times greater than that for an analogous 1422 nm emission. Besides, current injection into the active region of the 1500 nm VCSEL (Fig. 7) has happened to be much more non-uniform than that of the 1422 nm VCSEL: its value close to the active region edge is over 3.5 times higher than that corresponding to the active region centre. Therefore radial threshold-gain profile is in this case considerably more non-uniform than in the case of the 1422 nm VCSEL (Fig. 4). Besides in the 1500 nm VCSEL, temperature is the highest close to the active region edge. Both the above profiles may enhance unwanted emission of the higher order LP modes.

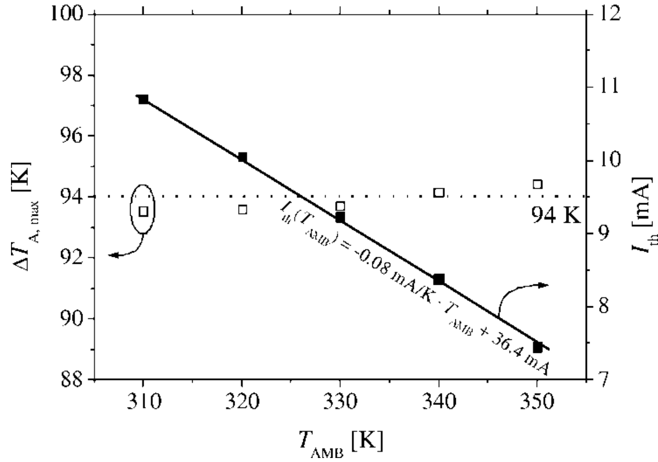

Fig. 8. Dependence on the ambient temperature T_{AMB} of the maximal active region temperature increase $\Delta T_{A,max}$ over RT and the threshold current I_{th} of the 5 μm VCSEL emitting the 1500 nm radiation

Active region temperature increase necessary to enhance the QW 1500 nm optical gain may also partly result from an increase in the ambient temperature T_{AMB} over RT. This is shown in Fig. 8 for the VCSEL re-designed for the 1500 nm emission (Table 1). For the lasing threshold, the maximum active region temperature increase over RT is nearly constant and equal to about 94 K disregarding the ambient temperature. On the opposite, the threshold current is steadily reduced for increasing T_{AMB}, because an additional current induced active region temperature increase necessary to shift the gain spectrum is gradually becoming lower.

5. Conclusions

Comprehensive computer simulation has been used to verify a possibility to highly detune GaAs-based GaInNAsSb/GaNAs QW VCSELs from the wavelength of

1422 nm, corresponding to the highest RT optical gain of its QW active region, to 1500 nm, closer to the wavelength used in the third generation of the fibre optical communication. Then the RT CW lasing operation of the 1500 nm VCSEL, with an identical active region to that of the 1422 nm one and the cavity properly re-designed for the 1500 nm wavelength (Table 1), may be reached for the active region temperature increased by about 94 K over RT which is necessary for a required QW gain shift to longer wavelengths. However, such a temperature induced CW RT VCSEL lasing operation at 1500 nm is reached for a threshold current as many as 17 times higher than that of the 1422 nm VCSEL.

References

[1] KONDOW M., UOMI K., NIWA A., KITATANI T., WATAHIKI S., YAZAWA Y., Jpn. J. Appl. Phys., 35 (1996), 1273.

[2] HA W., GAMBIN V., WISTEY M., BANK S., YUEN H., KIM S., HARRIS J.S., Electron. Lett., 38 (2002), 277.

[3] WISTEY M.A., *Growth of 1.5 μm vertical cavity surface emitting lasers by molecular beam epitaxy*, Doctoral Thesis, Stanford University (2005).

[4] VOLZ K., GAMBIN V., HA W., WISTEY M.A., YUEN H., BANK S., HARRIS J.S., J. Cryst. Growth, 251 (2003), 360.

[5] SARZAŁA R.P., NAKWASKI W., J. Phys.: Condens. Matter, 16 (2004), S3121.

[6] SARZAŁA R.P., MENDLA P., WASIAK M., MAĆKOWIAK P., BUGAJSKI M., NAKWASKI W., Opt. Quant. Electron., 36 (2004), 331.

[7] SARZAŁA R.P., IEEE J. Quant. Electron., 40 (2004), 629.

[8] SARZAŁA R.P., Semicond. Sci. Tech., 19 (2004), 1122.

[9] SARZAŁA R.P., *Diode Lasers for 2nd Generation of Fibre Optical Communication: Physical Simulation of an Operation and Optimization of Selected Laser Structure*, DSc Dissertation, Technical University of Łódź, Łódź, 2004

[10] OSIŃSKI M., NAKWASKI W., Chapter 5 [in:] *Vertical-Cavity Surface-Emitting Laser Devices*, Berlin, Springer, 2003, p. 135.

[11] WENZEL H.AND WÜNSCHE H.-J., IEEE J. Quant. Electron., 33 (1997), 1156.

[12] GODDARD L.L., BANK S.R., WISTEY M.A., YUEN H.B., EAO Z.L., HARRIS J.S., J. Appl. Phys., 97 (2005), 83101.

Received 28 April 2007
Revised 16 February 2008

Materials Science-Poland, Vol. 26, No. 1, 2008

Band structure of In chains on Si(335)–Au

K. SKROBAS, R. ZDYB*, M. KISIEL, M. JAŁOCHOWSKI

Institute of Physics, Maria Curie-Sklodowska University,
pl. M. Curie-Skłodowskiej 1, 20-031 Lublin, Poland

The crystallographic and electronic band structure of In induced reconstruction of Si(335)–Au surface have been studied with reflection high electron energy diffraction and angle resolved photoemission spectroscopy in ultrahigh vacuum conditions. The photoemission spectra recorded along chains show strongly dispersive band crossing the Fermi level while dispersionless spectra are found in the perpendicular direction. Diffraction experiments support one-dimensional character of the structures. A simple model of In reconstructed Si(335)–Au surface has been put forward.

Key words: one-dimensional structure; Si(335); In; ARPES; RHEED

1. Introduction

One-dimensional systems are very attractive objects for investigations because of their fundamental physical properties different from those of three- or two-dimensional systems, as well as for practical reasons consisting in rapid miniaturization of electronic components. Among many other metal–silicon systems, In–Si system has been studied for more than 40 years. Depending on In coverage and temperature, it reveals variety of reconstructions [1]. Among them there is 4×1 which shows a phase transition to 8×2 below 150 K, revealing one-dimensional character [2, 3]. Indium phases developed for submonolayer In coverages are found to be semiconducting, while those formed at around 1 monoatomic layer (ML), like 4×1 and $\sqrt{7}\times\sqrt{3}$ are metallic [1].

In the present paper, we report on investigation of In reconstructed Si(335)–Au vicinal surface. Electron diffraction and photoemission experiments show existence of one-dimensional metallic structures which are formed within submonolayer In coverages.

*Corresponding author, e-mail: zdybr@hektor.umcs.lublin.pl

2. Experimental

The experiments were performed under ultrahigh vacuum (UKV) with the base pressure of 7×10^{-11} mbar. The UHV system is equipped with a reflection high electron energy diffraction (RHEED) apparatus, an angle resolved photoemission spectroscopy (ARPES) setup, water cooled Au, In evaporators and quartz film thickness monitor. ARPES spectrometer consists of a helium lamp, an electron energy analyzer VGX900IC and a liquid nitrogen cooled manipulator which allows one to change both polar θ and azimuth φ angles.

In order to obtain Si(335) vicinal surface, p-type B-doped silicon was used. It was cut and oriented by means of X-ray diffraction technique with the accuracy of ±0.05°. Several flashes up to 1500 K in UHV were the final steps of substrate cleaning. In order to produce array of regularly distributed monoatomic steps 0.28 ML of Au was deposited on the surface kept at 900 K. 1 ML corresponds to 7.84×10^{14} atoms/cm^2 – the density of atoms in half of double layer of Si(111) plane. Subsequently, the substrate was annealed at 950 K for a few seconds and cooled to room temperature. Indium was deposited and annealed at 800 K for 60 s. During Au and In deposition, the pressure was in a high 10^{-11} mbar range. The whole sample cleaning and preparation procedures were controlled by RHEED.

In photoemission experiments, He I line (21.2 eV) with p-polarized radiation was used. Angular and energy resolution of the analyzer were fixed to 1.5° and 50 meV, respectively. Spectra were taken for two sample orientations, with step edges parallel and perpendicular to the plane of incident radiation. All measurements were performed at 120 K.

3. Results and discussion

Figure 1a shows a RHEED pattern of Si(335)–Au surface covered with 0.16 ML of In. The black spots denote high intensity diffracted beams associated with regularly

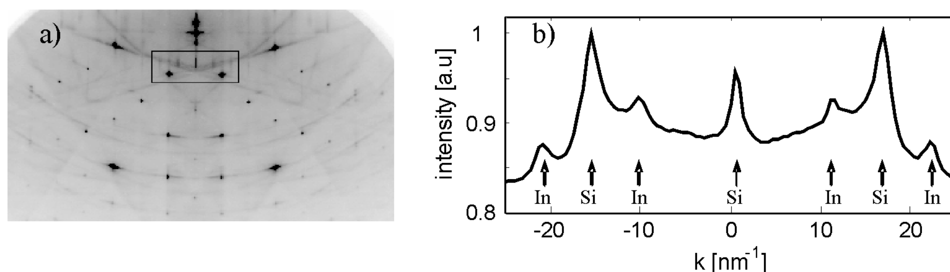

Fig. 1. RHEED pattern of Si(335)–Au surface covered with 0.16 ML of In and annealed at 800 K (a) and intensity profile taken from the marked region of a) (b); plane of incidence of the electron beam is perpendicular to the $[1\bar{1}0]$ direction

distributed monoatomic steps of Si(335)–Au substrate [4]. The presence of 0.16 ML of In deposited on that surface and annealed at 800 K is visible as additional, low intensity elongated streaks located between strong diffraction spots. They are much better visualized in the plot of intensity profile (Fig. 1 b), prepared from the marked region of the RHEED pattern. Indium induced peaks reach a broad maximum in the coverage range from 0.16 to 0.20 ML of In. The distance between neighbouring In and Si maxima Δk equals 5.43 nm^{-1} and corresponds to the period of $3a_{[1\bar{1}0]}$, where $a_{[1\bar{1}0]} = 0.384$ nm is the lattice constant along step edges.

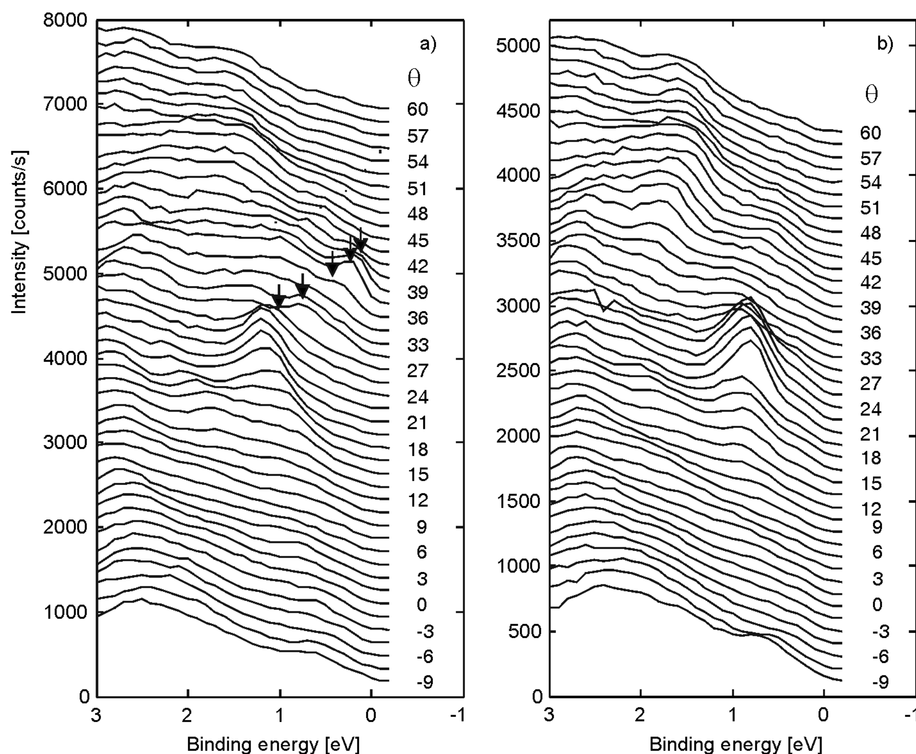

Fig. 2. ARPES spectra of: a) Si(335)–Au surface with 0.16 ML of In taken along step edges, b) bare Si(335)–Au. Spectra in Fig. 2a are shifted along intensity axis by a factor of 200 counts/s in order to prevent overlapping. Zero of binding energy denotes the Fermi energy. θ is an angle between surface normal and the entrance to electron energy analyzer. The arrows mark maxima which appeared after In deposition

Figure 2a shows ARPES spectra recorded for Si(335)–Au surface with 0.16 ML of In. The spectra were obtained for polar angle θ in the range from –9° to 60° every 1.5°, in the (110) plane parallel to the step edges of the substrate. The zero binding energy is at the Fermi energy, taken as the high kinetic energy threshold of the angle integrated spectrum. Figure 2b shows corresponding spectra recorded for Si(335)–Au substrate. Comparison of both sets of spectra shows that some of the features visible

for the substrate are also present in the spectra of indium covered surface. This is the high intensity peak at about 1 eV and 24° which shifts toward higher binding energies by about 0.38 eV after covering the surface with In. Other bands associated with bulk silicon are also visible at higher binding energies. A peak located at about 0.9 eV and 27° which moves toward the Fermi energy with increasing θ and approaches E_F at about 39° is a new feature found in the spectra of In covered surface.

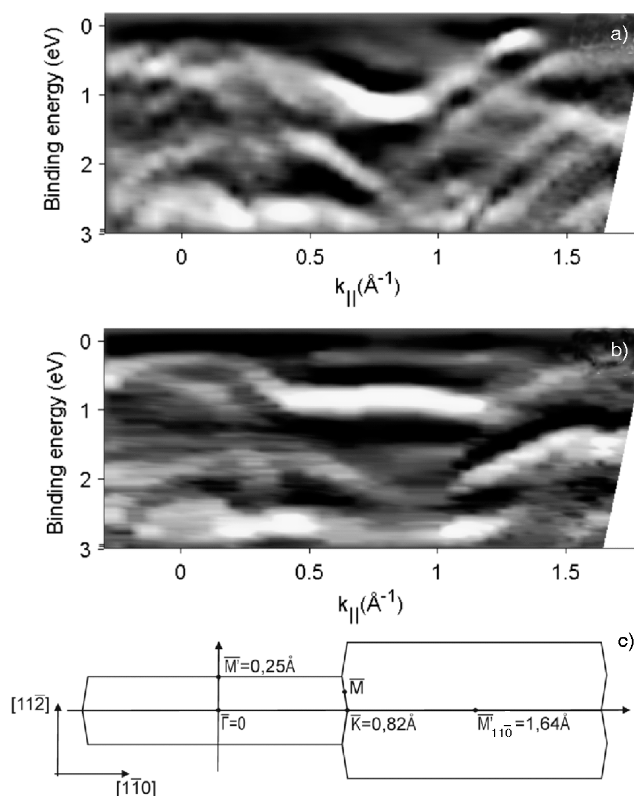

Fig. 3. Map of the second derivative of fotoemission intensity for In covered (a) and bare Si(335)–Au (b) surfaces; c) the surface Brillouin zone of Si(335) surface. The momentum component $k_{||}$ is parallel to the $[1\,\bar{1}0]$ direction

A very convenient way for presentation of ARPES spectra is displaying them as a map of the second derivative of photoemission intensity versus binding energy and wave vector component $k_{||}$. This procedure enhances weak features of acquired spectra. The result is shown in Fig. 3 for In covered (a) and bare (b) Si(335)–Au surfaces. The momentum component $k_{||}$, parallel to the $[1\,\bar{1}0]$ direction, spans over two Brillouin zones of the Si(335) surface (Fig. 3c). A minimum of highly dispersive band is located at $\overline{K}$ point and the band crosses the Fermi level at about 1.37 Å^{-1}, indicating a metallic character of the investigated system.

Photoemission spectra recorded across the step edges show no dispersive bands close to the Fermi level revealing one-dimensional character of the system. This is shown in Fig. 4 where two exemplary spectra, along (upper) and across (lower) the step edges, recorded at the same θ of 42°, are plotted.

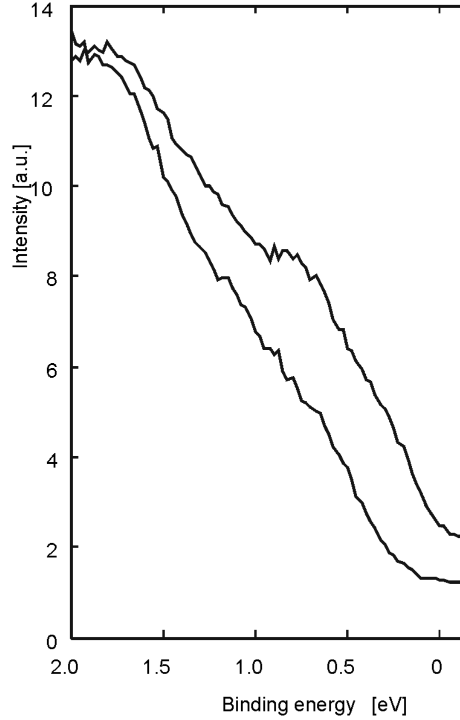

Fig. 4. ARPES spectra for $\theta = 42°$ along (upper curve) and across (lower curve) In chains

The unit cell of Si(335)–Au surface has a size of $\mathbf{1}a_{[1\bar{1}0]} \times 3(2/3)a_{[11\bar{2}]}$. Filling each unit cell with a single In atom requires coverage of 0.27 ML. The $3\times a_{[1\bar{1}0]}$ periodicity for coverages of 0.16 to 0.20 ML observed in RHEED experiment suggests an average occupancy of 2 In atoms per 3 unit substrate cells. This gives (2/3)×0.27 ML = 0.18 ML as an ideal coverage. Since unreconstructed Si(335) surface is composed of (111) terraces, some suggestions might be found in experiments on a flat Si(111) surface. For example the (4×1)-In reconstruction shows one-dimensional and simultaneously metallic character, but that reconstruction occurs at coverage of about 1 ML and temperatures below 450 °C [1, 5]. Within the temperature and coverage ranges studied in the experiments reported in this paper, the only possible reconstruction that can exist on a flat Si(111) surface, is the $(\sqrt{3}\times\sqrt{3})$ In [5] with the saturation coverage of 1/3 ML, which gives one In atom per $(\sqrt{3}\times\sqrt{3})$ unit cell [5].

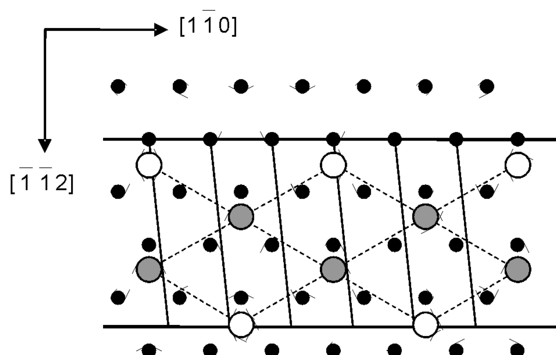

Fig. 5. Top view of unreconstructed Si(111) surface with marked $\sqrt{3}\times\sqrt{3}$ unit cells (dashed lines) and In adatoms (large circles). The horizontal lines define the width of (111) terrace of (335) surface. Several unit cells of (335) surface are also marked

Figure 5 shows a top view of (111) surface with marked several ($\sqrt{3}\times\sqrt{3}$) unit cells (dashed lines). Large circles indicate In atoms located at the T_4 sites [6]. Two horizontal lines indicate the $[1\bar{1}0]$ direction and might be thought as a position of step edges defining a (111) terrace of the (335) surface. Several unit cells of the (335) surface are also marked. There are three rows of In atoms which fit to the width of (111) terrace and one row at its edge. The coverage of 0.18 ML denotes the number of In atoms which are in two rows. There are many possibilities of arranging In atoms in a way to get $3a_{[1\bar{1}0]}$ periodicity. One of the possibilities is to remove two chains and leave the other two as they exist in the ($\sqrt{3}\times\sqrt{3}$) superstructure (e.g., shaded circles).

The arrangement of In atoms into zig-zag chain structure supports one-dimensional character of the grown structures shown by ARPES experiments. The smallest distance between indium atoms in a row, equal to $\sqrt{3}a_{[1\bar{1}0]}$, seems to be too large to be responsible for the observed in ARPES experiment metallic behaviour. The observed metallicity should be rather explained as a charge transfer to the substrate, possibly to Au monoatomic chain, and creation of an “effective” metallic chain as in the case of Pb on Si(335)–Au [7]. Trivalent In atoms act as donors what also explains the observed decrease of work function by about 0.15 eV and shift of bands to a higher binding energy.

4. Summary

Crystallographic and electronic structures of In reconstructed Si(335)–Au surface have been investigated. We found that 0.16 ML of In annealed at 800 K on the Si(335)–Au surface creates one-dimensional and metallic chains. A simple model explaining observed features has been proposed which assumes a new surface unit cell

of $3a_{[1\bar{1}0]} \times 3(2/3)a_{[11\bar{2}]}$ consisting of 2 In and 3 Au atoms inside. Such a simple model does not define exact position of In atoms on (111) terraces and certainly more studies, especially STM, are needed.

Acknowledgement

This work has been supported by grant No. N202 081 31/0372 of the Polish Ministry of Science and Higher Education.

References

[1] SARANIN A.A., ZOTOV A.V., KISHIDA M., MURATA Y., HONDA S., KATAYAMA M., OURA K., GRUZNEV D.V., VISIKOVSKIY A., TOCHIHARA H., Phys. Rev. B, 74 (2006), 035436 and references therein.
[2] PARK S.J., YEOM H.W., AHN J.R., LYO I.-W., Phys. Rev. Lett., 95 (2005), 126102.
[3] STEKOLNIKOV A.A., SEINO K., BECHSTEDT F., WIPPERMANN S., SCHMIDT W.G., CALZOLARI A., BUONGIORNO NARDELLI M., Phys. Rev. Lett., 98 (2007), 026105.
[4] ZDYB R., STRÓŻAK M., JAŁOCHOWSKI M., Vacuum, 63 (2001), 107.
[5] HASEGAWA S., TONG X., TAKEDA S., SATO N., NAGAO T., Prog. Surf. Sci., 60 (1999), 89.
[6] HANADA T., DAIMON H., INO S., Phys. Rev. B, 51 (1995), 13320.
[7] KISIEL M., SKROBAS K., ZDYB R., MAZUREK P., JAŁOCHOWSKI M., Phys. Lett. A, 364 (2007), 152.

Received 28 April 2007
Revised 16 February 2008

Materials Science-Poland, Vol. 26, No. 1, 2008

Analysis of electrical equivalent circuit of metal–insulator–semiconductor structure based on admittance measurements

S. KOCHOWSKI[1], M. SZYDŁOWSKI[1*], R. PASZKIEWICZ[2], B. PASZKIEWICZ[2]

[1]Institute of Physics, Silesian University of Technology, ul. Krzywoustego 2, 44-100 Gliwice, Poland

[2]Wrocław University of Technology, Faculty of Microsystem Electronics and Photonics, ul. Janiszewskiego 11–17, 50-372 Wrocław, Poland

An electrical equivalent circuit of Al–(thermal)SiO_2–(n)Si structure has been proposed and the results of analysis of circuit parameters have been compared with classical methods of investigations of metal–insulator–semiconductor (MIS) structures. The electrical equivalent circuit of the structure contains constant phase elements. The analysis of admittance in terms of frequency characteristics was performed for broad range of biases from inversion to accumulation. The parameters of MIS equivalent circuit determined from impedance spectroscopy data are in good agreement with values obtained by the classical analysis of capacitance–voltage and conductance–voltage characteristics as well as the conductance method.

Key words: *impedance spectroscopy; metal–insulator–semiconductor structure; constant phase element; electrical properties; silicon*

1. Introduction

Development of modern electronic technologies is determined by new semiconductor materials which make the integrated devices possible to work in broad ranges of frequencies and temperatures. The analysis of such modern materials requires applying various methods. Measurements and analysis of electrical characteristics of metal–insulator–semiconductor (MIS) structures are useful tools for investigation of various semiconductor materials. Impedance spectroscopy [1] is one of the methods of analysis of electrical admittance characteristics.

In recent years, we discussed the usability of impedance spectroscopy to characterize electron processes in the MIS structures made of gallium arsenide [2–4] and

*Corresponding author, e-mail: michal.szydlowski@polsl.pl

silicon [5]. The applied MIS electrical equivalent circuit included constant phase element (CPE) which made possible to describe frequency dispersion phenomena occurring in these systems. The CPE element has the admittance $Y_{\mathrm{CPE}} = Q(i\omega)^n$, where Q and n are frequency independent parameters. For a further estimation of usability of the method, the impedance spectroscopy analysis should be performed for systems which could be easily investigated by the classical methods of analysis of electrical characteristics.

Al–(thermal)SiO_2–(n)Si structures were the object of our investigations. We proposed an electrical equivalent circuit of MIS structure describing the frequency dispersion of admittance characteristics in a broad range of signal frequencies and gate voltages from inversion to accumulation. The analysis of admittance in terms of frequency characteristics was performed using impedance spectroscopy and by the classic conductance method. We have also estimated basic parameters of investigated structures from the analysis of capacitance–voltage and conductance–voltage characteristics. The results of calculated curves fitting to experimental admittance data have been presented and some parameters of the equivalent circuit were related to values obtained by the conductance method.

2. Experimental

The investigations have been performed on Al–SiO_2–Si structures with 103±7 nm SiO_2 dielectric layer obtained by the thermal oxidation at 1150 ºC under dry O_2 atmosphere on n-type (111) Si wafers of the resistivity of 1.5 Ω·cm. Before oxidation, silicon wafers were cleaned according to the standard procedure [6]. 0.5 μm thick gate electrodes of 1 mm in diameter were deposited by thermal evaporation of aluminum and photolithography successively. Aluminum layer was also used as a back ohmic contact to Si.

The measurements of the electrical characteristics have been done with a 4192A Hewlett Packard HF/LF impedance analyser working in a parallel circuit mode. The ac signal amplitude was kept at the value of 30 mV. The MIS capacitance and conductance versus bias (from –30 V to 10 V) at 1 MHz frequency as well as the MIS admittance versus frequency (from 500 Hz to 13 MHz) at a fixed bias (between –20 V and 10 V) have been recorded at room temperature.

3. Results and discussion

Figure 1 shows typical dependences of high frequency capacitance C and conductance G on bias U_g obtained at 1 MHz ac signal for the structures polarized from the inversion to the accumulation. According to Jakubowski et al. [7] and Witczak et al. [8] we have estimated the insulator capacitance $C_{OX} = 286\pm2$ pF, MIS serial resistance $R_S = 13.1\pm0.5\ \Omega$ and the Fermi level position in the bulk of semiconductor $u_b = 12.8\pm0.1$. Taking advantage of Ovsyuk [9] formulas, we used C_{OX} and u_b values to calculate theoretical dependence of space charge layer capacitance C_{SC} on the sur-

face potential v_s and of high frequency structure capacitance on the surface potential. The latter curve was used to plot (Fig. 1a (inset)) experimental dependence of surface potential v_s on bias U_g constructed by comparing experimental high frequency $C–U_g$ characteristics with calculated theoretical $C–v_s$ curve [10].

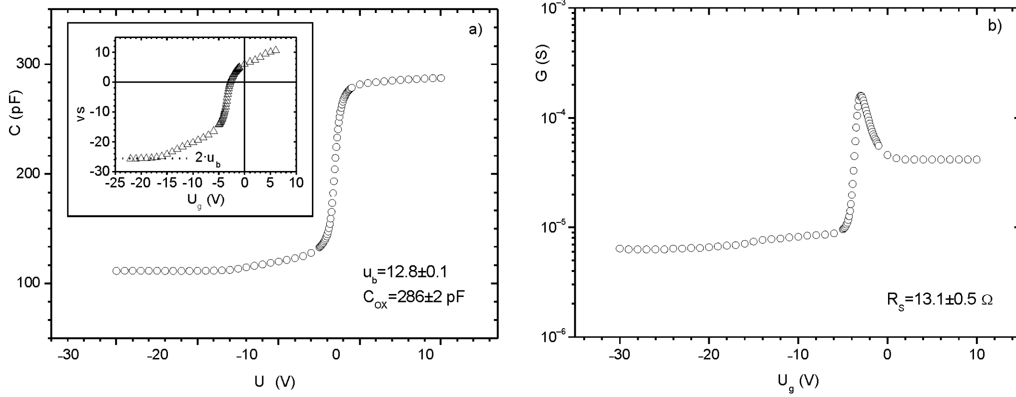

Fig. 1. Experimental $C–U_g$ (a) and $G–U_g$ (b) characteristics of Al–(thermal)SiO_2–(n)Si structure recorded at f = 1 MHz. The MIS structure was kept at 300 K. The inset shows the plot v_s vs. bias U_g constructed by comparing experimental high frequency $C–U_g$ characteristic with calculated theoretical $C–v_s$ curve [10]. The MIS capacitance C_{OX} as a $C–U_g$ maximum was determined from the characteristics, the Fermi level u_b calculated according to [7] and serial resistance Rs evaluated using formulas from [8]

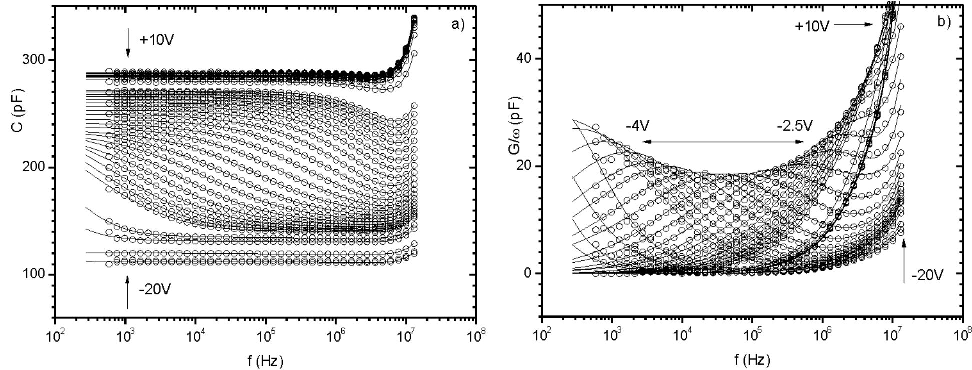

Fig. 2. Capacitance C and normalized conductance $G\omega^{-1}$ vs. frequency of Al–(thermal)SiO_2–(n)Si structures at various biases ($f = \omega/2\pi$). The sample kept at 300 K. Symbols represent experimental data while full lines are the best fits of experimental data using the circuits from Fig. 3. In Fig. b) one can see characteristic maxima of normalized conductance corresponding to frequency dispersion of capacitance in Fig. a) (biases from –4 V to –2.5 V)

In Figure 2, we present experimental dependences of MIS capacitance and normalized conductance $G\omega^{-1}$ on frequency measured at a fixed gate voltage. It is visible that changes of the capacitance and conductance take place over a wide frequency range. The normalized conductance $G\omega^{-1}$ peaks, whose frequency depends on the gate

voltage, occur and the capacitance dispersion exists in the frequency range where these maxima are observed. We managed to describe the determined characteristics by equivalent circuits presented in Fig.3. These circuits contain: insulator capacitance C_{OX}, serial resistance R_S, circuit inductance L, bias-dependent space charge layer capacitance C_{SC}, additional bias-dependent capacitance C_D, two constant phase elements $CPE_{1,2}$ characterized by $Q_{1,2}$ and $n_{1,2}$ parameters, and resistors $R_{1,2}$. The electrical equivalent circuit of the MIS structure simplifies for bias range $U_g < -5$ V (towards structure inversion, Fig. 3a) and $U_g > -3$ V (towards structure accumulation, Fig. 3c) while for $-5 \text{ V} \le U_g \le -3$ V (structure depletion) the circuit contains all elements (Fig. 3b).

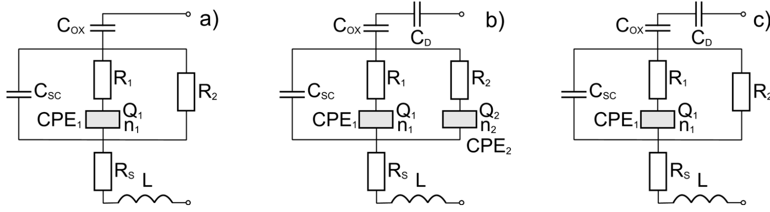

Fig. 3. Electrical equivalent circuits of the MIS structure for various bias ranges: a) $U_g < -5$ V, b) $-5 \text{ V} \le U_g \le -3$ V, c) $U_g > -3$ V, C_{OX} – insulator capacitance, R_S – serial resistance, L – circuit inductance, C_{SC} – bias-dependent space charge layer capacitance, C_D – additional bias-dependent capacitance, $CPE_{1,2}$ – constant phase elements characterized by $Q_{1,2}$ and $n_{1,2}$ parameters, $R_{1,2}$ – resistances

The estimation of the equivalent circuit parameters was performed by the Levenberg–Marquardt algorithm [11] of simultaneous fitting of capacitance and normalized conductance curves to experimental data using the OriginLab software. The best fitted values of the equivalent circuit parameters are presented in Fig. 4 and the theoretical dependences calculated for these data are shown as full lines in Fig. 2. From the data presented in Fig. 4, one can see that the frequency behaviour of the investigated structures is very well reproduced by the proposed equivalent circuits in a full range of measured biases. Good fitting of theoretical dependences to the experimental data (Fig. 2) as well as the monotonous dependence of the circuit parameters on the gate voltage (Fig. 4) suggest that the elements of the equivalent circuit reasonably represent physical processes in various parts of the investigated structures. The values of insulator capacitance C_{OX} and serial resistance R_S are, as expected, practically bias independent being in very good agreement with the results obtained from C–U_g and G–U_g characteristics (Fig. 4). The serial resistance can arise from different sources [12], the main one being the resistances of the semiconductor material as well as of the contacts and electrical connections. The value of the circuit inductance parameter L equals 0.12±0.02 μH, and is negligibly small and bias independent. The origin of the additional bias-dependent capacitance C_D is not clear at the moment. However, regarding this parameter made it possible to obtain monotonous dependence of C_{OX} capacitance on the gate voltage and its compatibility with the value obtained from the capacitance

–voltage characteristic. The estimated space charge layer capacitance C_{SC} coincides with theoretical C_{SC} curve calculated based on the u_b value determined from C–U_g characteristics for biases corresponding to inversion and depletion region of MIS structure (Fig. 4a). The essential features of the admittance characteristics of the MIS structures are described by the constant phase elements CPE_1 and CPE_2 connected in series with resistors R_1 and R_2, respectively.

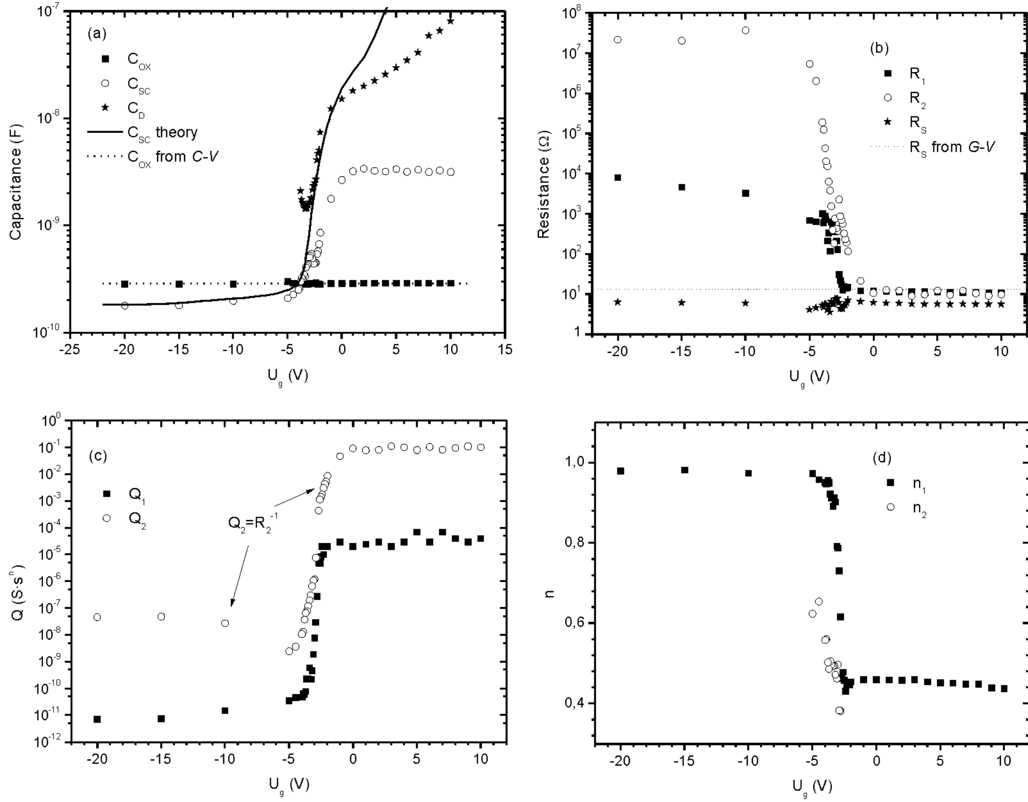

Fig. 4. Values of equivalent circuit parameters from Fig. 3 obtained at various biases U_g (symbols): a) C_{OX} – insulator capacitance, C_{SC} – bias-dependent space charge layer capacitance, C_D – additional bias-dependent capacitance; b) R_1 and R_2 resistances, R_S serial resistance; c) constant phase element parameters Q_1, Q_2 and parallel resistance $R_2 = Q_2^{-1}$; d) constant phase elements parameters n_1 and n_2. Dashed line in (a) represents constant insulator capacitance C_{OX} obtained from C–U_g characteristics. Full line in a) shows a theoretical curve of space charge layer capacitance C_{SC} vs. bias calculated according to Ovsyuk formulas [9] where the surface potential v_s was assigned to U_g using inset in Fig. 1a. Dotted line in b) represents constant serial resistance R_S obtained from G–V characteristics according to [8]

They are related to electron processes with a broad distribution of time constants around the characteristic values $\tau_1 = (R_1 Q_1)^{1/n_1}$ and $\tau_2 = (R_2 Q_2)^{1/n_2}$. The time constants were calculated using data from Fig. 4b, c, d and are presented in Fig. 5. We also used the Nicollian–Goetzberger–Lopez conductance method [13] to extract time constants

τ_{NGL} from measured normalized conductance in depletion. These time constants characterize exchange of electrons between SiO_2–Si interface and semiconductor states. The τ_{NGL} values, presented in Fig. 5, are in very good agreement with τ_2 values. This suggests that time constants τ_2 and τ_{NGL} are connected with the same electron process. Thus the constant phase element CPE_2 in series with R_2 resistance describes the dispersion phenomena evoked by the semiconductor–insulator interface states. The time constant τ_1 is practically gate voltage independent. This kind of behaviour points to the presence of the deep traps in the semiconductor space charge region. The CPE_1 element with the parameter $n_1 = 0.95$ for $U_g < -5$ V ($v_s < -13$, see Fig.1) has "capacitive" character (for pure capacitance $n = 1$) and together with R_1 resistance they characterize the time constant of monoenergetic electron traps in a lower part of the energy gap of the semiconductor. For $U_g > -3$ V ($v_s > 0$), what corresponds to the traps located in an upper part of the energy gap; the CPE_1 element with the parameter $n_1 = 0.46$ connected with R_1 resistance describes electron processes with a broad spectrum of time constants.

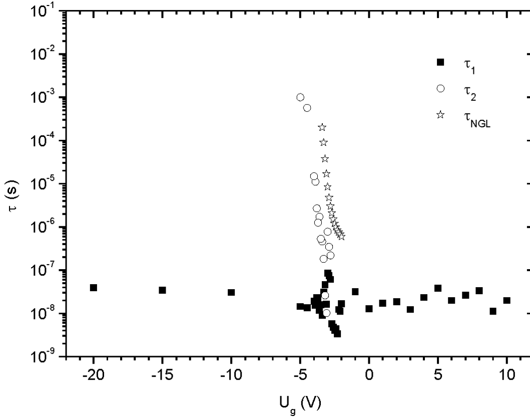

Fig. 5. Time constants τ at various biases U_g; τ_1 and τ_2 were calculated from Q_1, n_1, R_1 and Q_2, n_2, R_2 data presented in Fig. 4b–d. Time constant τ_{NGL} was estimated according to Nicollian–Goetzberger–Lopez method [13]

The presented results show that the proposed equivalent circuits with constant phase elements allow one to describe complex processes evoked by localized electron states in the MIS structures, pointing to the usability of the impedance spectroscopy method for the analysis of other materials and systems, especially where standard methods are difficult or impossible to apply.

4. Conclusions

We proposed the electrical equivalent circuit of Al–(thermal)SiO_2–(n)Si structure with constant phase elements describing frequency behaviour of admittance characteristics in a broad range of gate voltages and frequencies. The parameters of MIS equivalent circuit determined by the impedance spectroscopy method are in good agreement with the values obtained by the standard analysis of admittance–voltage

characteristics as well as the conductance method. The constant phase elements in series with resistances describe electron processes connected with localized electron states resulting in frequency dispersion of measured characteristics of structures.

Acknowledgements

The authors wish to thank Prof. Karol Nitsch from Wrocław University of Technology, Faculty of Microsystem Electronics and Photonics, for providing the samples and for many valuable discussions.

References

[1] MACDONALD J.R., *Impedance Spectroscopy*, Wiley, New York, 1987.
[2] KOCHOWSKI S., NITSCH K., Thin Solid Films, 415 (2002), 133.
[3] KOCHOWSKI S., NITSCH K., PASZKIEWICZ B., PASZKIEWICZ R., Thin Solid Films, 444 (2003), 208.
[4] KOCHOWSKI S., NITSCH K., PASZKIEWICZ B., PASZKIEWICZ R., SZYDŁOWSKI M., Appl. Surf. Sci., 235 (2004), 389.
[5] KOCHOWSKI S., SZYDŁOWSKI M., Zesz.Nauk. Pol. Śląskiej, Ser. Mat.-Fiz., 91 (2004), 199.
[6] *Model Laboratory Processes and Procedures, Bell Telephone Laboratories*, New Jersey, 1965.
[7] JAKUBOWSKI A., INIEWSKI K., Solid-State Electron., 26 (1983), 755.
[8] WITCZAK S.C., SUEHLE J.S., GAITAN M., Solid-State Electron., 35 (1992), 345.
[9] OVSYUK V.N., *Electron Processes in Semiconductors with Space-Charge Region*, Nauka, Novosibirsk, 1984 (in Russian).
[10] TERMAN L.M., Solid-State Electron., 5 (1962), 285
[11] PRESS W.H., TEUKOLSKY S.A., VETTERLING W.T., FLANNERY B.P., *Numerical Recipies in C. The Art of Scientific Computing*, Cambridge University Press, Cambridge, 2002.
[12] NICOLLIAN E.H., BREWS J.R., *MOS (Metal-Oxide-Semiconductor) Physics and Technology*, Wiley, New Jersey, 2003.
[13] NICOLLIAN E. H., GOETZBERGER A., LOPEZ A.D., Solid-State Electron., 12 (1969), 937.

Received 28 April 2007
Revised 16 February 2008

Materials Science-Poland, Vol. 26, No. 1, 2008

Technology and properties of GaAs doping superlattices

B. ŚCIANA[1*], D. RADZIEWICZ[1], D. PUCICKI[1], M. TŁACZAŁA[1], G. SĘK[2], P. POLOCZEK[2], J. MISIEWICZ[2], J. KOVÁČ[3], R. SRNANEK[3], A. CHRISTOFI[4]

[1]Faculty of Microsystem Electronics and Photonics, Wrocław University of Technology, ul. Janiszewskiego 11/17, 50-372 Wrocław, Poland

[2]Institute of Physics, Wrocław University of Technology, Wybrzeże Wyspiańskiego 27, 50-370 Wrocław, Poland

[3]Department of Microelectronics, Faculty of Electrical Engineering and Information Technology, Slovak University of Technology, Ilkovičova 3, 812 19 Bratislava, Slovakia

[4]Department of Materials, Imperial College London, London SW7 2AZ, England

Heterojunction and doping superlattices are widely used in many advanced semiconductor devices such as resonant tunnelling diodes, optical modulators, cascade lasers, tunable light emitting diodes and photodetectors. These structures exhibit nonlinear electrooptical properties. Nonlinear processes are governed by the Franz–Keldysh effect and the band-filling effect in the n-i-p-i superlattices and by the quantum-confined Stark effect in the case of n-i-p-i multiple quantum well structures. The paper presents investigations of GaAs n-i-p-i and p-i-p-i doping superlattices grown by atmospheric pressure metal organic vapour phase epitaxy. The properties of the obtained structures were examined using: EC–V method, SIMS spectrometry, photoluminescence and photoreflectance spectroscopy.

Key words: *doping superlattice; δ-doping; AP MOVPE; photoreflectance, photoluminescence*

1. Introduction

Unique properties of doping superlattices include a superlattice energy gap smaller than the gap energy of the bulk semiconductor, spatial separation of electron and hole wave functions, and smaller oscillator strength of optical transitions. These features are responsible for a prolongation of the carrier lifetime and a large reduction in the absorption coefficient [2]. Thus, doping superlattices are very attractive for application in tunable optoelectronic devices. Semiconductor doping superlattices are mainly fabricated by two epitaxial methods: molecular beam epitaxy (MBE) and metal organic

[*]Corresponding author, e-mail: Beata.Sciana@pwr.wroc.pl

vapour phase epitaxy (MOVPE). Employment of the δ-doped technique [3, 4] results in a spatial confinement of dopants to a single atomic plane. The paper presents the technology and properties of GaAs-based n-i-p-i and p-i-p-i superlattices deposed by atmospheric pressure metal organic vapour phase epitaxy (AP MOVPE). Various methods used for determination the spatial localisation of dopants and optical properties of the investigated structures are presented and discussed.

2. Experiment

The GaAs n-i-p-i and p-i-p-i doping superlattices were grown by AP MOVPE on (100)-oriented semi-insulating GaAs substrate, using an AIX 200 R&D Aixtron horizontal reactor. TMGa, AsH_3 (10% mixture with H_2), SiH_4 (20 ppm mixture with H_2) and DEZn were used as the growth and dopant precursors. High purity hydrogen was employed as a carrier gas. A δ-doping procedure "purge-doping-purge" was applied for formation of the n-type and p-type delta-doped regions. The n-i-p-i structure consisted of the alternating p-type (Zn) and n-type (Si) δ-doped regions, separated by 50 nm of undoped GaAs (periodicity: z_0 = 100 nm). The structure consisted of 5.5 periods. Designed sheet donor and acceptor concentrations were $N_A^{2D} = N_D^{2D} \approx 1\times10^{12}\,\mathrm{cm}^{-2}$. The p-i-p-i structure consisted of 10 of the p-type (Zn) δ-doped regions separated by 15 nm of undoped GaAs (periodicity: z_0 = 15 nm). The designed sheet acceptor concentration was $N_A^{2D} \approx 1\times10^{12}\,\mathrm{cm}^{-2}$. The thickness of the top undoped GaAs layer was 20 nm. For example the epitaxial structure, the scheme of the doping profile and the band diagram of the designed n-i-p-i structure are shown in Figs. 1, 2. AP MOVPE processes were carried out at 650 °C (n-i-p-i) and at 670 °C (p-i-p-i) under optimal growth conditions, estimated from earlier studies [5, 6].

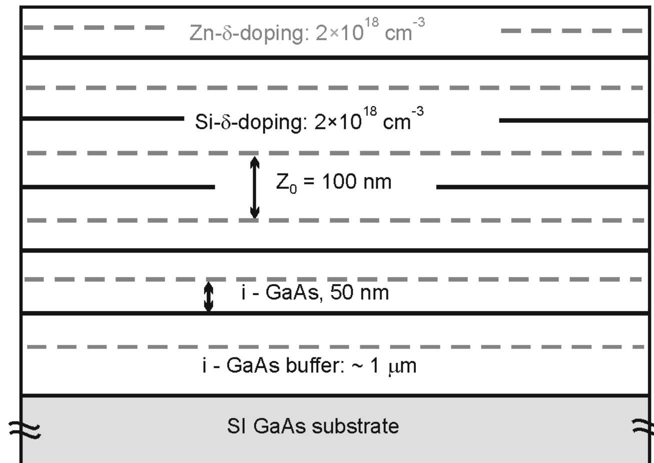

Fig. 1. Epitaxial structure of the n-i-p-i GaAs superlattice

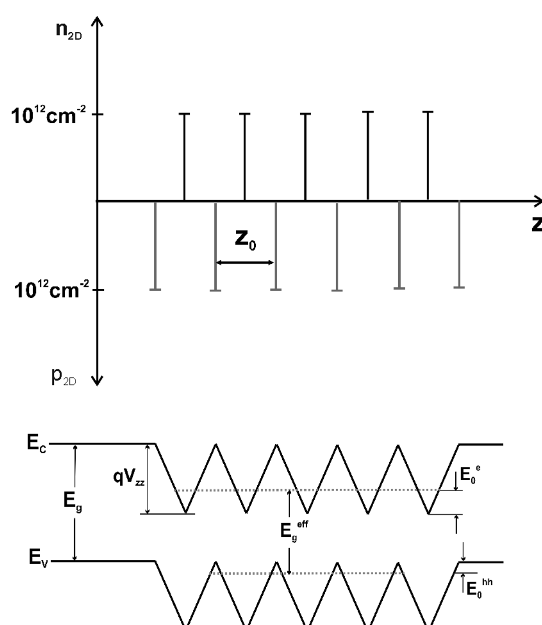

Fig. 2. Scheme of the doping profile and the band diagram of the designed n-i-p-i GaAs superlattice

3. Results and discussion

3.1. Electrochemical capacitance–voltage measurements

The carrier distribution across the investigated structures was measured using a Bio-Rad PN 4300 electrochemical capacitance–voltage (EC–V) profile at the frequency of 3 kHz. The method applies the capacitance–voltage analysis of a reverse bias electrolyte–semiconductor Schottky diode for evaluation of a free carrier concentration. The EC–V profiles of the n-i-p-i and p-i-p-i structures are presented in Figs. 3 and 4, respectively.

In the case of the long period n-i-p-i superlattice 6 spikes connected with the p-type δ-doped regions are visible. The best accuracy is obtained for the first peak with the maximum hole concentration of 5×10^{18} cm^{-3} and the width of 6 nm. The distance between p-type doped regions is about 85 nm ($< z_0 = 100$ nm). Next spikes exhibit lower hole concentrations and a significant profile broadening due to the influence of the etch non-uniformity and a large series resistance [7]. The presence of free carriers indicates that the n-i-p-i structure is not fully compensated (sample has got 6 p-type regions and 5 n-type regions). For a short period p-i-p-i structure, large EC–V profile broadening is observed, thus determination of the carrier concentration and localisation in the p-type δ-doped regions is impossible.

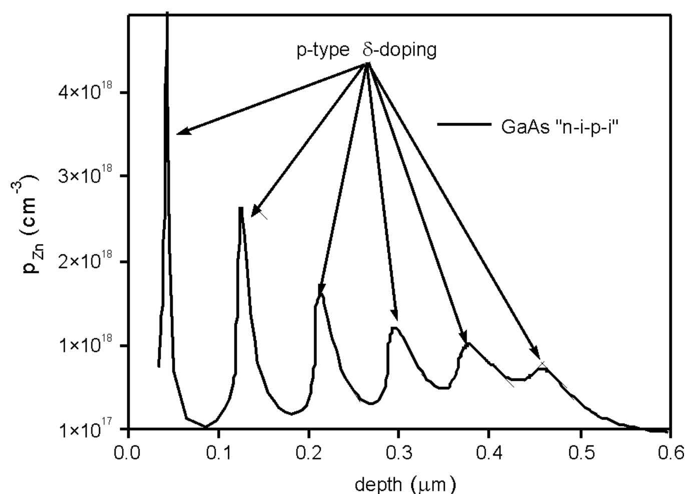

Fig. 3. Electrochemical capacitance-voltage profile of the n-i-p-i superlattice

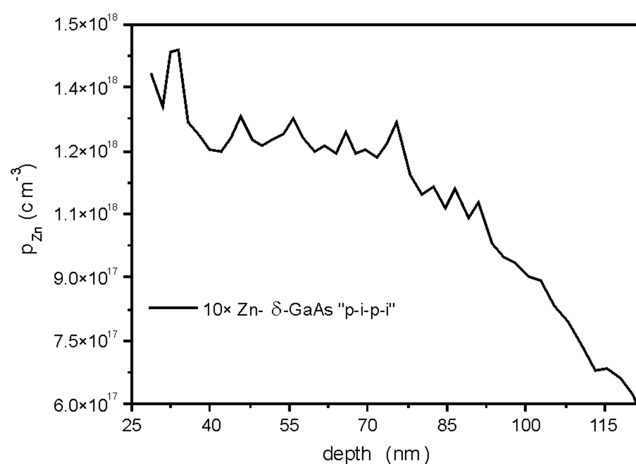

Fig. 4. Electrochemical capacitance-voltage profile of the p-i-p-i superlattice

3.2. Secondary ion mass spectrometry

Secondary ion mass spectrometry (SIMS) was applied for determination of the dopant distribution in the investigated structures. In contrast to the C–V profiling based on a free carrier effect, this method gives information about dopant atoms. The SIMS profiles of the n-i-p-i and p-i-p-i structures are shown in Figs. 5 and 6, respectively. All clearly resolved peaks connected with Zn and Si atoms localised in the δ-doped regions are visible in the figures. The superlattice period of 100 nm and

15 nm was estimated for the n-i-p-i and p-i-p-i structure, respectively, what corresponds very well to the designed values.

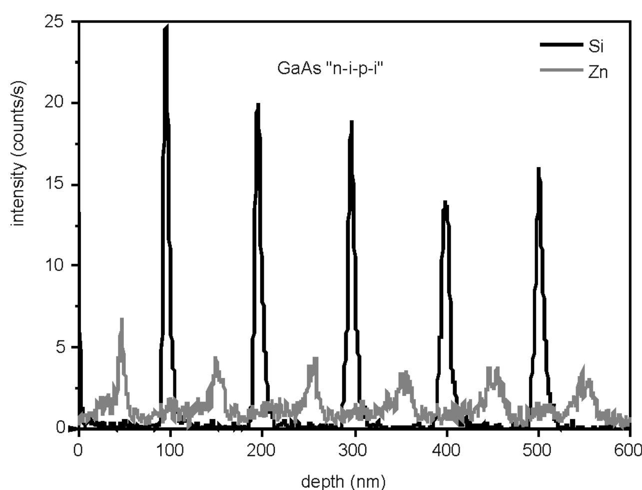

Fig. 5. SIMS profile of the n-i-p-i superlattice

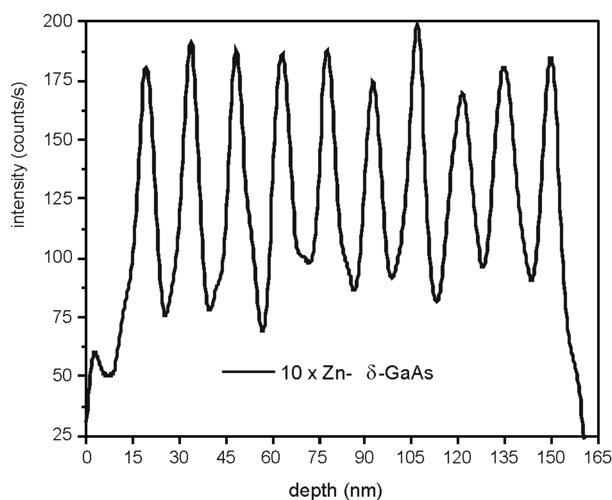

Fig. 6. Secondary ion mass spectrometry profile of the p-i-p-i superlattice

In Figure 5, the width of the SIMS peaks increases (6–9 nm for Si and 8–17 nm for Zn) upon the depth what could be connected with increasing the roughening of the sputtered crater with the sputtering time. In the case of deeper localised Zn atoms, the broadening can be also explained by diffusion. The SIMS profile of the p-i-p-i structure shown in Fig. 6 exhibits nearly the same peak width (9–10 nm). This structure is much thinner than the n-i-p-i superlattice, so both the growth and the sputtering times were shorter in this case.

3.3. Photoluminescence and photoreflectance measurements

Photoreflectance (PR) spectroscopy was applied for determination of the energy band structure of the doping superlattices. The method is a classical modulation spectroscopy. An internal electric field of the investigated material is modulated with an absorbed laser beam and the photoinduced changes in the reflectance spectrum are measured, yielding a derivative-like spectral response with a high sensitivity to optical transitions. Photoreflectance was measured using a 150 W tungsten halogen lamp as a probe beam source and 632.8 nm line of He-Ne laser as the pump beam, which was mechanically chopped at 275 Hz. Further details of the experimental PR set-up have been described elsewhere [8].

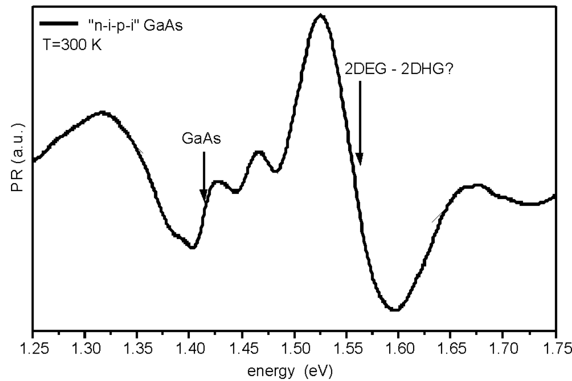

Fig. 7. Photoreflectance spectrum of the n-i-p-i superlattice

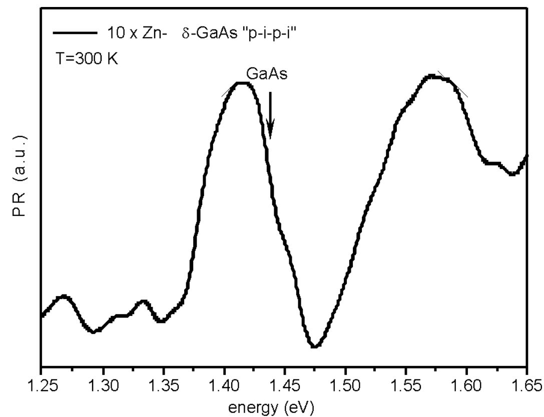

Fig. 8. Photoreflectance spectrum of the p-i-p-i superlattice

PR spectra of the n-i-p-i and p-i-p-i structures recorded at 300 K are shown in Figs. 7 and 8, respectively. PR spectrum of the n-i-p-i superlattice (Fig. 7) exhibits two optical transitions. The first weak transition at 1.42 eV is connected with the band-gap energy of GaAs (the undoped parts of the structure) and the second strong transition at 1.56 eV is

unusual for the bulk GaAs and comes probably from the transitions involving two-dimensional electron gas and two-dimensional hole gas. In the PR spectrum of the p-i-p-i structure (Fig. 8) the transition related to the band-gap energy of GaAs and some Franz –Keldysh oscillations (FKO) for higher energies are visible. FKO oscillations come from an internal electric field introduced by ionised Zn δ-doped centres.

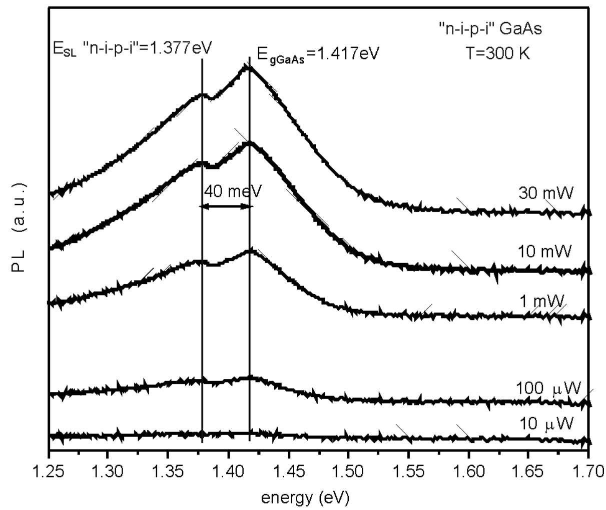

Fig. 9. Photoluminescence spectra of the n-i-p-i superlattice

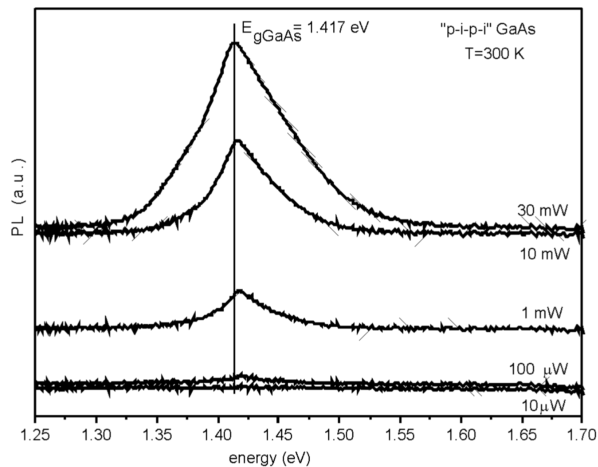

Fig. 10. Photoluminescence spectra of the p-i-p-i superlattice

Photoluminescence (PL) spectroscopy is an emission-like experiment giving information about various radiative recombination channels in semiconductors. PL spectra of the investigated structures were recorded using a standard experimental configuration with 532 nm line of a frequency doubled Nd:YAG laser as the excitation source,

and a cooled InGaAs PIN photodiode combined with 0.55 m focal length monochromator as the detection system. PL spectra of the n-i-p-i and p-i-p-i structures recorded at 300 K for various optical excitation intensities (10 μW–30 mW) are shown in Figs. 9 and 10, respectively. For the n-i-p-i structures (Fig. 9) beside the emission line related to the band-gap of GaAs (1.417 eV), an additional PL peak is visible at 1.377 eV. It is probably connected with subband transitions inside the V-shaped potential wells and corresponds to the effective band gap of the sawtooth n-i-p-i superlattice. The energy of this peak does not change upon variation of the excitation intensity. In the case of the p-i-p-i structure (Fig. 10), free carriers (holes) screen their parent ionised acceptors and only one PL peak related to band-gap of GaAs is observed.

4. Conclusions

The technology and properties of GaAs-based n-i-p-i and p-i-p-i superlattices are presented and discussed. The results of EC–V measurements indicate that in the case of multi-δ-doped structures, a precise determination of the carrier concentration in each δ-layer is impossible due to the etch non-uniformity and a large series resistance. For a short period superlattices the method is useless. Accurate localisation of Zn and Si atoms in δ-doped regions was possible by applying the SIMS technique. The SIMS profiles of the p-i-p-i superlattices indicate that AP MOVPE technology allows one to obtain a short period (z_0 = 15 nm) doping superlattice using Zn dopant. The optical transitions related to the sawtooth superlattice are visible in the PR and PL spectra of the long period n-i-p-i structures.

Acknowledgements

This work was partially supported by the Wrocław University of Technology statutory grant, the Ministry of Scientific Research and Information Technology, grant No. 515 002 31/0239, and by a bilateral cooperation Pol/Slov project.

References

[1] ANDO H., IWAMURA H., OOHASHI H., KANABE H., IEE J. Quant. Electr., 26 (1989), 2135.
[2] SCHUBERT E.F., HORIKOSHI Y., PLOOG K., Phys. Rev., 36 (1985), 1085.
[3] SCHUBERT E.F., J. Vac. Sci. Technol. A, 8 (1990), 2980.
[4] LI G., JAGADISH C., Solid-State Electr., 41 (1997), 1207.
[5] ŚCIANA B., RADZIEWICZ D., PUCICKI D., TŁACZAŁA M., SĘK G., Proc. of the 5th Intern. EuroConference ASDAM 2004, October 2004, Smolenice, Slovakia, pp. 111–113.
[6] ŚCIANA B., RADZIEWICZ D., PASZKIEWICZ B., TŁACZAŁA M., SITAREK P., SĘK G, MISIEWICZ J., KINDER R., KOVAC J., SRNANEK R., Thin Solid Films, 412 (2002), 55.
[7] SELL B., GATZKE C., FERNÁNDEZ J.M., Semicond. Sci. Technol., 13 (1998), 423.
[8] MISIEWICZ J., SĘK G., KUDRAWIEC R., SITAREK P., Thin Solid Films, 450 (2004), 14.

Received 28 April 2007
Revised 16 February 2008

Materials Science-Poland, Vol. 26, No. 1, 2008

Influence of the deposition parameters of nucleation layer on the properties of thick gallium nitride layers

J. PRAŻMOWSKA[1*], R. KORBUTOWICZ[1], R. PASZKIEWICZ[1],
A. SZYSZKA[1], A. PODHORODECKI[2], J. MISIEWICZ[2], M. TŁACZAŁA[1]

[1]Wrocław University of Technology, Faculty of Microsystem Electronics and Photonics, ul. Janiszewskiego 11/17, 50-372 Wrocław, Poland

[2]Wrocław University of Technology, Institute of Physics, Wybrzeże Wyspiańskiego 27, 50-370 Wrocław, Poland

Gallium nitride layers were grown on sapphire (0001) substrates on low temperature (LT)-GaN layer deposited by the HVPE method. HCl flow rates and deposition times of the nucleation layer were varied in the range of 8–10 cm^3/min and 5–9 min (with the step of 2 min), respectively. Morphologies of LT-GaN buffer layers and subsequent high temperature (HT)-GaN layers were examined by scanning electron microscopy. Photoluminescence spectra of HT-GaN layers were recorded which allowed us to evaluate the optical quality of thick HVPE HT-GaN layers.

Key words: *HVPE method; thick GaN layer; HT-GaN; LT-GaN*

1. Introduction

Gallium nitride and other AIII-N compounds are promising semiconductor materials for variety of applications including optoelectronic devices such as light-emitting diodes (LEDs), laser diodes (LDs) [1] and high-power electronic devices such as high electron mobility transistors (HEMTs) [2].

Heteroepitaxial growth of GaN by vapour phase transport has been developed for about 35 years [3]. Nakamura et. al. [4] reported that application of thin buffer layer could significantly improve quality of GaN layers grown by metalorganic vapour phase epitaxy (MOVPE). It is well known that application of low temperature (LT) -GaN or AlN layer could reduce misfit dislocations also in other technologies [5]. Actually, various materials are applied as buffer layers: LT-GaN [5–7], high temperature (HT)-GaN [8], AlN [8, 9, 10,], ZnO [11, 12]. Additionally, many complicated

[*]Corresponding author, e-mail: Joanna.Prazmowska@pwr.wroc.pl

techniques were developed allowing one to reduce the density of threading dislocations in heteroepitaxial GaN layers. The most common techniques applied for this purpose are epitaxial lateral overgrowth (ELOG) or pendeo-epitaxial overgrowth (PEOG) techniques [8, 13]. These techniques require dielectric layer deposition and lithography processes what complicates the growth of the layers and generates additional costs. Application of LT-GaN buffer layer allows reduction of the costs and simplifies the growth procedure by eliminating some technological steps. Though, the substrate nitridation and the growth of LT-GaN and subsequent HT-GaN layers could be performed in one-chamber multi-step technological process. It was found that conditions of deposition of buffer layers strongly influence the quality of thick HT-GaN layer. As a result, the reduction of the density of threading dislocations [14] could be obtained depending on the growth conditions of LT-GaN layers. Also the type of applied buffer layer influences the polarity and crystal quality of GaN layer [15, 7] and its morphology [6].

2. Experimental

Thick HT-GaN layers were deposited on sapphire (0001) substrates (10×10 mm^2) by atmospheric pressure hydride vapour phase epitaxy (HVPE) at a hot wall horizontal quartz reactor heated by a three-temperature section resistance furnace [16]. Nitrogen (6N) was the carrier gas and ammonia (NH_3, 7N) – the source gas. Flows of the gases were 4000 cm^3/min and 400 cm^3/min, respectively. GaCl was formed by the reaction of gaseous HCl (6N) and metallic liquid Ga (6N) at 920 °C. HCl was diluted by nitrogen (250 cm^3/min).

Multi-step growth process was adapted to grow thick GaN layers (Fig. 1). Before the growth process, sapphire substrates were degreased in organic solvents and etched in solutions of HF:H_2O (1:10). After cleaning, the sapphire substrates were rinsed in deionized water and dried in N_2 flow.

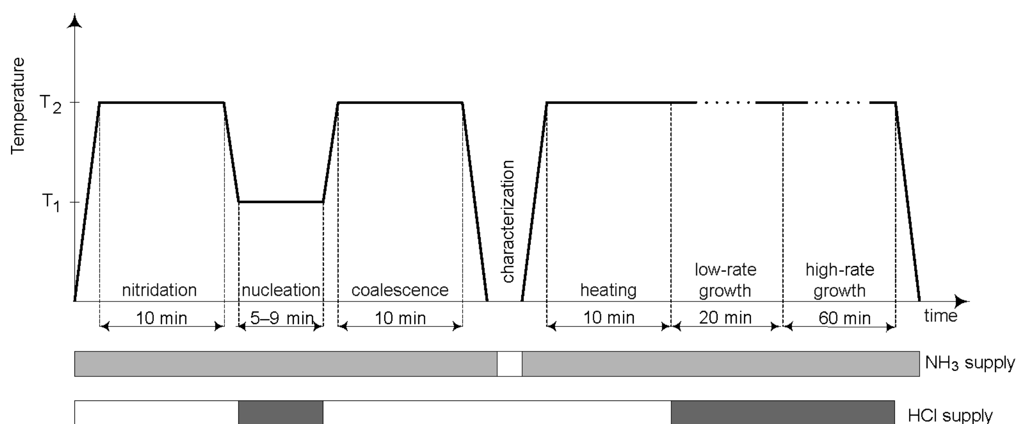

Fig. 1. Scheme of multi-step growth of GaN layers

First, sapphire substrates nitridation was performed in the atmosphere of the mixture of N_2:NH_3 (10:1) gases during 10 min, then nucleation layers were deposited at various HCl flows and times of deposition (t_n). Temperature was kept constant at 450 °C, HCl flows 8 and 10 cm^3/min and time intervals 5, 7 and 9 min were applied (Table 1).

Table 1. Flow rates of HCl and times of LT-GaN deposition

Sample	HCl flow rate [cm^3/min]	Time [min]
G87	8	5
G89	8	7
G91	8	9
G93	10	5
G95	10	7
G96	10	9

After LT-GaN epitaxy, the samples were heated for 10 min at 1050 °C in order to perform the migration of species and recrystallization. Further, the same samples were cooled down and SEM images were taken.

After characterization of LT-GaN layers, the samples were prepared as previously described and loaded to the epitaxial reactor. Heating of template substrates at 1050 °C in the mixture of N_2:NH_3 gases was performed to remove oxygen species and prevent the LT-GaN layer decomposition. Next, the HT-GaN (1050 °C) thick layers were deposited in a two-step growth process, first with a slow growth rate (about 6 μm/h), then with a high growth rate (> 20 μm/h). HCl flows were 10 and 30 cm^3/min per 20 and 60 min, respectively. Ammonia flow was 400 cm^3/min, N_2 carrier gas flow was 4000 cm^3/min and they remained unchanged during all steps of the growth process.

3. Results

Scanning electron microscopy images of LT-GaN layers are shown in Fig. 2. Samples G87, G89 and G91 were prepared with HCl flow rate 8 cm^3/min, other samples with HCl flow rate 10 cm^3/min. Depending on the deposition time of buffer layers and the flow rate of HCl, various densities of nucleation islands were observed. For the sample G87 (Fig. 2a) deposited for 5 min in the HCl flow 5 cm^3/min, the lowest density of nucleation layer was observed. The increase of the time interval of the buffer layer deposition caused the increase of the densities of nucleation sites and enlargement of the islands sizes (Fig. 2c). Apart from large crystallites (white points, about 1 μm in diameter) small crystallites (about 250 nm in diameter; density 80 per 100 μm^2) were also observed on the surface of sample G87. Islands on the surface of the sample G91 had, on average, about 4 μm in diameter. For the samples G93, G95 and G96 (HCl flow = 10 cm^3/min), the increase of the deposition time of the buffer layer had no significant influence. Sizes and densities of crystallites on the surfaces of

G93 and G96 samples were comparable. A comparison of surfaces of the samples G87 and G93 could lead to the conclusion that enhancement of deposition time caused the increase of density and size of nucleation islands what was not observed for other samples.

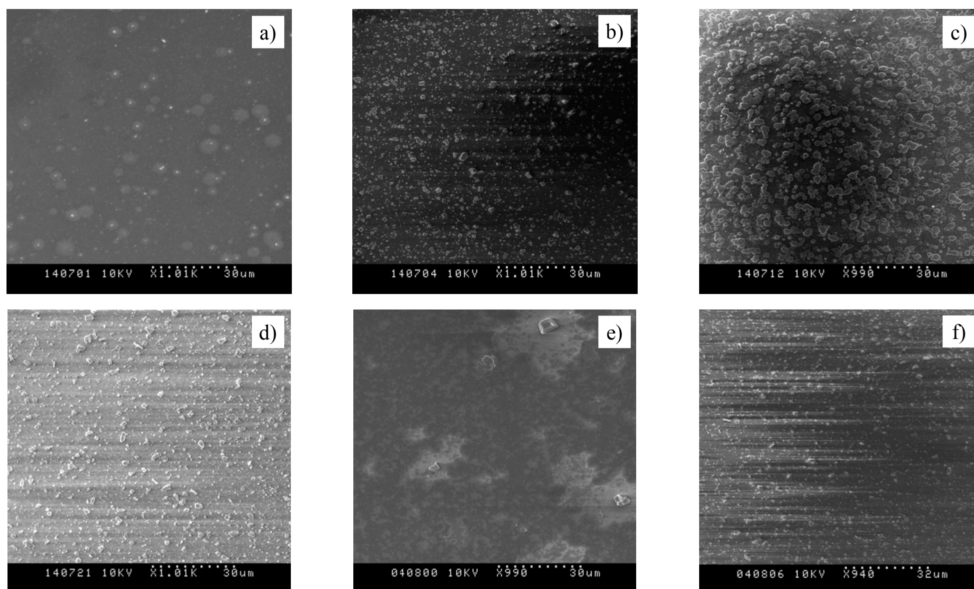

Fig. 2. SEM images of LT-GaN layers : a) G87, b) G89, c) G91, d) G93, e) G95, f) G96

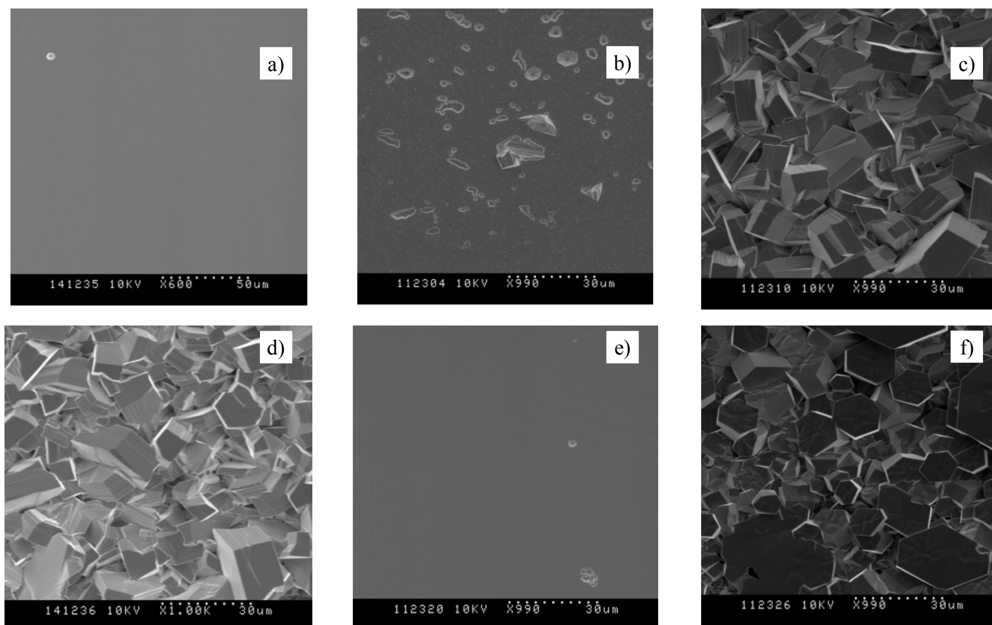

Fig. 3. SEM images of thick GaN layers: a) G87, b) G89, c) G91, d) G93, e) G95, f) G96

Next, thick HT-GaN layers were deposited on Al_2O_3/LT-GaN templates by the HVPE method. Thicknesses of these layers ranged from 10 to 20 μ. Scanning electron microscopy was used to determine the surface morphologies (Fig. 3), photoluminescence spectra were measured to evaluate the optical quality of the layers.

Morphologies of samples deposited on LT-GaN grown with HCl flow 8 cm^3/min were found to deteriorate on increasing the deposition times. The surface of the sample G87 was very smooth, whereas some irregularities could be observed on the surface of G89. On the surface of sample G91, polycrystalline growth was observed. No visible effect of the nucleation time of the layer on HT-GaN surface morphologies of other samples has been observed. The smoothest surface was obtained for the sample G95, the other ones were polycrystalline.

The sample G95 surface morphology could be closely related with growth rate (v_g) (Table 2). Low velocity of growth assured flat surface of the mentioned G95 and G87 samples. Table 2 contains also average thicknesses (t) of grown HT-GaN layers.

Table 2. Thicknesses and growth rates of GaN layers

Sample	t [μm]	v_g [μm/min]
G87	12.4	0.19
G89	21	0.31
G91	19.2	0.29
G93	17.3	0.26
G95	9.6	0.14
G96	14.8	0.22

Photoluminescence experiments were performed at room temperature by using the 330 nm line of a Xenon lamp as a pump beam. Full width at half maximum (FWHM) of the beam was of about 10 nm. The density of excitation power was 10 mW/cm^2. Silicon photodiode was applied as a detector for the emission signal collection. The PL spectra were not normalized to Xenon lamp spectra. Figure 4 shows PL for samples with the strongest emission.

The highest intensity of emission was observed for the sample G87. Two emission peaks were observed at 3.44 eV and 3.362 eV. The former one could be related to the band to band transition. The 3.362 eV peak was associated with an excitonic transition bound to dislocations or cubic inclusions in hexagonal GaN layers [17]. The samples G93 and G96 in spite of their crystalline surfaces have emission peaks near 3.4 eV. The maximum peak for the sample G93 was observed at 3.34 eV, the blue shift could be explained by residual tensile strain [18]. It has been identified as a defect-related donor–acceptor pair (DAP) transition by Trager-Cowan et al. [17]. Broad-band yellow emission was related to the presence of point defects in the GaN layer. A strong signal of the PL spectra observed in the range of 1.8 to 2.8 eV may be due to the lack of normalization of PL spectra to the pump beam spectra and this region will not be ex-

tensively analyzed in this paper. The measured FWHMs of PL spectra of samples were as follows: G87 – 0.34 eV, G93 – 0.32 eV, G96 – 0.42 eV. FWHM of the PL spectra of the sample G95 was about 0.21 eV. The samples G89, G91 and G93 exhibit a surprisingly weak emission.

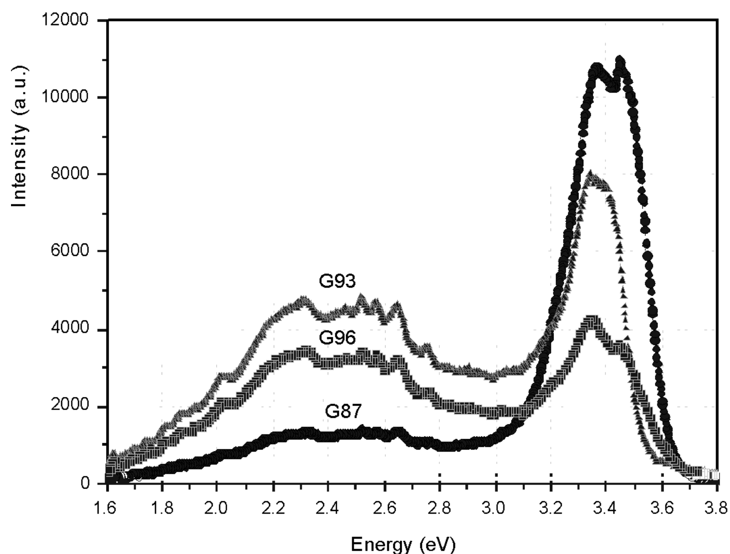

Fig. 4. PL spectra of GaN layers: G87, G93, G96

4. Conclusions

Layers of GaN were deposited by HVPE on Al_2O_3 (0001) substrates. LT-GaN layer grown in various process conditions was applied. The smoothest surface was obtained for the sample with LT-GaN deposited for 5 min in HCl flow rate 8 cm^3/min. Morphologies of samples deposited on LT-GaN obtained with HCl flow 8 cm^3/min were deteriorated on increasing deposition time. Three samples exhibited very strong emission related to near band to band transition. FWHM of main PL peaks of the samples spectra was very small what proved good optical qualities of the layers. A relatively weak yellow emission was also observed. The performed experiments showed that the optimal growth process parameters which allowed us to obtained GaN layers with good morphology were not sufficient to obtained layers with good optical properties. Earlier, we have observed a similar dependence for GaN layers grown by the MOVPE technique.

Acknowledgement

This work has been partially supported by the Polish Ministry of Science and Higher Education under the grants: no. PBZ-KBN100/1/1/2004, R02 018 02, PBZ-MEiN-6/2/2006 and the Wroclaw University of Technology statutory grant.

References

[1] NAKAMURA S., MUKAI T., SENOH M., Appl. Phys. Lett., 64 (1994), 1687.
[2] KIM H., TILAK V., GREEN B.M., SMART J.A., SCHAFF W.J., SHEALLY J.R., EASTMAN L.F., Phys. Stat. Sol. A, 188 (2001), 203.
[3] MARUSKA H.P., TIETJEN J., J. Appl. Phys. Lett., 15 (1969), 327.
[4] NAKAMURA S., Jpn. J. Appl. Phys., Part 2, 30 (1991), L1705.
[5] TEVERNIER P.R., ETZKORN E.V., WANG Y., CLARKE D.R., Appl. Phys. Lett., 77 (2000), 1804.
[6] SUGIURA L., ITAYA K., NISHIO J., FUJIMOTO H., KOKUBUN Y., J. Appl. Phys., 82 (1997), 4877.
[7] SUMIYA M., OGUSU N., YOTSUDA Y., ITOH M., FUKE S., NAKAMURA T., MOCHIZUKI S., SANO T., KAMIYAMA S., AMANO H., AKASAKI I., J. Appl. Phys., 93 (2003), 1311.
[8] PASKOVA T., VALCHEVA E., DARAKCHIEVA V., PASKOV P.P., ARNAUDOV B., MONEMAR B., BIRCH J., HEUKEN M., DAVIS R.F., GIBART P., Proc. 21st Century COE Joint Workshop on Bulk Nitrides, IPAP Conf. Series, 4 pp. 14–20.
[9] EBEL R., FEHRER M., FIGGE S., EINFELDT S., SELKE H., HOMMEL D., J. Cryst. Growth, 201/202 (1999), 433.
[10] Jeon H.C., LEE H.S., SI S.M., YEONG Y.S., NA J.H., PARK Y.S., KANG T.W., OH J.E., Current Appl. Phys., 3 (2003), 385.
[11] DETCHPROHM T., HIRAMATSU K., AMANO H., AKASAKI I., Appl. Phys. Lett., 61 (1992), 2688.
[12] GU S., ZHANG R., SHI Y., ZHENG Y., ZHANG L., KUECH T.F., Appl. Phys. A, 74 (2002), 537.
[13] MORGAN N.N., ZHIZHEN Y., YABOU XU., Mat. Sc. Eng., B90 (2002), 201.
[14] MURAKAMI H., KAWAGUCHI N., KANGAWA Y., KUMAGAI Y., KOUKITU A., J. Cryst. Growth, 275 (2005), e1149.
[15] SATO T., NAMERIKAWA M., SUZUKI M., SOUDA R., HASEGAWA F., Phys. Stat. Sol. (c), 0, No. 1 (2002), 338.
[16] PRAŻMOWSKA J., KORBUTOWICZ R., SYPEREK M., Proc. 2006 International Students and Young Scientists Workshop “Photonics and Microsystems” & British Council International Networking for Young Scientists Meeting “Photonics, Optoelectronics, Nanotechnology”, International Optoelectronics Workshop, Wrocław–Szklarska Poręba, Poland, June 30–July 2, 2006, Piscataway, NY, IEEE, cop. 2006, 46.
[17] TRAGER-COWAN C., MCARTHUR S., MIDDLETON P.G., O’DONNELL K.P., ZUBIA D., HERSEE S.D., Mater. Sci. Eng., B59 (1999), 235.
[18] ZHANG J.X., QU Y., CHENA Y.Z., UDDIN A., SHU YUAN, J. Cryst. Growth, 282 (2005), 137.

Received 28 April 2007
Revised 16 February 2008

Materials Science-Poland, Vol. 26, No. 1, 2008

A(III)B(V) detectors with graded active region

M. WOŚKO[1*], B. PASZKIEWICZ[1], A. SZYSZKA[1], W. MACHERZYŃSKI[1], D. RADZIEWICZ[1], B. ŚCIANA[1], R. PASZKIEWICZ[1], M. TŁACZAŁA[1], G. SĘK[2], P. POLOCZEK[2], M. MOTYKA[2], J. MISIEWICZ[2]

[1]Faculty of Microsystem Electronics and Photonics, Wrocław University of Technlogy, ul. Janiszewskiego 11/17, 50-372 Wrocław

[2]Institute of Physics, Wrocław University of Technlogy, Wybrzeże Wyspiańskiego 27, 50-370 Wrocław, Poland

Results of modelling and fabrication of photodetectors with composition graded active layers have been presented. Simulated and measured spectral characteristics of the proposed detectors have been shown. Advantages of such structures have been discussed with respect to conventional detectors with non-graded active areas as well as some technological problems of compositionally graded semiconductor layers.

Key words: *FGM; photodetector; compositionally graded material; epitaxy*

1. Introduction

Mechanical and electrical applications of functionally graded materials have been studied for many years. In most cases, the investigations focused on improvement of reliability and strength of composites for advanced ballistic, aircraft and automotive applications [1–3]. Progress in micro- and nanoelectronics, particularly improvement of epitaxial techniques, allowed one to grow materials with fully controlled doping and composition on a monolayer level. Introducing gradation in semiconductor structures results in improvement of optical and electrical properties of the devices [4–9].

The main goal of our work was to develop p-n photodetectors with compositionally graded active layers. Theoretical studies [10] show that gradation of composition in an emitter increases the total efficiency of the optoelectric transition by lowering the parasitic surface recombination; however reports on experimental investigation of graded photodetectors are rather scarce.

[*]Corresponding author, e-mail: mateusz.wosko@pwr.wroc.pl

We propose several basic compositionally graded p-n structures which could be practically used in photodetectors. They have been earlier simulated using our proprietary modelling software [11]. After theoretical optimization, two graded and one reference standard structure were fabricated by the metalorganic vapour phase epitaxy (MOVPE) technique. Wet anisotropic etching of the mesa and magnetron sputtering of metallic contact were applied to fabricate detector structures. Finally, both epitaxial structures and fabricated photodetectors were structurally, optically and electrically characterized.

2. Modelling and simulation

Because of several disadvantages of commercially available simulation programs, FMG – a proprietary software based on the finite element method and drift-diffusion model has been developed. The program calculates material properties based on their composition and doping. As a result, it allowed us to evaluate band structure of the material, potential distribution, optical generation function of carriers, band-to-band and SRH recombination rate and the value of currents flowing through the detector.

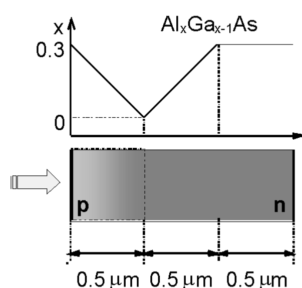

Fig. 1. Scheme of the investigated graded structure

Figures 1, 2 present a scheme, band-gap diagram and generation function diagram of the investigated "double graded" structure. Analyzing Figs. 2a, b, two main conclusions could be formulated. First, depending on the gradation profile, the graded area introduces internal electric field at the values ranging from 100 kV/m to 300 kV/m. There is not much information about dependence of Al content on the diffusion length of electrons in AlGaAs but one can assume that it changes from about 0.5 μm for pure GaAs to about 2 μm for $Al_{0.35}Ga_{0.65}As$ [12]. Thus the gradation can enhance the drift of generated minority carriers from the absorption region to the junction, especially in devices with relatively long emitters. As a result, the impact of surface recombination is decreased and the external quantum efficiency increases. Another phenomenon occurring in photodetectors with compositionally graded area is the "generation area localization". Since in compositionally graded detector structures, the band-gap width changes with the composition of the material, it is possible to obtain layers transparent for certain wavelengths (optical window effect). Moreover, in contrast to conventional photodetectors fabricated from homogeneous materials, in composition graded detectors the area where photons are absorbed changes smoothly with its energy, as is clear-

ly shown in Fig. 2b. This phenomenon can be utilized, e.g. for fabrication of wavelength sensitive photodetectors.

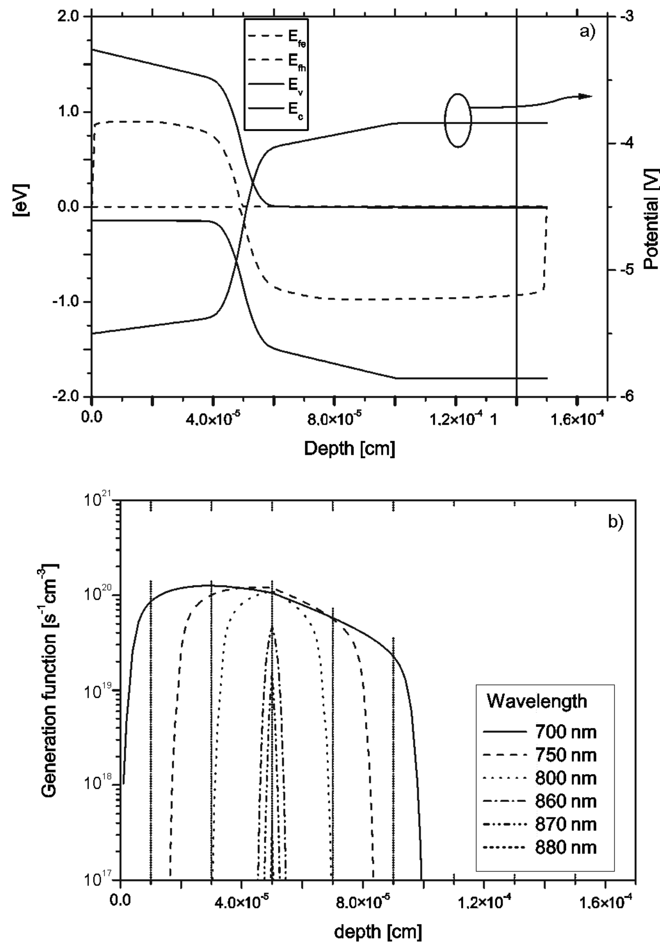

Fig. 2. Band-gap diagram (a) and generation function (b) of the investigated graded structure

Another advantage of detectors with compositionally graded active region is the possibility of adjusting spectral sensitivity of the device to the spectrum of the sun radiation. This kind of structures could replace widely reported cascade solar cells by a continuous change of absorption edge.

As a result of simulations and theoretical investigations [14], we proposed three structures of detectors shown in Fig. 3. The optimization of the structure consisted in a choice of the profile of the emitter composition and its length. The goal was to obtain spectral characteristics of a specified shape – weakly wavelength dependent or linearly wavelength dependent in a broad spectrum.

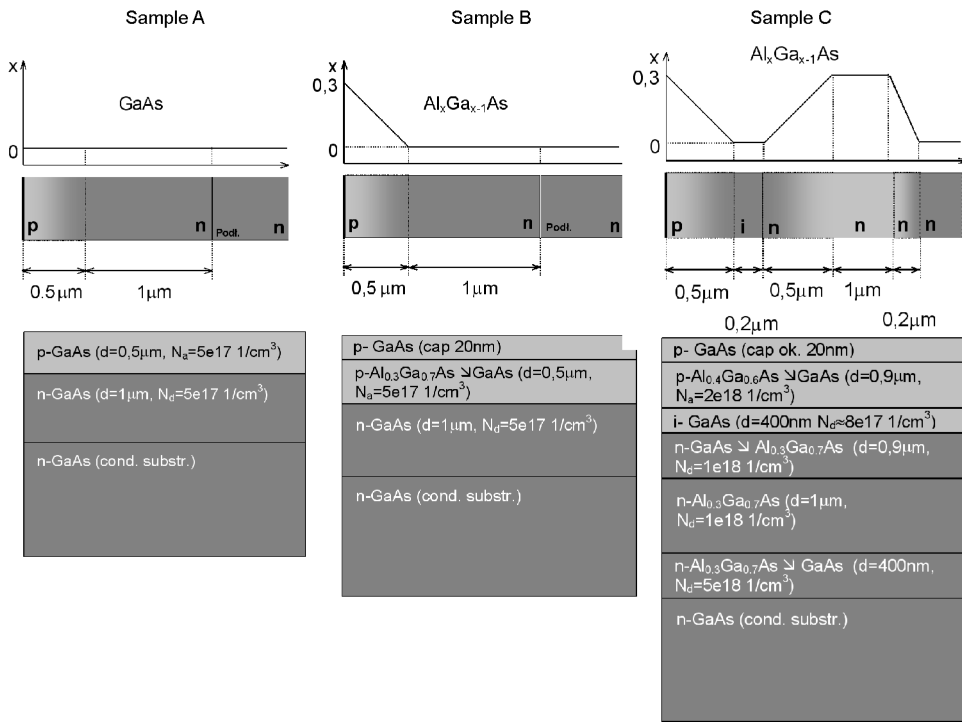

Fig. 3. Schemes of the investigated photodetectors

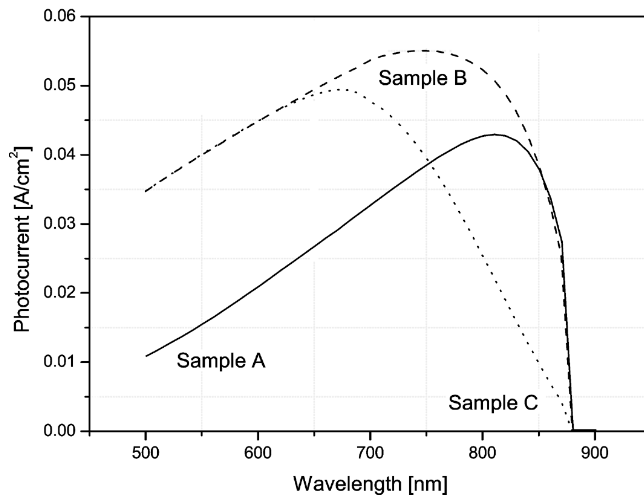

Fig. 4. Simulated spectral characteristic of the photodetectors

Figure 4 presents simulated spectral characteristics of the proposed detectors. If one compares the homogeneous detector structure (sample A) with the detectors with compositionally graded area (samples B and C), the difference of spectral characteris-

tics can be easily seen. In the case of sample B, a higher sensitivity and broadening of spectral characteristic in the low wavelength region was obtained. The spectral characteristic of photocurrent of sample C changes linearly with the wavelength.

3. Experimental

Investigated structures (Fig. 3) were fabricated by the MOVPE method in an AIX 200 AIXTRON reactor. Te-doped 2-inch GaAs conducting substrates were used. TMGa and TMAl precursors were applied as sources of Ga and Al. After growth procedures, the samples were structurally and electrically characterized by PVS and ECV techniques [15]. The obtained results are presented in Fig. 5.

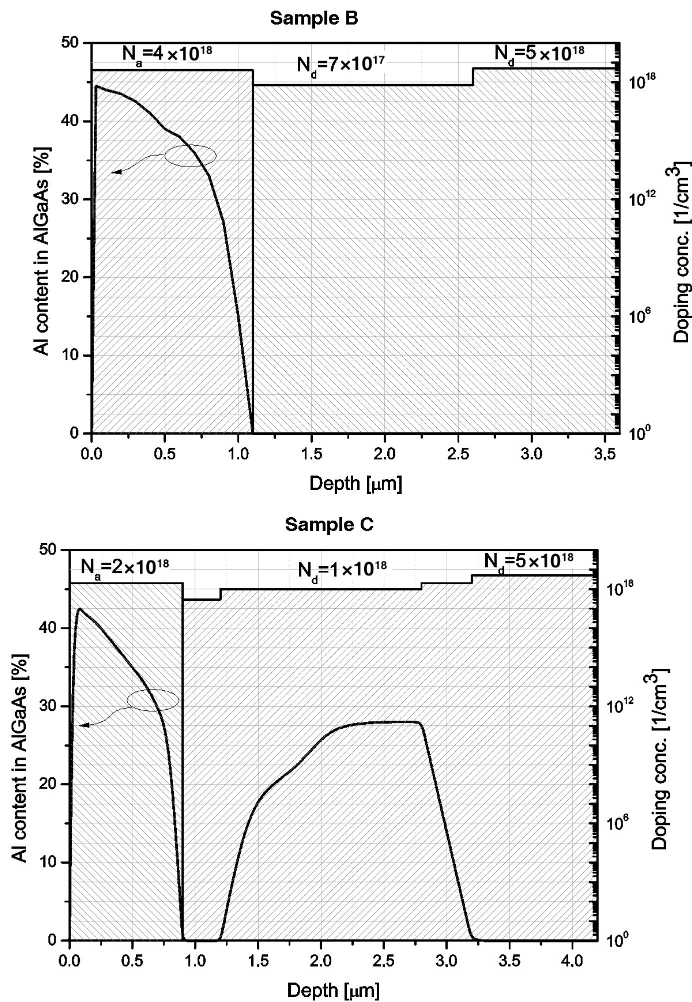

Fig. 5. Composition and doping of graded structures

As can be seen, composition and doping profiles differ from the theoretical ones (shown in Fig. 3). This is mainly due to a complex nature of the growth process of compositionally graded layers. The control of growth should include additional factors, mainly changing of growth rate and doping efficiency with altering of composition of the mixture of reagents. Mesa structures of the detectors were formed by wet anisotropic etching. Two different etching solutions were used. Composition of mixtures and process parameters are given in Table 1. Both solutions give good etching anisotropy and surface smoothness.

Table 1. Etching solutions for graded AlGaAs structures

Solution	Temperature [°C]	Etching rate [nm/min]
H_3PO_4:H_2O_2:H_2O (1:1:8)	23	819 (±5%)
H_3PO_4:H_2O_2:H_2O (1:1:40)		96 (±5%)

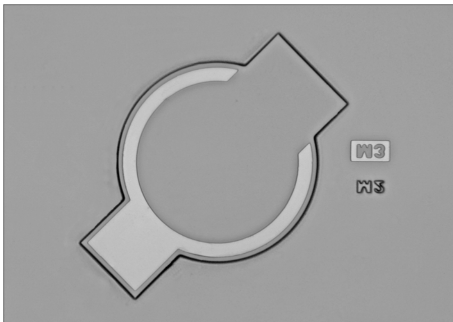

Fig. 6. Top view of the structure of the detector

Ohmic contacts were formed by using an electron beam and resistance evaporators and thermal annealing. To obtain good linear characteristics, several metallic multilayers were investigated: Ti/Pt/Au, Pt/Ti/Au, Ni/Ti/Au, Pt/Ti/Pt/Au to p-type AlGaAs and AuGe/Ni/Au to n-type GaAs from the bottom side. After sputtering, metallization was formed by the lift-off technique and annealed in a resistance furnace. The structure of the fabricated detector is shown in Fig. 6.

4. Results

Recorded spectral characteristics of investigated photodetectors are shown in Fig. 7. Higher sensitivities were obtained with samples B and C compared to a conventional GaAs p-n detector (sample A). Moreover, the maximum of sensitivity was shifted towards the low wavelength area because of the increase of Al content in the active layer. In the case of Sample B, a non-ideal "flat" characteristic was obtained

due to a high Al content in the emitter (compared to the theoretically evaluated one). The sensitivity of sample C exhibits a linear dependence upon wavelength in the range from 670 to 880 nm. The characteristic edge at 850 nm is connected with the absorption edge of the intrinsic GaAs layer of the p-i-n photodiode.

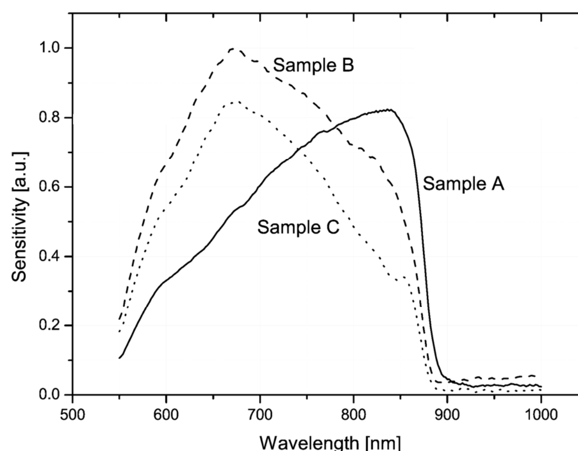

Fig. 7. Spectral characteristic of photodetectors with composition graded area

The differences between simulated and experimentally obtained spectral characteristics are caused by the imperfection of the mathematical model and by material properties data in the simulation software, as well by differences between the experimental profile of compositionally graded region and intended profile.

The deposition of compositionally graded layers by the MOVPE technique is an untrivial challenge because of complicated kinetics of the growth process. Contrary to the growth of homogeneous layers, in the case of compositionally graded materials, not only static parameters of epitaxial process like temperature, composition and pressure of gaseous atmosphere should be considered, but also composition of surface and predicted layers, inertness of the epitaxial system etc. The control of deposition of compositionally graded layers is the primary and most important problem which should be solved by using, e.g., computer aided design of the epitaxial process.

5. Conclusions

Novel AlGaAs photodetectors with compositionally graded active layers have been presented. Two basic types of photodetectors, with “flat” and wavelength dependent spectral characteristics were fabricated and characterized. The obtained results show that photodetectors with compositionally graded active layers can find advanced applications as spectrometers or colorimeters using cascade junctions in compositionally graded area to detect various wavelengths. It was shown that by using this type of structures, it was possible to modify spectral characteristics of devices in a wide spec-

tral range. Further epitaxial process optimization must be performed to gain a better control of the growth process of the epitaxial layers with gradual change of the composition.

Acknowledgement

This work has been partially supported by the grant of the Polish Ministry of Education and Science No. PBZ/100/1/1/2004, R0201802 and PBZ-MEiN-6/2/2006, EU Structural Funds in Poland – Ph.D scholarship No. 51 and Wroclaw University of Technology statutory grant.

References

[1] ZHAO J., AI X., DENG J., WANG J., J. Europ. Ceram. Soc., 24 (2004), 847.
[2] ICHINOSE N., MIYAMOTO N., TAKAHASHI S., J. Europ. Ceram. Soc., 24, (2004), 1681.
[3] CHIN E.S.C., Mat. Sci. Eng. A, 259 (1999), 155.
[4] KOVALENKO V.F., SHUTOV S.V., Semicond., 37 (2003), 38.
[5] VASILYEV YU.B., SUCHALKIN S.D., POLKOVNIKOV A.S., ZEGRYA G.G., J. Appl. Phys., 93 (2003), 2349.
[6] BAUMEISTER H., VEUHOFF E., POPP M., HEINECKE H., J. Cryst. Growth, 188 (1998), 266.
[7] LEE B., BAEK J.H., Appl. Phys. Lett., 68(1996), 2973.
[8] PIETERS B.E., ZEMAN M., VAN SWAAIJ R.A.C.M.M., METSELAAR W.J., Thin Solid Films, 451–452 (2004), 294.
[9] MAHDJOUB A., ZIGHED L., Thin Solid Films, 476 (2005), 299.
[10] MALACHOWSKI M.J., Solid State Electron., 42 (1998), 963.
[11] WOSKO M., PASZKIEWICZ B., PIASECKI T., PASZKIEWICZ R., PRAŻMOWSKA J., SZYSZKA A., MACHERZYŃSKI W., TŁACZAŁA M., Proc. 12th Int. Conf. Applied Physics of Condensed Matter, (2006), 83.
[12] ADACHI S., *Properties of Aluminium Gallium Arsenide*, INSPEC, London, 1993.
[13] CHIANG P.K., CHU C.L., YEH Y.C.M., Photovoltaic Specialists Conference, Conference Record of the Twenty-Eighth IEEE, (2000), 1002–1005.
[14] WOŚKO M., PASZKIEWICZ B., PIASECKI T., PASZKIEWICZ R., PRAŻMOWSKA J., SZYSZKA A., MACHERZYŃSKI W., TŁACZAŁA M., Proc. Int. Students and Young Scientists Workshop Photonics and Microsystems, (2006), 69–71.
[15] PASZKIEWICZ B., PASZKIEWICZ R., WOŚKO M., RADZIEWICZ D., ŚCIANA B., SZYSZKA A., MACHERZYŃSKI W., TŁACZAŁA M., Vacuum, 82 (2007), 389.

Received 28 April 2007
Revised 16 February 2008

Materials Science-Poland, Vol. 26, No. 1, 2008

Nanoscale heat transport

J. BODZENTA*

Institute of Physics, Silesian University of Technology, ul. Krzywoustego 2, 44-100 Gliwice, Poland

New physical phenomena connected with heat transport in structures with dimensions comparable with characteristic lengths of energy carriers are briefly reviewed. Problems with basic physical understanding of mechanisms responsible for energy transport in such structures are considered. In particular, the role of boundaries is discussed. Thermal properties of a few structures which dimensions influence heat transport, namely: superlattices and multilayered systems, nanoporous materials and nanotubes are analyzed. Problem of hot spots in electronic devices is also mentioned. The last part of the paper is devoted to methods of experimental investigation of thermal properties of nanostructures. Capabilities and shortcomings of two relatively new experimental techniques: picosecond reflectance thermometry and scanning thermal microscopy have been discussed.

Key words: *heat transport; nanostructure; nanoscale*

1. Introduction

Progress in technology created possibilities for fabrication of structures with dimensions of a few nanometers used in practical applications. Quantum dots, quantum wires and nanotubes became parts of electronic and optoelectronic devices [1, 2]. Thin films are also commonly used in various fields of technology. In many cases, thermal properties of nanoscale structures become very important. In construction of electronic devices the problem of heat abstraction form active regions must be solved. Thus, materials with possibly high thermal conductivity are demanded. On the other hand, there is also need for materials and structures with a low thermal conductivity which can play a role of thermal barriers. This is why knowledge of thermal properties of nanomaterials is important.

Thermal conductivity of thin dielectric films decreases with decreasing film thickness for films thinner than about 10 μm [3]. For films with thicknesses of about 100 nm, the thermal conductivity is typically 3–4 orders of magnitude lower than that

*E-mail: Jerzy.Bodzenta@polsl.pl

of bulk material. This fact can be explained in the frame of a classical theory of thermal conductivity of solids as the result of growing concentration of defects in the crystalline structure of thin films. A lower limit of the thermal conductivity defines its value for an amorphous sample [4]. On the contrary, analysis of heat transport in structures of nanometer size cannot base on the classical approach and entirely new physical effects must be taken into account. A question arises when it is justified to use the term “nanoscale”. The mean free path of electrons in metals is about 10 nm, and that of phonons in insulators and semiconductors is in the range from 10 nm to 100 nm at room temperature. The wavelengths are about (0.1–1) nm and (1–5) nm, respectively [5]. “Nanoscale effects” occur when the heat transport takes place in a structure of dimensions comparable with characteristic lengths of energy carriers. The next effect typical of the nanoscale is a confinement of dimensions in which heat transport can take place. In the other cases, the classical model of heat transport is usually adequate for interpretation of observed phenomena. Thus, there is no necessity for distinguishing such phenomena as nanoscale effects.

2. Theoretical models

The description of heat transport in a macroscale bases on Fourier’s law which relates the heat flux $\vec{j}_Q$ to the temperature gradient $\vec{\nabla}T$

$$\vec{j}_Q = -\kappa\vec{\nabla}T \tag{1}$$

where κ is the thermal conductivity. The form of the above equation testifies diffuse nature of heat transport. It is based on the assumption that energy transfer form warmer to colder regions of a medium is the result of random processes which lead to establishing new equilibrium in a system. In crystalline insulators, this process is connected with chaotic movement of phonons which are scattered by other phonons and structure imperfections. But it is also assumed that the medium can be divided into elementary volumes (subsystems), each consisting of a large number of particles which are in equilibrium. This local equilibrium is described by a local temperature related to the average energy of the subsystem of particles. Thus heat transport is a non-equilibrium process but energy is transferred between subsystems being in equilibrium, and heat flows on distances much longer than the mean free path of energy carriers. In the nanoscale, the mean free path of energy carriers is comparable with the size of a structure in which energy is transported, and the carriers interact mainly with boundaries of the structure. It is not possible to distinguish subsystems containing large numbers of particles in equilibrium. The question of temperature definition arises. In the classical approach, the energy is averaged over a large number of particles which causes that momentary energy fluctuations are insignificant. In the case of a subsystem comprising a few particles or even a single atom, such an averaging

makes no sense. A possible solution is to replace the averaging over a large number of particles (space averaging) by the averaging over time. The next problem is connected with the method of description of particle motion. In the classical approach, the mean kinetic energy of a particle is connected with temperature through the principle of equipartition of energy. In quantum mechanics, atoms in solids are treated as oscillators with quantized energy. Collective vibrations of atoms are described as phonons, which means that energy is calculated using the Bose–Einstein distribution. The formula connecting the mean energy of a particle with temperature differs from the one in the classical model. As a result, temperatures calculated from the classical model and the quantum model differ. It should also be noted that the phonon approach excludes definition of the temperature for a single atom.

The definition of temperature plays a key role in description of heat transport in the nanoscale. Various definitions of temperature lead to different theoretical models of phenomena connected with the heat transport. An example is the analysis of thermal properties of the diamond–lead boundary [6, 7].

As is mentioned above, in the nanoscale the mean free path of energy carriers is comparable with dimensions of a structure in which phonons propagate. Then the phonon motion is practically ballistic between structure boundaries and heat transport depends mainly on phonon scattering on the boundaries. Additionally, the boundary separates regions for which temperature can be defined and is a place where the temperature can abruptly change. Thermal properties of the boundary can be characterized by its thermal resistance

$$R_Q = \frac{\Delta T}{j_Q} \tag{1}$$

where ΔT is the temperature change at the boundary, and j_Q is the heat flux through it. The definition of the boundary thermal resistance is identical with the classic one. But in the nanoscale, the thermal resistance is used to describe the influence of the layer with the thickness d and effective thermal conductivity κ_{ef} on heat transport and the thermal resistance of such a layer is

$$R_Q = \frac{d}{\kappa_{ef}} \tag{2}$$

The concept of thermal resistances was used e.g., for interpretation of results of measurements of the thermal conductivity of polycrystalline diamond [8]. In the nanoscale, the thermal resistance characterizes the boundary, not the layer. Two basic theoretical models are used to describe behaviour of phonons at the boundary. In the acoustic-mismatch model phonons reflect and refract at the boundary, similarly to light at the boundary of two media with different refractive indices. The reflection and transmission coefficients of phonons depend on acoustic impedances $Z = \rho u$ of neighbouring media, where ρ is the mass density and u is the velocity of phonons

(sound velocity) [9, 10]. This model, however, does not explain scattering of phonons at the boundary of two regions of the same material and identical crystallographic structures but with different orientations in space. According to the acoustic-mismatch model, such an interface "does not exist" for phonons. Scattering at such a boundary can be explained in the frame of the diffuse-mismatch model; phonons at the boundary "forget" where they came from and they are randomly scattered [10]. In this model, each and every interface scatters phonons. Both models are helpful in interpretating experimental data but they do not describe real physical processes occurring at the interface. Thus they should be treated as a simple approximation.

Due to lack of acknowledged theoretical models, analyses of heat transport processes in nanostructures are based on numerical simulations with two approaches used. In the former one, the Boltzmann transport equation is solved numerically [11]. The Boltzmann transport equation is a fundamental equation of microscopic theory of irreversible processes. It allows taking into account quantum effects but requires understanding of phonon processes accompanying the heat transport. The other approach is based on integration of Newton's equation of motion for a group of interacting atoms. The interaction is described through an interatomic potential which is usually empirical [12]. This method is called molecular-dynamics simulations. Molecular-dynamics simulations are entirely classical and do not describe quantum effects.

Models of heat transport in nanostructures are in the initial stage of development. This development is stimulated by very interesting experimental investigations which show that the heat transport in such structures is connected with new phenomena, not observed in micro- or macroscale.

3. Experimental results

The first nanostructures in which interesting effects connected with heat transport were observed are superlattices and multilayers. Both structures contain alternating layers of different materials. In superlattices, the layers are single crystals (with exception of amorphous superlattices [13]), while multilayers are built from polycrystalline or amorphous films. From the point of view of thermal properties, both structures can be divided into two groups: structures in which the mean free path of energy carriers λ is longer than thicknesses of the films d ($\lambda > d$), and structures in which $\lambda < d$. In the former case, thermal properties in the direction perpendicular to the film planes are practically independent of thermal properties of the films and are defined by the properties of film interfaces. In the latter case, thermal properties of the system depend either on the properties of the films or the properties of interfaces. From the point of view of this paper, the case $\lambda > d$ is more interesting. In multilayers, heat transport in the direction perpendicular to the films is influenced by strongly defective regions at layer interfaces. These regions have very high thermal resistances resulting in very low effective thermal conductivities of the multilayers in this direction. The effective thermal conductivity of so called nanolaminates (multilayers containing a few nano-

meters thick films) is, for example, of the order of 0.1 $W \cdot m^{-1} \cdot K^{-1}$ [14]. Nanolaminates could be applied as thermal barriers protecting machine parts against high temperatures. But the problem with their stability at high temperatures must be solved.

As has been mentioned above, superlattices contain single-crystalline films with sharp interfaces. The characteristic dimension for a superlattice is its space period D. If the condition $\lambda < D$ is fulfilled, the thermal resistance of the superlattice can be calculated as a sum of thermal resistances of separate films and interfaces. The periodicity of the structure does not influence the heat transport. More interesting is the case when $\lambda > D$. Phonons "see" the periodicity of the structure which results in change of phonon dispersive curves and appearance of a band structure in their energy spectrum [15]. The consequence of the change of the phonon dispersive curves is a considerable decrease of the group velocity of phonons [16] and appearance of new scattering processes [17]. Both effects lead to a reduction of the mean free path of phonons and decrease of the thermal conductivity of the structure. In the majority of experimental investigations of thermal properties of superlattices, the thermal conductivity in the direction perpendicular to film planes decreases with the decreasing lattice period D (e.g., [18–20]). However, experimental results show that such a behaviour is not a universal rule [21]. There is also unsolved problem of existence of a lower limit of the thermal conductivity of superlattices. According to [22], this limit is defined by the thermal conductivity of an alloy with the same composition as the superlattice but other researchers claim that such a limit does not exist [19, 23].

Modern electronics is interested in insulators with low relative permittivities. SiO_2, commonly used in electronic device technology, has the relative permittivity $\varepsilon \approx 3.9$. From this point of view, very promising are nanoporous materials. This technology allows obtaining films with relative permittivities $\varepsilon < 2$ [24]. Sizes of pores are of the order of a few nanometers. Investigation of thermal properties of these materials reveals that the thermal conductivity decreases with increasing density of pores, e.g. threefold decrease of the density of porous SiO_2 (Xerogel) is connected with a drop of its thermal conductivity by one order of magnitude [25]. Similar results were obtained for $HSiO_{1.5}$ [26]. The attempt of interpretation of the experimental data in the frame of the classical theory of composite medium [27] did not give satisfactory results.

Very interesting results were obtained in investigations of heat transport in nanotubes. Nanotubes and nanowires are one-dimensional structures. Based on theoretical considerations for carbon nanotubes, their thermal conductivity along the axis can be as high as 6000 $W \cdot m^{-1} \cdot K^{-1}$ at room temperature [28]. This value is almost three times higher than the thermal conductivity of diamond (2200 $W \cdot m^{-1} \cdot K^{-1}$). Such a high thermal conductivity can be qualitatively explained by waveguiding of phonons along the nanotube resulting in a very long mean free path of phonons. Similar considerations carried out for nanowires lead to the conclusion that the thermal conductivity of these structures is considerably lower than that of bulk material [29, 30]. Experimental investigations of thermal properties of carbon nanotubes confirm the theoretical predictions. The measured thermal conductivity of a single-wall carbon nanotube is in the

range from 1750 $W \cdot m^{-1} \cdot K^{-1}$ to 5800 $W \cdot m^{-1} \cdot K^{-1}$ [31]. The thermal conductivity of multi-wall nanotubes is lower and does not exceed 1000 $W \cdot m^{-1} \cdot K^{-1}$ [32]. It is interesting to note that such thermal conductivity is characteristic of carbon nanotubes, e.g. the thermal conductivity of BN is much lower [33]. Quantum character of heat transport in nanotubes leads to appearance of an upper limit of heat conductivity. Thermal conductance is quantized, and the quantum of phonon conductance g_0 is [34, 35]

$$g_0 = \frac{\pi^2 k_B^2}{3h} T \tag{1}$$

Nanostructures cause not only changes in phonon dispersive curves but they also modify mechanisms of energy transfer between electrons and phonons, e.g. in MIS transistors the most efficient energy transfer from electrons to phonons takes place in a small volume near the drain [36]. “Hot spots” appear in the structure. Moreover, in polar semiconductors energy is mainly transferred to optical phonons with very small wave vectors. These phonons have very low group velocities, thus heat abstraction from “hot spots” is slow. A possible solution of this problem is to create additional structures which will convert “slow” optical phonons into “fast” acoustic phonons [37].

This review of effects connected with heat transport in nanostructures has only been limited to a few selected examples, however, it becomes clear that to understand processes responsible for energy transport in such structures a lot of theoretical and experimental investigations should be done.

4. Measuring methods

Only a few experimental methods have been reported to investigate heat transport in nanostructures. The first possibility is to create special nanostructures for this purpose. The example is a sophisticated structure produced for measurement of the thermal conductivity of a single nanotube [38]. A few micrometers long carbon multi-wall nanotube with the diameter of 14 nm was supported by two islands. On the top of the islands platinum heaters and thermometers were fabricated by electron beam lithography. The nanotube thermally bridged these islands. Such methods can be used in fundamental investigations of selected objects but each structure is produced to carry out a single investigation.

Probably the most universal method is the scanning thermal microscopy (SThM). The method was proposed by Williams and Wickramasinghe in 1986 [39]. Its operation principle is based on determination of temperature distribution at a sample surface by a sharp temperature-sensing tip. Present-day equipment for the SThM is typically an optional module of atomic force microscopes. Scanning thermal microscopes can operate in both steady-state and time-variable modes [40]. In the former case, the microscope allows imaging of temperature distribution connected with dc heat sources in

the sample. This mode can also be used for measurement of local thermal conductivity of a sample [41] but modulation methods, based on ac temperature field generated in the sample, offer a better spatial resolution and allow using lock-in detection to improve the signal-to-noise ratio [42].

The SThM provides a possibility for determination of local thermal conductivity in the range (0.1–320) $W \cdot m^{-1} \cdot K^{-1}$ with 0.2 $W \cdot m^{-1} \cdot K^{-1}$ resolution [43, 44]. Spatial resolution is limited by two factors – mean free paths of energy carriers and the size of a tip. The former factor determines the resolution of measurements carried out in air. It is in the range of (0.3–0.5) μm [45], being insufficient for examination of nanostructures. In liquids, the main free path is (0.1–10) nm and it is of the order of interatomic distances [43], so the resolution is limited by the size of the tip. At present, the resolution higher than 50 nm can be achieved. The SThM is a very promising technique but the analysis of experimental data is not a trivial task. Heat transport between the tip and the sample depends on a few mechanisms, whose contributions to the measured signal are difficult to evaluate [46]. This is why understanding of physical processes accompanying the SThM measurements is a basic condition of a proper interpretation of experimental data. A more detailed description of this technique can be found elsewhere [43, 47].

The method which can be used to investigate thermal properties of thin films is the picosecond reflectance thermometry (PRT) [48], being a modification of the classical flash method based on analysis of temperature response of a sample heated by a short light pulse [49]. Use of picosecond laser pulse for both generation of temperature disturbance and detection of temperature changes allows investigation of films with thicknesses of about a few tens of microns. PRT was used in investigations of thin metal films [50, 51], thermal resistance of film boundaries [52] or superlattices [53]. A theoretical model of PRT was put forward by Cahill [54]. Analysis of experimental data is obscured by the fact that at times as short as picoseconds, the equilibrium between various parts of the system (e.g. electrons and phonons) might not be reached. Thus the problem of the definition of temperature arises again.

The above examples do not exhaust possibilities of investigation of thermal properties of nanostructures. It should be underlined, however, that independently of the chosen method, a special attention should be paid to the analysis of experimental data. As results from the previous section, processes responsible for heat transport in the nanoscale are rather fragmentarily recognized, and theoretical models describing experimental data are quite complex.

5. Conclusions

Heat transport in the nanoscale is a very interesting field for both theoretical and experimental investigation. The knowledge of phenomena influencing energy transfer in structures with sizes from a few to a few tens of nanometers is far from being complete. There is a lot of work to be done for understanding physical foundations of ex-

perimentally observed effects. However, phenomena of heat transport in nanostructures are important not only for physicists. As nanostructures are used in technology, these problems are also meaningful in practice. New effects observed in nanotubes and multilayers can be utilized for fabrication of new materials with demanded thermal properties. More information about nanoscale heat transport can be found in review papers [47, 55] and in the book [56].

References

[1] *Frontiers in Electronics*, Y. Nishi, M.S. Shur, H. Wong (Eds.), *Selected Topics in Electronics and Systems*, Vol. 41, Word Scientific, Singapore, 2004.
[2] *Nanotubes and Nanowires*, P.J. Burke (Ed.), Selected Topics in Electronics and Systems – vol. 44, Word Scientific, Singapore, 2007.
[3] BODZENTA J., Chaos, Solitons, Fractals, 12 (1999), 2087.
[4] CAHILL D.G., WATSON S.K., POHL R.O., Phys. Rev. B, 46 (1992), 6131.
[5] CAHILL D.G., GOODSON K., MAJUMDAR A., J. Heat Transfer, 124 (2002), 223.
[6] HUBERMAN M.L., OVERHAUSER A.W., Phys. Rev. B, 50 (1994), 2865.
[7] SERGEEV A.V., Phys. Rev. B, 58 (1998), R10199.
[8] HARTMANN J., REICHLING M., MATTHIAS E., Progr. Nat. Acad. Sci., 6 (1996), S297.
[9] KHALATNIKOV I.M., Sov. Phys. JETP, 22 (1952), 687.
[10] SWARTZ E.T., POHL R.O., Rev. Mod. Phys., 61 (1989), 605.
[11] MAJUMDAR A., J. Heat Transfer, 115 (1993), 7.
[12] SCHELLING P.K., PHILLPOT S.G., KEBLINSKI P., Phys. Rev. B, 65 (2002), 144306.
[13] MAZURCZYK R., GAZICKI-LIPMAN M., WAGNER T., J. Wide Bandgap Mater., 9 (2001), 21.
[14] COSTESCU R.M., CAHILL D.G., FABREGUETTE F.H., SECHRUST Z.A., GEORGE S.M., Science, 303 (2004), 989.
[15] NARAYANAMURTI V., STÖRMER H.L., CHIN M.A., GOSSARD A.C., WIEGMANN W., Phys. Rev. Lett., 43 (1979), 2012.
[16] SIMKIN M.V., MAHAN G.D., Phys. Rev. Lett., 84 (2000), 927.
[17] REN S.Y., DOW J.D., Phys. Rev. B, 25 (1982), 3750.
[18] YU X.Y., CHEN G., VERMA A., SMITH J.S., Appl. Phys. Lett., 67 (1995), 3554.
[19] LEE S.-M., CAHILL D.G., VENKATASUBRAMANIAN R., Appl. Phys. Lett., 70 (1997), 2957.
[20] YAO T., Appl. Phys. Lett., 51 (1987), 1798.
[21] TOUZELBAEV M.N., ZHOU P., VENKATASUBRAMANIAN R., GOODSON K.E., J. Appl. Phys., 90 (2001), 763.
[22] HUXTABLE S., ABRAMSON A., TIEN C.L. MAJUMDAR A., Appl. Phys. Lett., 80 (2002), 1737.
[23] BORCA-TASCIUC T., LIU W., LIU J., ZENG T., SONG D.W., MOORE C.D., CHEN G., WANG K.L., GOORSKY M., REDETIC T., GRONSKY R., KOGA T., DRESSELHAUS M.S., Superlatt. Microstruct., 28 (2000), 199.
[24] YNAG S., MIRAU P.A., PAI C.S., NALAMASU O., REICHMANIS E., PAI J.C., OBENG Y.S., SEPUTRO J., LIN E.K., LEE H.J., SUN J.N., GIDLEY D.W., Chem. Mater., 14 (2002), 369.
[25] HU CH., MORGEN M., HO P.S., JAIN A., GILL W.N., PLAWSKY J.L., WAYNER Jr. P.C., Appl. Phys. Lett., 77 (2000), 145.
[26] COSTESCU R.M., BULLEN A.J., MATAMIS G., O'HARA K.E., CAHILL D.G., Phys. Rev. B, 65 (2002), 94205.
[27] LANDAUER R., *Electrical conductivity in inhomogeneous media* [in:] *Electrical Transport and Optical Properties of Inhomogeneous Media*, J.C. Garland, D.B. Tanner (Eds.), AIP, New York, 1978, p. 2.
[28] BERBER S., KWON Y.-K., TOMÁNEK D., Phys. Rev. Lett., 84 (2000), 4613.
[29] WALKAUSKAS S.G., BROIDO D.A., KEMPA K., J. Appl. Phys., 85 (1999), 2579.

[30] JIAUNG W.-S., HO J.-R., J. Appl. Phys., 95 (2004), 958.
[31] HONE J., WHITNEY M., PISKOTI C., Zettl A., Phys. Rev B, 59 (1999), R2514.
[32] CHOI T.Y., POULIKAKOS D., THARIAN J., SENNHAUSER U., Appl. Phys. Lett., 87 (2005), 013108.
[33] CHANG C.W., HAN W.-Q., ZETTL A., Appl. Phys. Lett., 87 (2005), 173102.
[34] SCHWAB K., HENRICKSON E.A., WORLOCK J.M., ROUKES M.L., Physica E, 9 (2001), 60.
[35] PENDRY J.B., J. Phys. A, 16 (1983), 2161.
[36] MAHAN G.D., J. Appl. Phys., 58 (1985), 2242.
[37] MIZOGUCHI K., HASE M., NAKASHIMA S., NAKAYAMA M., Phys. Rev B, 60 (1999), 8262.
[38] KIM P., SHI L., MAJUMDAR A., MCEUEN P.L., Phys. Rev Lett., 87 (2001), 215502.
[39] WILLIAMS C.C., WICKRAMASINGHE H.K., Appl. Phys. Lett., 49 (1986), 1587.
[40] POLLOCK H.M., HAMMICHE A., J. Phys. D: Appl. Phys., 34 (2001), R23.
[41] RUIZ F., SUN W.D., POLLACK F.H., VENKATRAMAN C., Appl. Phys. Lett., 73 (1998), 1802.
[42] FIEGE G.B.M., ALTES A., HEIDERHOFF R., BALK L.J., J. Phys. D: Appl. Phys., 32 (1999), L13.
[43] MAJUMDAR A., Ann. Rev. Mater. Sci., 29 (1999), 505.
[44] MEINDERS E., J. Mater. Res., 16 (2001), 2530.
[45] HISH G., BOUEVITSCH O., KOKOTOV S., LIEBERMAN K., Rev. Sci. Instrum., 66 (1995), 3300.
[46] SHI L., MAJUMDAR A., J. Heat Transfer, 124 (2002), 329.
[47] CAHILL D.G., GOODSON K., MAJUMDAR A., J. Heat Transfer, 124 (2002), 223.
[48] PADDOCK C.A., EESLEY G.L., J. Appl. Phys., 60 (1986), 285.
[49] PARKER W.J., JENKINS R.J., BUTLER C.P., ABBOTT G.L., J. Appl. Phys., 32 (1961), 1679.
[50] CLEMENS B.M., EESLEY G.L., PADDOCK C.A., Phys. Rev. B, 37 (1988), 1085.
[51] TAKETOSHI N., BABA T., ONO A., Jap. J. Appl. Phys., 38 (1999), L1268.
[52] SMITH A.N., HOSTETLER J.L., NORRIS P.M., Thermophys. Eng., 4 (2000), 51.
[53] CAPINSKI W.S., MARIS H.J., RUF T., CARDONA M., PLOOG K., KATZER D., Phys. Rev. B, 59 (1999), 8105.
[54] CAHILL D.G., Rev. Sci. Instrum., 75 (2004), 5119.
[55] CAHILL D.G., FORD W.K., GOODSON K.E., MAHAN G.D., MAJUMDAR A., MARIS H.J., MERLIN R., PHILLPOT S.R., Rev. J. Appl. Phys., 93 (2003), 793.
[56] CHEN G., *Nanoscale Energy Transport and Conversion*, MIT, Pappalardo Series in Mechanical Engineering, Oxford Univ. Press, Oxford, 2005.

Received 28 April 2007
Revised 16 February 2008

Materials Science-Poland, Vol. 26, No. 1, 2008

Preparation of ultra-large-scale catalysts for catalytic vapour deposition of carbon nanotubes

A. BACHMATIUK[1], R. J. KALEŃCZUK[1], M. H. RÜMMELI[2], T. GEMMING[2], E. BOROWIAK-PALEN[1*]

[1]Centre of Knowledge Based Nanomaterials and Technologies, Institute of Chemical Engineering and Chemical Technology, Szczecin University of Technology, ul. Pułaskiego 10, 70-322 Szczecin, Poland

[2]Leibniz Institute for Solid State and Materials Research, Helmholtzstr. 20, 01069-Dresden, Germany

One of the most important issues in the controlled synthesis of carbon nanotubes is finding a simple way to synthesize the catalyst nanoparticles with a controlled size. The preparation of iron nanoparticles via an organic route has been presented in the paper. The nanoparticles, of the diameter ranging between 9.5 and 31 nm, supported on magnesia, were used as a catalyst in chemical vapour deposition to produce bulk scale carbon nanotubes. Two carbon feedstocks (ethanol and cyclohexane) were examined. In the optimization process, the pyrolysis temperature was varied between 650 °C and 850 °C. In this simple approach, no additional carrier gas was used. Multiwalled carbon nanotubes with a very low diameter distribution (19.5±2.5 nm) were fabricated. Their composition was analysed via X-ray diffraction. The samples were characterized by the resonance Raman spectroscopy and high-resolution transmission electron microscopy.

Key words: *carbon nanotubes; transmission electron microscopy; Raman spectroscopy*

1. Introduction

Since their identification in 1991 [1], carbon nanotubes (CNTs) have been one of the most actively studied materials because of their unique structure and extraordinary physical properties. Many studies have been carried out on their synthesis. Arc discharge [1], laser ablation [2] and catalytic chemical vapour deposition (C-CVD) methods [3, 4], have been developed to synthesize CNTs. The C-CVD method is a promising technique for scaling up the production of CNTs with a relatively low cost. In the C-CVD approach, the structure of carbon materials obtained depends primarily on the catalyst size and carbon source [5, 6]. For instance, it has been shown that the diameter of the nanotubes is determined to an extent by the catalyst particles diameter [7]. Therefore, it is very important to find an efficient way to produce nanosized catalyst

[*]Corresponding author, e-mail: eborowiak@ps.pl

particles for synthesis of carbon nanotubes. In this study, we focused on two important aspects: the synthesis of ultra-large scale iron oxide catalyst particles with well defined diameters via an organic route (i), and the application of these catalyst particles supported on magnesia for the synthesis of carbon nanotubes in the C-CVD process (ii).

2. Experimental

Monodisperse metal oxide nanocrystals have been synthesized according to the following procedure:

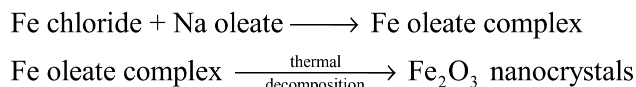

$$\text{Fe chloride + Na oleate} \longrightarrow \text{Fe oleate complex}$$

$$\text{Fe oleate complex} \xrightarrow[\text{decomposition}]{\text{thermal}} Fe_2O_3 \text{ nanocrystals}$$

In a single experiment, 9 g of the metal-oleate complex and 1.4 g of oleic acid (90%) were dissolved in 50 g of 1-octadecene (90%) at room temperature. The reaction mixture was heated up to 330 °C at a constant heating rate, and then kept at the desired temperature for 0.5 h. After reaching the temperature of 330 °C, a severe reaction occurred and the initial transparent solution became turbid and brownish.

The resulting solution was cooled down to room temperature. Afterwards, 130 cm^3 of ethanol was added to the solution to precipitate the nanocrystals which were separated by the centrifugation and then dried [8]. The diameter distribution of the produced nanocrystals was calculated from their XRD pattern. XRD was measured with a Philips X'Pert PRO.

The prepared catalyst nanoparticles were then placed in a beaker with butanol and magnesia powder. The molar ratios of the support and iron was: MgO:Fe= 60:1. This mixture was dispersed in an ultrasonic bath at room temperature for 1 h. Afterwards, it was dried on a hot plate at 150 °C with the magnetic stirrer for 0.5 h. Subsequently, the product was ground in a ceramic mortar to form a homogeneous powder of the catalyst precursor mix. In the next step, 30 mg of the catalyst mixture was placed in the centre of a horizontal tube furnace. C_2H_5OH or C_6H_{12} vapours were used as the carbon feedstocks during the reaction. In the same step of the synthesis, hematite particles were reduced to iron particles via hydrogen which was produced during the decomposition of the carbon sources. For each experiment, the vapour pressure of C_2H_5OH or C_6H_{12} was the same (50 mbar). Each carbon source was examined at the following temperatures: 650 °C, 750 °C, 850 °C. The dual time of the process was 0.5 h. Figure 1 shows the setup for the C-CVD reactor with ethanol or cyclohexane.

The as-produced material was purified to eliminate the catalyst and support material (MgO). This was achieved by a simple and efficient acid treatment [9]. The product was dissipated in 12 M HCl and ultrasonicated for 0.5 h. Afterwards, the solution was thoroughly washed with distilled water and acetone. Finally, the purified samples were annealed at 600 °C in a dynamic vacuum for 1 h to remove any remaining solvents.

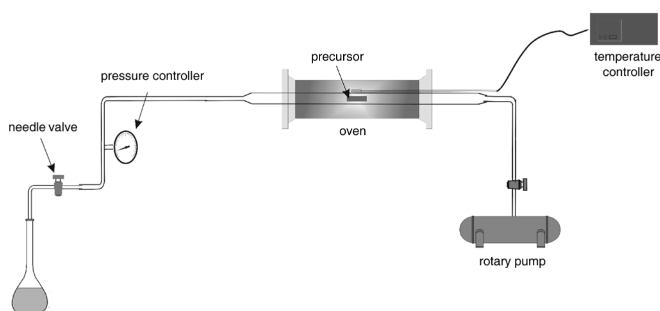

Fig. 1. Schematic setup of the CVD reactor

The morphology of the samples was studied using high-resolution transmission electron microscope (HRTEM) – FEI Tecnai F30. The sample preparation for HR-TEM study has been described elsewhere [10]. The quality of CNTs was determined using a Renishaw InVia Raman Microscope spectrometer.

3. Results and discussion

Figure 2 presents an XRD pattern of the prepared catalyst nanoparticles. The peaks indicated the presence of the hematite phase with a rhombohedral crystal structure. The calculation of the diameter distribution of the nanoparticles was based on the Scherrer equation [11] with help of the X'Pert HighScore Software [12]. In the inset of the Figure 2 the results of these calculations are presented. The crystal sizes range between 9.5 and 31.7 nm.

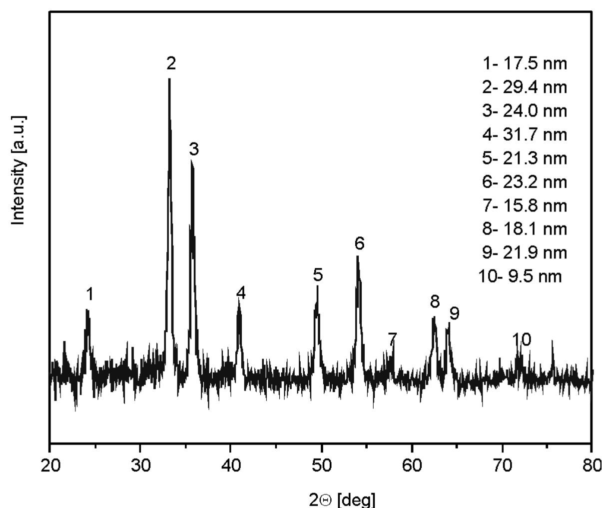

Fig. 2. XRD pattern of hematite nanocrystals

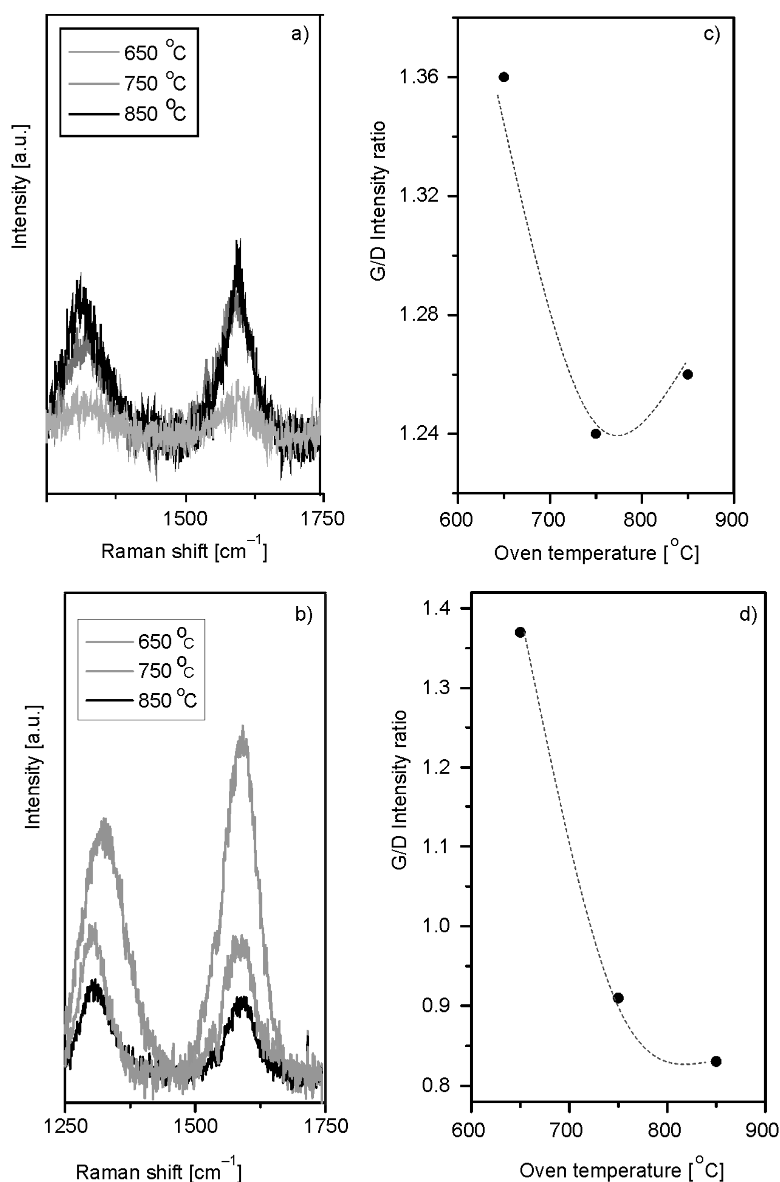

Fig. 3. Raman spectra of CVD synthesized MWCNT: a – ethanol feedstock, b – cyclohexane feedstock, for various oven temperatures and *G*/*D* ratio for various synthesis temperatures: c – ethanol feedstock, d – cyclohexane feedstock

Now we turn to the analysis of the CNT synthesized via the C-CVD technique using the above-described catalysts. Raman spectroscopy is a very efficient tool for the study of CNT. The so-called G-line is a characteristic feature of the graphitic layers and corresponds to the tangential vibration of carbon atoms. This mode is usually centred at ca. 1580 cm^{-1}. The second characteristic mode is observed at ca. 1300 cm^{-1} and is

a typical signature for defective graphitic structures (so called D-line or D-mode) [13]. The comparison of the ratios of these two peak intensities is a measure of the quality of the bulk samples. In addition, there is a third mode, named the radial breathing mode (RBM) which is very sensitive to the diameter of single-wall CNT (SWCNT) and double-wall CNT (DWCNT) [14].

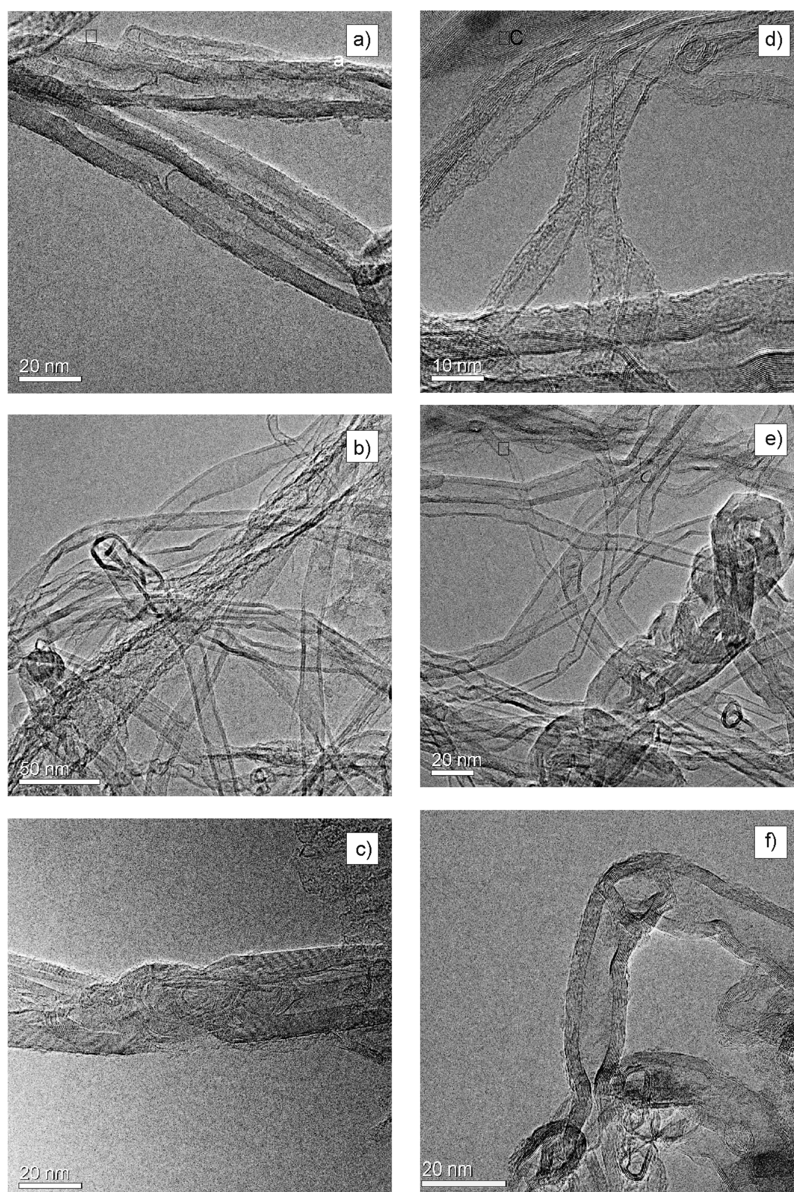

Fig. 4. TEM images of MWCNT synthesized in hotwall CVD at: a) 650 °C, b) 750 °C, c) 850 °C with ethanol as a feedstock, and at: d) 650 °C, e) 750 °C, f) 850 °C with cyclohexane as a feedstock

Raman studies showed that only the D- and G-bands were active in the ethanol feedstock and cyclohexane feedstock samples (Figs 3a, b, respectively). No RBM signal was detected for both series of the samples. Based on this one can rule out the formation of SWCNT or DWCNT in our samples. In order to determine the temperature influence on the quality of the bulk samples of the produced multiwalled CNTs (MWCNTs), the Raman spectra were normalized to the G mode. For the explored temperatures the highest G/D ratio (Figs. 3c, d) is observed at 650 °C which also indicates the highest quality and purity of these samples. The same trend is observed for both carbon feedstocks. This suggests that the prepared catalyst is not particularly sensitive to the carbon source.

Transmission electron microscopy was used to confirm the formation of MWCNTs. Figures 4 a, b, c present TEM images of the samples produced via our C-CVD process with ethanol as the feedstock at 650 °C, 750 °C, 850 °C, respectively. Figures 4 d, e, f present TEM images of the samples produced via C-CVD process with used of cyclohexane at 650 °C, 750 °C, 850 °C, respectively. The analysis of the images shows that the morphology of the materials synthesized with both carbon sources is similar. The MWCNTs formation is observed in all samples. Additionally, some bamboo-like structures with typical compartments in the interior of the multiwalled tubes were observed.

The outer diameters of the tubes were very similar and varied between 17 and 22 nm. The diameter distribution of ca. 5 nm is very low. A further observation shows that the samples are free from catalyst particles, which indicates the efficiency of the purification procedure. There are, however, some minor amorphous carbon deposits on the nanotubes.

4. Conclusions

We have synthesized carbon nanotubes using iron particles (with diameter size between 10 and 30 nm prepared in an organic route) using ethanol and cyclohexane as a carbon sources. The most efficient temperature for MWCNT synthesis was 650 °C were the G/D value was the highest indicating the highest yield and quality of MWCNTs. Finally, in the presented experimental efforts, we successfully produced iron nanoparticles via an organic technique. The resultant nanoparticles are suitable for the synthesis of MWCNTs with a low diameter distribution 19.5 ± 2.5 nm.

References

[1] IIJIMA S., ICHIHASHI T., Nature, 363 (1993), 603.
[2] THESS A., LEE R., NIKOLAEV P., DAI H., PETIT P., ROBERT J., XU C., LEE Y.H., KIM S.G., RINZLER A.G., COLBERT D.T., SCUSERIA G.E., TOMANEK D., FISCHER J.E., SMALLEY R.E., Science, 273 (1996), 483.
[3] SATISHKUMAR B.C., GOVINDARAJ A., SEN R., RAO C.N.R., Chem. Phys. Lett., 293 (1998), 47.
[4] COLOMER J.-F., STEPHAN C., LEFRANT S., VAN TENDELOO G., WILLEMS I., KONYA Z., FONSECA A., LAURENT CH., NAGY J.B., Chem. Phys. Lett., 317 (2000), 83.

[5] KITIYANAN B., ALVAREZ W.E., HARWELL J.H., RESASCO D.E., Chem. Phys. Lett., 317 (2000), 497.
[6] HAFNER J.H., BRONIKOWSKI M.J., AZAMIAN B.R., NIKOLAEV P., RINZLER A.G., COLBERT D.T., SMITH K.A., SMALLEY R.E., Chem. Phys. Lett., 296 (1998), 195.
[7] BONARD J.M., CHAUVIN P., KLINKE C., Nano Lett., 2 (2002), 665.
[8] PARK J., AN K., HWANG Y., PARK J.G., NOH H.J., KIM J.Y., PARK J.H., HWANG N.M., HYEON T., Nature Mater., 3 (2004), 891.
[9] BOROWIAK-PALEN E., PICHLER T., LIU X., KNUPFER M., GRAFF A., JOST O., POMPE W., KALENCZUK R J., FINK J., Chem. Phys. Lett. 363 (2002), 567.
[10] RÜMMELI M.H., BOROWIAK-PALEN E., GEMMING T., PICHLER T., KNUPFER M., KALBÁC M., DUNSCH L., JOST O., SILVA S.R.P., POMPE W., BÜCHNER B., Nano Lett., 5 (2005), 1209.
[11] LANGFORD J.I., WILSON A.J.C., J. Appl. Cryst., 11 (1978), 102.
[12] SADYKOV V.A., ISUPOVA L.A., TSYBULYA S.V., CHEREPANOVA S.V., LITVAK G.S., BURGINA E.B., KUSTOVA G.N., KOLOMIICHUK V.N., IVANOV V.P., PAUKSHTIS E.A., GOLOVIN A.V., AVVAKUMOV E.G., J. Solid State Chem., 123 (1996), 191.
[13] ANDO Y., ZHAO X., SHIMOYAMA H., Carbon, 39 (2001), 569.
[14] KUZMANY H., PLANK W., HULMAN M., KRAMBERGER C., GRÜNEIS A., PICHLER T., PETERLIK H., KATAURA H., ACHIBA Y., Eur. Phys. J., B 22 (2002), 307.

Received 28 April 2007
Revised 16 February 2008

Materials Science-Poland, Vol. 26, No. 1, 2008

Influence of substrate type and its placement on structural properties of TiO_2 thin films prepared by the high energy reactive magnetron sputtering method

D. KACZMAREK[1], E. L. PROCIOW[1], J. DOMARADZKI[1], A. BORKOWSKA[1*], W. MIELCAREK[2], D. WOJCIESZAK[1]

[1]Faculty of Microsystem Electronics and Photonics, Wrocław University of Technology, ul. Janiszewskiego 11/17, 50-372 Wrocław, Poland

[2]Electrotechnical Institute, ul. Skłodowskiej-Curie 55-61, 50-369 Wrocław, Poland

The paper presents studies of the influence of substrate type and its placement on structural properties of TiO_2 thin films prepared by the high energy reactive magnetron sputtering method. During the deposition, conditions of the magnetron powering have been especially selected to enhance the nucleation energy. Thin films were deposited on Si(100) and SiO_2. Substrates were placed on a plate at three distances from the centre of the target. Selected substrates were also placed under various angles with respect to the plate. Thin films were examined using X-ray diffraction (XRD) and atomic force microscopy (AFM). XRD analysis showed existence of TiO_2-rutile phase with preferred (110) orientation and AFM measurements revealed nanocrystalline structure of the films.

Key words: *TiO_2; thin films; reactive sputtering; structural properties*

1. Introduction

Due to its optical, electrical and chemical properties, TiO_2 has been one of the most intensively studied metal oxides in the recent years. Though TiO_2 can exist in three different phases (brukite, anatase, rutile), only rutile is thermodynamically stable at ambient conditions. TiO_2 thin films can be amorphous, polycrystalline or mixed, depending on the deposition method. Another very important factor is crystallite size. It has been reported that oxides with grains in the range of nanometers (less than 100 nm) possess a lot of unique properties [1]. Such nanocrystalline materials can be used for new applications in sensors, photodetectors, nanotransistors, solar cells, optical

[*]Corresponding author, e-mail: agnieszka.borkowska@pwr.wroc.pl

coatings, switches and modulators [2]. That is why structural properties of titanium dioxide and their correlation with methods of their fabrication are of great interest. Magnetron sputtering [3] is one of numerous techniques applied so far to deposit TiO_2 thin films.

In this work, influence of substrate type and its placement on structural properties of TiO_2 thin films have been presented.

2. Experimental procedure

Thin films were prepared by the high energy reactive magnetron sputtering (HE RMS) method using Ti target [4]. During the deposition, special conditions of the magnetron powering have been selected to enhance the nucleation energy. Prepared thin films exhibited highly ordered nanocrystalline structure. Thin films were deposited on Si(100) and SiO_2. Substrates were placed on a plate with special tilted and hemispherical holders in three zones from the centre of the target (Fig. 1).

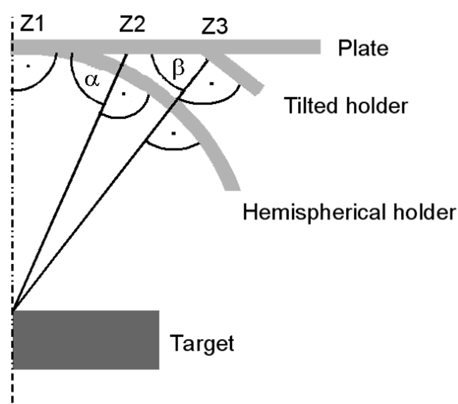

Fig. 1. Side view of a plate with special tilted and hemispherical substrate holders in the deposition process of TiO_2 thin films; Z1, Z2, Z3 – internal, medium and external zones, respectively

Structural properties were investigated by means of X-ray powder diffraction (XRD), performed using DRON-2 powder diffractometer with Fe-filtered CoK_α radiation. Average size of crystallites was calculated from XRD spectra in a conventional way according to the Scherrer formula [5]. The topography was studied using atomic force microscope (AFM) (Veeco PicoForce) working in a contact mode.

3. Results and discussion

All examined thin films revealed the existence of TiO_2-rutile phase (Tables 1, 2). In Table 1, dependences of structural parameters of TiO_2 thin films on the substrate inclination angle and distance from the target in the deposition process, placed in Z3 with base cut perpendicular (⊥) to plate radius have been presented. The analysis

shows that preserving constant distance to the plate radius and decreasing the substrate (S1, S2) inclination angle (α, β) results in increasing the difference between the interplanar distances (Table 1). The grain size D does not change.

Table 1. Dependence of structural parameters of TiO_2 thin films on the substrate inclination angle and distance from the target in deposition process; base cut perpendicular (⊥) to plate radius*

Sample	Substrate	Zone	Placement	Phase	D [nm]	d [nm]	d_{PDF} [nm]	$d - d_{PDF}$ [nm]
S1	Si(100)	Z3	plate	rutile	7.9	0.3268	0.3247	tension 0.0028
S2			tilted holder		7.8	0.3255	0.3247	tension 0.0008
S3			hemispherical holder		6.7	0.3247	0.3247	relaxation 0
S4	SiO_2		hemispherical holder		8.7	0.3250	0.3247	tension 0.0003

*D – grain size (nm), d – interplanar distance (nm), d_{PDF} – interplanar distance (nm) from PDF file [6].

Table 2. Dependence of structural parameters of TiO_2 thin films on base cut placement relative to plate radius*

Sample	Substrate	Zone	Placement	Base cut	Phase	D [nm]	d [nm]	d_{PDF} [nm]	$d - d_{PDF}$ [nm]
S5	Si(100)	Z2	hemispherical holder	⊥	rutile	5.6	0.3259	0.3247	tension 0.0012
S6				||		5.8	0.3242	0.3247	compression –0.0005

D – grain size (nm), d – interplanar distance (nm), d_{PDF} – interplanar distance (nm) from PDF file [6].

Concurrently, decreasing the distance to the plate radius and substrate inclination angle results in a decrease of grain size (S1, S2). On the hemispherical holder (S3, Table 1), the structure of thin film becomes relaxed ($d - d_{pdf} = 0$) and the grain size smaller. The grain size of the film deposited on SiO_2 is ca. 30% larger than that of deposited on Si in the same zone (Z3), (S4, Table 1).

In Table 2, a dependence of structural parameters of TiO_2 thin films (in Z2) on the placement of the base cut relative to the plate radius has been presented. It can be seen that the grain size is closely the same for both samples (S5 and S6). However, in the case of parallel (||) placement of the base cut with respect to the plate radius, the film was compressed compared to the PDF value (S6, Table 2) contrary to perpendicular (⊥) placement, in which thin films were tensed compared to PDF.

Figures 2 and 3 present AFM images of TiO_2 thin films on Si(100) placed on a hemispherical holder in Z2 with the base cut parallel (||) and perpendicular (⊥) to the

plate radius, respectively. AFM images confirm nanocrystalline structures of the films. As can be seen, the grains have the same dimensions and a higher degree of ordering can be seen in the case of sample S6 (Fig. 3).

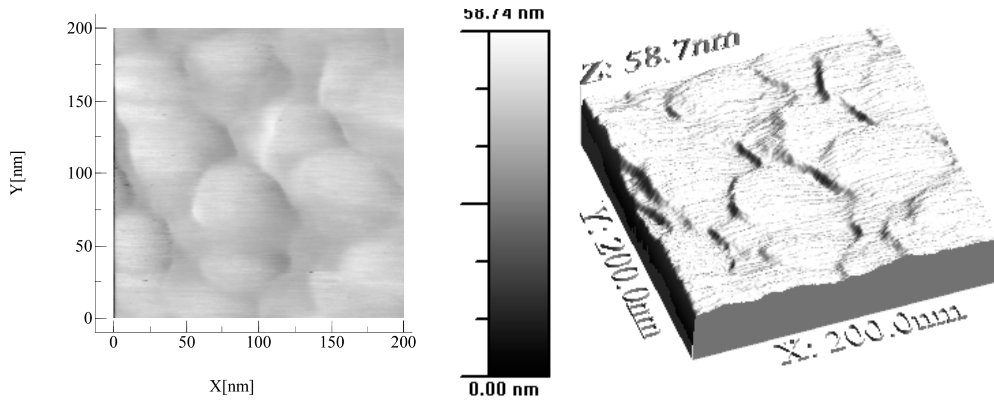

Fig. 2. AFM images of TiO_2 thin film on Si(100) placed on a hemispherical holder in Z2; base cut perpendicular (⊥) to plate radius (sample S5)

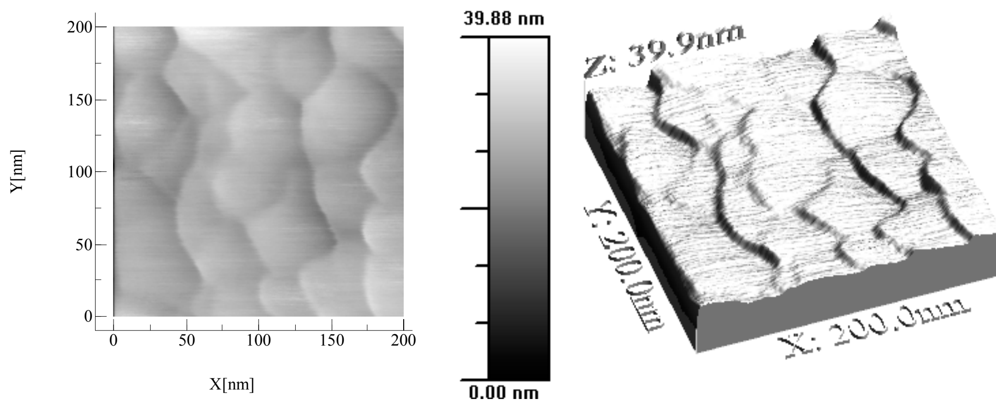

Fig. 3. AFM images of TiO_2 thin film on Si(100) placed on a hemispherical holder in Z2; base cut parallel (||) to plate radius (sample S6)

4. Conclusions

The type of used substrates (monocrystalline, amorphous) as well as the way of their placement with respect to the target have the influence on the structure of TiO_2 thin films. The sizes of TiO_2 nanocrystalites on SiO_2 substrate are on average larger by about 30% in comparison to the grain sizes of those deposited on Si. Substrate placement with respect to the target (distance and angle) influences the grain size as well as the compression of the examined TiO_2 thin films.

Acknowledgement

This work was financed from the sources granted by the Department of Scientific Research for science development in years 2006–2008 as a research project and from the statute sources given by the Polish Ministry of Science and Education. The authors acknowledge R. Wasielewski from the Institute of Experimental Physics, University of Wroclaw for the AFM measurements.

References

[1] TULLER H.R., Solid State Ionics, 131 (2000), 143.
[2] DIEBOLD U., Surf. Sci. Rep., 48 (2003), 53.
[3] DOMARADZKI J., BORKOWSKA A., KACZMAREK D., PROCIOW E.L., Opt. Appl., 35 (2005), 425.
[4] PROCIOW E.L., DOMARADZKI J., KACZMAREK D., BERLICKI T., Patent PL 382163, April 17, 2007.
[5] KLUG H., ALEXANDER L., *X-ray diffraction procedures*, Wiley, New York, 1974.
[6] *Powder Diffraction File*, Joint Committee on Powder Diffraction Standards ASTM, Philadelphia, PA, 1967, Card 21-1276.

Received 28 April 2007
Revised 16 February 2008

Materials Science-Poland, Vol. 26, No. 1, 2008

Palladium nanocrystals and their properties

E. CZERWOSZ[1*], P. DŁUŻEWSKI[2], J. KĘCZKOWSKA[3],
M. KOZŁOWSKI[1,2], M. SUCHAŃSKA[3], H. WRONKA[1]

[1] Tele&Radio Research Institute, ul. Długa 44/50, 00-241 Warsaw, Poland

[2]Institute of Physics PAN, al. Lotników 36/46, 02-668 Warsaw, Poland

[3]Kielce University of Technology, al. 1000-lecia PP 7, 25-312 Kielce, Poland

Films composed of Pd nanocrystals embedded in fullerene C_{60} matrix have been studied by TEM, AFM, UV-VIS absorption methods. Data on the structure of Pd nanocrystals was obtained from electron diffraction of selected areas and the size distribution for Pd nanocrystals was found from dark field TEM images. UV-VIS absorption spectra showed the shift of C_{60} characteristic bands connected with the ligand field effect. Electric characteristics were recorded for the initial dry film and film wetted by various liquid agents (benzene, ethanol, toluene).

Key words: *palladium nanocrystals; TEM; AFM; UV-VIS absorption; electric properties*

1. Introduction

Grain boundaries make up a major portion of a material in the nanoscale, and strongly affect its properties and processing. Properties of nanomaterials deviate from those of single crystals or polycrystals and glasses with the same average chemical composition. This deviation results from the size and dimensionality of nanometer-sized crystallites as well as from numerous interfaces between crystallites. Nanocrystallites of bulk inorganic solids exhibit size dependent properties such as lower melting points, higher energy gaps, and nonthermodynamic structures [1, 2]. In comparison to macro-scale powders, increased ductility has been observed in nanopowders of metal alloys [2, 3].

One of the primary applications of metals such as Pd is their use as heterogeneous catalysts in a variety of reactions. Due to their vastly increased surface area over macro-scale, palladium and its compounds are ultra-high activity catalysts. They are also used as starting materials for a variety of reactions.

[*]Corresponding author, e-mail: czerwosz@pie.edu.pl

Palladium and its compounds show a high and selective affinity towards hydrogen, resulting in their volume expansion. Fibre Bragg gratings attached to palladium elements are used to monitor the resultant strain from the hydrogen uptake. The technique is aimed at monitoring hydrogen at low concentrations, down to a few hundred ppm, where H_2 is the result of polymer materials ageing [4]. All palladium sensors are based on the phenomena of adsorption and dissociation of hydrogen containing molecules.

In this paper, we show a new method of preparation of Pd nanocrystals embedded in fullerene matrix. The system exhibits properties predisposing it to apply it as a liquid sensing element.

2. Experimental

Pd nanocrystalline films were prepared by the physical vacuum deposition method (PVD) by evaporation from two separated sources of fullerene C_{60} and palladium acetate. The films were deposited on various substrates (glass, Si, metal foils). The distance from the sources to the substrate was the same for all processes. The composition and film structure changed upon changing temperatures of the sources.

The structures, morphologies, topographies and compositions of the films were studied by the transmission electron microscopy (TEM) with the electron diffraction of selected area method (EDSA), atomic force microscopy (AFM) and atomic absorption spectroscopy analysis (ASA). Electronic properties of fullerene based matrices were studied by absorption spectroscopy in the UV-VIS region. The changes in film resistivities were studied using the experimental set-up presented in Fig. 1. A sample was placed in a special holder (Fig.1a). The holder was prepared in a special way allowing one to omit the problem of preparation of metallic electric contacts. The electric contacts in the holder were realized only by a mechanic contact of a metal tip with the surface of the film.

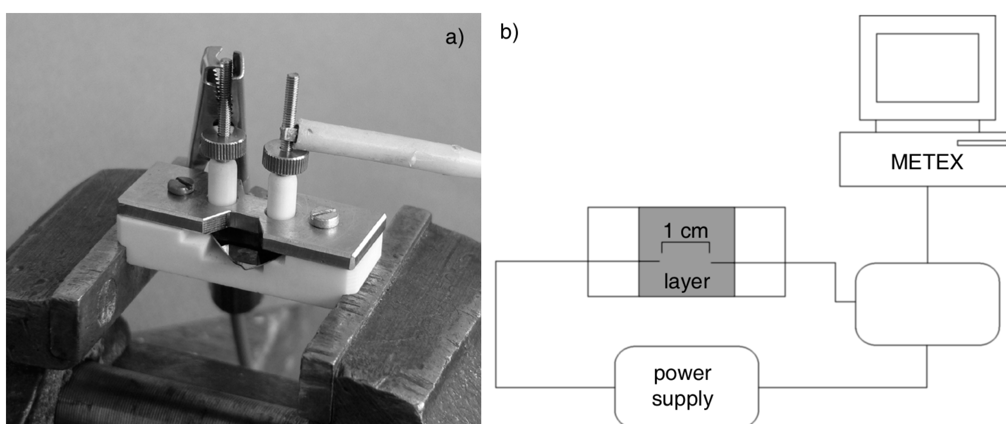

Fig. 1. Detailed view of the sample holder (a) and experimental set-up for measurements of resistivity (b)

The signal resulting from a liquid introduced onto the sample surface was measured as a function of time and recorded by the computerized system (Fig. 1b). The films contained from 20 wt. % to 39 wt. % of palladium which was connected with the Pd content in the substrate (maximum 44 wt. %).

The film structure was studied by electron diffraction and transmission electron microscopy (TEM). TEM investigations were performed with the JEOL-2000EX electron transmission microscope operating at 200 keV incident beam energy. The film topography was investigated with the atomic force microscope EXPLORER2000 in the non-contact mode in ambient atmosphere with the tip model MLCT-EXMT-A.

Absorption spectra were measured using the system which consisted of the DT-MINI-GS deuterium tungsten halogen light source, the S2000 miniature fiber optic spectrometer (Ocean Optics) which is a low-cost, high-performance system easily configured for UV-VIS-Shortwave NIR applications from 200 nm to1100 nm.

3. Results and discussion

The TEM images of all the films show dark objects identified as Pd nanocrystals by the dark field image and EDSA techniques (Figs. 2, 3). In Figure 2a, diffused rings for Pd nanocrystals diffraction are seen, in Fig. 2b, diffraction for the C_{60} crystalline fcc type structure is shown and in Fig. 2c both types of diffraction patterns are presented.

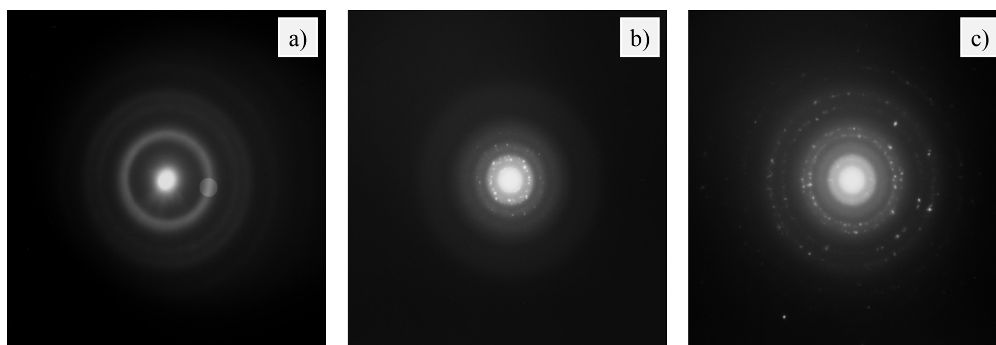

Fig. 2. EDSA patterns for the film containing 29 wt. % of Pd:
a) Pd(111), b) C_{60}(111), c) Pd(111) and C_{60}(111)

Pd nanocrystals are of fcc type and their sizes, determined from TEM images, range from 1.5 nm to 5 nm. The size distribution of Pd nanocrystal diameters film containing ~30 wt. % the Pd is presented in Fig. 3. It seems that with lowering the temperature of the source containing a palladium compound, the content of palladium in the film decreases, and the sizes of Pd nanocrystals increase.

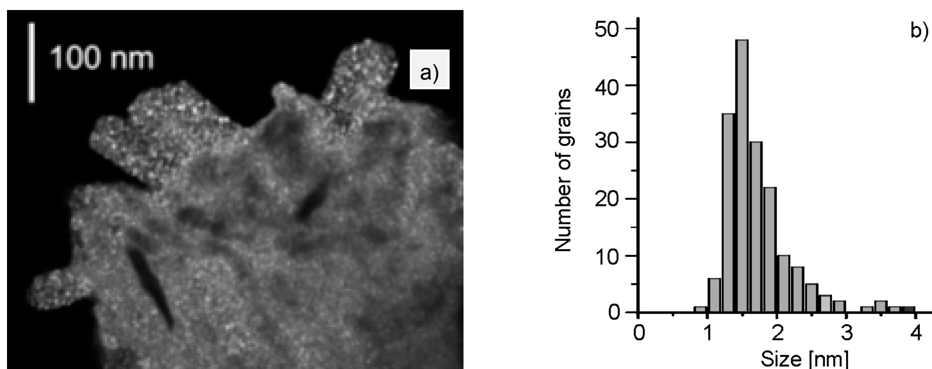

Fig. 3 TEM image (dark field mode) of a selected area (a)
and size distribution for Pd nanocrystals observed in this area (b)

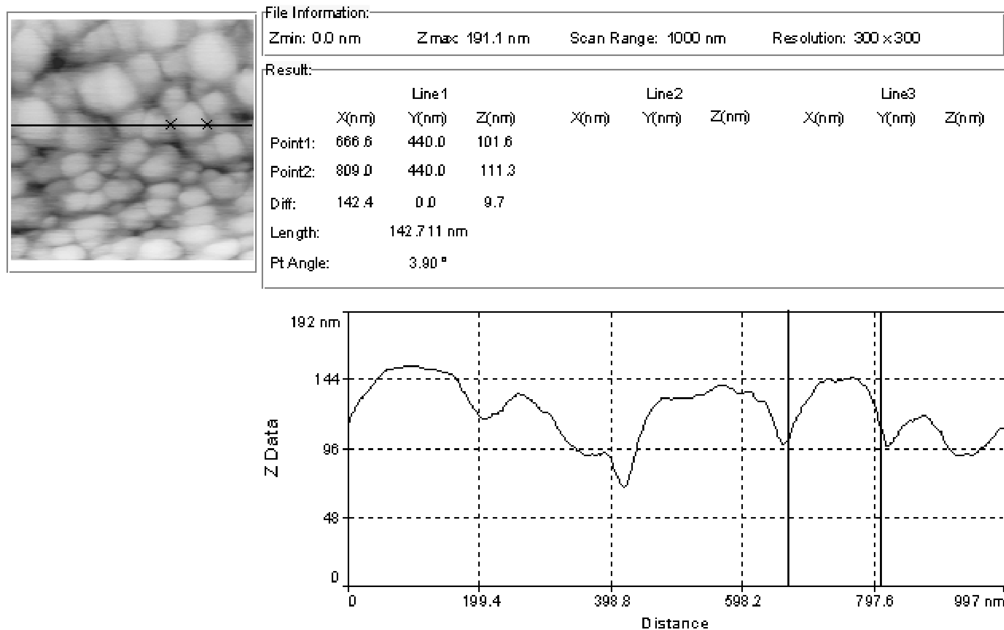

Fig. 4. AFM image of the film containing 23.5wt. % of Pd
and the profile analysis along the line shown in the image

Analysis of the AFM images points to a developed surface of each sample. The samples with Pd content higher than 30 wt. % have dendrite-like topography (Fig. 5) while those with a lower Pd content have a hillock-like topography (Fig. 4). The profile analysis along a line enables one to determine nanocrystal sizes (diameter and height). The diameters of the objects forming the film surface with a lower Pd content are about 100–200 nm while those with a higher Pd range from 200 nm to 500 nm. The heights of the objects are the same in all cases.

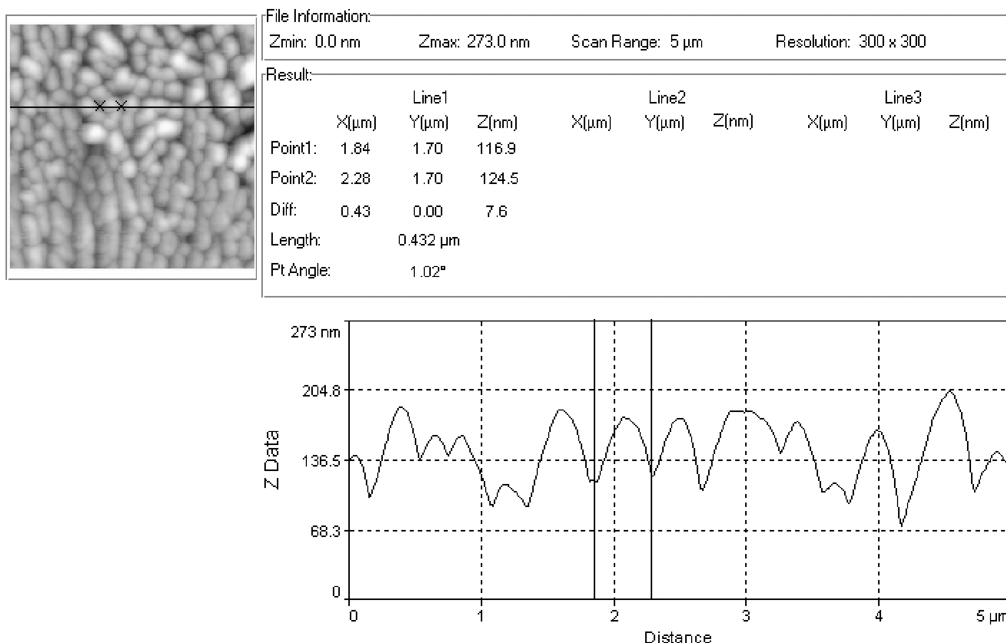

Fig. 5. AFM image of the film containing 30 wt. % of Pd
and the profile analysis along the line shown in the image

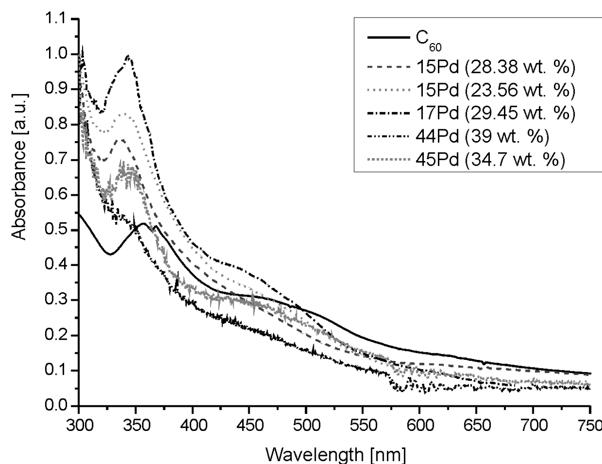

Fig. 6. Absorption spectra of Pd-C_{60} samples with various contents of Pd and of C_{60} film

UV-VIS absorption spectra of the samples with various Pd content and for a pure C_{60} film are presented in Fig. 6. In Table 1, the results of decomposition of these spectra into Gaussian shape bands are given (the adjustment coefficient was about 5%). In this table, the origin of particular bands is also presented according to Fig. 7. It can be seen that with increasing Pd content in the film, the maxima of the bands placed at ca. 290 and 340 nm shift toward higher wavelengths while the maximum of the band

at ca. 400 nm shifts towards lower wavelengths. The band located at the wavelength higher than 500 nm is much more sensitive to increase of Pd content. The origin of this band is not clear at the moment.

Table 1. Spectral parameters of the bands in the absorption spectra of samples with various Pd contents (λ – wavelength, $\Gamma_{1/2}$ – full width at a half maximum, I – intensity at a maximum)

Pd content	$h_g \to t_{1g}$			$h_u \to t_{1g}$			*		
	λ [nm]	$\Gamma_{1/2}$ [nm]	I [a.u.]	λ [nm]	$\Gamma_{1/2}$ [nm]	I [a.u.]	λ [nm]	$\Gamma_{1/2}$ [nm]	I [a.u.]
23.56 wt. %	331	77	121	427	116	62	501	142	20
28.38 wt. %	330	59	73	393	143	109	579	161	15
29.45 wt. %	337	50	74	402	171	148	599	45	10
34.7 wt. %	341	43	37	402	227	144			
Pure C_{60} film	341			467					

The resistivity was calculated based on measurements of voltage changes on the sample with known value of the current intensity. The results of resistivity measurements along a film for different liquids are presented in Table 2. The measurements of the film electric response in the presence of different liquids (ethanol, benzene) show a reversible time dependent current–voltage characteristics with short time (tenths of a second) of system response on the liquid dosage.

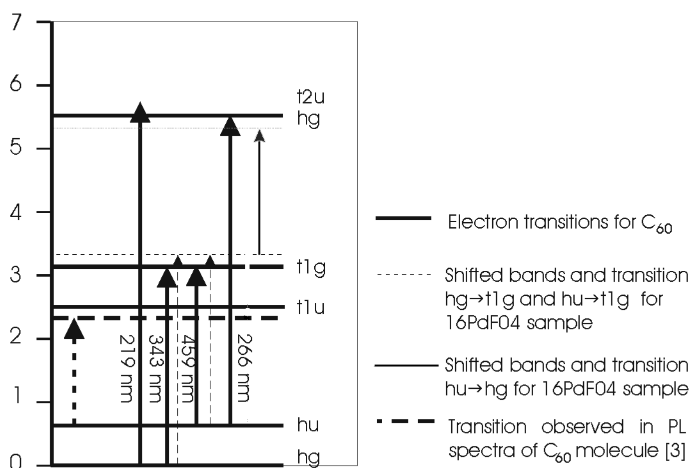

Fig. 7. Electronic structures of C_{60} molecule and the system Pd +C_{60} (for sample 16PdF04) [5]

Table 2. Resistivities along a film for different liquids

Pd content	Dry film [MOhm·cm]	Film wetted [kOhm·cm]	
		Ethanol	Benzene
27 wt. % 34 wt. %	>>20	10 000	2500

4. Conclusions

The structure of the film formed from Pd nanocrystals placed in the Pd-C_{60} matrix has been confirmed by the TEM results. In dark field images, Pd nanocrystals were visible with sizes between 1.5 nm and 5 nm (depending on the Pd content) and the related EDSA patterns showed the fcc type of their structure. For bigger areas, diffraction patterns connected with the C_{60} fcc type crystalline structure have also been observed. On the other hand, the UV-VIS absorption spectra exhibit bands that may be attributed to the C_{60}–M (where M is a metal atom) electronic structure. Such spectra were also observed for the C_{60}–Hg system [5]. The band shifts observed in [5] were connected with changes in electronic structure of C_{60} molecules due to the existence of a ligand field connected with metal atoms or particles.

AFM images show that the topography of the films also depends on the Pd content and is more complicated, and the surface is more developed for samples with a higher Pd content.

References

[1] ALIVISATOS A.P., Science, 271 (1996), 933.
[2] HAHN K.H., BEDULA K., Scripta Metall., 23 (1989), 7.
[3] HAUBOLD T., BOHN R., BIRRINGER R., GLEITER H., Mater. Sci. Eng. A, 153 (1992), 679.
[4] MAIER R.R.J., BARTON J.S., JONES J.D.C., MCCULLOCA S., JONES B.J.S., BURNELL G., Meas. Sci. Technol., 17 (2006), 1118.
[5] GRYCUK T., CZERWOSZ E., Fullerene Sci.Techn., 5/6 (1997), 1275.

Received 28 April 2007
Revised 16 February 2008

Materials Science-Poland, Vol. 26, No. 1, 2008

Application of multiwall carbon nanotubes to microfluidic systems

B. CICHY[1*], W. STRĘK[2], J. DZIUBAN[1], A. GÓRECKA-DRZAZGA[1]

[1]Faculty of Microsystem Electronics and Photonics, Wrocław University of Technology, ul. Janiszewskiego 11/17, 50-372 Wrocław, Poland

[2]Institute of Low Temperature and Structure Research, Polish Academy of Sciences, ul. Okólna 2, 50-422 Wrocław, Poland

A new idea of potential application of miniature light sources (micro-FED) have been presented for excitation of fluorophore dyes used in biochemical investigations. Such light sources are based on field emission phenomena in diode type structures. Surfaces of cold cathodes were modified by electrophoretic deposition of multiwall carbon nanotubes, whereas anode surfaces utilize nanocrystalline phosphors with lanthanide-doped YAG matrices. Spectral characteristics of the light sources are in a good agreement with excitation spectra of a series of well known fluorescent dyes.

Key words: *nanotubes; nanoparticles; lab-on-a-chip; fluorescent dyes*

1. Introduction

There has been a great interest in identification and characterization of various functional molecules in the field of biochemistry and protein studies. Specialized techniques, e.g, flow cytometry allow one to group heterogeneous population of cells to functional subsets [1]. Identification of a variety of functionally distinct cells and their localization in the environment is also essential in lots of studies, e.g. estimating events occurring *in vivo*. The identification and localization is usually performed by use of fluorophore dyes. Their molecules chemically attached to investigated particles serve as fluorescent markers that can be detected by dedicated hardware. An impressive amount of fluorophores with various excitation energies have been characterized in literature, according to fluorescence specificities and binding properties to various particles [2]. An example of popular dyes is the rhodamine family, commonly used

[*]Corresponding author, e-mail: bartlomiej.cichy@pwr.wroc.pl

due to their high resistance to photodegradation, high emission intensity and pH insensitivity [3]. Long-wavelength emitting carbocyanines (Cy3, Cy5, Cy5.5, Cy7) are also used in fluorescence microscopy or flow cytometry [4] as well as fluorescein, Lucifer yellow or Alexa dyes, more photostable and fluorescent than the spectral analogues listed above. It is also worth noting that Alexa dyes exhibit very broad range of pH insensitivity (4–10) and retain very bright light emission on conjugation [3].

The aim of this work was to develop efficient miniature light sources based on field emission effect whose fabrication process is simple in comparison to solid state p-n junction devices. Such a light source should also provide an effective light emission and its luminescence spectra have to cover excitation lines of particular fluorophore dyes. Finally, the construction of pondered light sources should allow to "on-chip" assembly with portable micromechanical real time bio-analysers.

2. Experimental

Light sources have been prepared as diode type field emission devices. Cathode surfaces have been modified by electrophoretical deposition of distinct nanoparticles. Multiwall carbon nanotubes (MWNT) were used to prepare the cathode. Nanotubes received from Shenyang National Laboratory for Materials Science, Shenyang, China (SNL) were delivered as raw material, containing large amounts of amorphous carbonaceous particles and catalyst impurities (Fig. 1a). Beside impurities, the raw material was also characterized by a considerable inhomogeneity, mainly due to the presence of carbon fibres and various types of nanotubes (Fig. 2). It is important for future applications to have the tubes pure enough for the following electrophoretical deposition. Therefore it was necessary to employ certain purification procedures.

Two methods were used to purify raw tubes. The first of them included thermal annealing of raw MWNTs in air at 250 ºC for 12 hours. This purification method presumably utilizes the fact that MWNT and other carbonaceous particles have different thermal oxidation rates [5]. It is considered that carbonaceous particles are burned first out due to faster selective etching. However, as time proceeds, more carbon nanotubes are exposed and have more chance to be attacked by oxygen molecules. A possibility of oxidation of the nanotubes being the main disadvantage, nevertheless the method theoretically is able to eliminate amorphous carbon impurities [6]. The other approach consists in purification in acidic solution [7]. The tubes were treated for few hours with diluted solution of nitric acid to dissolve iron compounds and oxidize amorphous carbon particles. Temperature of the reaction was maintained at 60 ºC with intensive ultrasonic stirring. Finally, the samples were washed a few times with deionized (DI) water and immersed in isopropyl alcohol (IPA).

X-ray diffraction analysis was used to determine impurities in the material before and after purification. The morphology of cleaned MWNT was examined by the AFM microscopy. Nanotubes immersed in IPA were enriched by addition of magnesium nitrate hexahydrate ($Mg(NO_3)_2 \cdot 6H_2O$) in order to facilitate electrophoretic deposition.

The salt served as a binder necessary in electrophoretic deposition to glue the tubes to selected substrates and imposed positive charge onto suspended particles. The sol prepared in such a way was used to deposit the tubes on selected substrates. Two classes of substrates were used: plane substrates as glass slices with ITO layer used also for cathode and anode electrodes, and patterned substrates which contained mainly porous silicon (PS) and Si substrate with array of dry etched silicon tips covered with thin Cr layer (used only as cathode substrates).

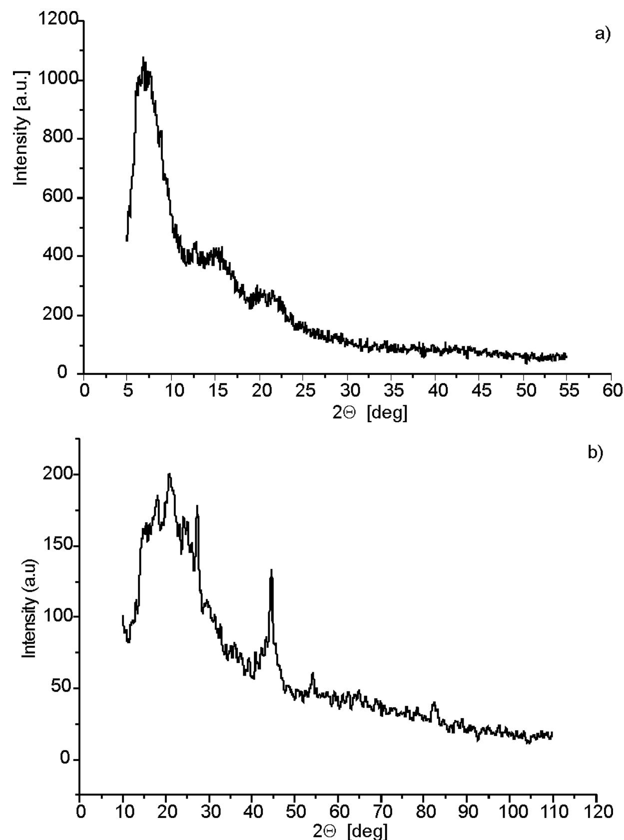

Fig. 1. XRD spectra of: a) raw multiwall carbon nanotubes (MWNT), b) nanotubes thermally annealed at 250 °C in air

Electrodes were prepared by electrophoretical modification of the surfaces. As deposited phosphors, we chose widely used YAG:Re ($Y_3Al_5O_{12}$: Re = Ce^{3+}, Tb^{3+}, Eu^{3+}) doped matrices [8]. Yttrium aluminum garnet (YAG) is a very promising host for rare-earth-doped phosphors [9]. Its typical synthesis route is based on solid state reaction and requires high temperatures of 1600 °C and prolonged heating to obtain pure phases [10]. Therefore, the main effort has been focused on wet chemical methods such as sol-gel synthesis. Its advantages are inexpensive precursors, convenient process control, low sintering temperatures and large mass production [11]. The starting materials

for the combustion synthesis method were as follows: $Al(NO_3)_3 \cdot 9H_2O$, Y_2O_3, citric acid ($C_6H_8O_7 \cdot H_2O$) and lanthanide oxides as dopant sources. The oxides were diluted in concentrated nitric acid to obtain corresponding nitrate solutions. Stoichiometric

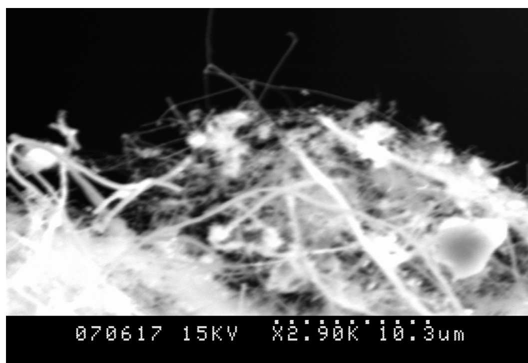

Fig. 2. SEM image of raw MWNT

amounts of the nitrates were dissolved in DI water and mixed together. The ratio of citric acid to nitrate was maintained at 1:1. The solution was continuously stirred at 60 °C until it turned to yellowish sol. In the next step, the sol was rapidly heated to about 200 °C to initiate the autocombustion process, i.e., a self propagating process between the reducing citrate and oxidizing nitrate groups [9]. The product looked like brown fluffy foam and did not reveal any crystal structure (Fig 3).

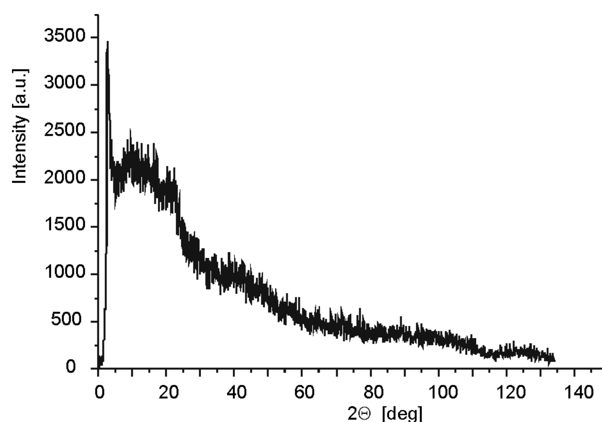

Fig. 3. XRD spectra of as prepared YAG combustion precursor

The precursor was sintered at various temperatures in a muffle furnance in ambient atmosphere to transform the amorphous precursor to YAG phase (Fig. 4). As prepared phosphor was then dispersed in IPA with addition of magnesium nitrate and likewise nanotubes were electrophoretically deposited on ITO substrates. Anodes and cathodes were assembled together with 250 μm mica or 400 μm silicon spacers. As

prepared sources were placed in a vacuum chamber and pumped out to 10^{-3} hPa followed by the field emission and cathodoluminescence measurements.

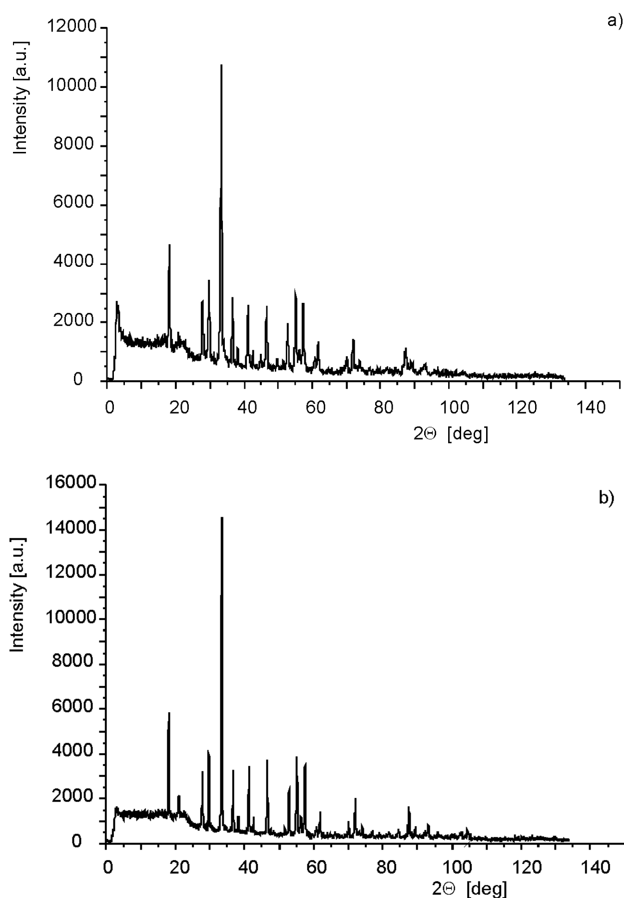

Fig. 4. XRD spectra of the combustion YAG precursor sintered at: a) 800 °C, b) 1100 °C

3. Results and discussion

The results of applied purification procedures have been assessed by the X-ray diffraction and morphology of the nanotubes was examined by scanning electron microscopy (SEM) and atomic force microscopy (AFM) (Fig. 5). The obtained carbon nanotubes can be purified also by thermal annealing and by liquid phase purification in acidic solutions, as was mentioned in the preceding section. Thermal annealing of raw samples eliminated much of amorphous carbonaceous particles (Fig. 1b). However, the diffraction spectra still contain peaks from catalyst compounds. After the liquid phase purification, the diffraction intensities of iron compound peaks were significantly reduced. Therefore, good results can be achieved by the multi-technique purifica-

tion procedures. None of these procedures were able to improve the homogeneity of the purified material, what is still a week point of these samples. AFM scans show that the purified samples contain mainly straight multiwalled carbon nanotubes. It is likely that beyond straight MWNTs, the material contained also Y shaped tubes (Fig. 6).

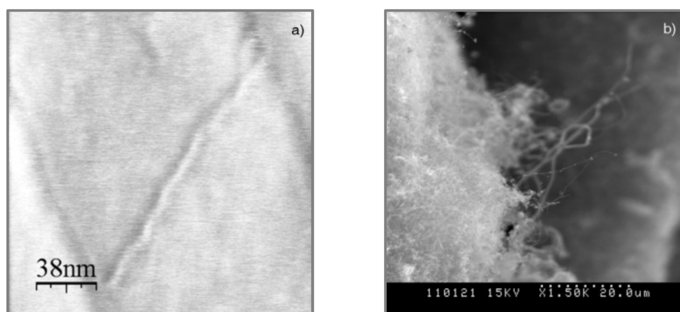

Fig. 5. MWNT morphology after purification examined by a) AFM microscopy, b) SEM microscopy

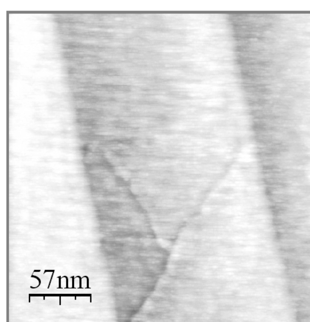

Fig. 6. AFM image of a possible Y shaped nanotube

Major diameters of the MWNT tubes amount to ca. 30 nm and carbon fibre diameters to a few hundreds nanometers. It is obvious that more demanding applications or deposition procedures will require very homogeneous phases. X-ray spectra of purified MWNT show also (002) peaks slightly shifted to higher angle values (Fig. 1b). This feature is presumably connected with tensions in the structure after intensive sonication during the purification procedure. Moreover, it is also likely that the intensive sonication could lead to breaking up the outer walls of the tubes. The sol-gel combustion method for preparation of phosphors is well known and can provide quite a good alternative for the solid state synthesis. The obtained YAG matrices did not contain other stable phases as YAM ($Y_4Al_2O_9$) or YAP ($YAlO_3$) in the system of Y_2O_3–Al_2O_3 (Fig. 4). Taking advantage of the Scherrer–Debye formula, it is possible to estimate the grain size of prepared YAG matrices to amount to ca. 65 nm after annealing at 1100 °C.

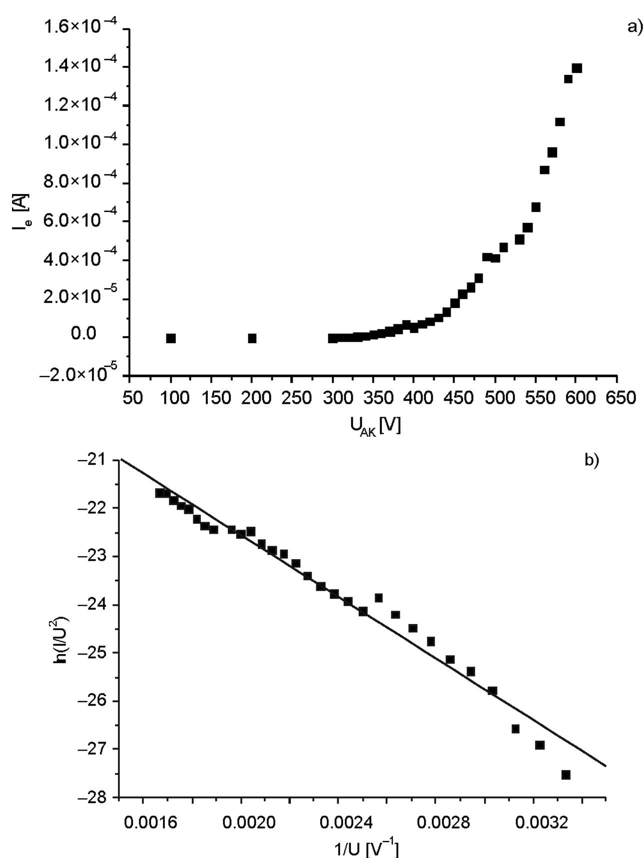

Fig. 7. Field emission characteristics: a) *I–V* characteristic, b) Fowler–Nordheim plot; cathode covered by deposited of MWNT tubes. The distance between cathode and anode fixed at 250 μm

4. Conclusions

Field emission characteristics of the prepared sources show very high current densities even if the deposited layers of the tubes on every substrate are very inhomogeneous and

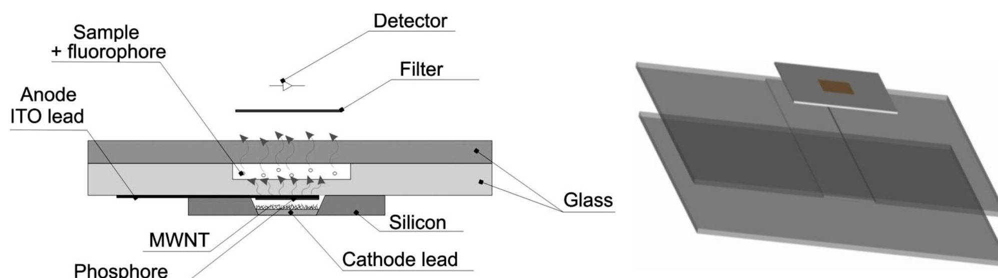

Fig. 8. Integration of miniaturized field cathodes with microfluidic portable systems for real time analyses

messy. It is also quite possible that the deposited layer can provide some type of reorganization on impact of the electric field what can explain a high field amplification factor (Fig. 7).

Such a flat light source after few changes can be assembled to an appropriate microfluidic system utilizing optical detection with fluorescent dyes (Fig. 8). Preparing the cathode in silicon with microengineering techniques allows one to bond the electron source to an appropriate borosilicate glass thereby obtaining solution ready for use. Spectral characteristics of obtained phosphors are in a good agreement with absorption spectra of well known fluorophores such as Rhodamine 6G, Alexa dyes or carbocyanines. Further work of the present authors will aim at designing sources allowing for efficient field emission and at obtaining efficient phosphors with low emission thresholds.

Acknowledgement

This work was partially supported by the Statutory Project of the Wrocław University of Technology. We express special thanks to Miłosz Grodzian M. Sc. from the Institute of Experimental Physics of Wrocław University for his help with AFM imaging.

References

[1] TSURUI H., NISHIMURA H., HATTORI S., HIROSE S., OKUMURA K., SHIRAI T., J. Histochem. Cytochem., 48 (2000), 653.
[2] LATT S.A., ELHANAN S., EISENHARD M., J. Histochem. Cytochem., 27 (1979), 65.
[3] PANCHUK-VOLOSHINA N., HAUGLAND R.P., BISHOP-STEWARD J., BHALGAT M.K, MILLARD P.J., MAO F., LEUNG W.Y., HAUGLAND R.P., J. Histochem. Cytochem., 47 (1999), 1179.
[4] BERLIER J.E., ROTHE A., BULLER G., BRADFORD J., GRAY D.R., FILANOSKI B.J., TELFORD W.G., YUE S., LIU J., CHEUN CH.Y., CHANG W., HIRSCH J.D., BEECHEM J.M., HAUGLAND R.P., HAUGLAND R.P., J. Histochem. Cytochem., 51 (2003), 1699.
[5] PARC Y.S., CHOI Y.CH., KIM K.S., CHUNG D.CH., BAE D.J., AN K.H., LIM S.CH., ZHU X.Y., LEE Y.H., Carbon, 39 (2001), 655.
[6] COLOMER J.F., PIEDIGROSSO P., FONSECA A., NAGY J.B., Synth. Metals, 103 (1999), 2482.
[7] CHEN H., CHEN Y., WILLIAMS J.S., Proc. 1st Nanomaterials Conference, Research School of Physical Sciences and Engineering, The Australian National University, Canberra 2000, Australia.
[8] PSUJA P., HRENIAK D., STRĘK W., Photonics and Microsystems, International Students and Young Scientists Workshop, June 2006, pp. 50–54.
[9] QIU F., PU, X., LI J., LIU X., PAN Y., GUO J., Ceramics Int., 31 (2005), 663.
[10] XIA G., ZHOU S., ZHANG J., WANG S., XU J., J. Alloys Comp., 421 (2006), 294.
[11] XIA G., ZHOU S., ZHANG J., XU J., J. Crystal Growth, 279 (2005), 357.

Received 28 April 2007
Revised 16 February 2008

Materials Science-Poland, Vol. 26, No. 1, 2008

SIMS depth profiling of thin boron nitride insulating films

M. CWIL[1,2*], P. FIREK[3], P. KONARSKI[1], A. WERBOWY[3]

[1]Tele&Radio Research Institute, ul. Ratuszowa 11, 03-450 Warsaw, Poland

[2]Faculty of Physics, Warsaw University of Technology, ul. Koszykowa 75, 00-662 Warsaw, Poland

[3]Institute of Microelectronics and Optoelectronics,
Warsaw University of Technology, ul. Koszykowa 75, 00-662 Warsaw, Poland

Secondary ion mass spectrometry (SIMS) has been used to determine depth profiles of thin boron nitride films adapted as insulators in metal–insulator–semiconductor (MIS) devices. The negative secondary ion detection has been chosen to overcome the sample surface charging due to Ar^+ primary ion beam bombardment and to determine the elemental distribution without an electron flood gun treatment. Thin boron nitride films of 20–200 nm thickness were obtained by the radiofrequency plasma-assisted chemical vapour deposition method on Si-substrate with various flows of the gas source. The effect of silicon diffusion from the substrate into the insulator on nitrogen detection due to multiply charged Si ion mass interferences is observed. In order to entirely eliminate the silicon contribution to nitrogen signal in SIMS, we propose to produce BN film on two substrates (e.g., Si and GaAs) simultaneously and then to determine the nitrogen profile. The data obtained for MIS devices formed by covering the BN film with Al layer reveal also Al presence in the insulating film.

Key words: *SIMS; boron nitride; depth profiling; charging effects*

1. Introduction

Due to wide band gap, good chemical inertness, thermal stability and conductivity as well as enhanced hardness, cubic boron nitride (c-BN) is suitable for numerous potential applications. These cover such areas as high-temperature and high-power electronics, UV (including deep UV) detection, and light emitting devices or structures intended to work in chemically harsh environments [1–3]. However, recently the most promising applications of this material are wear resistant coatings and electrical insulation for metal–insulator–semiconductor (MIS) devices [4–6].

[*]Corresponding author, e-mail: cwil@if.pw.edu.pl

In this paper, secondary ion mass spectrometry (SIMS) study is presented of thin insulating boron nitride films (20–200 nm thick), deposited on Si or GaAs substrates using the plasma method. However, the interpretation of SIMS data is not straightforward in the presence of surface contaminations and matrix effects in which the sputtered ion yield depends strongly on the local film chemistry. The picture is further complicated by a factor, characteristic of insulating materials, limiting the secondary ion emission (often the secondary ion signal is eliminated entirely; this is not the case here) induced by net electric field at the sample surface produced by charged beam bombarding. This effect strongly depends on the penetration depth of primary ions as well as on the resistivity of the investigated layer and its thickness.

The observed features of the SIMS profiles have been discussed in terms of common mass interferences, matrix dependence and charging of nonconductive films during Ar^+ beam sputtering. Boron, nitrogen and silicon depth profiling have been discussed in detail as well as distribution of contaminations in the examined structures. Investigations of the BN gate insulator of complete MIS devices, accomplished by covering the BN/Si structure with an Al-layer provide additional information on factors disturbing the depth profile due to aluminum and silicon diffusion into the BN film.

2. Experimental details

Boron nitride films were produced on p-type Si (conductivity σ = 6–8 Ω·cm) or monocrystalline GaAs <100> oriented substrates using the radio frequency (RF) plasma-assisted chemical vapour deposition (PACVD) method [7–9]. The substrates were used to test technological parameters of the boron nitride material. Insulating layers were synthesized from $(C_2H_5)_3B$ vapours carried by nitrogen (2 cm^3/min or 3 cm^3/min). Complete MIS devices with boron nitride playing the role of the insulator were obtained by means of vacuum evaporation of round Al gate electrodes (1 mm in diameter).

The thicknesses of the formed layers were evaluated by ellipsometry measurements and confirmed also by the sputtering rate and the depth of the eroded craters after SIMS analysis using a Tencor α-step 100 profilometer. The thicknesses of thin BN films were in the range of 20–200 nm, while those of the cover Al-layers were ca. 100–500 nm, depending on the evaporation time.

The SIMS measurements have been performed using an SAJW-05 instrument with a low energy (5 keV) Ar^+ beam of ca. 100 μm in diameter at 45° to the normal of the sample surface. The apparatus was equipped with a 16 mm Balzers quadrupole mass spectrometer and Physical Electronics argon ion gun.

3. Results and discussion

In this section, the influence of positively charged Ar^+ ion beam on the sputtering process of the nonconductive boron nitride films will be discussed. The charge build-

up effect for positive secondary ion sputtering is shown in Fig. 1. The distributions of positive $^{11}B^{+}$, $^{16}O^{+}$, $^{28}Si^{+}$ secondary ions show that after eroding 180 nm of the whole BN film, the sample charging disappeared. This indicates that the BN films with thicknesses lower than about 20 nm are not affected by charge build-up effects during both positive and negative SIMS characterization. Moreover, the sample charging effect is not so strong and does not move the energy distribution totally out of the energy window of the mass analyzer with the result that some positive secondary ions are detected. The ion intensities increase with the sputter time (depth) meaning that the sample charge disappears in thinner insulating films. In order to eliminate such effects during depth profiling, one can either apply neutralization of accumulating charge by electron bombardment [10] or perform negative secondary ion analysis [11]. For the negative ion detection such an effect does not work since negative ions can migrate through a positive electric field.

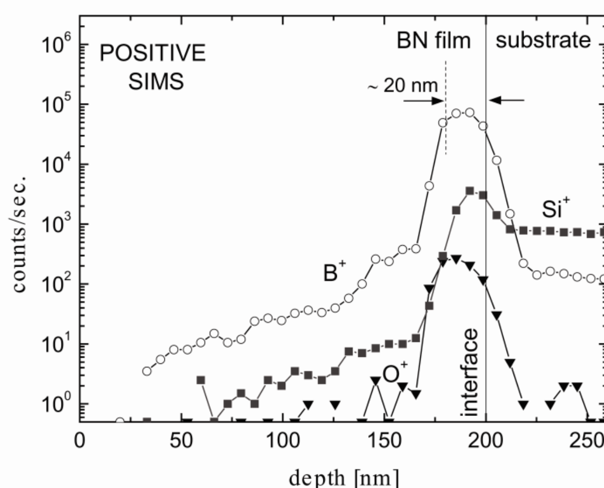

Fig. 1. Surface charging of the BN film during positive analysis of secondary ions: $^{11}B^{+}$, $^{16}O^{+}$ and $^{28}Si^{+}$

We focus on the investigation of BN films with the use of negative SIMS detection. We compare the depth profiles of two BN films (180 and 200 nm thick) deposited on a Si substrate at various flows of the gas source $(C_2H_5)_3B$ (2 cm^3/min – sample #1 and 3 cm^3/min – sample #2) to test nitrogen and boron incorporation into the film. This is shown in Fig. 2, where selected negative secondary ion signals are plotted in function of depth. The results show that the BN films and the BN/Si interface regions are highly oxidized, but in the case of sample #1, the effect is clearly visible which might worsen dielectric properties of a MIS device based on such a BN film. The thickness of the oxide layer at the substrate (BN/Si interface) is about 30 nm. Thus, surface charging for positive secondary ion analysis (Fig. 1) after partial recovery of the BN film might be less effective due to the much lower resistivity of the material closer to

the BN/Si interface. However the presence of oxygen in the sputtering film increases the secondary ion yields, especially metals. In Figure 2, the secondary B^- intensity depends strongly on the oxygen distribution in the BN film that results in identical shapes of B and O profiles due to the so called matrix effects. Nitrogen is located in the interface region in the case of sample #1 and is rather more homogeneously distributed in the BN film of sample #2. Electrical measurements of complete MIS structures have shown better properties (higher resistivities) of the device based on the BN insulator fabricated at the gas flow of 3 cm^3/min (sample #2).

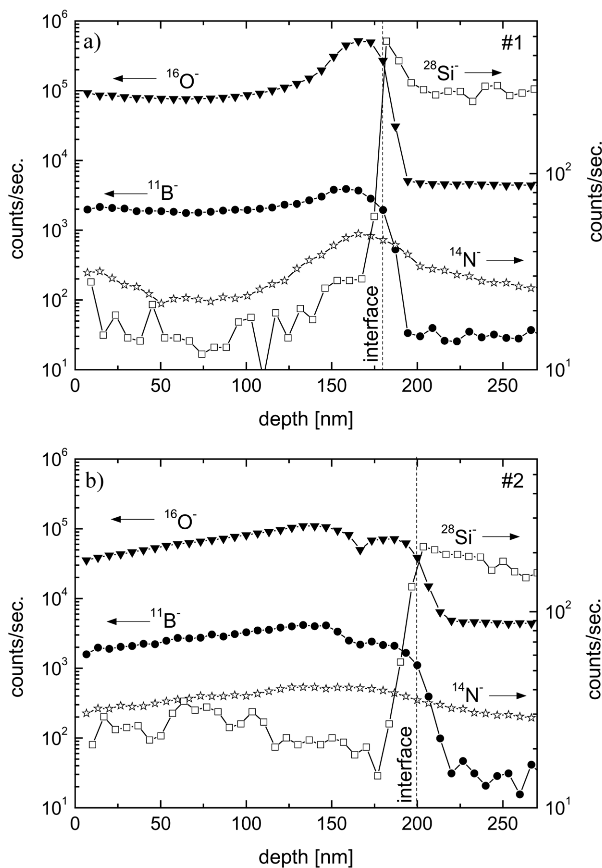

Fig. 2. Negative SIMS depth profiles of the boron nitride films deposited on Si-substrate using various source gas flows: a) 2 cm^3/min, b) 3 cm^3/min

In view of the fact that $^{28}Si^{2-}$ ion has the same mass to charge ratio as $^{14}N^-$ ion (also single-ionized molecule with two ^{14}N atoms has the same mass to charge ratio as $^{28}Si^-$; the ratio is 28 in both cases), the distribution of nitrogen can be overestimated, when silicon diffusion into the BN film is not excluded during BN film deposition. Selected mass interferences in SIMS analysis of the Al/BN/Si structures are shown in Table 1.

Table 1. Selected mass interferences in SIMS analysis of the Al/BN/Si structures

Ion mass [a.m.u.]	Ion
14	^{14}N, $^{28}Si^{2+/-}$, CH_2
28	$^{14}N_2$, ^{28}Si, C_2H_4
29	^{29}Si, $^{10}B^{19}F$
30	^{30}Si, $^{11}B^{19}F$
25	$^{11}B^{14}N$, C_2H
26	CN, ^{10}BO
38	$^{11}B_2O$, $Al^{11}B$
36	C_3, $^{11}B_2N$
43	AlO, $^{11}BO_2$

In order to completely eliminate multiple charged Si ion mass interference on nitrogen monitoring (especially in the interface region), the depth profiles of BN films deposited simultaneously on Si or on GaAs substrates have been determined.

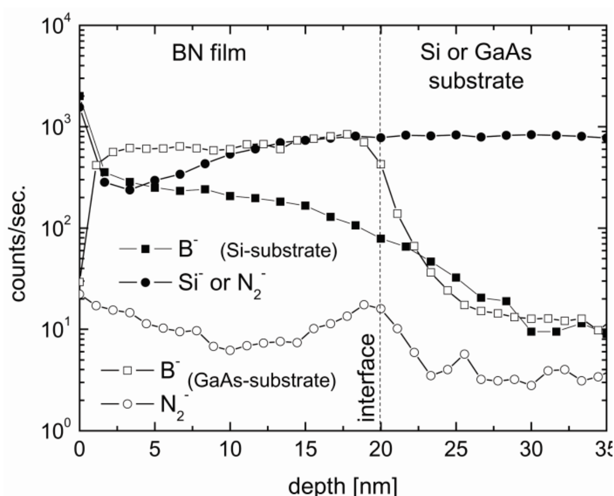

Fig. 3. Negative SIMS depth profiling of the BN films deposited on Si (full symbols) and GaAs (open symbols) substrates

Figure 3 gives an example of depth profiles for a thin 20 nm thick BN film on Si substrate compared with the depth profile of a thin BN film (the same thickness) deposited on GaAs substrate. We present negative SIMS analysis of $^{11}B^-$ and secondary ion intensities with mass equal 28 a.m.u. ($^{14}N_2^-$ and $^{28}Si^-$). The results show a remarkable difference in the ion signal measured for 28 a.m.u. species in films deposited at different substrates. These observations might indicate that Si diffuses into the BN film and leads to nitrogen signal overestimation in the BN/Si structure. We assume the same elemental concentration in both films, however there are some differences in

boron profiles and no differences in oxygen intensities (not shown in the figure). However, oxygen presence in the BN film can highly increase the emission of silicon (diffused from substrate) during SIMS sputtering.

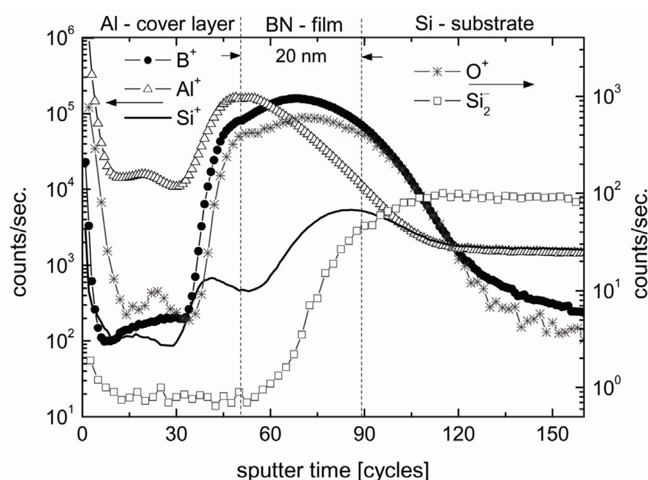

Fig. 4. Depth profiling of the Al/BN/Si MIS device based on a 20 nm thick insulating BN film

The depth profile taken for negative and positive SIMS of complete MIS devices based on thin BN film is shown in Fig. 4. We select the 20 nm thickness of the gate insulator to avoid charge accumulation during positive ion measurements, which are desirable for Al layer characterization. In addition, the positive SIMS analysis allows one to exclude numerous mass interferences observed for the negative analysis. The interface regions are highly oxidized (Fig. 4) resulting in the increase of $^{27}Al^+$ (at the Al/BN interface) and $^{28}Si^+$ (at the BN/Si interface) emissions. Moreover, aluminum and silicon diffuse into the insulator. Thus higher content of oxygen located at the interfaces enhanced secondary ion yields of Al and Si measured in these regions. The profile of negative Si_2^- illustrates that such molecular ions are relatively matrix insensitive and represents more realistic concentration of silicon in the Al/BN/Si structures.

4. Conclusions

We have discussed Ar^+ SIMS depth profiling of thin boron nitride insulating films created on Si substrates. Charge build-up effects of the sample surface have been observed for positive ion detection when thickness of the insulating film is higher than about 20 nm. Negative mode of SIMS is proposed for depth profiling of such materials without compensating beam treatment. The elemental depth profiling in the BN films shows that basic constituent monitoring is affected by matrix effects caused by oxygen contamination (boron recording) as well as by ion mass interferences due to

silicon diffusing from substrate (nitrogen recording). In order to find which of the features of the 14 a.m.u. species profile might be attributed to nitrogen, and which are due to Si diffusing from the substrate, the depth profiling should be derived from BN films deposited simultaneously on both Si and GaAs substrates. The study of complete MIS devices with Al electrodes in front of the BN insulators indicates also aluminum diffusion into the insulator.

Elemental depth profiling of BN films taking into consideration distribution of contaminations in the insulator or/and in the interface regions is a necessary step for achieving further progress in the MIS technology.

References

[1] *High-Temperature Electronics*, R. Kirschmann (Ed.), IEEE Press, Piscataway, 1999.

[2] GIELISSE P., *Wide Bandgap Materials in Future Electronic Applications*, Proc. of 24th International Conference IMAPS Poland, Rytro, 2000, p. 115.

[3] NOOR M.S., Solid-State Electr., 46 (2002), 203.

[4] CHORE S.M., CHAUDHARI G.N., MANORAMA S.V., BATH A., Semicond. Sci. Techn., 17 (2002), 1141.

[5] WERBOWY A., FIREK P., SZMIDT J., OLSZYNA A., GAŁĄZKA M., J. Wide Bandgap Mater., 9 (2002), 169.

[6] DUMONT H., BAYLE B., BONNETOT B., Phys. Stat. Sol. c, 0 (2003), 2470.

[7] MITURA S., J. Phys., 4 (1991), C2.

[8] HAŚ Z., MITURA S., CŁAPA M., SZMIDT J., Thin Solid Films, 136 (1986), 161.

[9] MITURA S., J. Crystal Growth, 80 (1987), 417.

[10] GUZMAN DE LA MATA B., DOWSETT M.G., MORRIS R.J.H., J. Vacuum Sci. Techn. A: Vacuum, Surfaces, and Films, 24 (2006), 953.

[11] CWIL M., KONARSKI P., BIENIEK T., BECK R.B., Phys. Stat. Sol. a, 203 (2006) 2200.

Received 28 April 2007
Revised 16 February 2008

Materials Science-Poland, Vol. 26, No. 1, 2008

Optical and electrical properties of TiO_2 doped with Tb and Pd

J. DOMARADZKI*, D. KACZMAREK, E. L. PROCIOW,
A. BORKOWSKA, T. BERLICKI, K. SIERADZKA

Faculty of Microsystem Electronics and Photonics, Wrocław University of Technology,
ul. Janiszewskiego 11/17, 50-372 Wrocław, Poland

Optical and electrical properties of TiO_2 doped with 0.6 at. % Tb and 9 at. % Pd have been investigated. Thin films were deposited by low pressure hot target reactive sputtering from a metallic Ti–Tb–Pd mosaic target on silicon and glass substrates. Total concentration of Tb and Pd was determined using an energy disperse spectrometer. Optical properties were studied by means of optical transmission. It has been shown that Tb dopant does not make any significant changes in the transmission level. Pd dopant shifts the fundamental absorption edge of TiO_2 towards longer wavelengths and decreases the transmission to about 40%. For electrical characterization of the prepared thin films, temperature dependent resistivity and current–voltage (*I–V*) characteristics have been examined. It has been shown that incorporation of Pd and Tb into TiO_2 matrix modifies its properties allowing one to obtain p-type oxide-semiconductor electrically and optically active at room temperature. Additionally, based on *I–V* measurements, the formation of heterojunction at the interface of thin film–silicon was confirmed.

Key words: *terbium; palladium; TiO_2; thin films; transparent oxide semiconductor*

1. Introduction

Transparent oxide semiconductors (TOS) with n- and p-type electrical conduction are of great interest due to fabrication of transparent junction-based devices [1–3]. To form a p–n junction transparent for visible light, oxide semiconductors with band gap wider than 3 eV are needed. A major difficulty in the fabrication of fully functional transparent oxide-based devices is still low electrical performance of TOS. Therefore the development of methods for modification of electrical properties of thin oxide films is of great importance. Another important issue is integration of various TOSs with a standard silicon technology.

*Corresponding author, e-mail: jaroslaw.domaradzki@pwr.wroc.pl

Our previous studies have shown that doping of titanium dioxide, as a base oxide, with various transition and noble metals could modify its certain properties [4]. For example, doping with Pd allows a p-type oxide semiconductor to be obtained [5]. Recently TiO_2 has been reported to be used as a host matrix for various rare earth elements, i.e. Tb [6, 7]. In this paper, optical and electrical properties of TiO_2 doped with Tb and Pd have been described.

2. Experimental procedure

Thin films of TiO_2:(Tb, Pd) were prepared by the low pressure hot target reactive sputtering (LP HTRS) method from metallic Ti–Tb–Pd mosaic target and deposited on silicon and glass substrates. The sputtering process was carried out under low pressure (< 0.1 Pa) of pure oxygen as a working gas and with the additionally heated target (hot target). Optical properties of TiO_2:(Tb, Pd) thin films were studied by means of optical transmission in the spectral range from 250 nm to 1100 nm. Measurements of direct current (d.c.) electrical resistivity (ρ_{dc}) were done using the standard four-point probe method in a temperature range from 300 K to 900 K. Current–voltage (*I–V*) measurements have been performed at room temperature using an electrical characterization system based on a Keithley's 2000 multimeter and 6517A electrometer.

3. Results and discussion

Tb and Pd contents in TiO_2:(Tb, Pd) thin films determined with the energy disperse spectrometer (EDS) amount to ca. 0.6 at. % and 9 at. %, respectively. EDS spectrum of TiO_2:(Tb, Pd) thin film on silicon is shown in Fig. 1. The detected Si signal, visible in the spectra, is due to the substrate.

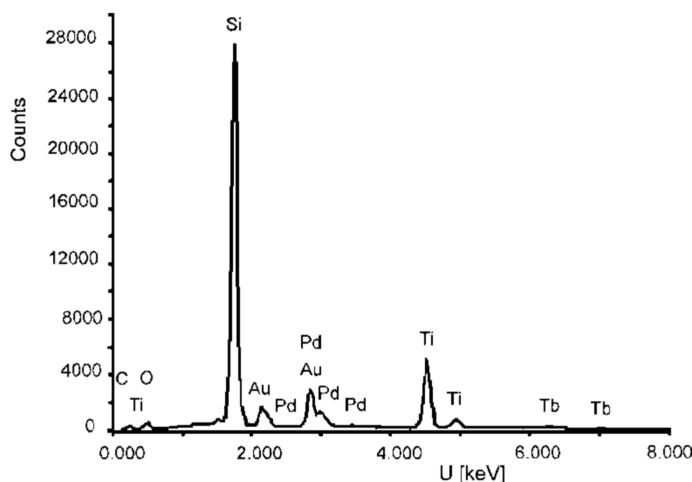

Fig. 1. EDS spectrum of TiO_2:(Tb, Pd) thin films on silicon

Optical transmission characteristics of undoped TiO_2, TiO_2:Tb (0.4 at. %) and TiO_2:(Tb, Pd) thin films are shown in Fig. 2. It has been shown that Tb dopant does not cause any significant changes in the transmission level as compared to pure TiO_2. Incorporation of Pd dopant shifts the position of the fundamental absorption edge (ca. 330 nm) toward longer wavelengths, with the transmission decreasing to about 40 % in the visible region.

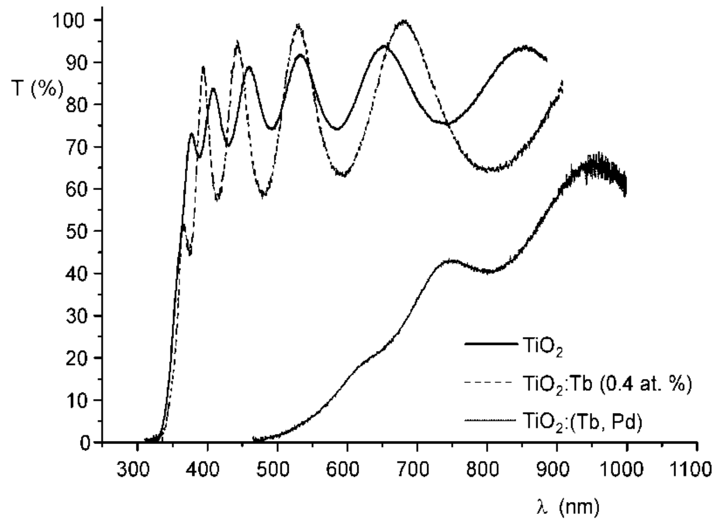

Fig. 2. Optical transmission spectra of undoped TiO_2, TiO_2:Tb (0.4 at. %) and TiO_2:(Tb, Pd) thin films on SiO_2

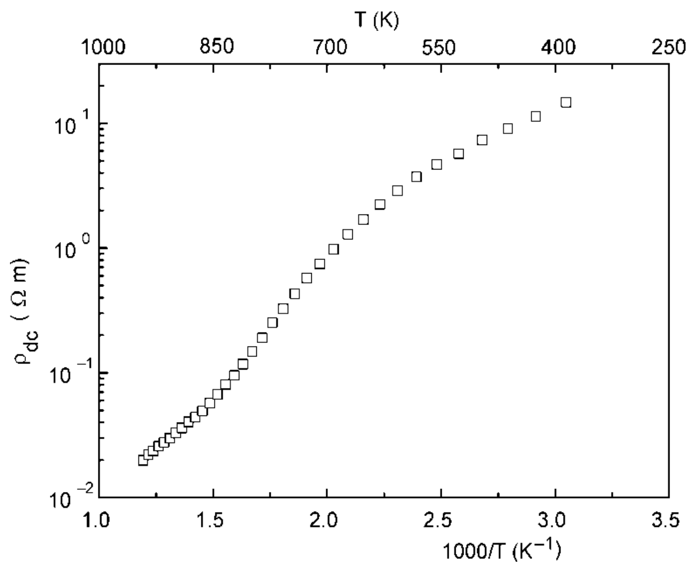

Fig. 3. Dependence of d.c. resistivity of TiO_2:(Tb, Pd) thin films on temperature

Identification of charge transport phenomena requires experimental determination of the temperature dependent electrical resistivity (ρ_{dc}). Figure 3 shows the dependence of d.c. electrical resistivity on temperature of the prepared TiO_2:(Tb, Pd) thin films. A non-linear behaviour can be seen, indicating a complex mechanism of electrical conduction in the films. Thus, determination of the activation energy from the slope is difficult.

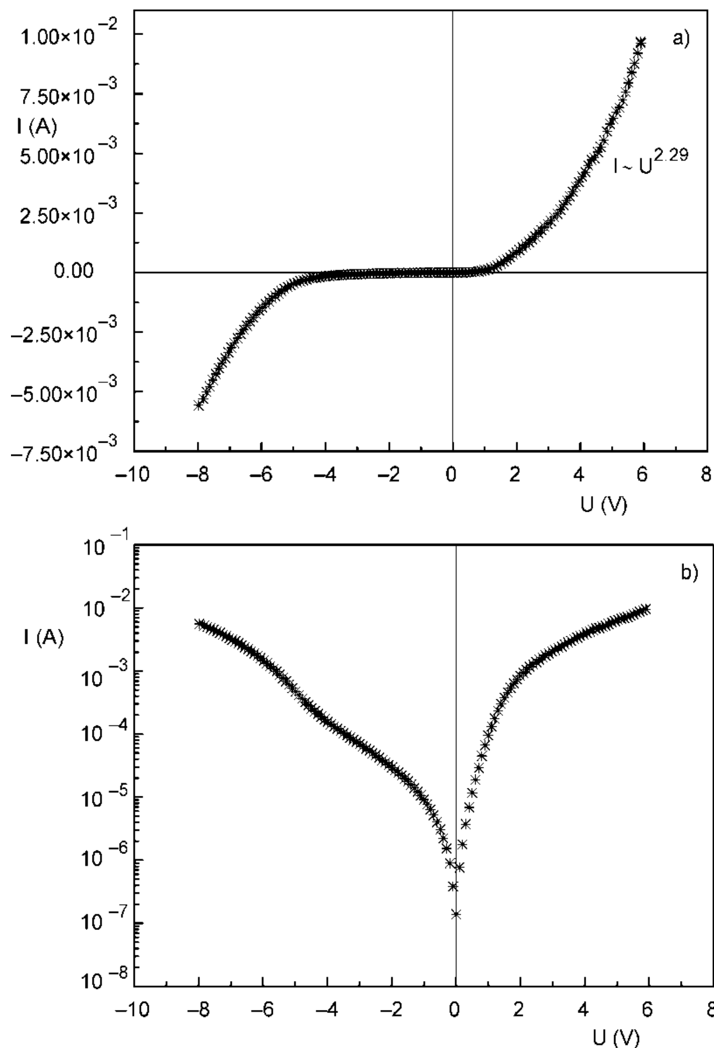

Fig. 4. *I–V* characteristics of TiO_2:(Tb, Pd) thin films on silicon recorded at 300 K: a) linear scale and b) semi-logarithmic co-ordinate system

I–V characteristics of the p-type semiconducting TiO_2:(Tb, Pd) thin films as deposited on p-type silicon recorded at 300 K are presented in Fig. 4. A strong non-linear

(diode like) behaviour could be observed in Fig. 4a. The current flowing in the forward direction exhibits the power dependence on the applied voltage ($I \sim U^{2.29}$) which suggests the space charge limited current (SCLC) mechanism of charge transport in the examined structure. SCLC conduction is often observed in materials with low concentration of thermally generated carriers. From the shape of the characteristic, shown in a semi-logarithmic co-ordinate system (Fig. 4b), the presence of strong depletion for backward biased structure ($U < 0$ applied to silicon substrate) at the prepared heterojunction is clearly seen.

4. Conclusions

Optical and electrical properties of TiO_2 doped with Tb and Pd have been presented. It was shown that incorporation of Pd and Tb dopants into TiO_2 matrix modified its properties; a p-type oxide-semiconductor electrically active at room temperature was obtained, although the transparency to visible light was decreased.

I–V characteristics showed a strong diode like behaviour depending on the direction of current flow and revealed a space charge limited current (SCLC) conduction mechanism in the forward biased structure. The obtained results indicate that it is possible to apply TiO_2:(Tb, Pd) thin films to fabricate integrated TOS–Si microstructures.

Acknowledgement

This work was financed from the sources granted by the Department of Scientific Research for science development in the years 2006-2008 as a research project and from the statute sources of the Polish Ministry of Science and Education.

References

[1] TONOOKA K., BANDO H., AIURA Y., Thin Solid Films, 445 (2003), 327.
[2] CARCIA P.F., MCLEAN R.S., *Transparent Oxide Semiconductor Thin Films Transistors*, PCT U.S. Patent WO 2004/034449 A2, April 22, 2004.
[3] DOMARADZKI J., J. Non-Cryst. Solids, 352 (2006), 2328.
[4] DOMARADZKI J., BORKOWSKA A., KACZMAREK D., PROCIOW E., J. Non-Cryst. Solids, 352 (2006), 2324.
[5] DOMARADZKI J., Thin Solid Films, 497 (2006), 243.
[6] JIA Ch., XIE E., PENG A., JIANG R., YE F., LIN H., XU T., Thin Solid Films, 496 (2006), 555.
[7] MOON B.K., JEONG J.H., YI S.-S., KIM S.C., CHOI H., KIM J.H., Optical Materials, 28 (2006), 676.

Received 28 April 2007
Revised 16 February 2008

Materials Science-Poland, Vol. 26, No. 1, 2008

Comparative X-ray investigation of Ni/Cu systems heated in the 250–350 °C temperature range

B. GĄGOROWSKA[1*], B. KUCHARSKA[2], M. DUŚ-SITEK[1], A. TOKARZ[2]

[1]Częstochowa University of Technology, Faculty of Materials Processing Technology and Applied Physics, Institute of Physics, al. Armii Krajowej 19, 42-200 Częstochowa, Poland

[2]Częstochowa University of Technology, Faculty of Materials Processing Technology and Applied Physics, Institute of Material Engineering, al. Armii Krajowej 19, 42-200 Częstochowa, Poland

Results of investigation of structural properties of Cu/Ni multilayers have been presented. Samples were obtained by the electrochemical method and after deposition they were heated from 250 ºC to 350 ºC. The increase of the heating temperature and of the Cu thickness in multilayers caused a decrease of intensities of peaks corresponding to (111) planes. The phenomenon results from the formation of a solid solution in the interfaces. Heating of multilayers in the investigated temperature range resulted in the increase of tensile stresses in external layers and of compressive stresses in substrate adjacent layers.

Key words: *multilayers; electrochemical method; solid solution; tensile stress; compressive stress*

1. Introduction

For last few years, systems of thin metallic multilayers have been often used in magnetic recording and reading. In order to achieve a higher density of information packing, what is followed by smaller size of indicators, multilayers' borders contribute in the whole volume of the multilayer system. Therefore, the physical state of an interface has a significant effect on electric, magnetic and structural properties of the whole system. The multilayer systems of transition metals may be used as magnetoresistential or hallotronic indicators of magnetic field [1].

The aim of this paper was to compare properties of Ni/Cu multilayer systems heated in the 250–350 ºC temperature range, concerning the change of interplanar d_{111} and d_{200} distances for various thicknesses of the systems of monolayers heated at various temperatures.

*Corresponding author, e-mail: b.gagorowska@op.pl

The results are a part of investigations of Ni/Cu systems in terms of their structural, magnetic and emissive properties. With regard to magnetic properties, the multilayers were heated in the passed higher range of temperatures (heating up of these systems probably will change coupling from antyferromagnetically in ferromagnetically [2]).

2. Experimental

Single-crystalline n-type silicon (100) oriented wafers (Sb doped, $\rho = 0.017\ \Omega\cdot m$) were used as substrates for deposition. The thickness of the Si substrate was 280 ± 25 μm. Before the main process, it was suitably treated, rinsed in detergent and acetone and activated in 10% HF.

A mixture of 1.5 mol $Ni(SO_3NH_2)_2$, 0.01 mol $CuSO_4$ and 0.5 mol H_3BO_3, at 20 °C and pH equal to 3.5 was used to deposit Ni/Cu multilayers. The deposition potential for Cu layers was equal to –500 mV and for Ni layers –900 mV. The systems consisted of 100 double layers deposited in the form of circles of ca. 1 cm in diameter; Ni layers were 20 Å thick and the thicknesses of Cu layers were 8, 9, 18 or 19 Å. The thickness of a layer was estimated using the charge flow during electrochemical deposition. All electrochemical experiments and deposition processes were carried out in a standard three-electrode electrochemical cell equipped with a platinum net as a counter electrode and a saturated calomel electrode (SCE) as a reference electrode. More details relating to the electrochemical method of deposition have been described elsewhere [3–5]. Based on the literature [4–6], it was assumed that the layers of the Ni/Cu systems are continuous ones.

The multilayer systems were investigated after deposition and after heating for 1 h under the 10^{-6} Pa vacuum at 250, 300 and 350 °C. After heating, the multilayers and the furnace were cooled simultaneously. Structural changes which appeared during heating were studied by the X-ray diffraction method performed on a Seifert 3003TT diffractometer with the use of filtered CoK_α radiation in the 45–64° angle range. All X-ray measurements were made under the same, allowing direct comparison of diffractograms.

3. Results and discussion

The X-ray analysis revealed that inside the applied angle range the (111) and (200) reflexes arising from Cu and Ni, respectively, were present. The proximity of diffraction peaks ((111) for Cu and Ni, and (200) for Cu and Ni) did not allow one to separate these peaks under measurement conditions.

An insignificant broadening and increase of peak intensities was observed. The recorded peaks were characterized by small half-widths, high maximum intensities

and precise symmetries in relation to the axis determining the angular position of the analyzed maximum (Fig. 1); no attempts were made to separate them.

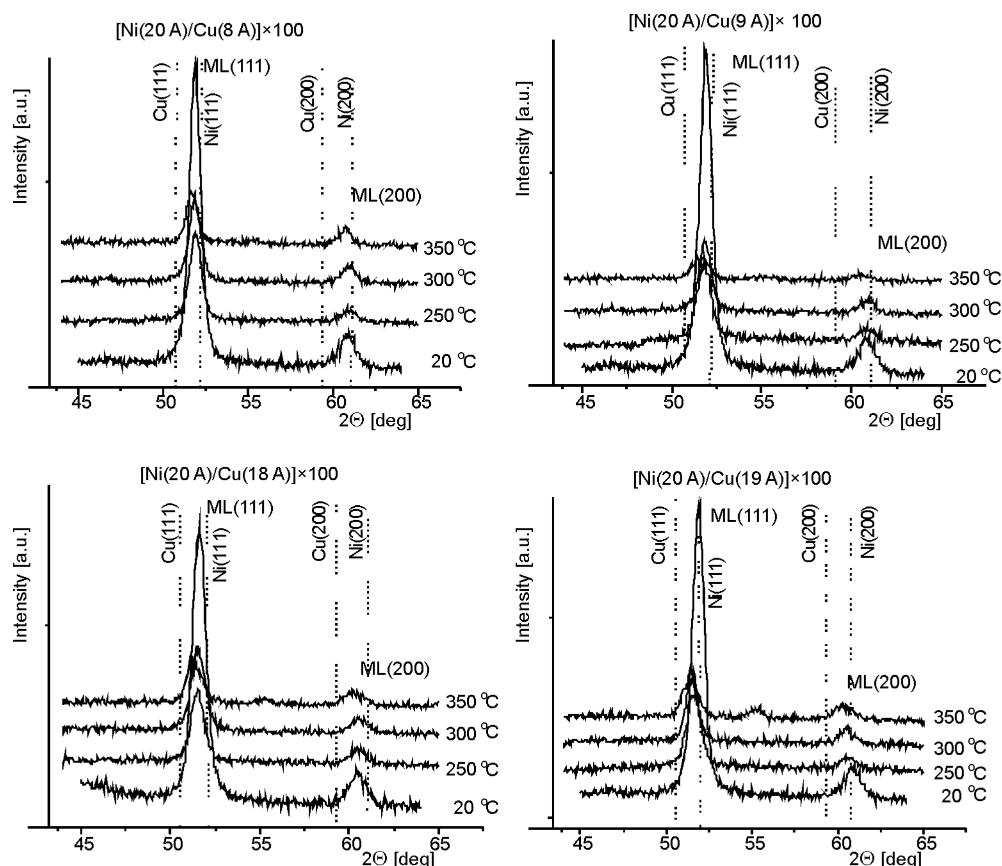

Fig. 1. Diffractograms of Ni/Cu multilayers (d_{Ni} = 20 Å, d_{Cu} = 8, 9, 18 and 19 Å) before and after heating

From the comparison of (111) reflexes for multilayers with Cu thicknesses equal to 8 Å and 1.8 Å, it was confirmed that the applied proportions of the thicknesses of multilayers did not cause any changes in the integral intensity of the reflex, resulting, however, in its shift. In the $Ni_2Cu_{0.8}$ multilayer with an excess of Ni, the maximum of the reflex is shifted towards the position characteristic of pure Ni with respect to the same reflex measured in the $Ni_2Cu_{1.8}$ containing approximately equal proportions of both elements (cf. Fig. 2). It was found that relative intensity of reflex (111) strongly decreases upon increasing temperature of heated multilayers. In as-obtained multilayers, the relative intensity of the (200) reflex is very low, and only in multilayers heated at 350 °C it approaches standard intensities of Cu and Ni ($I_{(111)}$100% : $I_{(200)}$46/42%).

Using the Bragg equation, the values of interplanar distances have been calculated. The results of investigation have been compared with those obtained for multilayers which were not heated (Figs. 3 and 4).

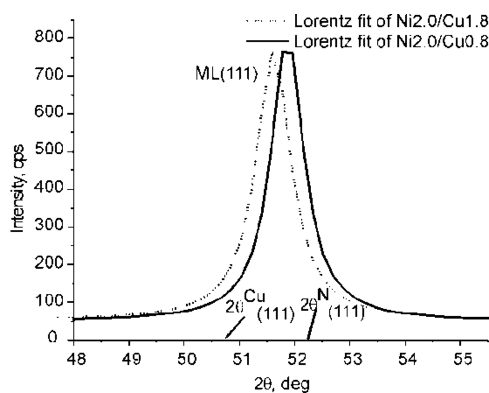

Fig. 2. Lorentz fit for diffractograms of Ni/Cu multilayers (d_{Ni} = 20 Å, d_{Cu} = 8 and 18 Å) for the peak (111)

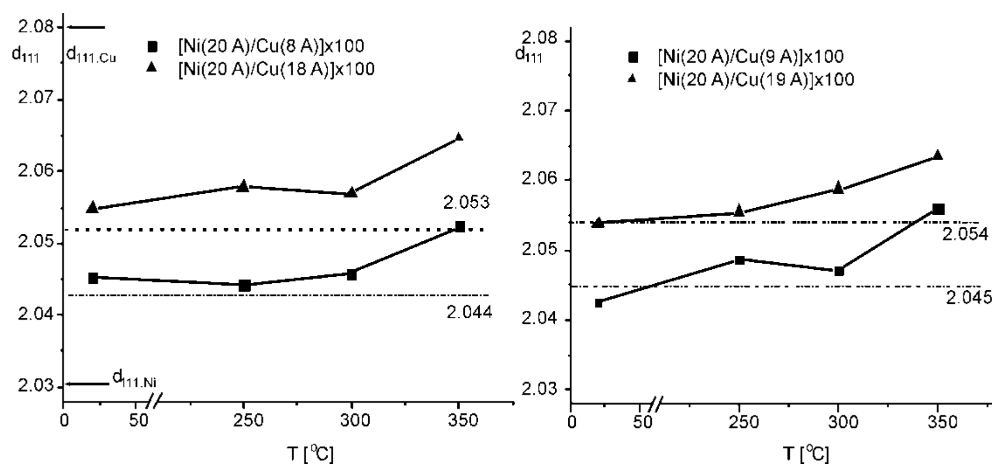

Fig. 3. Experimental d_{111} values for Ni/Cu multilayers (dotted lines show average $d_{111(Cu+Ni)}$ calculated for a given thickness of sublayers)

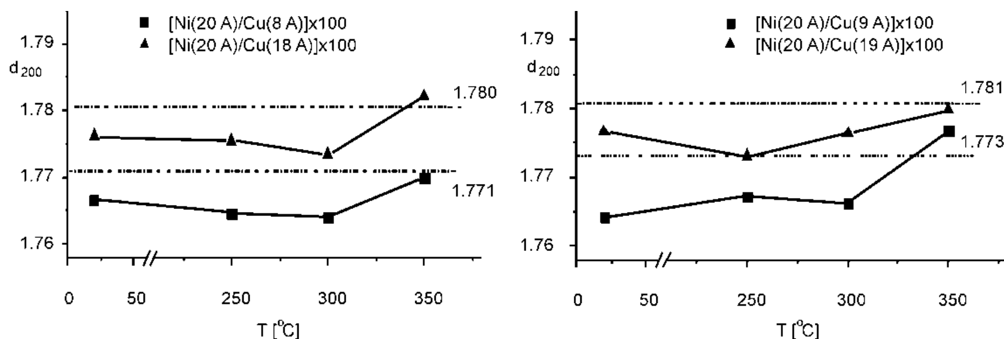

Fig. 4. Experimental d_{200} values for Ni/Cu multilayers (dotted lines show average $d_{111(Cu+Ni)}$ calculated for a given thickness of sublayers)

The trends of changes of interplanar distances in multilayers, independent of Cu and Ni contributions have been observed. In Figures 2 and 3, the interplanar distances

are given for the alloy obtained by the traditional method; it forms a solid solution in which the mass contribution of components corresponds to that in multilayers (dotted line). The calculated interplanar distances for diffractions arising from (111) and (200) planes of these systems are also shown. They are presented taking into account changes of a nonmagnetic spacer. The mass contribution of components was calculated based on the layer thicknesses determined from measurements of the charge during electrochemical deposition.

Comparison of interplanar distances determined by diffractometric measurements with those calculated for a theoretical continuous solid solution shows that experimental d_{111} values for multilayers are higher, while the experimental d_{200} values are lower than the theoretical ones.

The observed changes of interplanar distances and of relative intensities of observed diffractions, and their broadening may result from:

- formation of solid solutions, especially in border regions of sublayers (interfaces),
- kind, structure and thickness of interfaces,
- presence of stresses in multilayer planes, especially in the border regions.

Moreover, as is shown in Fig. 3, the interplanar distances connected with (111) reflexes increase upon increasing temperature. For initial, unheated system (d_{Cu} = 8 and 18 Å), the d_{111} distances were 2.045 Å and 2.055 Å, respectively. After heating at 350 °C, the d_{111} values for these multilayers increase to 2.052 Å and 2.065 Å, respectively. A similar trend was observed in multilayers with d_{Cu} = 9 and 1.9 Å.

The analysis of the interplanar distances connected with the (200) reflexes does not indicate their distinct increase with temperature. Up to 300 °C, the d_{200} values decrease, and only after heating at 350 °C they increase up to the theoretical value (Fig. 4). For all multilayers, the intervals between points representing d values for 250 and 350 °C have a nearly identical slope. A deviation from linearity occurs for 300 °C, when first cracks in the multilayers were observed [7]. This may suggest that the similarity of structures explains the facility of formation of solid solutions. A factor limiting formation of solid solution is rather the number of atoms replaced by atoms of the other metal, and not their weights. The most probable is the formation of a substitutional solid solution in which replacement of atoms by other ones occurs [8]. After Goldschmidt [9], the substitutional solutions may by present only in the case when the radii of one kind of atoms do not differ from the radii of the other ones more than 15%; in the case of the investigated multilayer $\Delta r \approx 3\%$. Since the system analyzed in this work consists of multilayers of nanometric dimensions, one cannot rule out that some atoms may occupy interstitial positions, or statistically disordered or nonstoichiometric systems may be present in border regions. The additional diffraction maximum obtained for various thicknesses of Cu heated only at 350 ° C (Fig. 5) confirms probability of formation of solid solution.

The intensity of additional maxima increases with the thickness of the nonmagnetic spacer (Fig. 5). It is possible that in solid solutions stable over wide range of compositions (during homogenization), some superstructures may be present. Their forma-

tion involves creation of a certain state of atom ordering in a statistically disordered solid solution; in the ordered state, both Cu and Ni atoms occupy given lattice sites in the crystal lattice. It is known that such superstructures cause the appearance of new interferences in the diffraction pattern arising from lattice planes for which at a statistically disordered distribution of atoms the structure factor was equal to zero.

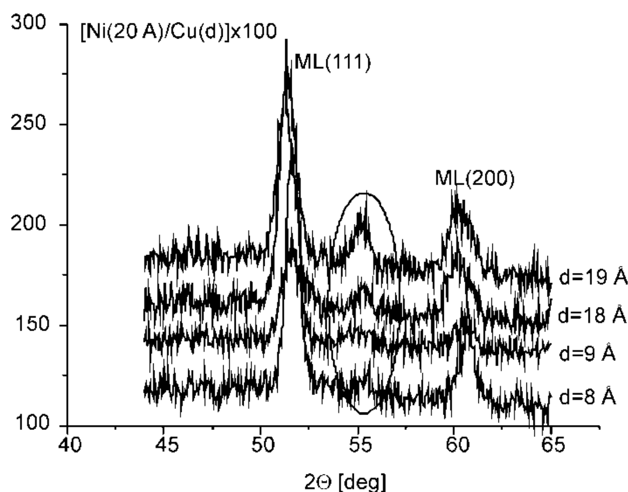

Fig. 5. Diffraction patterns for Ni/Cu systems (d_{Cu} =8, 9, 18 and 19 Å), heated at 350 ºC

The analysis of changes of d values in function of heating temperature (Fig. 5) allows one to suggest that the resultant tensile stresses in (111) planes increase during heating, whereas in (200) planes they are compressive transforming into tensile ones above 300º C. One cannot also exclude the fact that the lowering of d_{200} value results from the formation of a solid solution based on nickel. Therefore, it may be assumed that increase of stresses resulting from the thermal expansion of multilayers most strongly influences the increase of interplanar distances and that the deviations from the linearity at 300 ºC arise from a relaxation of stresses as a result of cracks [7]. A simultaneous formation of solid solution is confirmed by changes of relative intensities of reflexes.

4. Conclusions

The Ni/Cu multilayers of the Ni layer thickness 20 Å and the Cu layer thickness 8, 9, 18 and 19 Å deposited by electrochemical method on Si(100) substrate are thermally stable up to 250 ºC [2]. At 350 ºC the multilayers undergo a total deformation and exfoliation from the substrate. The interplanar distances of multilayers differ from interplanar distances in conventional alloys of identical compositions; d_{111} distances are higher and d_{200} are lower than in the alloy.

Heating of multilayers between 250 ºC and 300 ºC results in an increase of tensile stresses in external layers and increase of compressive stresses in layers adjacent to the substrate. The cracks of a multilayer at 300 ºC cause decrease of stresses, while upon heating at 350 ºC, only tensile stresses occur as a result of the loss of adhesion to the silicon substrate; due to these tensile stresses the coating undergoes a deformation. As a result of heating of multilayers in the 250–350 °C range, Ni/Cu solid solutions are formed causing a favoured (111) orientation.

References

[1] BARSHILIA C.H., RAJAM K.S., Surface Coating Techn., 155 (2002) 195.

[2] JIMBO M., KARIYA T., IMADA R., FUJIWARA Y., TSUNASHIMA S., J. Magn. Magn. Mater., 165 (1997) 304.

[3] TOKARZ A., NITKIEWICZ Z., WOLKENBERG A., Electr. Techn. Int. J., 35 (2003), 1.

[4] TOKARZ A., Polish J. Appl. Chem., 49 (2005), 283.

[5] TOKARZ A., FRĄCZEK T., BAŁAGA Z., NITKIEWICZ Z., Rev. Adv. Mater. Sci., 15 (2007), 247.

[6] TOKARZ A., STOKŁOSA H., *Application of the SEM Technique In Examination of Cross-Sections of Cu/Ni, Cu/Co and NiFe/Cu Multilayers Deposited Electrolytically* (in Polish), Wyd. Politechniki Częstochowskiej WIPMiFS, ser. Metalurgia, Częstochowa 2006, pp. 551–554.

[7] GĄGOROWSKA B., DUŚ-SITEK M., KUCHARSKA B., TOKARZ A., *Effect of Annealing on the Stability of CuNi Multilayers* (in Polish), Wyd. Politechniki Częstochowskiej WIPMiFS, seria Metalurgia, Częstochowa 2007 (in press).

[8] KANAK J., STOBIECKI T., WIŚNIOWSKI P., GŁADYSZEWSKI G., MAASS W., SZYMAŃSKI B., J. Magn. Magn. Mater., 239 (2002), 329.

[9] AZAROFF L.V., *Struktura i właściwości ciał stałych*, PWN, Warszawa, 1960, pp. 97–428 (In Polish).

Received 28 April 2007
Revised 16 February 2008

Materials Science-Poland, Vol. 26, No. 1, 2008

Anisotropic strain relaxation and surface morphology related to asymmetry in the formation of misfit dislocations in InGaAs/GaAs heterostructures

Ł. GELCZUK[1*], M. DĄBROWSKA-SZATA[1], J. SERAFIŃCZUK[1], A. MASALSKA[1], E. ŁUSAKOWSKA[2], P. DŁUŻEWSKI[2]

[1]Faculty of Microsystem Electronics and Photonics, Wrocław University of Technology, ul. Janiszewskiego 11/17, 50-372 Wrocław, Poland

[2]Institute of Physics, Polish Academy of Sciences, al. Lotników 32/46, 02-668 Warsaw, Poland

Partially relaxed InGaAs/GaAs heterostructures with a small lattice mismatch (less than 1%), grown by metalorganic vapour-phase epitaxy have been studied by the transmission electron microscopy, atomic force microscopy as well as X-ray diffractometry. A regular network of 60° misfit dislocations formed at the (001) interface in two orthogonal ⟨110⟩ crystallographic directions has been revealed. A close correspondence between distribution of the interfacial misfit dislocations and undulating surface morphology in the form of a characteristic cross-hatch pattern has been observed. The structural analysis applied for the samples oriented either in $[\bar{1}10]$ or [110] perpendicular directions, using reciprocal lattice mapping, revealed anisotropic strain relaxation, related to the asymmetry in the formation of α and β misfit dislocations along these both directions, respectively.

Key words: *misfit dislocation; strain relaxation; surface morphology; semiconductor heterostructure; InGaAs*

1. Introduction

Lattice mismatched InGaAs/GaAs heterostructures have found a wide range of technological applications in many novel optoelectronic and electronic devices. Investigations of such systems with a small lattice mismatch can be very instructive because they provide an invaluable information for understanding dislocation related strain relaxation mechanisms [1]. An elastic strain in epitaxial layers, resulting from a difference in lattice parameters between the substrate and the layer, can be released by the formation of misfit dislocations at the interface and their glide, provided that the layer

*Corresponding author, e-mail: lukasz.gelczuk@pwr.wroc.pl

thickness exceeds a certain critical value [2]. Both strain and misfit dislocations, usually accompanied by threading dislocations, can significantly affect electrical and optical properties of the epitaxial layers.

In heteroepitaxial III–V ternary compounds with a zinc-blende structure and a small lattice mismatch (less than 1.5%), the strain relaxation occurs primarily by the formation of a 2D network of 60° misfit dislocations, referred to as α and β, typically running in two orthogonal ⟨110⟩ crystallographic directions at the (001) interface [3]. The glide planes are the {111} planes. By taking into account a different nature of the dislocation motion and the type of the atom located in the most distorted core position, four types of 60° dislocations can be distinguished [4]. The first two kinds of dislocations are called shuffle set dislocations if their motion is within two widely spaced {111} planes, and the latter two are glide set dislocations if their motion is within two narrowly spaced {111} planes. The dislocation core in the III(A)–V(B) compounds can consist of either A or B elements, therefore, the four types of dislocations, termed briefly A(g), B(g) and A(s), B(s), are indicated for glide set and shuffle set configurations, respectively. It was shown experimentally [5] that the mobile 60° misfit dislocations in III–V heterostructures are of the glide set. The α and β dislocation cores in the predominant glide set configurations are terminated by group V atoms and group III atoms, respectively. In the heterostructures grown under compressive strain conditions (e.g., $In_xGa_{1-x}As$/GaAs), α and β dislocations are oriented along the $[\bar{1}10]$ and [110] directions, respectively, while in heterostructures grown under tensile strain, the directions are reversed [2]. Different core structures of α and β misfit dislocations lead to significant differences in their dynamic activities and electronic properties. In fact, a distinct difference, depending on the kind of dopant impurities, between the glide velocities of both types of dislocations has been revealed experimentally in several III–V compound semiconductors [6, 7]. In undoped or n-type doped GaAs-based semiconductor crystals, the α dislocations have a higher glide velocity than the β dislocations while in p-type crystals, the situation is opposite. It manifests itself in the asymmetrical formation of both types of dislocations in ⟨110⟩ directions, resulting in the anisotropic misfit strain relaxation of the epitaxial layer [3, 8–11]. It is worth noting that the misorientation of the GaAs substrates can lead to the opposite results in strain relaxation comparing with those typically observed for the exactly (001)-oriented GaAs substrates, as it was reported in several papers [3, 12, 13].

Another characteristic effect associated with the presence of dislocations is undulating surface morphology with ridges and grooves parallel to the intersection of dislocation slip planes with the crystal surface, generally known as a cross hatch. The cross-hatch pattern is often observed in many lattice mismatched semiconductor heterostructures in partial relaxation conditions, e.g. SiGe/Si, InGaAs/GaAs, GaAsP/GaAs and the other III–V semiconductor systems [11, 14–20], where the ridges and grooves oriented along the $[\bar{1}10]$ and [110] directions on the surface are exhibited. Despite frequent observations of a cross-hatch surface morphology and proposals of several mechanisms describing the rise of this morphology, its origin is still controversial and unresolved.

One of the mechanisms proposed for cross-hatch development is an enhanced growth over strain relaxed regions due to fluctuations of composition in the epitaxial layer by the anisotropy of surface diffusion [14, 15]. As alternative explanations, surface undulations resulting primarily from generation of misfit dislocations and a glide process [11, 16–20] have been proposed. A very interesting model, explaining the cross-hatch pattern formation, has been recently put forward by Andrews et al. [21–23]. Within this model, the cross hatch is mainly attributed to the production of surface steps during plastic relaxation of the misfit strain and their subsequent elimination by a lateral mass transport.

In this paper, we report the results of studies of anisotropic strain relaxation and surface morphology related to the asymmetry in the formation of misfit dislocations at the interface of partially relaxed $In_xGa_{1-x}As/GaAs$ heterostructures with a small lattice mismatch.

2. Experimental

$In_xGa_{1-x}As$ epitaxial layers grown on the (001)-oriented GaAs substrates by means of metalorganic vapour-phase epitaxy (MOVPE) technique were investigated. The growth was performed in an atmospheric pressure MOVPE system, fitted with the AIX-200 R&D horizontal reactor made by AIXTRON. The organometallic group III precursors TMGa (trimethylgallium) and TMIn (trimethylindium) were transported by passing H_2 through bubblers and controlled by the pressure level in bubblers. AsH_3 was used as the arsenic source reactant. The structures consisted of a (001) oriented n^+-GaAs substrate, a 0.5 μm thick GaAs buffer layer doped with Si to a net donor concentration of about 2×10^{17} cm^{-3}, and of the $In_xGa_{1-x}As$ epitaxial layer, with a small indium content x, 7.7% (structure A) and 8.6% (structure B), and different thicknesses h_c, about 0.16 μm and 0.28 μm, respectively. The epitaxial layers were not intentionally doped but the background net doping concentration with donors revealed by C–V measurements was equal to about 10^{16} cm^{-3}. Due to the difference in lattice parameters between $In_xGa_{1-x}As$ layers and the GaAs substrate of about 0.55% and 0.62% for samples A and B, respectively, the epitaxial growth was performed under a compressive misfit strain. All the epitaxial layers were grown at the same temperature equal to 670 °C and different times in order to achieve the thicknesses just above the critical value, i.e. to obtain partially relaxed samples [24].

Structural properties of the partially relaxed $In_xGa_{1-x}As$ epitaxial layers were examined by means of high-resolution X-ray diffraction (HRXRD) measurements using a Philips Materials Research Diffractometer (MRD) equipped with a four-crystal Bartels Ge monochromator and Bonse/Hart analyser. The (220) reflection of a monochromator was used with $CuK_{\alpha1}$ radiation and triple-axis configurations were applied for recording 2D reciprocal lattice maps (RLMs).

The discrimination between two perpendicular $\langle 110\rangle$ directions on the (001) surface of heterostructures was made by subjecting the samples to selective chemical

etching in the $HF:H_2SO_4:H_2O_2$: (2:2:1) solution [25] diluted in 1:1 proportion in water, for 45 s at room temperature. This etching gives rise to a characteristic microrelief in the form of quasi-parallel grooves (with the heights equal to about 250 nm) on the (001) GaAs surface, oriented in $[\bar{1}10]$ direction (Fig. 1).

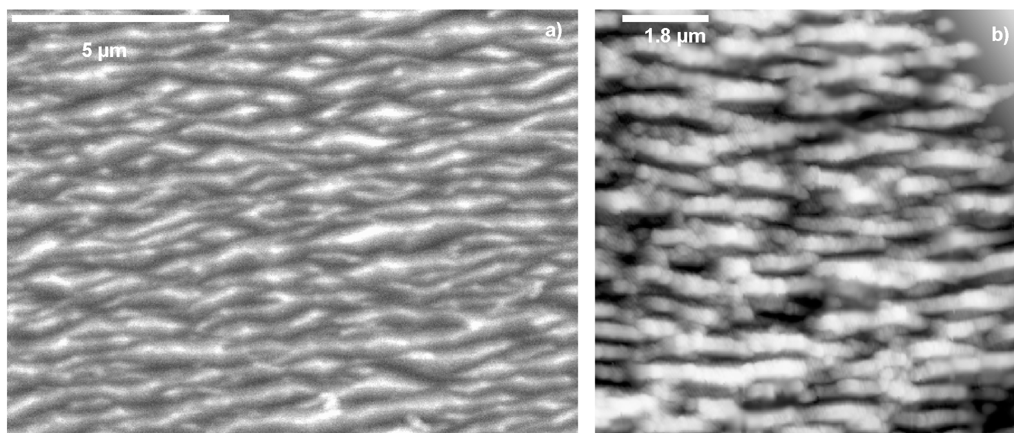

Fig. 1. Exemplary SEM (a) and AFM (b) images of a microrelief obtained by anisotropic chemical etching of the $In_{0.077}Ga_{0.923}As$/GaAs (structure A) surface

The surface morphology of the $In_xGa_{1-x}As$ epilayers was characterized by atomic force microscopy (AFM). The etched samples were also studied by scanning electron microscopy (SEM). Additionally, transmission electron microscopy (TEM) has been exploited to reveal the network of misfit dislocations at the heterostructure interface and the probable presence of threading dislocations in the epitaxial layer.

3. Results and discussion

3.1. Distribution of misfit dislocations and surface morphology

The distribution of misfit dislocations was obtained by the TEM method which allows a direct imaging of individual dislocations. In Figure 2, the cross-sectional TEM images of the both heterostructures are presented. In these images, one can see a clearly outlined interface between the epitaxial layer and the substrate, including a periodic array of misfit dislocations with an average spacing of 50 nm. However, no threading dislocations were observed in the heteroepitaxial layers, what means that the epilayer included less than 10^7 cm^{-2} of threading dislocations. Furthermore, an exemplary planar view TEM image of the $In_{0,086}Ga_{0,914}As$/GaAs heterostructure interface (structure B), shown in Fig. 3, revealed a regular 2D network of 60° misfit dislocations

oriented in two orthogonal ⟨110⟩ crystallographic directions at the (001) interface, with a linear density of about 10^5 cm^{-1}.

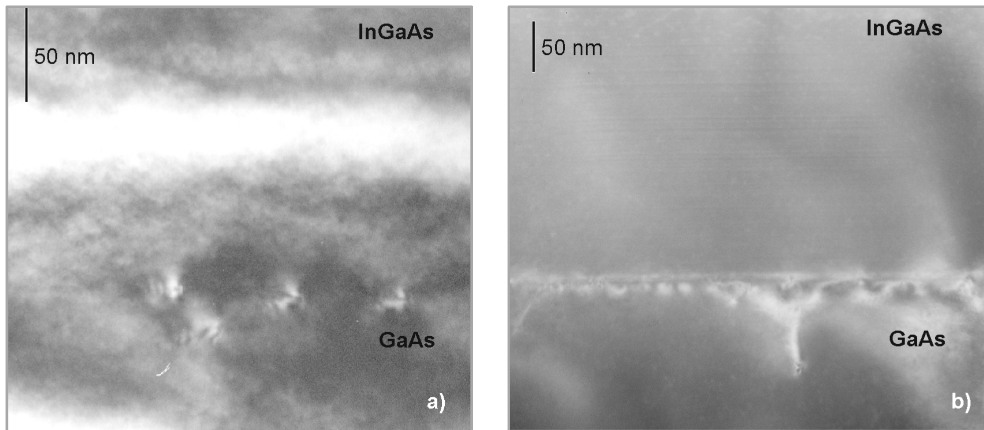

Fig. 2. TEM bright-field images showing the cross-sectional views of $In_xGa_{1-x}As$/GaAs heterostructures: a) structure A with $x = 0.077$, b) structure B with $x = 0.086$

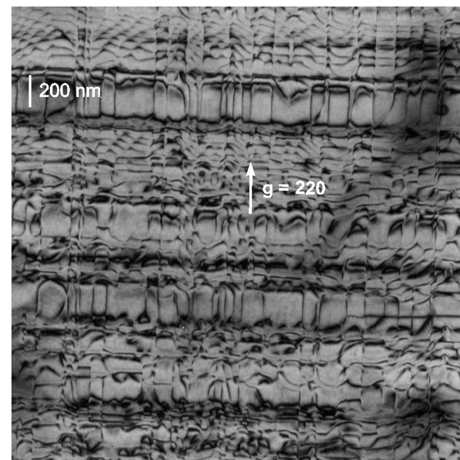

Fig. 3. An exemplary TEM image showing a network of misfit dislocation at the interface plane of the $In_{0.086}Ga_{0.914}As$/GaAs heterostructures (structure B)

A detailed analysis of the planar view image (Fig. 3) showed that about 38% more misfit dislocations running along [$\bar{1}$10] (α-type dislocations) were detected as compared to those along perpendicular [110] direction (β-type dislocation). It is in good agreement with the previous results [8–10] but it contradicts the recent results by Yastrubchak et al. [11]. The difference can be explained by the use of p-doped layers investigated by the authors [11], in which the glide velocity of β-type dislocations is higher than that of α-type ones, in contrast to the undoped or n-type doped GaAs -based heterostructures, used in this communication, where the α-type dislocations have a higher glide velocity in comparison to that of β-type ones [6, 7].

The studies of surface morphology have also been performed for all investigated heterostructures by atomic force microscopy (AFM), prior to chemical etching. The most pronounced surface morphology was observed for the structure B with $x = 0.086$, showing a well-defined cross-hatch pattern in the form of ridges and grooves oriented along two perpendicular ⟨110⟩ directions on the (001) epitaxial layer surface (Fig. 4).

The average peak-to-peak spacings between the ridges along the $[\bar{1}10]$ direction were equal to 2.1 μm and those along [110] – 3.2 μm. The undulations were equal to about 2 nm peak-to-valley amplitude. As was mentioned earlier, such a cross-hatch morphology is often observed in many semiconductor heterostructures with a lattice mismatch, such as SiGe/Si, InGaAs/GaAs, and other III–V semiconductor systems [11, 14–20], grown on (001)-oriented or slightly misoriented substrates. It is widely accepted that a cross-hatch pattern reproduces a network of underlying interfacial misfit dislocations, as a consequence of their local strain fields. A direct comparison of misfit dislocation distribution obtained by TEM with the results of AFM has confirmed these findings. A linear density of misfit dislocations estimated from AFM measurements of surface undulations was equal to about 10^4 cm^{-1} but we observed about 37% higher density of α misfit dislocations, running along $[\bar{1}10]$ direction, than β misfit dislocations along $[110]$ direction.

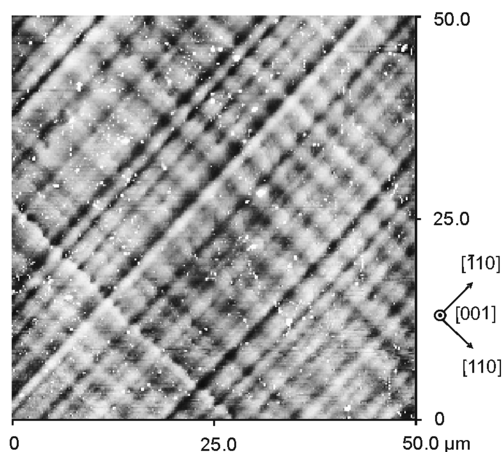

Fig. 4. AFM image (50×50 μm^2) of the $In_{0.086}Ga_{0.914}As/GaAs$ (structure C) surface morphology showing a well defined cross-hatch pattern

One can notice that the distribution of misfit dislocations at the interface, obtained by the analysis of a planar view TEM image, exhibits the same asymmetry. These results can prove almost one-to-one correspondence between the arrangement of interfacial misfit dislocations obtained by TEM and the cross-hatch surface morphology, observed by AFM. However, it is worth noting that in this case, each undulation cannot be associated only with an individual misfit dislocation but with a bunch of few closely spaced dislocations, for which a superposition of strain fields can evoke a single undulation. A planar view TEM image (Fig. 3) showing a nonuniform distribution of misfit dislocations in each of the ⟨110⟩ directions confirms these findings. It can

explain a significantly lower density (about one order of magnitude) of misfit dislocations estimated from AFM observations in comparison to TEM. This is in agreement with the model proposed by Andrews et al. [21-23]. In this model, the formation of a single undulation requires a contribution of a group of misfit dislocations gliding on different slip planes. In contrast, higher [17] or the same [11] densities of misfit dislocations with reference to their real densities observed by TEM sometimes can be obtained by means of AFM. Nevertheless, the AFM technique can be still an effective tool for measuring the asymmetric formation of misfit dislocations at the interface of the partially relaxed epitaxial layers with a small lattice mismatch and small thicknesses, just above the critical value, but the estimation of the dislocation density can be incorrect.

3.2. Anisotropic misfit strain relaxation

The anisotropy of misfit strain relaxation in partially relaxed $In_xGa_{1-x}As$/GaAs heterostructures has been investigated by means of XRD by recording and analyzing 2D reciprocal lattice maps (RLMs) for (224) asymmetrical reflections. The measurements were performed at room temperature, with the sample oriented either in $[\bar{1}10]$ or $[110]$ crystallographic directions perpendicular to the X-ray diffraction plane [26].

Figure 5 shows asymmetrical (224) RLMs obtained for the structures A and B. The horizontal axis corresponds to the reciprocal lattice vector in the diffraction plane, parallel to the surface of the heterostructure, either along $[\bar{1}10]$ or the $[110]$ crystallographic direction while the vertical axis corresponds to the reciprocal lattice vector perpendicular to the surface, i.e. along $[001]$ direction. From the sizes and positions of reciprocal lattice peaks one can get information on crystal imperfections, like point defects and dislocations as well as changes of lattice parameters of the epilayer unit cell due to strain relaxation.

The vertical and diagonal dotted lines denote the RLM peak positions expected for the case of fully strained (pseudomorphic) and fully relaxed layers, respectively. The RLM peaks located at the intersection of both lines correspond to the GaAs substrates while the other distinctly scattered peaks correspond to individual $In_xGa_{1-x}As$ epilayers. In Figure 5, the epilayer RLM peaks for all investigated heterostructures are located between these two lines. This means that all the structures are partially relaxed, and, moreover, this relaxation is strongly anisotropic, being larger along the $[110]$ direction than along the $[\bar{1}10]$ direction. These findings confirm the results obtained by TEM and AFM, and discussed in the previous subsection. A higher misfit strain relaxation observed along the [110] direction is in agreement with a higher density of α misfit dislocations running in the $[\bar{1}10]$ direction at the interface and causing a larger relaxation of the layers along the perpendicular direction. The structure A exhibits a smaller strain relaxation. It is almost fully strained along $[\bar{1}10]$ direction but partially relaxed along the [110] direction. This feature can explain the fact that we did not manage to detect any distinct cross-hatch pattern on the surface of this structure. On

the other hand, the structure B exhibits a larger strain relaxation in both ⟨110⟩ directions, therefore the cross-hatch surface morphology is clearly visible (Fig. 4) for this structure.

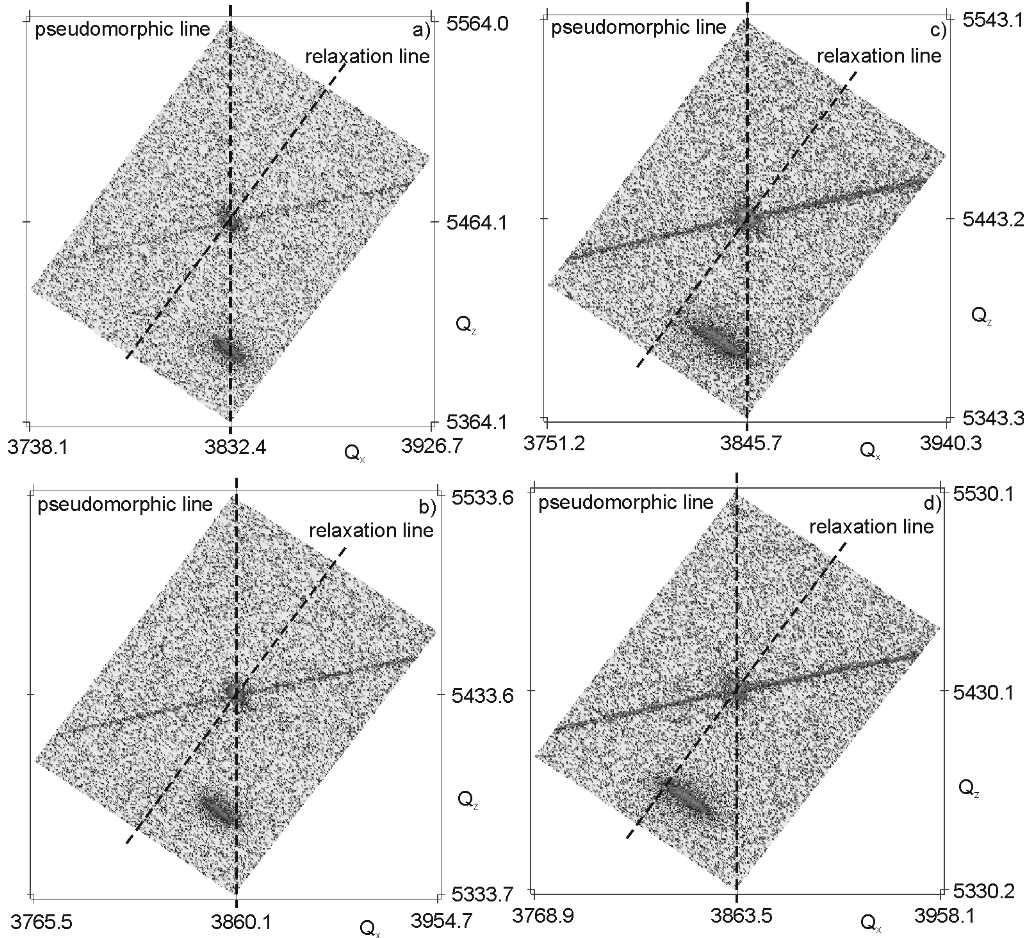

Fig. 5. The RLMs for the asymmetric (224) reflection of the $In_xGa_{1-x}As/GaAs$ heterostructures: a, b) structure A with $x = 0.077$, c, d) structure B with $x = 0.086$. The vertical axis is in the [001] direction and the horizontal axis is either along $[\bar{1}10]$ (a, c) or [110] (b, d) crystallographic directions. The RLM units are in $\lambda/2d$, where $\lambda = 1.540597$ Å and d is the lattice spacing of (224) planes

4. Conclusions

TEM, AFM and XRD techniques have been successfully employed for studying both anisotropic strain relaxation and surface morphology, related to the asymmetry in the formation of interfacial misfit dislocations of the partially relaxed $In_xGa_{1-x}As/GaAs$ heterostructures with a small lattice mismatch and grown by MOVPE. TEM investigations

revealed a regular network of 60° misfit dislocations of α and β type, running along two orthogonal $\langle 110 \rangle$ crystallographic directions at the (001) interface of the heterostructure. This network was also reproduced on the surface, as a well-defined cross-hatch pattern, observed by AFM. A distinct anisotropy of strain relaxation along two orthogonal $\langle 110 \rangle$ directions in the (001) plane has been detected by means of XRD investigations. It was in good agreement with the asymmetry observed in the formation of interfacial misfit dislocations. A higher glide velocity of α dislocations along $[\bar{1}10]$ direction in undoped InGaAs epitaxial layers resulted in a higher density of misfit dislocations of this type in the $[\bar{1}10]$ direction and a larger misfit strain relaxation in these layers along the perpendicular $[110]$ direction.

Acknowledgements

The authors are grateful to D. Radziewicz (Wrocław University of Technology) for growing the InGaAs/GaAs heterostructures and to J. Kozłowski (Wrocław University of Technology) for helpful discussions and advices concerning the XRD results.

References

[1] PICHAUD B., BURLE N., PUTERO-VUAROQUEAUX M.,CURTIL C., J. Phys. Cond. Matter, 14 (2002), 13255.
[2] TE NIJENHUIS J., VAN DER WEL J., VAN ECK E.R.H., GILING L.J., J. Phys. D: Appl. Phys., 29 (1996), 2961.
[3] GOLDMAN R.S., KAVANAGH K.L., WIEDER H.H., EHRLICH S.N., FEENSTRA R.M., J. Appl. Phys., 83 (1998), 5137.
[4] HIRTH J.P., LOTHE J., *Theory of Dislocations*, 2nd Ed., Wiley, New York, 1982.
[5] VAN DER WEL P.J., TE NIJENHUIS J., VAN ECK E.R.H., GILING L.J., Semicond. Sci. Techn., 7 (1992), A63.
[6] YONENAGA I., SUMINO K., J. Cryst. Growth, 126 (1993), 19.
[7] YONENAGA I., J. Phys. III France, 7 (1997), 1435.
[8] FOX B.A., JESSER W.A., J. Appl. Phys., 68 (1990), 2739.
[9] ROMANATO F., NAPOLITANI E., CARNERA A., DRIGO A.V., LAZZARINI L., SALVIATI G., FERRARI C., BOSACHI A., FRANCHI S., J. Appl. Phys., 86 (1999), 4748.
[10] SALVIATI G., FERRARI C., LAZZARINI L., NASI L., DRIGO A.V., BERTI M., DE SALVADOR D., NATALI M., MAZZER M., Appl. Surf. Sci., 188 (2002), 36.
[11] YASTRUBCHAK O., WOSINSKI T., DOMAGALA J.Z., ŁUSAKOWSKA E., FIGIELSKI T., PECZ B., TOTH A.L., J. Phys. Cond. Matter, 16 (2004), S1.
[12] WERNER P., ZAKHAROV N.D., CHEN Y., LILIENTAL-WEBER Z., WASHBURN J., KLEM J.F., TSAO J.Y., Appl. Phys. Lett., 62 (1993), 2789.
[13] GOLDMAN R.S., WIEDER H.H., KAVANAGH K.L., Appl. Phys. Lett., 67 (1995), 344.
[14] HSU W.P., FITZGERALD E.A., XIE Y.H., SILVERMAN P.J., CARDILLO M.J., Appl. Phys. Lett., 61 (1992), 1293.
[15] SAMONJI K., YONEZU H., TAKAGI Y., OHSHIMA N., J. Appl. Phys., 86 (1999), 1331.
[16] CHANG K.H., GIBALA R., SROLOVITZ D.J., BHATTACHARYA P.K., MANSFIELD J.F., J. Appl. Phys., 67 (1990), 4093.
[17] BEANLAND R., AINDOW M., JOYCE T.B., KIDD P., LOURENCO M., GOODHEW M.P.J., J. Cryst. Growth, 149 (1995), 1.
[18] LUTZ M.A., FEENSTRA R.M., LEGOUES F.K., MOONEY P.M., CHU J.O., Appl. Phys. Lett., 66 (1995), 724.

[19] TAKANO Y., MASUDA M., KOBAYASHI K., KUWAHARA K., FUKE S., SHIRAKATA S., J. Cryst. Growth., 236 (2002), 31.
[20] YASTRUBCHAK O., WOSINSKI T., ŁUSAKOWSKA E., FIGIELSKI T., TOTH A.L., Microchim. Acta, 145 (2004), 267.
[21] ANDREWS A.M., ROMANOV A.E., SPECK J.S., BOBETH M., POMPE W., Appl. Phys. Lett., 77 (2000), 3740.
[22] ANDREWS A.M., SPECK J.S., ROMANOV A.E., BOBETH M., POMPE W., J. Appl. Phys., 91 (2002), 1933.
[23] ANDREWS A.M., LESAR R., KERNER M.A., SPECK J.S., ROMANOV A.E., KOLESNIKOVA A.L., BOBETH M., POMPE W., J. Appl. Phys, 95 (2004), 6032.
[24] FITZGERALD E.A., *Properties of Lattice-Matched and Strained Indium Gallium Arsenide*, P. Bhattacharya (Ed.), IEE EMIS Datareviews Series, 8, 1993, p. 6.
[25] YASTRUBCHAK O., ŁUSAKOWSKA E., MORAWSKI A., DEMCZUK O., WOSIŃSKI T., Phys. Stat Sol. (c), 1 (2004), 401.
[26] HALLIWELL M.A.G., *Advances In X-Ray Analysis*, 33, C. S. Barrett (Ed.), Plenum Press, New York, 1990, p. 61.

Received 28 April 2007
Revised 16 February 2008

Materials Science-Poland, Vol. 26, No. 1, 2008

Microstructure and magnetic properties of nanocrystalline Fe-based alloys

M. HASIAK[1*], M. MIGLIERINI[2], J. KALETA[1], J. ZBROSZCZYK[3], H. FUKUNAGA[4]

[1]Institute of Materials Science and Applied Mechanics, Wrocław University of Technology, ul. Smoluchowskiego 25, 50-370 Wrocław, Poland

[2]Department of Nuclear Physics and Technology, Slovak University of Technology, Ilkovičova 3, 812-19 Bratislava, Slovakia

[3]Institute of Physics, Technical University of Częstochowa, al. Armii Krajowej 19, 42-200 Częstochowa, Poland

[4]Faculty of Engineering, Nagasaki University, 852-8521 Nagasaki, Japan

Microstructure and magnetic properties of nanocrystalline $Fe_{82}(Zr_4Nb_3)B_{10}Cu_1$ and $Fe_{80}(Zr_4Mn_3)B_{12}Cu_1$ alloys with different content of the crystalline phase have been investigated. Changes in the microstructure with progressing crystallization were observed by the room temperature Mössbauer spectroscopy. Good soft magnetic properties and frequency characteristics were found in the nanocrystalline $Fe_{82}(Zr_4Nb_3)B_{10}Cu_1$ and $Fe_{80}(Zr_4Mn_3)B_{12}Cu_1$ samples with 50-60% of the crystalline α-Fe phase.

Key words: *amorphous alloy; nanocrystalline alloy; Mössbauer spectroscopy; hysteresis loop; core losses*

1. Introduction

Nanocrystalline Fe–Zr–B–(Cu) alloys patented under the trade name NANOPERM with bcc Fe grains of about 20–30 nm exhibit good soft magnetic properties i.e., high saturation magnetization, low coercivity and good frequency characteristics [1-3] resulting from the presence of fine grains magnetically interacting with each other [4]. Moreover, magnetic properties of nanocrystalline Fe–Zr–B–(Cu) alloys strongly depend on the microstructure of precursors which can be modified by the conditions during the sample preparation. Addition of Nb, Hf, Mn, Ti and other metalloid atoms to the NANOPERM type alloys during fabrication leads to an improvement of their soft magnetic properties [5, 6].

*Corresponding author, e-mail: mariusz.hasiak@pwr.wroc.pl

The aim of this paper is to study effects of Nb and Mn addition on the formation of nanocrystalline structures and magnetic properties of partially crystallized Fe–Zr-(Nb, Mn)–B–Cu alloys.

2. Experimental

Rapidly solidified ribbons of $Fe_{82}(Zr_4Nb_3)B_{10}Cu_1$ and $Fe_{80}(Zr_4Mn_3)B_{12}Cu_1$ alloys were obtained by a single roller melt-spinning method in argon protective atmosphere. The width and thickness of the investigated samples were 2.20 mm and 0.02 mm, respectively. Ribbons in the as-quenched state were partially crystallized which was confirmed by X-ray diffraction using a URD-6 (VEB Carl Zeiss, Jena) diffractometer. The changes in the microstructure were examined at room temperature by the Mössbauer spectroscopy in a transmission geometry using a ^{57}Co source in a Rh matrix. Mössbauer spectra obtained for $Fe_{82}(Zr_4Nb_3)B_{10}Cu_1$ and $Fe_{80}(Zr_4Mn_3)B_{12}Cu_1$ alloys in the as-quenched state and after heat treatment were evaluated by hyperfine field distributions using the NORMOS package program [7]. Isothermal annealing was performed at 773 K and 823 K under the vacuum of about 5×10^{-3} Pa for various time periods. AC and DC magnetic measurements were carried out upon 100 mm long ribbons using a M-H Loop Tracer (Tesla) and equipment for magnetic measurements MMS-4001 (Ryowa Electronics).

3. Results and discussion

Precursors of $Fe_{82}(Zr_4Nb_3)B_{10}Cu_1$ and $Fe_{80}(Zr_4Mn_3)B_{12}Cu_1$ alloys were partially crystallized already in the as-quenched state as confirmed by X-ray diffractometry and Mössbauer spectroscopy. X-ay diffraction patterns show narrow peaks corresponding to the crystalline α-Fe phase superimposed upon a broad amorphous reflection. Mössbauer spectra of as-quenched (a.q.) and annealed $Fe_{82}(Zr_4Nb_3)B_{10}Cu_1$ and $Fe_{80}(Zr_4Mn_3)B_{12}Cu_1$ alloys are shown in Fig. 1 together with their spectral components. Corresponding hyperfine field distributions $P(B)$ are drawn alongside each spectra. The spectra consist of broad, overlapped lines assigned to disordered structural positions of resonant atoms, whereas sharp narrow lines indicate a presence of bcc-Fe crystallites. The experimental data were fitted by separate independent blocks of hyperfine field distributions and a sextet of Lorentzian lines using the NORMOS package program.

Magnetic properties of the NANOPERM type alloys strongly depend on their microstructure [8, 9]. Both investigated samples of $Fe_{82}(Zr_4Nb_3)B_{10}Cu_1$ and $Fe_{80}(Zr_4Mn_3)B_{12}Cu_1$ alloys show rather poor soft magnetic properties in the as quenched states. Dependences of magnetic flux densities on magnetic field obtained for the investigated samples are presented in Fig. 2 in the form of magnetic hysteresis loops. The as-quenched Nb- and Mn-containing ribbons exhibit the saturation magnetic flux density (B_s) of about 1.3 T and 1.0 T, respectively. The coercivity (H_c) of the as-quenched $Fe_{80}(Zr_4Mn_3)B_{12}Cu_1$

alloy is equal to 30 A/m being three times lower than that of the $Fe_{82}(Zr_4Nb_3)B_{10}Cu_1$ alloy. Upon increasing annealing temperature up to 823 K ($Fe_{82}(Zr_4Nb_3)B_{10}Cu_1$) and 773 K ($Fe_{80}(Zr_4Mn_3)B_{12}Cu_1$), an increase of B_s and decrease of H_c for both investigated samples is observed. The maximum saturation magnetic flux density of about $B_s = 1.6$ T was achieved for the Mn-containing ribbon annealed at 773 K for 0.5 h, and $B_s = 1.4$ T was found for the Nb-containing ribbon annealed at 823 K for 0.5 h. Furthermore, optimum annealing conditions lead to a decrease in the coercivity

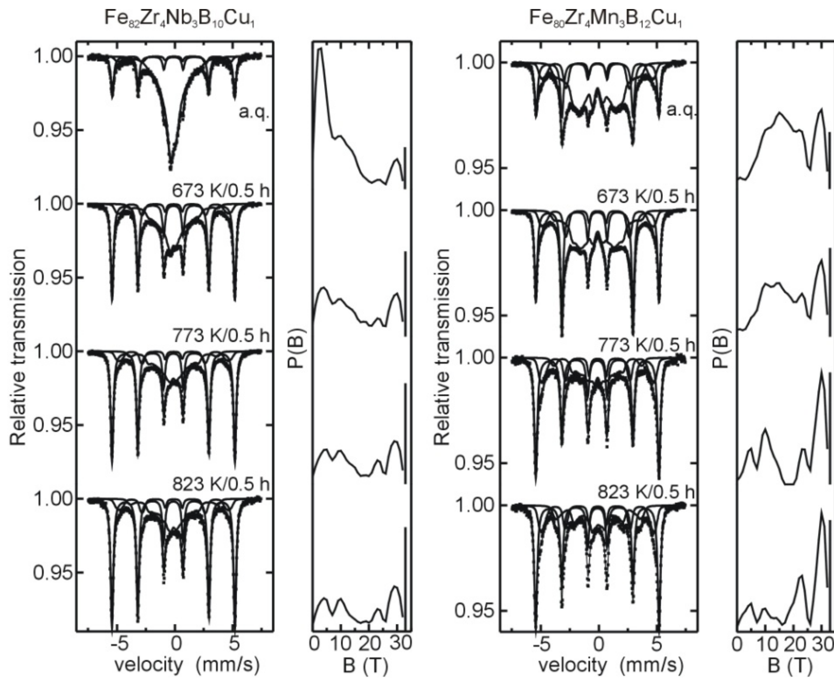

Fig. 1. Mössbauer spectra and hyperfine field distributions of the $Fe_{82}(Zr_4Nb_3)B_{10}Cu_1$ and $Fe_{80}(Zr_4Mn_3)B_{12}Cu_1$ alloys

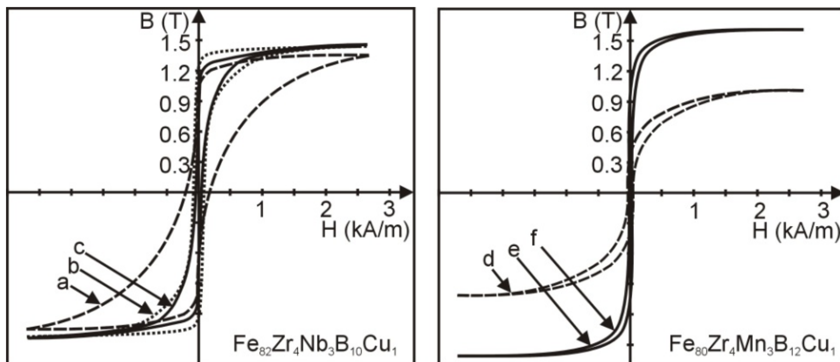

Fig. 2. DC hysteresis loops for the $Fe_{82}(Zr_4Nb_3)B_{10}Cu_1$ (a, b, c) and $Fe_{80}(Zr_4Mn_3)B_{12}Cu_1$ (d, e, f) alloys in the as-quenched state (a, d) and after 0.5 h annealing at 773 K (b, e) and 823 K (c, f)

to 40 A/m and 20 A/m for the $Fe_{82}(Zr_4Nb_3)B_{10}Cu_1$ and $Fe_{80}(Zr_4Mn_3)B_{12}Cu_1$ alloys, respectively. DC hysteresis loops obtained for the $Fe_{80}(Zr_4Mn_3)B_{12}Cu_1$ alloy after 0.5 h annealing at 773 K and 823 K are almost identical (Fig. 2, curves e and f).

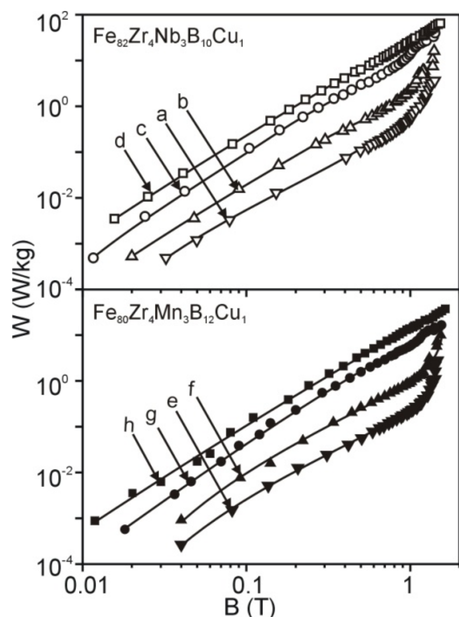

Fig. 3. Dependences of core losses (W) on induction (B) for the $Fe_{82}(Zr_4Nb_3)B_{10}Cu_1$ alloy (a, b, c, d) and $Fe_{80}(Zr_4Mn_3)B_{12}Cu_1$ alloy (e, f, g, h) after 0.5 h annealing at 823 K and 773 K, respectively, measured at the frequency of 50 Hz (a, e), 200 Hz (b, f), 1 kHz (c, g), and 2 kHz (d, h)

AC magnetic properties of the investigated alloys annealed at optimum conditions are presented in Fig. 3 as dependences of core losses (W) on magnetic induction (B) for various frequencies. The core losses monotonically increase with induction for all investigated samples. In addition, the core losses of both samples are higher with increasing frequency of measurement due to eddy currents. The sample with Mn exhibits systematically lower values of W than the one with Nb.

Dependences of the effective permeability (μ_e) and the loss factor $\tan\delta$ upon the magnetic field H are plotted in Figs. 4 and 5, respectively ($\tan\delta = \mu''/\mu'$; the real (μ') and imaginary (μ'') parts of permeability express the components of the induction B which are in phase with the magnetic field H and delayed by the phase angle of 90° from H, respectively [10]). The effective permeability measured at the frequency of 250 Hz increases for all investigated samples to its maximum at the magnetic field range 45–55 A/m and then decreases (Fig. 4). The maximum value of μ_e for the Nb -containing sample is shifted towards higher magnetic fields than that of the Mn -containing sample. The increase of the maximum effective permeability up to 13 000 and 9200 after 0.5 h annealing of the $Fe_{80}(Zr_4Mn_3)B_{12}Cu_1$ alloy at 773 K and the $Fe_{82}(Zr_4Nb_3)B_{10}Cu_1$ at 823 K is connected with an irreversible structural relaxation during the heat treatment process. It is worth noting that the effective permeability does not show appreciable deviations from those presented in the figure in a wide range of the measuring frequencies up to few kHz.

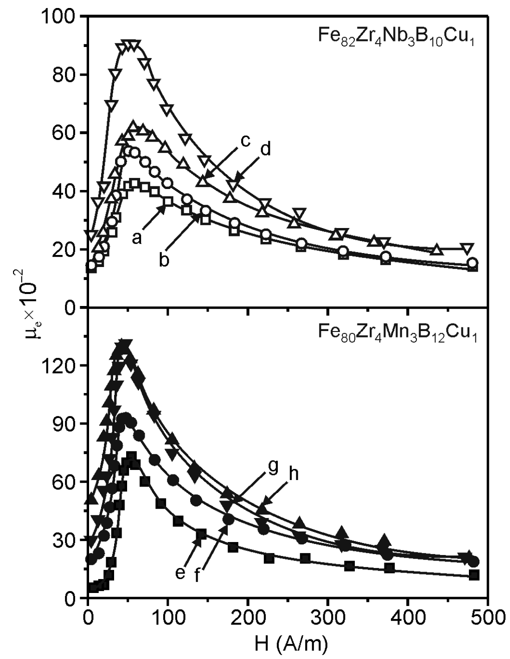

Fig. 4. Effective permeability (μ_e) vs. magnetic field (H) for the $Fe_{82}(Zr_4Nb_3)B_{10}Cu_1$ (a, b, c, d) and $Fe_{80}(Zr_4Mn_3)B_{12}Cu_1$ (e, f, g, h) alloys in the as-quenched state (a, e) and annealed at 673 K (b, f), 773 K (c, g) and 823 K (d, h) for 0.5 h measured at the frequency of 250 Hz

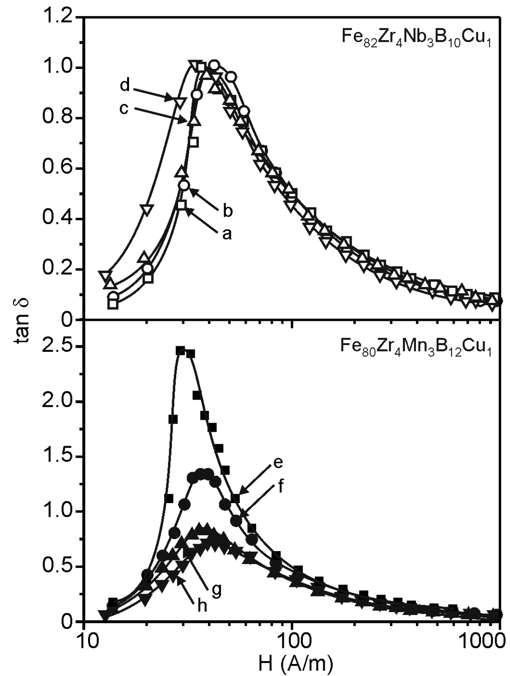

Fig. 5. Dependences of the loss factor (tanδ) on magnetic field (H) at $f = 250$ Hz for the $Fe_{82}(Zr_4Nb_3)B_{10}Cu_1$ (a, b, c, d) and $Fe_{80}(Zr_4Mn_3)B_{12}Cu_1$ (e, f, g, h) alloys in the as quenched state (a, e) and annealed for 0.5 h at 673 K (b, f), 773 K (c, g) and 823 K (d, h)

Dependences of the loss factor tanδ on the magnetic field (Fig. 5) for the both alloys exhibit a similar behaviour as the effective permeabilities. The loss factor of the

as-quenched sample with Mn is two times higher than that of the $Fe_{82}(Zr_4Nb_3)B_{10}Cu_1$ alloy. After annealing, the values of $\tan\delta$ are similar for both investigated samples. It should be noted that the maximum loss factors were obtained at lower magnetic fields than the maximum effective permeability.

4. Conclusions

The results of magnetic measurements for the nanocrystalline $Fe_{82}(Zr_4Nb_3)B_{10}Cu_1$ and $Fe_{80}(Zr_4Mn_3)B_{12}Cu_1$ alloys with various amounts of the crystalline phases have been reported. Nanocrystalline alloys with the bcc grain fraction higher than 50% of the sample volume exhibit good soft magnetic properties. Nb and Mn-containing samples show the maximum permeabilities of 9200 and 13 000, respectively, at the magnetic field of about 50 A/m. Moreover, the ribbons of the $Fe_{82}(Zr_4Nb_3)B_{10}Cu_1$ and $Fe_{80}(Zr_4Mn_3)B_{12}Cu_1$ alloys annealed at 773 K and 823 K show low core losses which increase with the frequency of measurement.

Acknowledgements

This work was supported by the grants PBZ/MEiN/01/2006/09 (M. Hasiak) and VEGA 1/4011/07, APVT 20-008404 (M. Miglierini).

References

[1] SUZUKI K., KATAOKA N., INOUE A., MAKINO A., MASUMOTO T., Mater. Trans. JIM, 31 (1990), 743.
[2] MAKINO A., BITOH T., INOUE A., MASUMOTO T., J. Appl. Phys., 81 (1997), 2736.
[3] MAKINO A., BITOH T., KOJIMA A., INOUE A., MASUMOTO T., Mater. Sci. Eng. A, 304-306 (2001), 1083.
[4] SUZUKI K., HERZER G., CADOGAN J.M., J. Magn. Magn. Mater., 177–181 (1998), 949.
[5] MÜLLER M., GRAHL H., MATTERN N., KÜHN U., Mater. Sci. Eng. A, 226-228 (1997), 565.
[6] SUZUKI K., MAKINO A., KATAOKA N., INOUE A., MASUMOTO T., Mater. Trans. JIM, 32 (1991), 93.
[7] BRAND R.A., *NORMOS program*, Universität Duisburg, 1999.
[8] VARGA L.K., LOVAS A., POGÁNY L., KISS L.F., BALOGH J., KEMÉNY T., Mater. Sci. Eng. A, 226–228 (1997), 740.
[9] HASIAK M., MIGLIERINI M., YAMASHIRO Y., CIURZYŃSKA W.H., FUKUNAGA H., J. Magn. Magn. Mater., 239 (2002), 506.
[10] CHIKAZUMI S., *Physics of Ferromagnetism*, Clarendon Press, Oxford, 1997.

Received 28 April 2007
Revised 16 February 2008

Materials Science-Poland, Vol. 26, No. 1, 2008

Submicron suspended structures based on A(III)B(V) epitaxial layers

M. KRAMKOWSKA*, A. SZYSZKA, B. ŚCIANA, I. ZUBEL

Faculty of Microsystem Electronics and Photonics, Wrocław University of Technology,
ul. Janiszewskiego 11/17, 50-370 Wroclaw, Poland

A technological process has been described for fabrication of suspended structures on GaAs substrate with AlGaAs/GaAs epitaxial multi-layers deposited by the AP MOVPE method. The patterns of beams and bridges with various dimensions were made by the photolithography method. The structures were fabricated by wet chemical etching in two systems of solutions based on phosphoric or citric acid with hydrogen peroxide. The former one enabled etching through the deposited epitaxial layers down to the GaAs substrate. The latter one allowed a selective etching of GaAs over AlGaAs. In effect, a beam made of AlGaAs layer was released and formed the suspended structure. As an etching mask, AZ 1813 positive photoresist was used. A series of rectangular beams with various planar dimensions and submicrometer thicknesses was fabricated. The elaborated process may be used for fabrication of suspended structures for various applications.

Key words: *GaAs; A(III)B(V) epitaxial layers; AP MOVPE; suspended beam*

1. Introduction

Properties of A(III)B(V) compounds such as high piezoresistive constant, low thermal conductivity, relatively high Seebeck coefficient, direct band gap, high electron mobility and high saturation velocity are interesting for various applications. By combining micromechanical properties with good optomechanical sensitivity, piezoelectricity and piezoresistivity, III–V micromachined devices offer new opportunities for micro-electro-mechanical-systems (MEMS) and micro-opto-electro-mechanical -systems (MOEMS) applications. Many examples of devices such as infrared thermopiles, pressure sensors, resonators, based on A(III)B(V) compounds have been reported [1–3].

Epitaxial layers of A(III)B(V) compounds grown by the MOVPE technique offer high flexibility and precision in micromachining. Wet chemical etching, commonly

*Corresponding author, e-mail: malgorzata.kramkowska@pwr.wroc.pl

used in production of 3D micro-mechanical structures formed from a substrate or a multilayer structure, employs two main features of the etching process. The former one is based on preferential etching, utilizing etch rate anisotropy and the fact that due to zinc blende crystal structure of the compounds, the etching of A(111) planes proceeds much slower than the all other ones. The latter approach uses the differences in etch rates of the layers with various chemical compositions, leading to so-called etching selectivity. The layer with a higher etch rate plays a role of sacrificial layer and is etched off whereas the second one forms a structural layer which is released during the process.

Suspended structures like beams, bridges or cantilevers play an important role in fabrication of various types of sensors and integrated optoelectronic devices based on A(III)B(V) compounds. The structures can be used as carriers for active devices or as sensing elements in various types of sensors. In the solutions, the suspended structures secure thermal isolation of active part of a circuit or form a mechanical part of various types of sensors subject to various enforcing factors. In this work, a procedure of obtaining such structures in laboratory conditions is described.

2. Experimental

Deposition of epitaxial layers. Epitaxial AlGaAs/GaAs heterostructures were grown by atmospheric pressure metal organic vapour phase epitaxy (AP MOVPE) in an AIX200 R&D horizontal reactor. The following epilayers were deposited on (100) - oriented semi-insulating (SI) GaAs substrate:

- undoped (UD) GaAs buffer (thickness 0.5 μm),
- undoped (UD) AlGaAs (thickness 1.05 μm),
- undoped (UD) GaAs "cap" (thickness 0.05 μm).

A schematic presentation of the AlGaAs/GaAs heterostructure is shown in Fig. 1.

Layer	Thickness
GaAs „cap"	d = 0.05 μm
$Al_{0.31}Ga_{0.69}As$	d =1.05 μm
GaAs – „buffer"	d = 0.3 μm
SI GaAs (100)	

Fig. 1. Schematic presentation of AlGaAs/GaAs heterostructures

The growth process was carried out at 700 °C. Trimethylgallium (TMGa), trimethylaluminum (TMAl) and arsine (AsH_3, 10% mixture in H_2) were used as the growth precursors. High purity hydrogen was employed as a carrier gas. The aluminum

content in AlGaAs epilayer was 31%. High resolution X-ray diffraction was used for estimation of the thicknesses of all epilayers and AlGaAs composition.

Etching solutions. Many etching systems for A(III)B(V) compounds have been described in the literature. Clawson [4] compiled literature reports describing etching of the compounds. The choice is, however, very difficult as many results are not reproducible between different laboratories. Actually, the etching procedures and the compositions of etching solutions should be individually elaborated for a particular purpose. In the work, etching systems based on phosphoric acid and citric acid have been tested. Solution of phosphoric acid enables non-selective etching of GaAs and AlGaAs epitaxial layers, necessary in the initial stage of suspended beams fabrication. The solutions based on citric acid maintain etch rate selectivity of GaAs layer over AlGaAs. However, the selectivity depends on the ratio of citric acid and hydrogen peroxide. Therefore, a series of experiments was carried out at room temperature in a wide range of solution compositions. For the preparation of etching solutions, 50% water solution of citric acid and 30% solution of hydrogen peroxide were used. The etching depth was measured by the interferometric method on the boundaries between etched and non-etched areas. At the ratio of $C_6H_8O_7{:}H_2O_2$ exceeding 2, the etch rate selectivity decreased dramatically; at the ratios below 2, the morphology of etched surfaces underwent deterioration. The compositions of selected solutions with corresponding etch rates and selectivities are presented in Table 1.

Table 1. Set of etching solutions and basic parameters of the etching process

Composition of etching solution	V [nm/min]		Selectivity
	GaAs	AlGaAs	
$C_6H_8O_7{:}H_2O_2$ 2:1	472	18.9	25
$H_3PO_4{:}H_2O_2{:}H_2O$ 8:1:1	800	800	none
$H_3PO_4{:}H_2O_2{:}H_2O$ 1:1:40	80	80	none

Design and fabrication of a suspended beam. The idea of fabrication of suspended beam structure is shown in Fig. 2. At the first stage of the fabrication process, holes in the GaAs/AlGaAs epitaxial layers are etched with phosphoric acid solution to expose GaAs substrate. At the second stage, citric acid based solution is used to release the AlGaAs structure. Since the second solution is selective with respect to AlGaAs, the vertical and lateral etching of underlying GaAs results in releasing of AlGaAs suspended beam structure.

As an etching mask, a positive photoresist AZ 1813 was used. The structures of beams, crosses and bridges with different widths and lengths were patterned by the

photolithography method. A section of the mask pattern is shown in Fig. 3. The beam width was designed in three basic dimensions: 7, 16 and 24 μm.

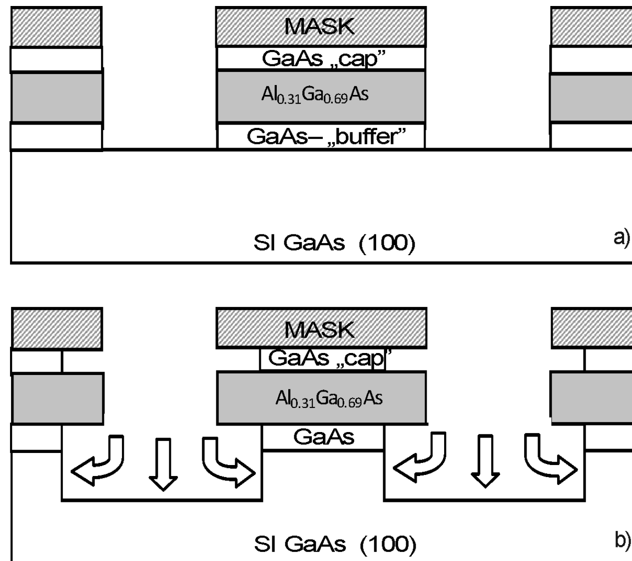

Fig. 2. Schematic presentation of two stages of fabrication of a suspended beam:
a) photolithography and nonselective etching of the heterostructure,
b) selective etching of GaAs substrate and releasing of AlGaAs layer

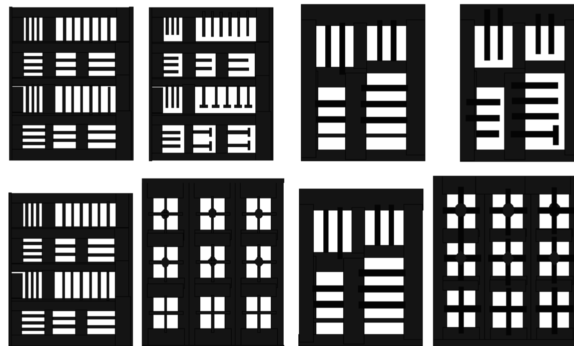

Fig. 3. A module of etching mask pattern with the structures for fabrication of suspended bridges, beams and masses

3. Results and discussion

SEM images of etched structures after the first stage of etching are shown in Fig. 4. The etching was carried out in phosphoric acid solutions (Table 1). No significant differences in the etching results obtained in “fast” and “slow” etching solutions

were observed. In both cases SI GaAs surface was exposed. Depending on the composition of the etching solution, the duration of etching process was 15 or 1.5 min, respectively.

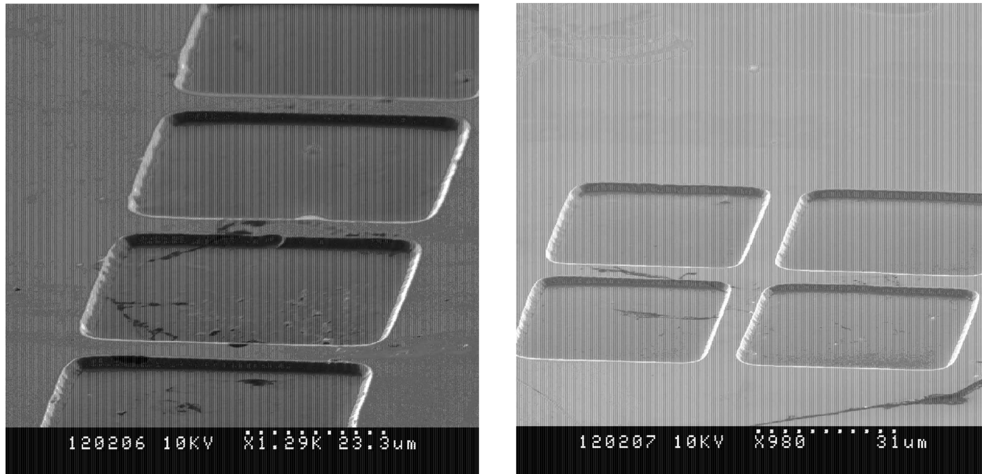

Fig. 4. SEM images of etched structures after the first stage of fabrication process (etching in phosphoric acid)

In the second stage, the structures were etched in citric acid solution assuring etching selectivity of AlGaAs over GaAs. SEM images of released beam structures with the width of 7 μm are shown in Fig. 5. The AlGaAs layer provided almost perfect etch stop to the etching solution, withstooding a prolonged etching process even after collapsing of the photoresist mask.

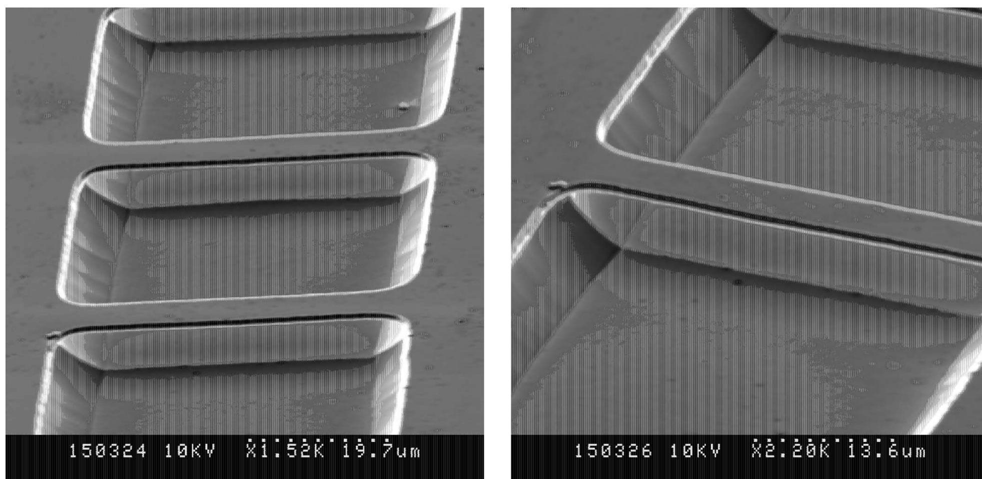

Fig. 5. SEM images of released AlGaAs structures

The release of beams was possible only in one crystallographic direction. The structures containing crossed beams were linked with the substrate even after a prolonged etching time (Fig. 6).

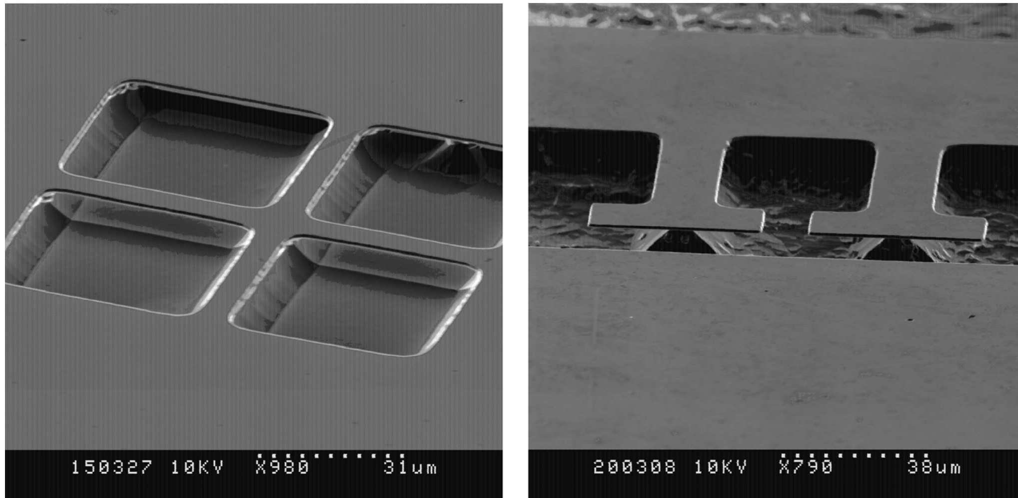

Fig. 6. SEM images of cross structures with released and not released beams

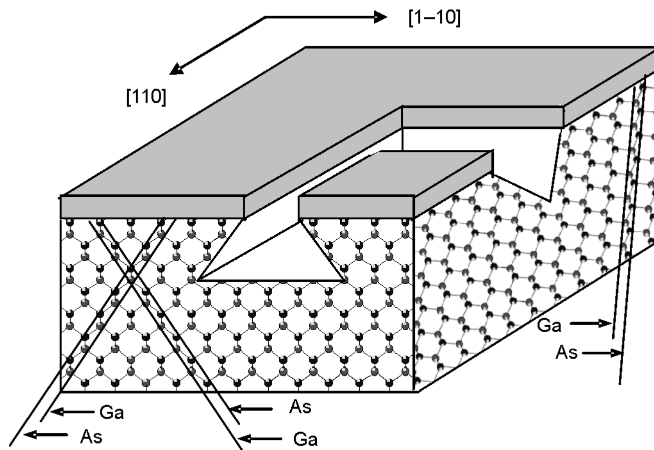

Fig. 7. Schematic presentation explaining different shapes of grooves etched in GaAs in [110] and [1–10] crystallographic directions

The process of etching of monocrystalline GaAs in majority of acid solutions is strongly affected by the etch rate anisotropy. The fact stems from the crystal structure of GaAs which causes that different crystallographic planes are etched with different etch rates. The planes with the lowest etch rates form a lateral profile of etched concave structures. Usually, these are (111) planes, which are the most densely populated.

In GaAs, the (111) planes can be either Ga or As terminated. The (111) planes of A-type – terminated by Ga atoms, are characterized by the lowest etch rates. In (001) oriented GaAs wafers, the planes are situated in two crystallographic directions: [110] and [1–10]. In these two directions, the (111) A-type planes are inclined either at obtuse or acute angles with respect to the wafer surface. It makes that concave structures etched in (001) wafers may form holes with either triangular or trapezoidal cross-sections (Fig. 7).

Only the structures with (111) planes of A-type, inclined at acute angles toward the substrate have a chance to be released in an anisotropic etching process. Therefore, an appropriate mask pattern layout is of crucial importance in the fabrication process. To obtain released crossed structures, the etching solution with isotropic character, assuring also selectivity of etching of GaAs over AlGaAs, should be employed. Work on the development of such etching formulas is in progress.

Acknowledgements

This work has been supported by a statutory grant no R02 018 02 granted by Polish Ministry of Science and Information Society Technologies.

References

[1] LECLERCQ J.L., RIBAS R.P., KARAM J.M., VIKTOROVITCH P., Microelectron. J., 29 (1995), 613.
[2] LATINSKY P., BURIAN E., DRZIK M., HASCIK S., MOZOLOVA Z., KUZMIK J., J. Micromech. Microeng., 10 (2000), 293.
[3] IWATA N., WAKAYAMA T., YAMADA S., Sens. Actuat. A, 111 (2004), 26.
[4] CLAWSON A.R., Mat. Sci. Eng., 31 (2001) 1.

Received 28 April 2007
Revised 16 February 2008

Materials Science-Poland, Vol. 26, No. 1, 2008

Structure of 310S steel-based Fe–Cr–Ni coatings

B. KUCHARSKA*

Institute of Materials Engineering, Częstochowa University of Technology
al. Armii Krajowej 19, 42-200 Częstochowa, Poland

Parameters have been presented of fabrication and characterisation of microcrystalline coatings applied by the magnetron sputtering method in a pure Ar atmosphere at the pressure of 0.03 Pa and the table voltage of –50 V. Coatings of the AISI 310S steel were applied on an AISI 310S steel substrate for 1 h. The characterization of the coatings in terms of phase composition was made by the XRD, GXRD and TEM techniques. It was found that the coatings have a columnar bcc-type structure, different from that of steel being sputtered. In the coating structure, an fcc phase has also been found by the TEM technique. The bcc structure is metastable, and as early as after 15 min of annealing at 600 °C it transforms into the fcc phase but a certain amount of unconverted bcc phase remains in the structure. The texture of the bcc structure varies along the coating thickness starting from (211) at the substrate to (110) in near-surfacial part. The transformation of the metastable bcc phase into the fcc phase as a result of 30 min annealing at 600 °C does not remove the texture but changes the crystallographic texturing plane $(211)_{bcc}$ to $(220)_{fcc}$.

Key words: *microcrystalline coating; magnetron sputtering; columnar structure*

1. Introduction

The magnetron sputtering deposition (MSD) method is one of the basic and most important methods of vacuum deposition (PVD). It is successfully used to deposit thin coatings for a wide range of applications, such as electronic equipment and magnetic recording media, as well as for improving the wear resistance, corrosion resistance and heat resistance of elements. The MSD technique parameters include Ar pressure in the magnetron chamber, substrate temperature, the distance between the targets and the surface being coated, and the magnitude of voltage applied to the substrate [1, 2]. In an investigation into the optimization of the MSD process, a correlation between the process parameters and the properties and microstructure of coatings has been found. The process parameters define the coating deposition rate which, in turn, determines the size of grains in the coatings and their hardness.

---

*E-mail: bratek@mim.pcz.czest.pl

Coatings of corrosion resistant steels, widely used in industrial conditions, exhibit increased resistance to oxidation, corrosion and erosion compared to steels of the same composition. The most modern grades of austenitic steels, including 310S steel, are also used for coatings [3–6]. Under normal conditions (including sub-zero treatment), these steels have an austenitic structure resulting from the stabilizing effect of Ni. However, during the deposition of coatings of these steels by the PVD methods such as magnetron sputtering, metastable phases of the bcc structure may form in the coatings, despite the amount of nickel being as high as 25% [7]. It was found that more Ni was necessary to stabilize the fcc phase in sputtered Fe–Cr–Ni steels. The fcc single phase can be formed at room temperature in as-sputtered 330S steel coatings (36 wt. % of Ni) [8].

The paper presents results of the X-ray examination of the phase composition of AISI 310S steel coatings deposited by the magnetron method on an AISI 310S steel substrate. The phase structure on the coating cross-section was examined immediately after deposition and after a short-duration annealing at 600 °C.

2. Material

Coatings of 310S heat-resisting steel, deposited on a substrate of the same steel by the magnetron sputtering method, were examined. The starting steel had an austenitic structure with numerous precipitates of chromium carbide. The magnetron targets were two discs, each of the dimensions of 63×49×2 mm^3, and those of the coating substrate were 10×10×1 mm^3 commercial sheet cut-outs of the same steel grade. Prior to the deposition of coatings, the steel surface was cloth buffed and washed with acetone in an ultrasonic washer. After suspending the cut-outs in the magnetron vacuum chamber, both the coating substrate surfaces and the targets were additionally cleaned for several minutes by a glow-discharge method under an argon pressure of approx. 3 Pa. During coating deposition, the temperature of the cut-outs was ca. 150 °C. Other parameters of the magnetron deposition process were as follows: argon flow pressure 0.03 Pa, table polarization potential –50V, and the distance between the targets and the substrate 200 mm. Two targets situated opposite to one another, each of a power of 3 kW, were used. The time of coating deposition was 1 h.

Table 1. Chemical composition of the substrate/targets (standard) and the coating (EDX analysis), wt. %

Steel	C max	Si max	Mn max	S max	Cr	Ni	Fe
310S	0.1	1.5	2.0	0.015	24–26	19–22	rest
coating	–	0.7	1.3	–	25.8	18.6	53.7

In the previous investigation, a uniform dispersion of constituent elements in coatings of this composition and deposited with this method was shown. EDX measure-

ments showed that the chemical composition of coatings corresponded to the contents of alloying elements in the 310S steel used for the targets. The Ni content was at the level of 19 wt. % (Table 1). An analysis on the coating cross-section also showed a uniform distribution of constituent element over the coating thickness [9]. The coating thickness, as determined microscopically, was 8.5 μm.

3. Experimental

The coatings were subject to observations using an electron transmission microscope Philips CM 20 and examined on a Seifert 3003TT polycrystalline diffractometer. The coating cross-sections were subject to examination by TEM. The XRD examination was performed directly on the coating surfaces using filtered $K_{\alpha}Co$ (0.17902 nm) radiation. The X-ray examination was carried out by the classical method in the diffraction angle range 2θ of 40–110° and by the constant-angle exposure method in the angular range of occurring reflections (111) from the fcc phase and (110) from the bcc phase [9]. In X-ray measurements on a diffracted beam, long Soller slits were used, which limited the diffusion of the diffracted beam to 0.4°. The intensity of diffraction reflections was measured with a stepwise counter shift of 4 s/step. The Bragg angles were read out from the reflection maxima. Coatings as magnetron-deposited (after 2 months of storage at room temperature) and coatings subject to one-time and two-time annealing at 600 °C for 15 min were examined. The annealing was carried out in ambient atmosphere.

3. Results

The coatings examined had a globular surface morphology, typical of magnetron-deposited coatings. On their cross-sections, the coatings had a columnar structure. Due to a local insufficiently tight adhesion of columns to one another, discontinuities occured within the coating. A separation of columns appeared on substrate irregularities (Fig. 1).

The XRD analysis, performed in the symmetric diffraction geometry, showed that, in spite of the fact that the austenitic steel targets had been sputtered, the coating had a ferritic bcc structure (Fig. 2). In the angular range applied, the diffraction pattern obtained from the 310S steel contains reflections typical of the fcc austenitic structure (111), (200) and (220). In the diffraction pattern obtained from the coating, weak reflections from the fcc phase occur, similar as in the substrate steel, but reflections from the bcc phase are dominant. The bcc phase is characterized by a strong texture of (211) planes and an abnormally weak (110) reflection. Due to the coating thickness (8.5 μm) being smaller than the depth of $K_{\alpha}Co$ radiation penetration into the coating material, the reflections from the austenitic phase originate from the substrate.

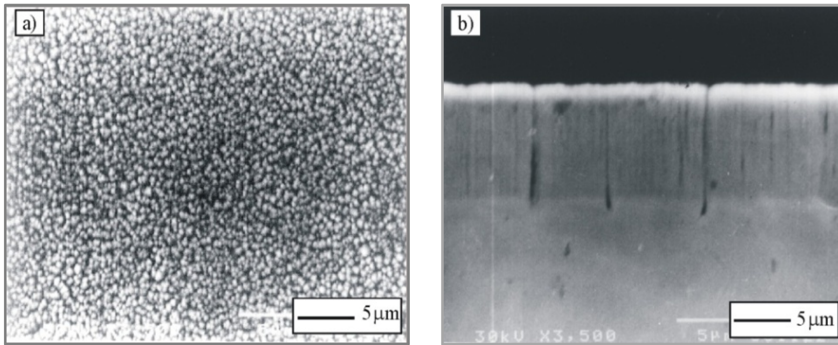

Fig. 1. Globular morphology of the coating surface (a) and the coating cross-section with a visible column separation on substrate surface irregularities

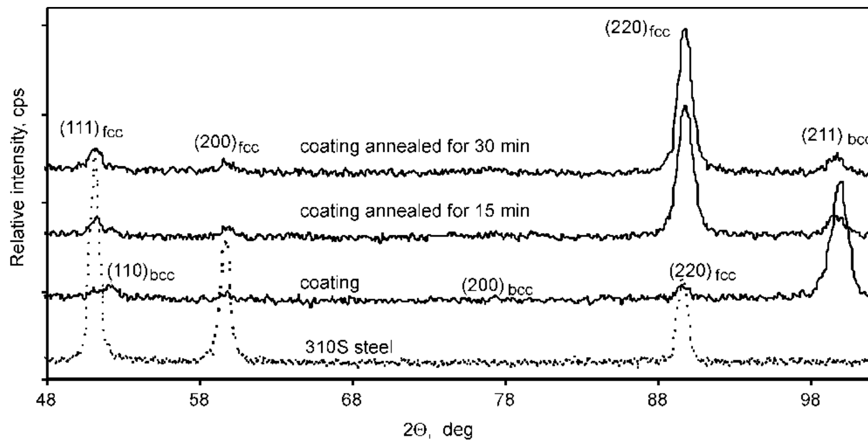

Fig. 2. Diffraction patterns of 310S steel and coating before and after annealing at 600 °C in air atmosphere (the intensities of reflections from the steel has been decreased respectively); the details are given in Table 2

Table 2. Details of the diffraction patterns shown in Fig. 2

d, nm	0.207	0.203	0.180	0.143	0.126	0.117
Structure	fcc	bcc	fcc	bcc	fcc	bcc
Relative intensity, %						
310S steel	100	–	61	–	42	–
Coating	10	19	9	7	14	100
Coating, 15 min	21	–	12	9	100	19
Coating, 30 min	19	–	12	6	100	15

Diffractions from the coating cross-sections, obtained using the electron transmission microscopy, also indicated a predominance of the bcc phase in the coating structure. In the electron diffraction image, beside the strong reflections from the bcc phase, weak reflections from the fcc phase also appear. This means that small amounts of the fcc phase are present in the coating structure (Fig. 3b).

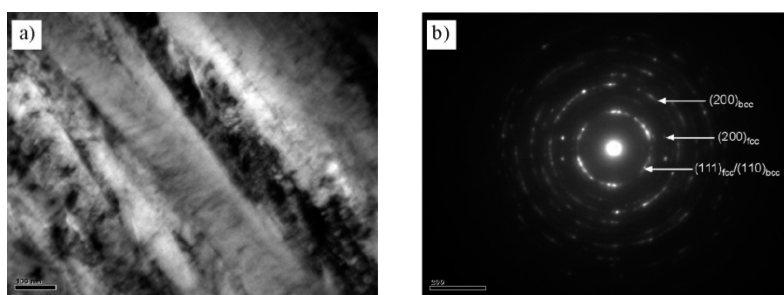

Fig. 3. Highly defected bcc phase columns in the coating (a)
and the electron diffraction from the coating at its mid-thickness (b)

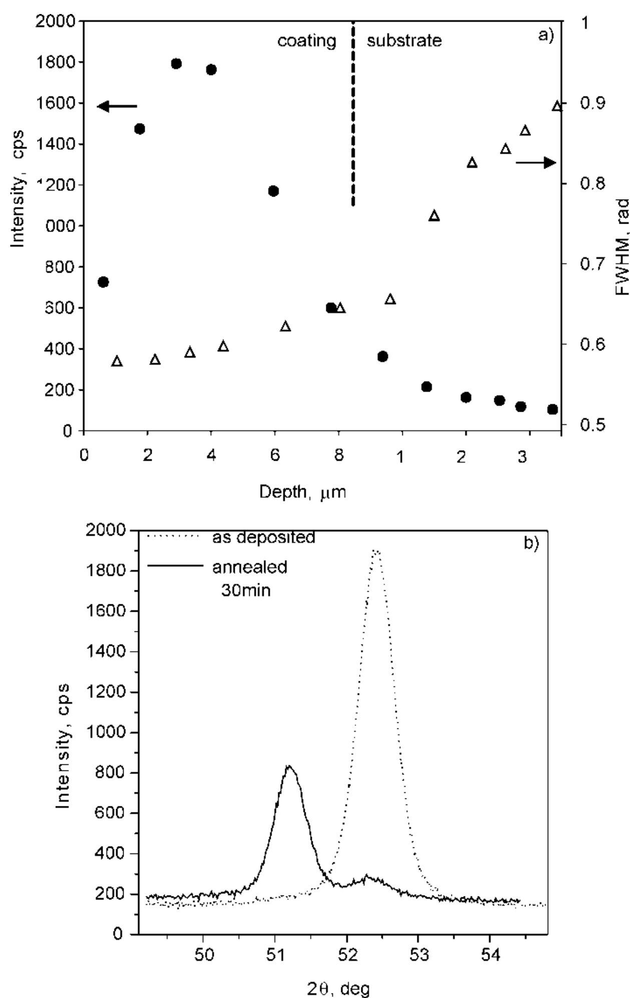

Fig. 4. Intensity of reflection 110 as a function of measurement depth (a)
and comparison of main reflections of as deposited or annealed at 600 °C/30 min
310S steel determined for the coating at the depth ca. 3 μm (b)

The TEM observations indicate that the bcc phase columns have diameters ranging from 0.2 μm to 0.5 μm and exhibit features of highly defected structures (Fig. 3a). The degree of structure defecting (and the associated size of subcrystallites) increases from the coating surface towards the substrate. The electron diffractions from the outer part of the coating are typical of polycrystalline structures. The diffractions from the coating near the substrate exhibit more continuous rings typical of amorphous structures. Figure 3 shows an intermediate diffraction image, obtained in the area of the coating mid-thickness. The defecting of the coating structure was also reflected in the profile of diffraction peaks obtained in GXRD examinations and originating from deeper coating layers, through decreasing their intensity and increasing their half-intensity width (Fig. 4a). The highest intensity of reflection (110) from the bcc phase was determined for the measurement depth in the range of 3–3.5 μm (Fig. 4a).

After short annealing, the diffraction image of the coatings totally changed. As early as after 15 min of annealing at 600 °C, the bcc and the fcc phases coexist in the coating. Intensities of the (110) reflections from the bcc phase decreased, and the fcc phase was predominant in the coating. The transformation of the metastable phase bcc into the fcc phase did not remove the coating texture. As a result of the change in crystallographic structure, the texture of (211) planes in the bcc phase was taken over by planes of the (220) type in fcc phase. Re-annealing of the coating under the identical conditions did not result in any changes in the coating structure. A summary of the relative intensities of reflections recorded after annealing of the coating is given in Table 2. In the diffraction image of the annealed coatings, similarly as for the non-annealed coating, the reflections from the fcc phase can be partially summed with the reflections from the coating substrate, since in the classical measurement the beam of radiation penetrated into a depth greater than the coating thickness, whereas the reflections from the bcc originate solely from the bulk of coating. In Figure 4b diffraction patterns obtained by the GXRD methods for measurement depth corresponding to intensity maximum read from Fig. 4a are compared. It results from these diffractogramms that after 30 min of annealing at 600 °C certain amount of bcc phase in the coating structure remained which did not undergo transformation. Because of texturization, a direct evolution of phases concentration is hard to accomplish. The set of diffractions determined for various depths of X-ray penetration into as deposited 310S coating has been demonstrated elsewhere [10].

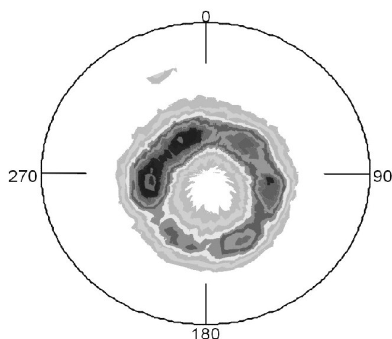

Fig. 5. Polar figure of {111} planes; coating annealed at 600 °C for 15 min

5. Discussion

Chemical composition of coatings (EDX analysis performed from the coating cross-section) was contained within the quantitative limits specified for 310S steel. The amount of austenite-stabilizing Ni corresponded to the lower limit of content specified for 310S steel. Thus, during the magnetron deposition of coatings, the Cr/Ni quantitative ratio, which would have changed the steel structure to bcc, did not change. This indicates that in the process of magnetron deposition of the coatings under investigation, factors determining phase compositions of the coatings are the deposition process parameters. Two-phase composition of the tested coatings which has been obtained in the process conditions is in good agreement with the "substrate temperature-Ni contents" for sputtered austenitic steels diagram presented by Zhang et al. [6]. As results from this diagram, monophase austenitic structure in sputtered 310S steel is formed upon substrate temperature exceeding 200 °C. The structure of 310S steel-based coatings on 310S substrate has also been tested by Liu et al. [4], however, the thickness of the coatings was much lower than those examined in the present paper. The authors found monophase bcc structure of the coatings although they did not mention the substrate temperature. As results from the empirical diagram [6], formation a pure bcc phase at temperatures higher than 0 °C is impossible. One can assume that the coating thickness and rate of its deposition may affect phase composition of the final coating. The coatings thickness certainly influences its texturization. Based on diffractogramms of as sputtered 310S steel (Figs. 2 and 4b) one may conclude that the bcc phase shows a strong texturization of (211) planes at the substrate whereas in near-surfacial parts the (110) planes texture predominates.

It was also found that the bcc phase transformation into fcc phase takes place just after annealing of sputtered 310S steel at 600 °C during 15 mins. This temperature is clearly lower than that reported in literature (700 °C/1 h and 800 °C/20 min) [6]. Malavasi et al. [11] reported a constant disorientation of planes in the bcc phase around the axis perpendicular to the coating substrate. The same disorientation in a converted fcc phase was additionally demonstrated in this paper.

6. Conclusions

310S austenitic steel-based Fe–Cr–Ni coatings magnetron-deposited on a substrate of the same steel exhibited (with the process parameters applied) a structure of a bcc type with slight amounts of fcc phase detectable by TEM technique. The bcc columnar structure exhibits a texture which varies along the coating thickness from (211) at the substrate to (110) in near-surfacial parts of the coating.

The bcc structure is metastable, and as early as after 15 min of annealing at 600 °C it transforms into the fcc phase. A certain amount of unconverted bcc-phase remains in the structure.The transformation of the metastable bcc phase into the fcc phase during

30 min annealing at 600 °C does not remove the texture, but it changes the texturing planes from $(211)_{bcc}$ to $(220)_{fcc}$.

References

[1] KUKLA R., Surf. Coating Techn., 93 (1991), 1.
[2] WINDOW B., Surf. Coating Techn., 71 (1995), 93.
[3] GRUNDY P.J., MARSH J.M., J. Mater. Sci. Lett., 13 (1978), 677.
[4] LIU Z., WANG G., GAO W., Mater. Charact., 54 (2005), 466.
[5] GODBOLE M.J., PEDRAZA A.J., ALLARD L.F., GEESEY G., J. Mater. Sci., 27 (1992), 5585.
[6] ZHANG X., MISRA A., SCHULZE R.K., WETTELAND C.J., WANG H., NASTASI M., J. Mater. Res., 19 (2004), 1696.
[7] MALAVASI S., OUELDENNAONA A., FOOS M., FRANTZ C., J. Vac. Sci. Techn., 5 (1987), 1888.
[8] ZHANG X., MISRA A., SCHULZE R.K., WETTELAND C.J., WANG H., NASTASI M., J. Mater. Res., 19 (2004), 1696.
[9] KUCHARSKA B., WENDLER B., DANIELEWSKI M., Inż. Mater., 3 (2006), 463 (in Polish).
[10] KUCHARSKA B., Inż. Mater., 3–4 (2007), 419 (in English).
[11] MEUNIER C., VIVES S., BERTRAND G., Surf. Coating Techn., 107 (1998), 149.

Received 28 April 2007
Revised 16 February 2008

Materials Science-Poland, Vol. 26, No. 1, 2008

Application of flowable oxides in photonics

S. LIS[1*], R. DYLEWICZ[1], J. MYŚLIWIEC[2], A. MINIEWICZ[2], S. PATELA[1]

[1]Faculty of Microsystem Electronics and Photonics, Wrocław University of Technology,
ul. Janiszewskiego 11/17, 50-372 Wrocław, Poland

[2]Institute of Physical and Theoretical Chemistry, Wrocław University of Technology
Wybrzeże Wyspiańskiego 27, 50-370 Wrocław, Poland

Polymer hydrogen silsesquioxane (HSQ) solution in methyl isobutyl ketone (MIBK) commercially known as FOx (flowable oxide) is an alternative material to silicon dioxide obtained by chemical deposition. Standard process to obtain amorphous SiO_2 film from polymer HSQ includes: deposition by spin coating, removal of solvent by softbake on hotplate and oxidation of materials by heating in an oven or oxygen plasma treatment. Having parameters similar to those of SiO_2, polymer HSQ after softbake is sensitive to an electron beam and also to wavelengths below $\lambda = 157$ nm. Due to those factors, it can be used as a high resolution (20 nm details) negative mask in next generation lithography and in e-beam lithography. Removal of FOx after hardbake is possible only with dry etching or in HF solution. The paper reports on possibilities of application of HSQ polymer for integrated optoelectronics. Technology of obtaining an SiO_2 layer from HSQ polymer is described. Measurements of thickness, refractive index and transmittance from 200 nm to 800 nm are reported for the fabricated layers.

Key words: *hydrogen silsesquioxane; polymer HSQ; flowable oxide photonics*

1. Introduction

Integrated optics is one of the most rapidly growing areas of science. The material base for optoelectronics devices and photonics structures is still growing. New methods for fabrication of optoelectronic structures or modification of existing ones are continuously created, and new materials are used in those processes. One of the materials, polymer hydrogen silsesquioxane (HSQ), is especially promising in nanoengineering applications. Most popular use of HSQ is a high-resolution negative inorganic e-beam resist. Trellenkamp [1] reported 20 nm wide lines fabricated from HSQ using electron beam lithography. HSQ is sensitive to radiation below $\lambda = 157$ nm [2] and behaves like a negative photoresist for these wavelengths. However, due to low

*Corresponding author, e-mail: szymon.lis@pwr.wroc.pl

sensitivity, it has been considered useless for next generation lithographies (NGLs). On the other hand, this low sensitivity is related to high resolution capabilities of HSQ. Peuker [2] proposed use of “mix-and-match” combinations of e-beam lithography with NGLs. Another idea is to use HSQ in room temperature nanoimprint lithography. The pattern is transferred to suitably prepared HSQ polymer. According to Chen [3], details of size from micrometric scale down to sub 100 nm have been successfully fabricated. A possibility to replace PECVD SiO_2 used as a mask in dry etching process by HSQ amorphous silica has also been investigated. Lauvernier [4] applied HSQ as a mask in RIE technique on GaAs. The value of etching selectivity was compared to PECVD SiO_2 relative to GaAs. For HSQ polymer, selectivity varied from 3 to 7 depending on oxidation conditions. The best results were obtained for oxidation in oxygen plasma. Silicon dioxide fabricated by PECVD method exhibits etching selectivity to GaAs of about 7.

In this paper, results of our investigation of optical parameters of layers fabricated with HSQ polymer are presented. HSQ amorphous silica layers are compared to PECVD SiO_2 and thermal oxides.

2. Experimental

Silicon wafers were spin coated with FOx®-13 from DowCorning HSQ solution in methyl isobutyl ketone (MIBK). Surfaces were cleaned in butyl alcohol, acetone, isopropyl alcohol and baked at 200 °C for 30 minutes directly before coating. According to the producer, it is possible to achieve amorphous silicon dioxide of the thickness between 174 nm and 333 nm from FOx-13. The applied procedure consists in spin-coating of the material, solvent removal and densification by baking on a hot plate for 120 s at 150 °C and next for 120 s at 220 °C. The layers were transformed to amorphous silica by curing at 325 °C for 60 min. Their thicknesses and refractive indices were measured using a single wavelength ellipsometer EL-7 at λ = 632.8 nm. Standard deviation of the ellipsometer for thickness measurements is $\sigma_t = \pm 1.2$ nm, and for the refractive index $\sigma_n = \pm 0.006$. Transmittance was measured with a spectrophotometer Thermospectronic, UNICAM UV 300 at the wavelength range 200–800 nm. Beside measurements of HSQ layers, thermal silicon dioxide (t = 200 nm) and PECVD SiO_2 (t = 128 nm) were also measured.

3. Results

3.1. Thickness and refractive index

The samples were prepared at various rotational speeds to characterize the process of coating. Table 1 presents results of thickness measurements. Due to a high level of

contamination of air in the laboratory, it was not possible to obtain high quality films at 1000 rpm. The best layers were obtained at 4000 rpm. (Fig. 1).

Table 1. Thicknesses of films obtained with various rotational speeds of a spin-coater

Np.	Rotational speed [rpm]	Thickness [nm]	Refractive index	Conditions
1	1000	–	1.386	$T = 21$ ºC $H = 36\%$
2	2000	242		
3	3000	200		
4	4000	162		
5	5000	150		
6	6000	138		

Fig. 1. Thin layers of spin-on dielectrics (HSQ polymer) coated at various rotational speeds: a) 1000 rpm, b) 2000 rpm, c) 3000 rpm, d) 4000 rpm, e) 5000 rpm

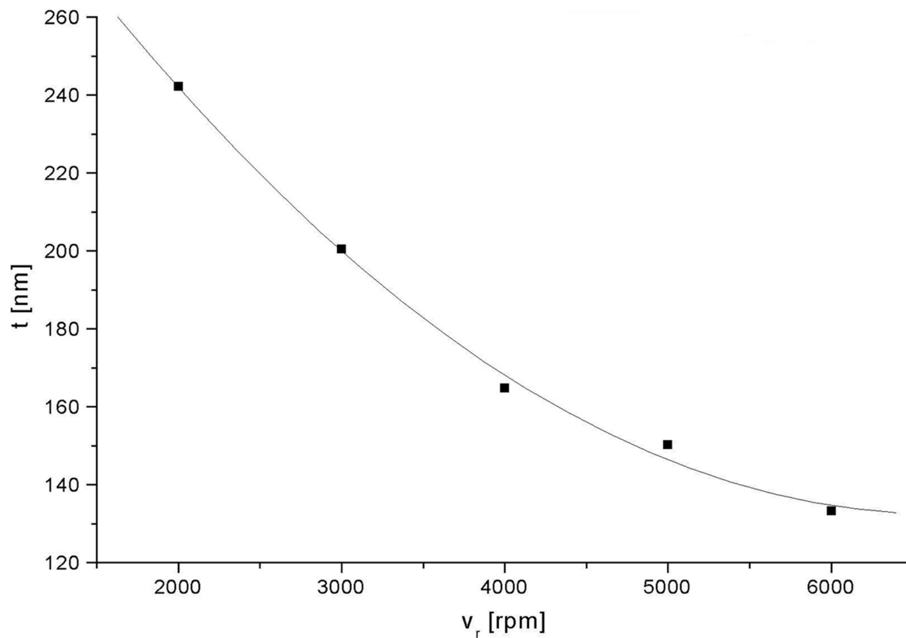

Fig. 2. Dependence of thickness of HSQ layers on the rotational speed of a spin-coater

The dependence of thickness on the rotational speed for fabricated layers is presented in Fig. 2. Parabolic type of dependence is typical of spinned material, being a result of faster solvent evaporation at higher rotational speeds. Measurement points were approximated by a 2nd degree polynomial, to allow thickness prediction in future processing:

$$t = 356.02 - 0.06714V_r + 5.04286\times10^{-6}V_r^2 \quad (1)$$

where t is the layer thickness [nm], V_r – rotational speed of a spin-coater [rpm].

Table 2. Refractive indices of SiO_2 films fabricated by various methods

Technology	Refractive index
HSQ SiO_2	1.398
Thermal SiO_2	1.450
PECVD SiO_2	1.477

Table 2 shows results of measurements of refractive indices for silica films fabricated by various methods. The refractive index for silica obtained from HSQ polymer has the lowest value of n equal to 1.398 whereas thermal dioxide has n = 1.450 at λ = 632.8 nm. The imaginary part of refractive index is very small: $k = 8.8\times10^{-6}$ at λ = 632.8 nm for HSQ SiO_2. In [2] it is stated that the real refractive index stays constant from 400 nm to 800 nm and is equal to 1.4. In the common PECVD process, the presence of impurities is possible as SiO_2 is obtained from silane gases e.g., SiH_4. SiO_2 from HSQ polymer was obtained by chemical polymerization, and some residues of solvent may remain in amorphous SiO_2 structures.

3.2. Reflectance

Reflectance was measured for silica films fabricated by various methods: thermal silica (t = 200 nm), PECVD (t = 128 nm) and for silica from HSQ (t = 162 nm) for various oxidation times: 0, 60 and 120 minutes (Fig. 3). Visible features of the spectra are most probably related to light interference within the films and onset of molecular absorption in near infrared region. Generally, spectra of PECVD, FOx and thermal oxides are very similar. However, the peak at λ = 700 nm does not occur for thermal silica. Other peaks are related to light interference in a film, for FOx layer (t = 162 nm, n = 1.398) the theoretical wavelengths of interference occur at λ = 300 nm and λ = 181 nm for the interference orders m = 1 and 2, in agreement with results shown in Fig. 3. The shifts of peaks for other samples are reflected in the differences of optical paths of light. As was mentioned previously, the maximum at λ = 715 nm (1.73eV) is related to molecular absorption. This peak is not observed in thermal oxide and is sup-

posedly due to absorption of some sort of residues remaining after chemical processing or is a result of differences in the structure of oxides.

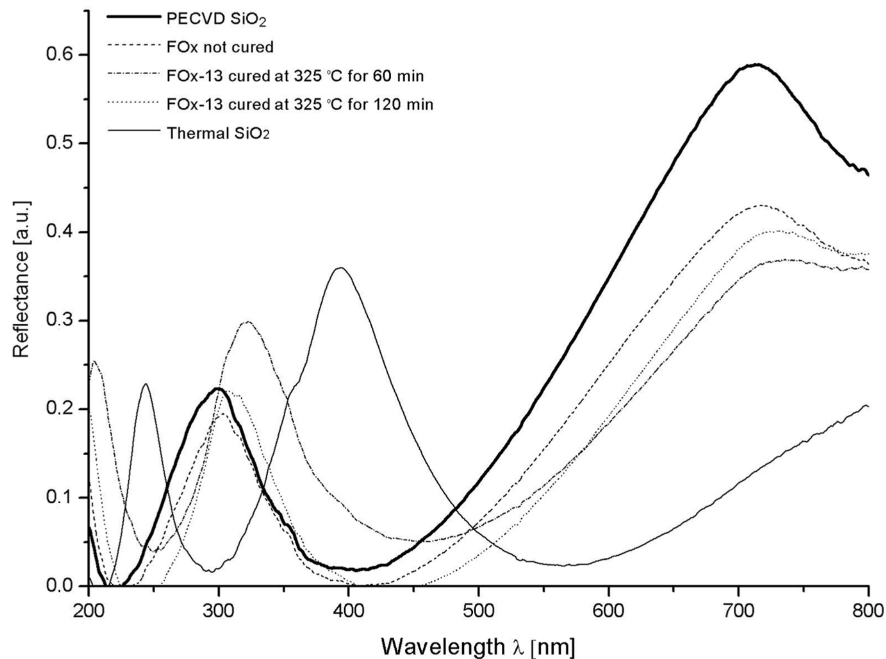

Fig. 3. Reflectance spectra of silicon dioxide prepared by various procedures

4. Conclusion

Optical properties of thin SiO_2 layers obtained from HSQ polymer were investigated. Comparison of FOx to PECVD and thermal silicon dioxide has also been reported. Beside standard application of FOx as a high resolution negative e-beam resist and other typical technological applications like mask in dry etching process, silica layers fabricated from HSQ polymer can be used in integrated optics. Possibility of achieving good quality films with a specific thickness and low refractive index is promising for usage of this material in fabricating grating couplers or optical surface for planar waveguides. The biggest advantage of HSQ polymer is the possibility to obtain amorphous SiO_2 thin layer on any surface, similar to PECVD silica, simply and relatively cheap.

Acknowledgements

This work has been supported by Polish State Committee for Scientific Research during 2006–2009 under Grant No. 350-730 W12.

References

[1] TRELLENKAMP S., MOERS J., VAN DER HART A., KORDOS P., LUTH H., Microelectr. Eng., 67–68 (2003), 376.
[2] PEUKER M., LIM M.H., SMITH H.I., MORTON R., VAN LANGEN-SUURLING A.K., ROMIJN J., VAN DER DRIFT E.W.J.M., VAN DELFT F.C.M.J.M., Microelectr. Eng., 61–62 (2002), 803.
[3] CHEN Y., TAO J., ZHAO X., CUI Z., SCHWANECKE A.S., ZHELUDEV N.I., Microelectr. Eng., 78–79 (2005), 612.
[4] LAUVERNIER D., GARIDEL S., LEGRAND C., VILCOT J.P., Microelectr. Eng., 77 (2005), 210.
[5] O'FAOLAIN L., KOTLYAR M.V., TRIPATHI N., WILSON R., KRAUSS T.F., J. Vac. Sci. Techn. B, 24 (2006), 336.

Received 28 April 2007
Revised 16 February 2008

Materials Science-Poland, Vol. 26, No. 1, 2008

Application of microelectrodes for investigation of the oxygen electrode reaction in selected solid electrolytes

A. RAŹNIAK*, P. TOMCZYK

Faculty of Fuels and Energy, AGH University of Science and Technology,
al. Mickiewicza 30, 30-059 Krakow, Poland,

In a solid oxide fuel cell (SOFC), the most often used solid electrolyte is yttria stabilized zirconia. Usually, SOFC of a tubular geometry operates at ca. 1000 °C. To decrease the temperature of the cell, it is necessary to reduce the thickness of electrolyte or replace yttrium-stabilized zirconium with an other electrolyte of a much higher ionic conductivity. A potential candidate for an electrolyte in intermediate temperature SOFC is gadolinia doped ceria. The largest energetic losses in a fuel cell of this type, apart of ohmic polarizations, are attributed to slow kinetics of the cathodic process. In this work, investigated oxygen electrode reaction for two various electrolytes: yttria stabilized zirconia and gadolinia doped ceria. The measurements were conducted using microelectrodes for which analysis of kinetic parameters of the electrode reaction is easier. Gold electrodes were applied in the experiments. Although Au is a good electrocatalyst for oxygen reduction, almost no research has been done for this metal so far. The performance of the electrode and results of impedance measurements have been presented and discussed.

Key words: *fuel cell; oxygen electrode; microelectrode; solid electrolyte; YSZ; GDC*

1. Introduction

Solid electrolytes with high oxygen ion conductivity are of special interest for their application in high temperature electrochemical systems such as solid oxide fuel cells (SOFC), oxygen sensors and oxygen pumps. Fuel cells are efficient generators of electric energy. They are usually fed with a fuel produced by reforming of natural gas. Among fuel cells, SOFCs are one of the most promising energy converters with a great potential for high efficiency and low pollution [1, 2]. Generally, yttria stabilized zirconia (YSZ) is used as an electrolyte material in SOFCs operating at 800–1000 °C. Reduction of the operating temperature allows one to use cheaper construction materials and more reliable seals in the cell. Thus, investigations aimed at de-

*Corresponding author, e-mail: razniak@agh.edu.pl

creasing the operating temperature down to 500–700 °C are often focused on new electrolyte materials [3]. Gadolinia (CGO) or samaria doped ceria (CSO) are attractive candidates for electrolytes which could be employed in the intermediate temperature solid oxide fuel cells (IT-SOFC). IT-SOFC can be used in small scale combined heat and power applications (e.g., stand-alone residential units), remote location power generators and also for transport means [4, 5].

Although the thermodynamics of YSZ and gadolinia doped ceria (GDC) is well understood, a controversy still persists on the mechanism and kinetics of the electrode processes occurring in these electrolytes. The most extensive research into processes occurring in SOFC has been made, by an analogy to a state-of-the-art fuel cell, for porous electrodes. One of possible reasons for unsatisfactory understanding of the oxygen electrode reaction in solid ionics is the fact that porous electrodes have complex and difficult to determine structure and geometry. To avoid problems associated with porous electrodes at solid state electrolytes, a number of researchers have used a concept of microelectrodes, well known from liquid electrochemistry. In the solid state electrochemistry, the microelectrodes are frequently applied in polymer electrolytes whereas they are less commonly employed in ionic solids.

2. Experimental

This work is aimed at comparison of the kinetic parameters of the oxygen electrode reaction occurring in two solid electrolytes (YSZ and GDC) in analogous conditions. The work was done, first of all, for Au quasi-point electrodes because of two reasons:

- Regarding metallic electrodes, the papers published to date described almost exclusively the behaviour of Pt microelectrodes [6–8]. It is of interest to examine phenomena occurring at the microelectrodes made of materials other than Pt, e.g. Au, which is not much worse electrocatalyst for the oxygen electrode reaction than Pt.
- Au is more plastic than Pt at high temperatures. Therefore, in the conditions of high temperature measurement, a well defined contact between this metal and the electrolyte can be formed easier than in the case of Pt needle.

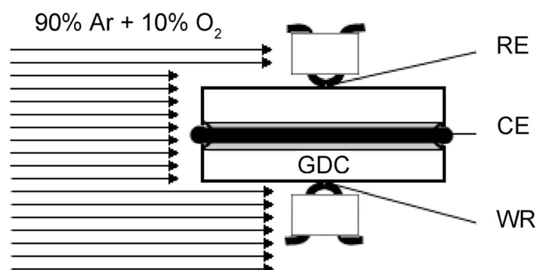

Fig. 1. Side view of the measurement cell: RE – reference electrode, CE – counter electrode, WR – working electrode

The side view of the measurement cell is shown in Fig. 1. The YSZ and GDC disks (10 mm in diameter and ca. 3 mm thick) were formed from powdered com-

pounds pressed isostatically under 250 MPa. Then, the samples were sintered for 2 h at 1500 ^{o}C in air. A co-precipitation calcination method was used to prepare powders of gadolinia doped ceria (with 20% mol Gd_2O_3) and yttria stabilized zirconia (8% mol Y_2O_3). Both disks were produced at the Faculty of Materials Science and Ceramics of AGH, University of Science and Technology in Cracow. The procedure was similar to this described in papers [9–11]. The XRD method was used to determine cell parameters of the samples.

Both flat sides of the disk were polished with a 2000 waterproof alumina abrasive paper and afterwards with 1 μm diamond paste. Two quasi-point electrodes were placed at the polished surfaces, one opposite to the other as is shown in Fig. 1. The quasi-point electrode was made by passing a wire 0.3 mm in diameter throughout two holes of alumina bead – one electrode was made of gold wire (working electrode) and the other from platinum wire (reference electrode). The platinum wire (0.3 mm in diameter), which was used as a counter electrode, was placed in a furrow grooved around the side surface of the disk just in the middle of the side. To improve contact between the Pt wire and the electrolyte, the furrow was smeared with a platinum paste. The electrodes and disk were assembled inside an alumina holder and gripped together due to action of springs with a force of about 0.5 N. The cell with the holder was then placed inside an alumina envelope, which provided a gas-tight separation from the outer atmosphere. Finally, the whole system was put into a horizontal electric furnace. An inlet of the gases was located a few millimeters from the side wall of the disk providing the gases to flow directly to the electrodes. A set up of gas flow controllers allowed one to control the composition and flow rates of gases introduced into the cell.

Before the experiment, the cell was heated to 900–1000°C and held at this temperature for about one hour. In these conditions, gold and platinum became soft and the quasi-point electrodes, pressed by the springs to the disk, increased contact areas between the metal and electrolyte. The contact areas and lengths of three phase boundaries could be determined after completing the experiments, when the cell was disassembled and the electrodes were examined with a scanning microscope.

The flattened part of the metal surface corresponded to the area being in direct contact with the electrolyte. An example of the view of the Au electrode after completing experiment with GDC electrolyte is shown in Fig. 2. In this case, the contact area of the Au electrode and length of three phase boundary were estimated geometrically at 0.15 mm^2 and 1.62 mm, respectively. All electrochemical experiments were performed at 700 °C under atmosphere of $0.1O_2 + 0.9Ar$ at ambient pressure. The flow rate of the gases into the electrochemical cell was equal to 50 cm^3/min. The potential of the Au working electrode was measured vs. the reference platinum quasi-point electrode, located at the opposite side of the disk. The chronoamperometric (CA) and electrochemical impedance spectroscopy (EIS) techniques were used in the measurements. Due to long-term effects of the electrode polarization, the dependences of the current on the time of polarization were recorded during at least 15 h. In the CA experiments, the microelectrodes were polarized stepwise from the rest potential down to –0.3 V

(for GDC to –0.6 V). To get additional information, the EIS was applied to determine and characterize the impedance of the electrode before the polarization and at the end of the potential step.

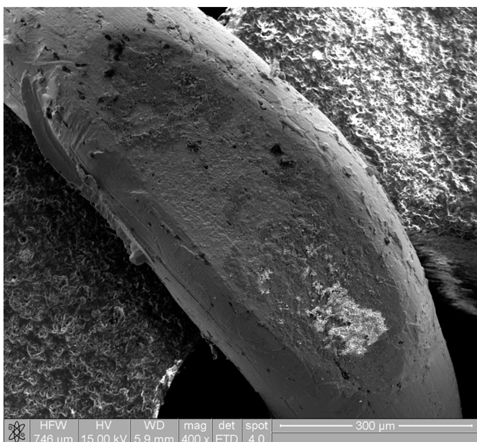

Fig. 2. SEM images of the flattened part of the Au electrode

The samples were measured with GPES (CA) and FRA (EIS) modules of an Autolab PGSTAT 30 interfaced with a computer. The impedance spectroscopy measurements were performed in the frequency range from 0.001 Hz to 1 MHz using 10 mV amplitude of the sinusoidal voltage. For analysis of the impedance data, a program provided by the producer based on a complex non-linear regression least-squares fit was used.

3. Results and discussion

According to Steele [12], the highest ionic conductivity of doped ceria is exhibited by $Ce_{0.8}Gd_{0.2}O_{2-x}$. The conductivities of gadolinia doped ceria at 700 °C determined by various authors [4, 12–20] are given in Table 1.

Table 1. Conductivities at 700 °C of gadolinia doped ceria $Ce_{0.8}Gd_{0.2}O_{2-x}$

σ_{el}/(mS·cm^{-1})	45.70	67.99	35.00	45.20	77.00	18.20	42.50	26.70	19.00	18.50	47.00	35.20
Reference	[13]	[14]	[14]	[15]	[12]	[16]	[17]	[17]	[18]	[19]	[4]	[20]

Considering the scatter in the data of conductivities (Table 1) determined by various authors, it should be emphasized that the actual values obtained are distinctly dependent on the bulk and grain boundary resistivity, i.e., they reflect different conditions of the sample fabrication [5].

In the case of metallic electrodes, the reaction occurs exclusively at the three phase boundary (TPB). Therefore, it is very important to determine the length of this boundary. The data presented further in this paper will be normalized vs. the length of TPB.

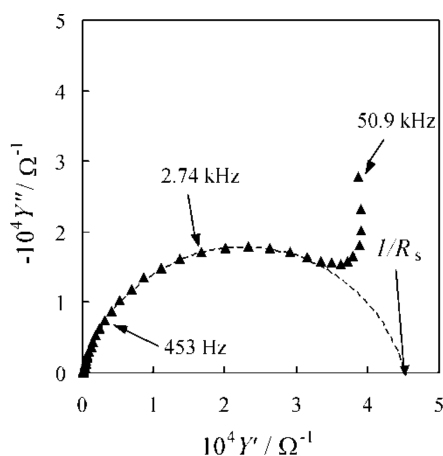

Fig. 3. Admittance complex plots for the Au quasi-point electrode placed at the YSZ electrolyte (temperature 700 °C, polarization potential –0.3 V, $p(O_2)$ = 0.1 bar)

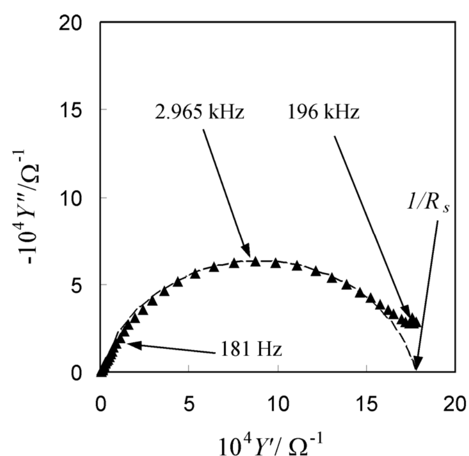

Fig. 4. Admittance complex plots for the Au quasi-point electrode placed at the GDC electrolyte (temperature 700 °C, polarization potential –0.3 V, $p(O_2)$ 0.1 bar)

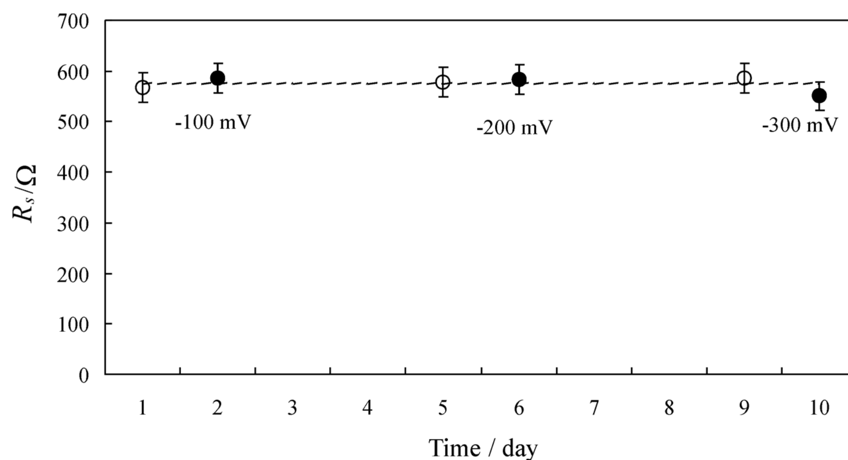

Fig. 5. R_s, resistance of the electrolyte, determined from the admittance complex plots for the Au quasi-point electrode placed at the GDC electrolyte. The empty and full circles correspond to the unpolarized and polarized electrode, respectively (temperature 700 °C, $p(O_2)$ 0.1 bar)

In Figures 3 and 4, the characteristic complex admittance plots of the Au electrode placed at the YSZ and GDC electrolytes are presented. For these plots, it is relatively easy to fit a semicircle representing polarization admittance of the oxygen electrode. The right crossing points of the semicircle with the Y' axis can by attributed to the total admittance of the electrolyte which comprises bulk and grain boundary effects. As can be seen in Fig. 5, the resistance of the electrolyte R_s, calculated from the admittance data, is independent of the duration of the experiment and polarization of the electrode. Determination of the electrode resistance from the complex impedance plots

(Figs. 6 and 7) is less precise because of a small number and uncertainty of experimental points in the required range of high frequencies.

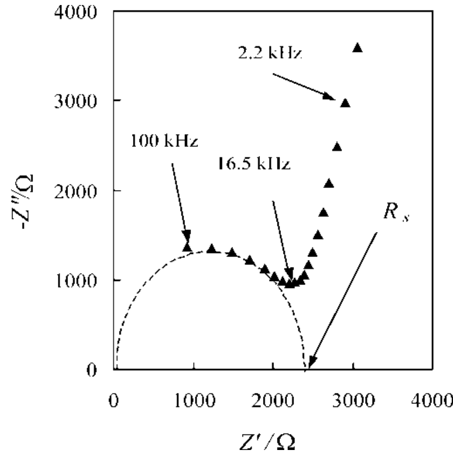

Fig. 6. Impedance complex plots for the Au quasi-point electrode placed at the YSZ electrolyte (temperature 700 °C, polarization potential –0.3 V, $p(O_2)$ = 0.1 bar)

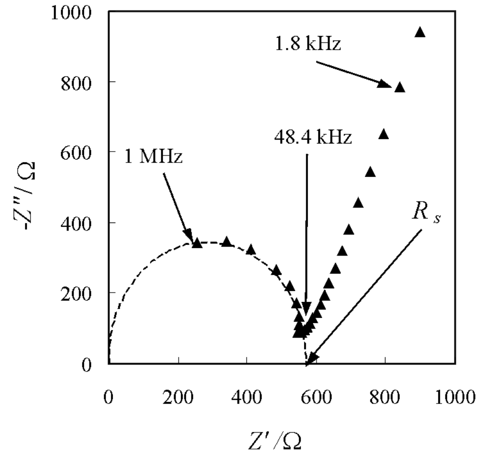

Fig. 7. Impedance complex plots for the Au quasi-point electrode placed at the GDC electrolyte (temperature 700 °C, polarization potential –0.3 V, $p(O_2)$ 0.1 bar)

For a perfectly circular point electrode, the electrolyte resistance R_s determined by the impedance spectroscopy, according to the Newman formula is equal to [21]:

$$R_s = \frac{\pi}{2 l_{\text{circle}} \sigma_{\text{el}}} \tag{1}$$

where l_{circle} is the TPB length of perfectly circular electrode and σ_{el} is the specific conductivity of the electrolyte. However, the metallic electrodes used in our work were not perfectly circular. Therefore, we have used the corrective factor

$$\gamma = \frac{l_{\text{ellipse}}}{l_{\text{circle}}} \tag{2}$$

which increases the TPB length according to the elliptical deformation of the electrode used in our experiments (Fig. 2). l_{ellipse} and l_{circle} are the perimeters of an ellipse and a circle, respectively. Hence, Eq. (1) could be rewritten for the elliptical electrodes in the form:

$$R_s = \frac{\pi}{2 \gamma l_{\text{circle}} \sigma_{\text{el}}} \tag{3}$$

The perimeter of an ellipse is approximately equal to:

$$l_{\text{ellipse}} = \pi \left[1.5(a+b) - \sqrt{ab} \right] \tag{4}$$

where a and b are the semimajor and semiminor axes. The measure of an electrode deformation vs. the perfect circle is a factor ξ equal to the ratio of semimajor and semiminor axes:

$$\xi = \frac{a}{b} \tag{5}$$

Hence

$$\gamma = \frac{l_{\text{ellipse}}}{l_{\text{circle}}} = 0.75(\xi + 1) - 0.5\sqrt{\xi} \tag{6}$$

For all electrodes used in our experiments, the deformation factor was equal approximately to $\xi = 2.9$, hence the corrective factor was assumed to be $\gamma = 2.1$.

Taking the average value of GDC conductivities equal to $\sigma_{(\text{el})\text{av}} = 40 \pm 19$ mS·cm^{-1} from Table 1 and R_s from Fig. 5, we can estimate l_{ellipse} of our electrodes. For the example shown in Fig. 2, it was calculated to be 1.44 mm, as compared to 1.62 mm measured geometrically from the image of the flattened part of the electrode (Fig. 2). $\sigma_{\text{el}} = 32.4$ mS·cm^{-1} of our electrolyte sample was also determined directly from the EIS measurements. In this experiment, large reversible Pt electrodes were deposited on the both sides of a disk. Taking this value of the conductivity, we calculated $l_{\text{ellipse}} = 1.77$ mm. Regarding a possible scatter of the σ_{el} due to various ways of preparation, the agreement between calculated and geometrical determined values of tree phase boundary can be considered acceptable. To avoid the problems with the procedure of geometrical determination of l_{TPB} for each single electrode, we used calculated values with σ_{el} determined individually for our electrolyte sample.

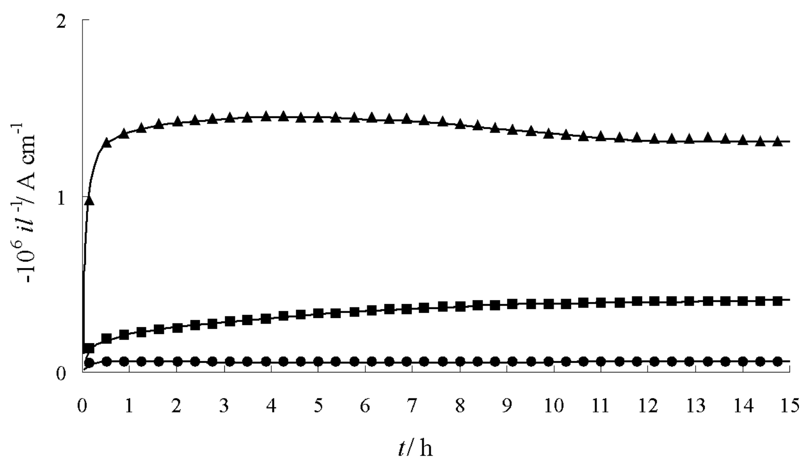

Fig. 8. Dependences of the current normalized vs. tree phase boundary length, on the time of polarization for the Au quasi-point electrode placed at the YSZ electrolyte. Triangles, squares and circles correspond to the polarization electrode potentials: –0.3 V, –0.2 V and –0.1 V, respectively, (temperature 700 °C, $p(O_2) = 0.1$ bar)

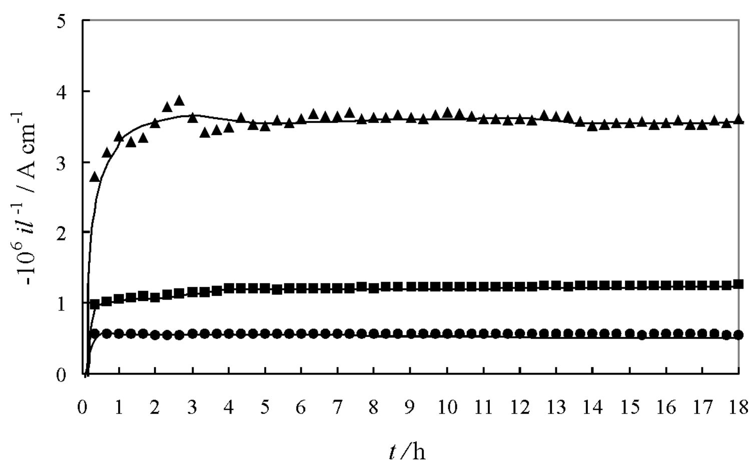

Fig. 9. Dependences of the currents normalized vs. tree phase boundary length on the time of polarization for the Au quasi-point electrode placed at the GDC electrolyte. Triangles, squares and circles correspond to the polarization electrode potentials: –0.3 V, –0.2 V and –0.1 V, respectively, (temperature 700 °C, $p(O_2)$ 0.1 bar)

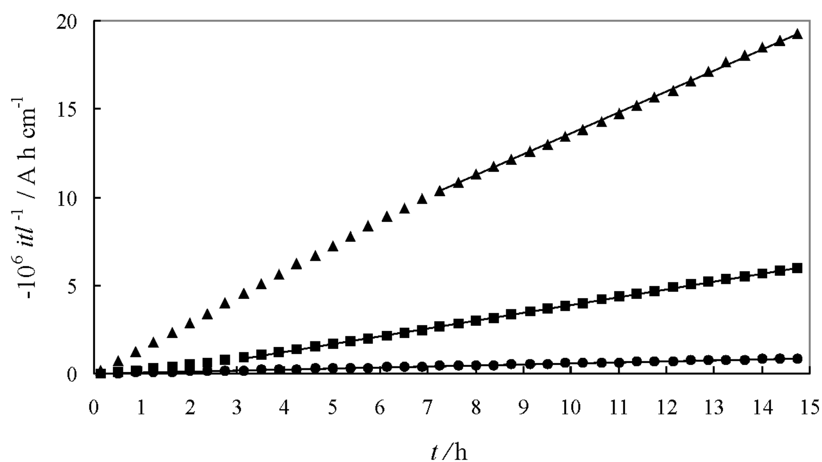

Fig. 10. Dependences of the itl^{-1} product on the time of polarization for the Au quasi-point electrode placed at the YSZ electrolyte. Triangles, squares and circles correspond to the polarization electrode potentials: –0.3 V, –0.2 V and –0.1 V, respectively, (temperature 700 °C, $p(O_2)$ 0.1 bar)

The dependences of the currents drawn from the electrode under the polarization of –0.1, –0.2 and –0.3 V on time for YSZ and GDC electrolytes are shown in Figs. 8 and 9, respectively. The current values were normalized vs. the TPB lengths, determined according to the procedure described earlier in this paper. Two distinct features of these dependences can be seen: the currents need a relatively long time to be stabilized when the electrode is polarized (i). It is especially clearly seen for the intermediate value of the polarization (–0.2 V); the currents, normalized vs. the TPB length, for the GDC electrolyte are distinctly higher than these for the YSZ electrolyte (ii).

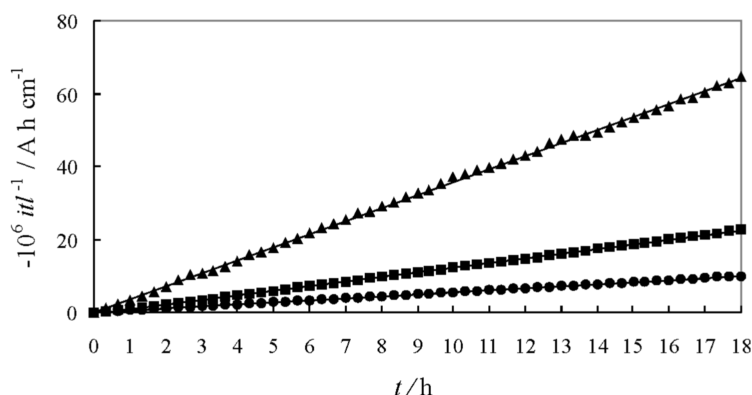

Fig. 11. Dependences of the itl^{-1} product on the time of polarization for Au quasi-point electrode placed at the GDC electrolyte. Triangles, squares and circles correspond to the polarization electrode potentials: –0.3 V, –0.2 V and –0.1 V, respectively, (temperature 700 °C, $p(O_2)$ 0.1 bar)

Because of the phenomenon described in entry (i), we made an attempt to estimate the asymptotic values of the currents $(il^{-1})_\infty$ i.e., their values after infinitely long time of polarization. From our previous numerous data obtained for the YSZ electrolyte [22], we have found that the character of the current–time dependence in this case could be fitted (after passing over some initial points) with the hyperbolic equation

$$il^{-1} = (il^{-1})_\infty \pm \frac{\text{const}}{t} \tag{7}$$

Hence, the most convenient way to estimate the $(il^{-1})_\infty$ values is to calculate the slopes of the linear regressions (itl^{-1}) vs. t fitted to the experimental points. These dependences, for the data presented in Figs. 8 and 9, are shown in Figs. 10 and 11, respectively. The linear character of the dependences shown in Figs. 10 and 11 confirms that the assumed Eq. (7) can be used to describe the behaviour of the electrode performance under polarization.

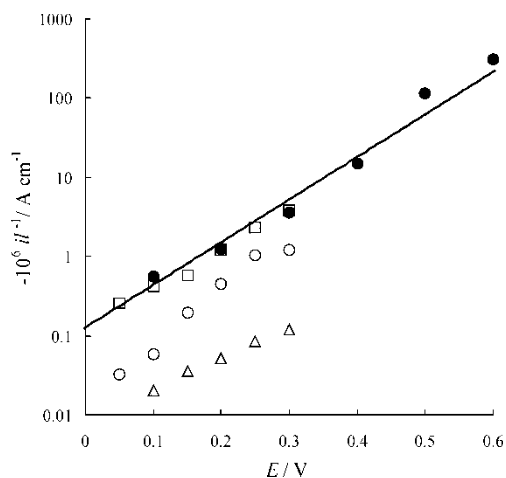

Fig. 12. The Tafel plots of $(il^{-1})_\infty$ vs. E for the GDC (full circles, $p(O_2)$ = 0.1 bar) and YSZ electrolytes (empty squares, circles and triangles correspond to $p(O_2)$ equal to 1.0, 0.1 and 0.01 bar, respectively, temperature 700 °C)

The Tafel plots of $\log(il^{-1})_\infty$ vs. E for the YSZ and GDC electrolytes are presented in Fig. 12. In this figure, we additionally present the data for the YSZ electrolyte obtained under the partial pressures of O_2 equal to 0.01 and 1.0 bar. The calculated values of the apparent exchange currents normalized vs. the TPB length and Tafel slopes are given in Table 2. As can be seen, at the partial pressure of oxygen equal to 0.1 bar, the apparent exchange current for GDC is distinctly higher than that for YSZ. This favours use of GDC over YSZ in IT SOFC. The calculated Tafel slopes are similar for all the considered cases, pointing to much the same mechanism of the oxygen reduction for both the electrolytes investigated [23]. Under this assumption, the average value of αn could be calculated for all the data presented in Table 2. It is equal to αn = 1.05 ±0.21, indicating that α is approximately equal to 0.5.

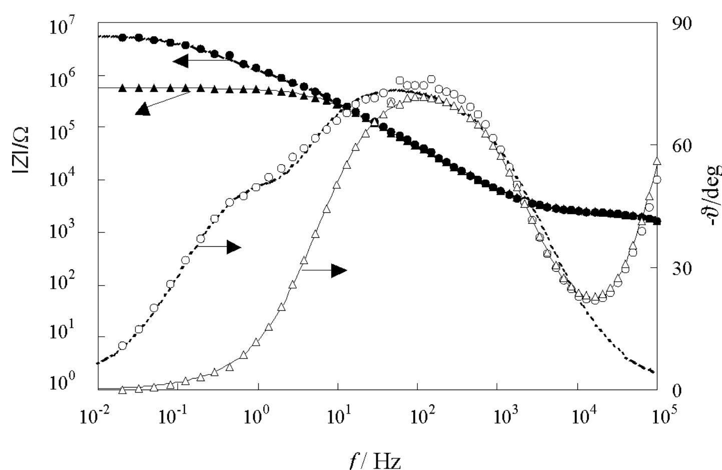

Fig. 13. Bode plots for the Au quasi-point electrode placed at the YSZ electrolyte (●, ○ unpolarized electrode, ▲, △ electrode polarized at –0.3 V; temperature 700 °C, $p(O_2)$ 0.1 bar)

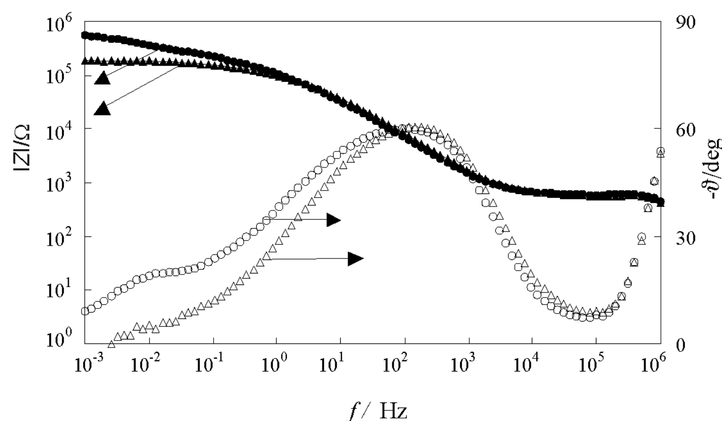

Fig. 14. Bode plots for the Au quasi-point electrode placed at the GDC electrolyte (●, ○ unpolarized electrode, ▲, △ electrode polarized at –0.3 V; temperature 700 °C, $p(O_2)$ 0.1 bar)

A similar character of the impedance Bode plots for the unpolarized and polarized electrodes at YSZ and GDC (disappearance of the additional branch at the phase dependence for the polarized electrodes) also confirms this similarity (Figs. 13 and 14). The complex impedance plots, normalized vs. the TPB length, are shown in Figs. 15 and 16 for the YSZ and GDC, respectively. The lower impedances observed for the GDC than YSZ can be correlated with the apparent exchange currents given in Table 2. The impedance data are now under detailed analysis which, together with the data obtained for an extended range of O_2 partial pressures and other electrode materials, will be presented in our further paper.

Table 2. Exchange currents and αn factors determined from The Tafel plots of the oxygen electrode reaction

Electrolyte	$p(O_2)$/bar	$-10^9 i_0 l^{-1}$/A·cm^{-1}	αn
GDC	0.1	100.8	1.11
YSZ	0.01	6.7	0.84
YSZ	0.1	15.4	1.32
YSZ	1.0	137	0.92

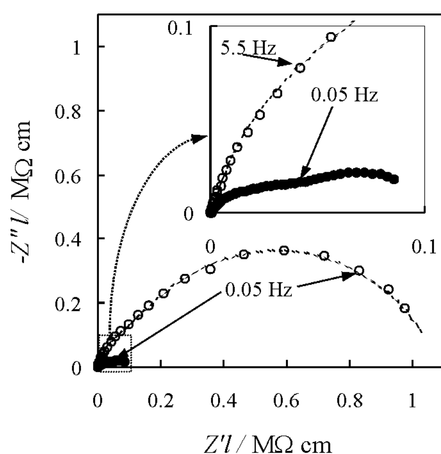

Fig. 15. Impedance complex plots of the unpolarized Au quasi-point electrode placed on the YSZ (○) and GDC (●) electrolyte (temperature 700 °C, polarization potential 0 V, $p(O_2)$ 0.1 bar)

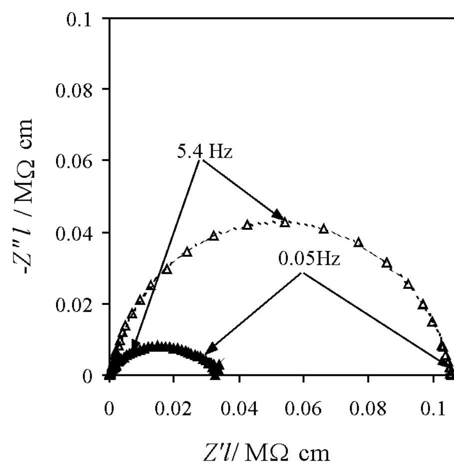

Fig. 16. Impedance complex plots of the polarized Au quasi-point electrode placed at the YSZ (△), and GDC (▲) electrolyte (temperature 700 °C, polarization potential –0.3V, $p(O_2)$ = 0.1 bar)

4. Conclusions

The paper presents the data obtained for the Au quasi-point electrodes in contact with two various electrolytes: yttria stabilized zirconia and gadolinia doped ceria. To

normalize the data obtained for the YSZ and GDC electrolytes, the procedures of determining the TPB length were discussed. Finally, the values of TPB lengths were estimated based on admittance measurements and specific conductivity of the electrolyte sample determined by EIS measurements. The CA dependences recorded for the durations lasting several hours showed that GDC is a better electrolyte for IT – SOFC than YSZ. Similar conclusions were drawn from the results obtained with EIS spectroscopy.

Acknowledgement

This work was financially supported by the AGH University of Science and Technology in Cracow under the contract No. 10.10.210.74.

References

[1] MINH N.Q., TAKAHASHI T., *Science and Technology of Ceramic Fuel Cells*, Elsevier, Amsterdam, 1995.
[2] GELLINGS P.J., BOUWMEESTER H.J.M., *The CRC Handbook of Solid State Ionics Electrochemistry*, CRC Press, Boca Raton, FL, 1997.
[3] TULLER H.L., Solid State Ionics, 131 (2000), 143.
[4] STEELE B.C.H., Solid State Ionics, 129 (2000), 95.
[5] MOGENSEN M., SAMMES N.M., TOMPSETT G.A., Solid State Ionics, 129 (2000), 63.
[6] JACOBSEN T., ZACHAU-CHRISTIANSEN B., JØRGENSEN M., Electrochim. Acta, 46 (2001), 1019.
[7] JACOBSEN T., BAY L., Electrochim. Acta, 47 (2002), 2177.
[8] BREITER M. W., LEEB K., FAFILEK G., J. Electroanal. Chem., 434 (1997), 129.
[9] PĘDZICH Z., HABERKO K., Ceramic Int., 20 (1994), 85.
[10] PAWŁOWSKI A., BUĆKO M. M., PĘDZICH Z., Mater. Res. Bull., 37 (2002), 425.
[11] DUDEK M., MOLENDA J., Mater. Sci.-Poland, 24 (2006), 45.
[12] STELLE B.C.H., *Oxygen Ion Conductors*, [in:] *High Conductivity Solid Ionic Conductors*, T. Takahasi (Ed.), World Scientific, Singapore, 1989, p. 402.
[13] KUDO T., OBAYASHI H., J. Electrochem. Soc., 122 (1975), 142.
[14] YAMAMOTO O., Electrochim. Acta, 45 (2000), 2423.
[15] KUDO T., OBAYASHI H., J. Electrochem. Soc., 123 (1976), 415.
[16] INABA H., TAGAWA H., Solid State, 83 (1996), 1.
[17] RIESS I., BRAUNSHTEIN D., TANNHAUSER D.S., J. Am. Ceram. Soc., 64 (1981), 479.
[18] BALAZS G. B., GLASS R.S., *Conductivity measurements of ceria based solid electrolytes using AC impedance*, [in:] *Ionic and Mixed Conducting Ceramics*, T.A. Ramanarayanan, W.L. Worrell, H.L. Tuller (Eds.), Proc. 2nd Intern Symp., The Electrochemical Society, 1994, p. 478.
[19] EGUCHI K., SETOGUCHI T., INOUE T., ARAI H., Solid State Ionics, 52 (1992), 165.
[20] TIANSHU Z., HUANG H., KILNER J., HING P., Solid State Ionics, 148 (2002), 567.
[21] NEWMANN J., Electrochem. Soc., 113 (1966), 501.
[22] TOMCZYK P., ŻUREK S., MOSIAŁEK M., in preparation.
[23] BARD A.J., FAULKNER L.F., *Electrochemical Methods Fundamental and Applications,* Wiley, New York, 1980.

Received 28 April 2007
Revised 16 February 2008

Materials Science-Poland, Vol. 26, No. 1, 2008

Determination of indium and nitrogen content in four-component epitaxial layers of $In_xGa_{1-x}As_{1-y}N_y$ deposited on GaAs substrate

J. SERAFIŃCZUK*, J. KOZŁOWSKI

Faculty of Microsystem Electronics and Photonics, Wrocław University of Technology,
Micro- and Nanostructure Metrology Group, ul. Janiszewskiego 11/17, 50-372 Wrocław, Poland

The paper presents a new method of determination of the percentage content of indium (x) and nitrogen (y) in four-component epitaxial layers of $In_xGa_{1-x}As_{1-y}N_y$, based on a distance between a layer and a substrate reflection for rocking curves obtained from high resolution X-ray diffraction. In the method, a symmetrical (004) and at least two asymmetrical (e.g., (224) and (115)) reflections are taken into consideration. For the investigated ranges of the values of the x, y parameters of the four components, we have described the dependences of distances between reflections $\Delta\omega_{(004)} = f_1(x,y)$, $\Delta\omega_{(224)} = f_2(x,y)$, $\Delta\omega_{(115)} = f_3(x,y)$ based on the rocking curve simulation software HRS (High Resolution Simulation – Philips). Based on the result, we present a procedure which allows us to characterize parameters of the epitaxial layers. The properties of the proposed procedure have been verified on experimental examples.

Key words: *X-ray; epitaxial layer; InGaAsN*

1. Introduction

One of the commonly applied methods of structural characterization of epitaxial layers is rocking curve simulation based on numerical solution of Takagi-Taupin's equations [1–3]. Rocking curves simulation software, e.g. HRS (High Resolution Simulation, Philips) [4, 5] allows one to determine precisely composition of multilayers what is very useful in characterization of various types of three-component layers. The distance between the reflection of the layer and reflection of the substrate characterizes the content of individual components of the layer. Unfortunately, application of this method to four-component layers like $In_xGa_{1-x}As_{1-y}N_y$ is limited. The limitation is connected with independent influence of the individual contents of components of the layer on the reflection location with reference to the substrate layer.

*Corresponding author, e-mail: Jaroslaw.Serafinczuk@pwr.wroc.pl

Therefore, determination of the contents of elements in four-component layers is possible only in combination with other methods such as, e.g., photoreflectance [6]. This results from the fact that the same distances between reflection from the layer and reflection from the substrate for different contents of In and N may be obtained (Fig. 1). Thus, an additional method is needed that would allow us to determine the content of one of the components of the layer.

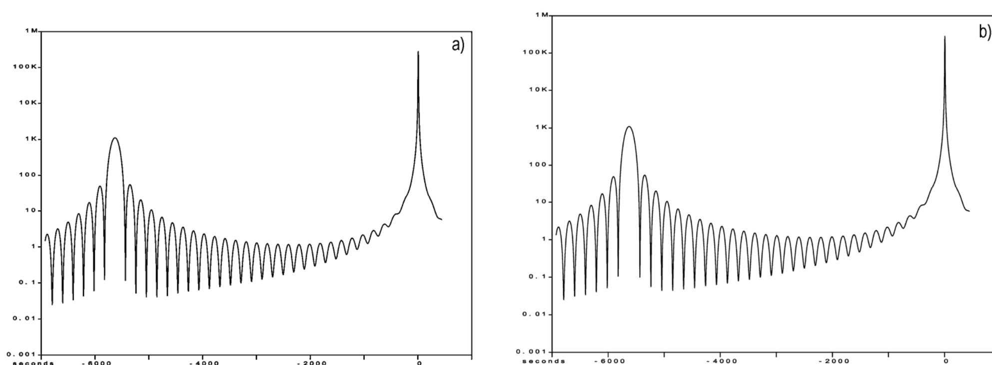

Fig. 1. Rocking curves (004) for $In_xGa_{1-x}As_{1-y}N_y$/GaAs layer: a) $x = 27.5\%$, $y = 2\%$, b) $x = 22.5\%$, $y = 0.75$

In the paper, we describe a new method for determination of the contents of individual components of the layer based on XRD measurements and rocking curves simulation software.

2. Determination of indium and nitrogen contents in four-component epitaxial layers

The first step of the method is to determine (using simulation software) the matrix of distances between layer and substrate reflections for the assumed range of contents of In and N in the investigated layer. Such simulation has been carried out for a few reflections, e.g. (004), (224), (115). As a result, the matrix with distances between reflections $\Delta\omega$ can be obtained (Fig. 2).

N	In		
	10%	…	35 %
0.5%	…	…	…
…	…	$\Delta\omega$	…
2.5%	…	…	…

Fig. 2. Matrix of distances between peaks and the contents of In and N in the layers

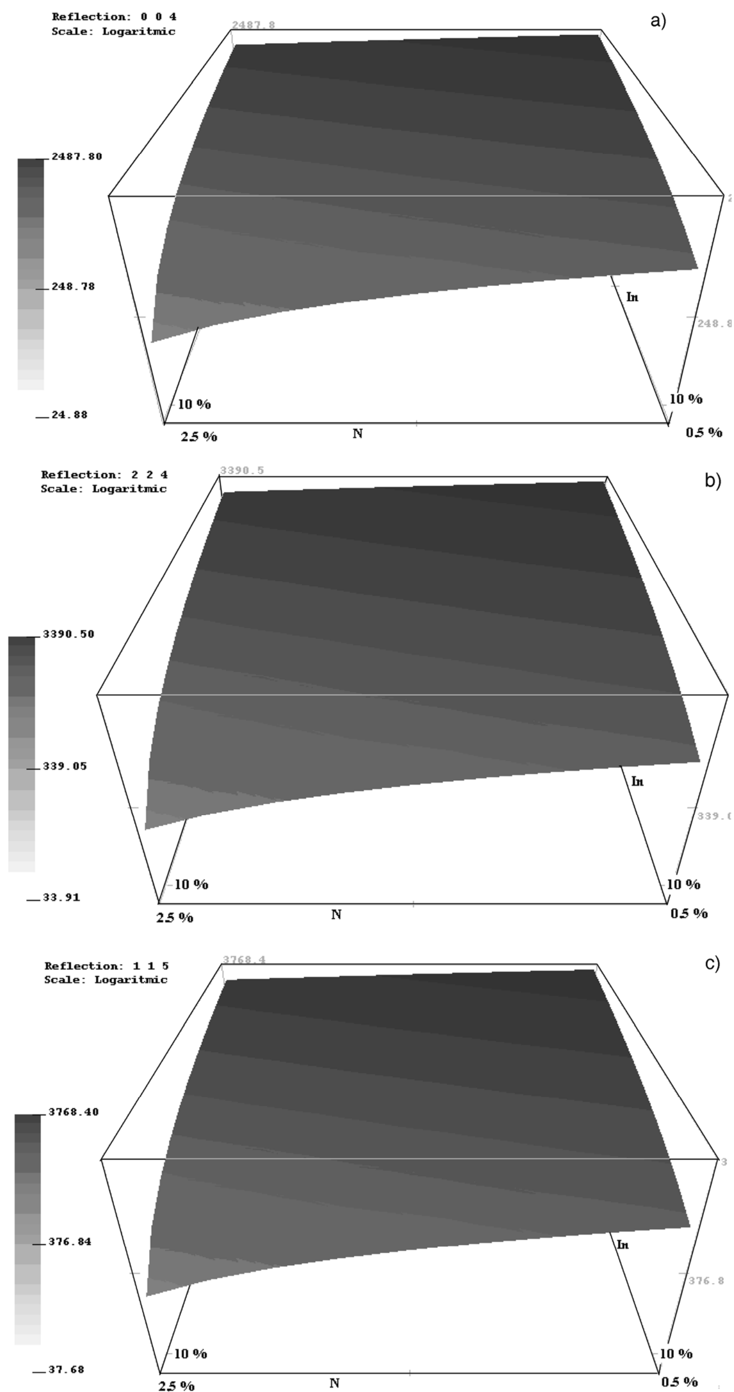

Fig. 3. Three-dimensional presentation of the relationship between In and N contents of a layer and distances between reflections: a) $\Delta\omega_{(004)} = f_1(x, y)$, b) $\Delta\omega_{(224)} = f_2(x, y)$, c) $\Delta\omega_{(115)} = f_3(x, y)$ for InGaAsN layers

The matrix is three-dimensional, where X and Y axes are the In and N contents in the layer for a given reflection, and Z axis is the distance between reflections of the simulated curve (Fig. 3). It is possible to describe each individual reflection by analytical equations (based on the matrix) determining three-dimensional spaces. Such spaces for each InGaAsN layer are well described by the formula

$$Z = AX^2 + BX + CY + D$$

For all considered spaces, the equations are as follows:

$$\Delta\omega_{(004)} = -2.666X^2 + 8.318X - 27.79Y + 0.03652 \quad (1)$$

$$\Delta\omega_{(224)} = -3.94\ X^2 + 11.46X - 37.82Y + 0.0449 \quad (2)$$

$$\Delta\omega_{(115)} = -4.532\ X^2 + 12.80X - 42.01Y + 0.04856 \quad (3)$$

The derived functions are shown in the form of three-dimensional charts in Fig. 3. In the next step, a system of equations for two reflections has been solved. Instead of Z, we have taken a real value of the distance between reflections from the rocking curve of InGaAsN layer. If the solution of such an equation equation exists, the values of X and Y will be directly obtained, being the searched values of In and N contents in the layer. Unfortunately, for the considered InGaAsN layers, an unequivocal solution of such a system of equations does not exist. Thus, for the matrices $\Delta\omega_{(hkl)} = f_1(x,y)$, an algorithm determining the value of $\Delta\omega$ and related contents of In and N has been designed. The algorithm is based on a comparison of the points of the matrix with distances between reflections taken from the measurement. Because the matrix contains discrete values of $\Delta\omega$, the value that is provided to the algorithm must be specified in the range of $\Delta\omega \pm \delta\omega$, where $\delta\omega$ is given as ± 0.5% of $\Delta\omega$.

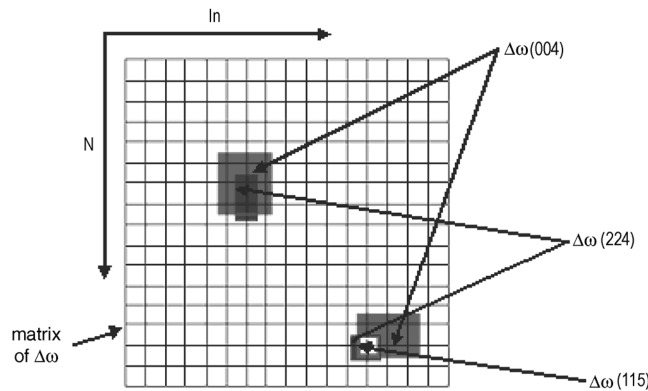

Fig. 4. General idea of the process of finding a solution

For a single reflection, a few In and N contents may be comparable with measured $\Delta\omega$. Therefore, the algorithm operates on a number of reflections, decreasing the prob-

ability of occurrence of the same value of $\Delta\omega$ for different pairs of In and N (Fig. 4). Common values obtained for three reflections were assumed as a solution.

3. Conclusions

The distances between reflections from a layer and a substrate have been calculated in four-component $In_xGa_{1-x}As_{1-y}N_y$ epitaxial layers. A new algorithm was designed allowing determination In and N content in InGaAsN layers. The algorithm is versatile for all four-component layers, if only the Takagi–Taupin equations are applicable. As an example, calculations have been performed for a layer containing 35% of In and and 2.5% of N. The distances between reflections (Fig. 5) have been obtained as follows: $\Delta\omega_{(004)}$ = 6904 arcsec, $\Delta\omega_{(224)}$ = 9432 arcsec, $\Delta\omega_{(115)}$ = 10498 arcsec.

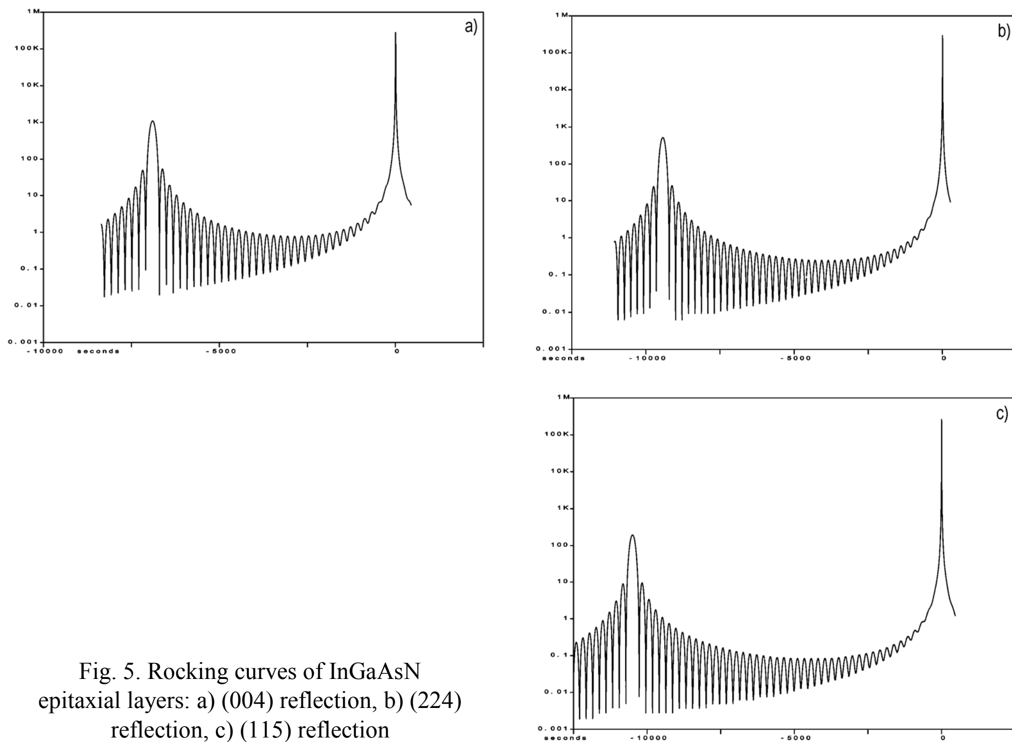

Fig. 5. Rocking curves of InGaAsN epitaxial layers: a) (004) reflection, b) (224) reflection, c) (115) reflection

Based on the applied algorithm, the following contents of In and N have been found:

reflection (004): In = 35% , N = 2.5% and In = 27.5% , N = 0.75%,
reflection (224): In = 35% , N = 2.5% and In = 27.5% , N = 0.75%,
reflection (115): In = 35% , N = 2.5%.

The correct values have been obtained for all three reflections. Moreover, the structure with a distance between reflections in the range of ±0.5% of $\Delta\omega$ was found.

This result confirms that upon increasing the number of reflections, the probability of choosing an incorrect pair of solutions decreases.

Acknowledgements

This work was supported by the Statutory Grant No. 343332 of The Faculty of Microsystem Electronic and Photonics of Wrocław University of Technology.

References

[1] TAKAGI S., Acta Cryst., 15 (1962), 1311.
[2] TAKAGI S., J. Phys. Soc. Japan, 26 (1969), 1239.
[3] TAUPIN D., Bull. Soc. Fran. Miner. Cryst., 87 (1964), 469.
[4] *PC-HRS high Resolution Simulation – User Guide*, Philips Electronics N.V., 1993.
[5] FEWSTER P. F., CURLING C. J., J. Appl. Phys., 62 (1987), 4154.
[6] IBANEZ J., KUDRAWIEC R., MISIEWICZ J., SCHMIDBAUER M., HENINI M., HOPKINSON M., J. Appl. Phys., 100 (2006), 093522.

Received 28 April 2007
Revised 16 February 2008

Materials Science-Poland, Vol. 26, No. 1, 2008

Fabrication of thin metallic films by arc discharges under ultra-high vacuum conditions

P. STRZYŻEWSKI[1], M. J. SADOWSKI[1], R. NIETUBYĆ[1*],
K. ROGACKI[2], T. PARYJCZAK[3], J. ROGOWSKI[3]

[1]The Andrzej Soltan Institute for Nuclear Studies (IPJ),
Department of Plasma Physics and Technology, 05-400 Otwock-Świerk, Poland

[2]Institute of Low Temperature and Structure Research, Polish Academy of Sciences,
P. O. Box 1410, 50-950 Wrocław 2, Poland

[3]Institute of General and Ecological Chemistry, Technical University of Łódź,
ul. Żeromskiego 116, 90-924 Łódź, Poland

Cathodic arc deposition technology offers an excellent approach to producing pure metal, alloy and compound films at very high rates and with excellent adhesion and density. High ion energy is the main factor allowing one to produce more compact films, with much stronger adhesion to the substrate than those obtained by other methods. It was shown that the cathodic arc working in ultra-high vacuum (UHV) conditions solves the problem of the oxygen contamination originating from water vapour thus paving the road to applications where very pure metallic films are needed. The paper presents systems used for deposition of thin coatings by means of arc discharges performed under the UHV conditions. The most important experimental results and characteristics of the arc-deposited thin superconducting films are discussed, and the progress achieved recently in the formation of such films is described.

Key words: *arc deposition; metallic film; high vacuum; TiN layers*

1. Introduction

Vacuum arc deposition is one of the oldest techniques used for thin film deposition. It is often applied in the industry to deposit hard protective coatings upon cutting and forming tools as well as decorative coatings such as golden-colour TiN layers. Moreover, this technique may also be used for more demanding technological applications in optics and electronics. The interest in vacuum arc evaporation arises primarily from the nature of the arc discharge plasma and its properties in relation to high qual-

[*]Corresponding author, e-mail: R.Nietubyc@ipj.gov.pl

ity film growth. In principle, this phenomenon is a plasma discharge between two metallic electrodes under vacuum. It is usually characterized by a low-voltage (20–40 V), high-current discharge (50–200 A) initiated under high vacuum (10^{-9}–10^{-10} mbar) and taking place in vapours of the cathode material [1]. High deposition energy of the condensing species is essential for the film growth and promotes adhesion as well as disruption of columnar growth. Furthermore, estimates of energies required for the high quality film growth, which are based on ion-surface interaction models, indicate that energies of the order of 25–100 eV are also desirable for activating surface atom displacements and maintaining good crystallinity of the underlying bulk layers. Unfortunately, this technique is plagued by macro-particles emitted from the cathode surface which are deposited onto the substrates and consequently deteriorate uniformity of the film. The dimensions of macro-particles are usually within the range of 0.1–10 μm. In order to eliminate the micro-droplets from vacuum-arc plasma and in consequence from the deposited film, one can apply various magnetic filters.

Within a frame of the Coordinated Accelerator Research in Europe (CARE) program (concerning the construction of large linear accelerators), a research group from the IPJ Swierk, Poland achieved a considerable progress in the development of the cathodic arc technology [2]. The main activity of this group is concentrated on the deposition of thin pure metallic films. Such layers can reveal their superconducting properties after cooling down to cryogenic temperatures, and they can be applied as new approaches in accelerator technologies. The deposition of the superconducting thin films is not a trivial issue. Some metals (like Nb and Pb), revealing superconductivity in the bulk forms, sometimes do not demonstrate such properties when they are used in the forms of thin layers. There are two main factors which can influence the layers superconductivity: a good quality (mainly density and surface homogeneity) and their very high purity. In order to fulfil the above requirements, a new concept of the deposition of thin super-conducting layers by means of arc discharges under ultra-high vacuum (UHV) conditions, has been developed. This new approach may solve the problem of elimination of contaminations originating from residual gases in a vacuum chamber. Moreover, the UHV arc technique of thin film deposition enables high quality and surface homogeneity to be achieved.

The main aim of this paper is to describe various UHV facilities designed and tested at the IPJ Swierk, Poland. Another aim is to show examples of the deposited metal (Nb and Pb) layers and to present results of the investigation of their morphological and structural characteristics as well as their possible applications in nanotechnology.

2. Experimental

It should be noted that very low pressures can be achieved only when all parts of the deposition system are designed and built in accordance with the UHV technology requirements. In our case, all the vacuum chamber components and accessories, as well as all vacuum connections, were manufactured using only high purity materials:

stainless-steel, oxygen-free high conductivity (OFHC) copper and high-quality ceramics (shielded from the arc). Our UHV arc facility was equipped with an oil-free pumping system consisting of a two-stage fore-vacuum pump and a turbo-molecular pump. It allowed one to reach a basic pressure lower than 10^{-8} mbar after 24 h of baking at 150 ºC. The reliable triggering (ignition) of arc discharges is often a serious problem, even in the industrial arc-based devices. In HV systems, thin layers of gases and impurities that are formed upon the surface of electrodes, facilitate the starting of an arc discharge. Under UHV conditions, high-temperature baking of the vacuum chamber reduces thickness of such layers. The described effects, as well as requirements that all other sources of impurities must be eliminated, make the arc ignition more difficult. After testing many triggering methods from the point of view of the operational reliability and cleanness, we have finally decided to use a laser beam, introduced through an appropriate vacuum-tight glass window, and focused upon the cathode surface. Under such conditions the arc discharge can be triggered extremely reliably without introducing any additional impurity. Our arc sources have been equipped with Nd:YAG lasers (532 nm, 50–100 mJ, 10 ns), and the mastering of the laser ignition technique appeared to be decisive for improving properties of the deposited layers.

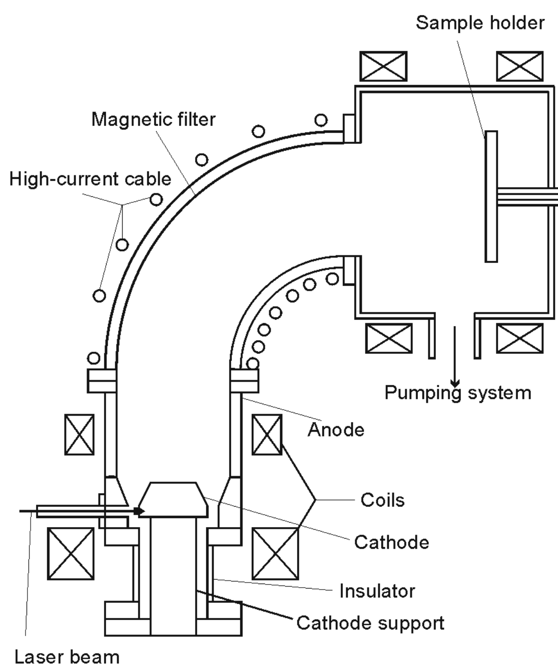

Fig. 1. Scheme of a UHV arc facility with a planar cathode and a knee-type magnetic filter

In the performed experiments, the used set-up was made of a plasma arc source equipped with a truncated cone cathode (Fig. 1). The cathode was fixed upon a water-cooled support placed inside a vacuum chamber. The lowest possible arc current for

stable operation in the DC mode was found to be about 60 A for the cathode made of niobium and 23 A for that made of lead. The cooling system of the anode had an upper limit of an arc current equal to about 140 A. To eliminate the micro-droplets deposition on the substrate, a magnetic filter was applied, deflecting arc plasma whilst the micro-droplets were caught upon walls. Two knee-type filters, as well as a T-shaped filter have been designed for the microdroplets removal. All of them based on water cooled tubes equipped with CF100 flanges. The knee-types filters differed in the curvature radii. The applied magnetic field deflected ion trajectories and let them pass along the knee- or T-shaped filters, while the microdroplets could be collected upon the filter walls. The magnetizing current was drawn through windings made of a copper cable wrapped around the filter channel. In the T-shaped filter, an additional coil was applied in the branch region in order to assure a smooth bending of the magnetic field lines. The samples were mounted upon a sample holder consisting of a massive copper (OFHC Cu) flange (Fig. 1).

The substrates for coating were mounted upon a holder fixed to the electrically insulated copper flange. That enabled bias voltage to be applied and due to heat exchange assured a stable temperature during the deposition process. In order to increase ion impact energy, bias voltages (from –20 V to –200 V) were applied to the substrate in a DC or kHz frequency mode. The facility enabled several substrates to be coated simultaneously. A detailed description of the planar arc facility constructed at IPJ Swierk can be found elsewhere [2–5].

3. Formation and properties of UHV arc deposited metallic thin films

3.1. Formation of Nb and Pb films

During a single deposition process, four substrates were coated simultaneously, e.g. Nb/Cu, Nb/sapphire, Pb/Cu and Pb/sapphire. The sample temperature was changed from room temperature up to 250 °C at the end of the process. For all samples the –70 V bias voltage was applied and the deposition rate with the system operated with arc currents of 80–100 A, was about 1 nm/s. The rise of pressure from the base value to 10^{-6} mbar was observed when the arc discharge was started. After that, the pressure stayed almost stable at the latter value throughout the whole deposition process. In situ mass spectroscopy showed that the gas pressure rise during the arc discharge was almost exclusively caused by hydrogen. Its partial pressure was more than 3 orders of magnitude higher than that of other contaminants.

3.2. Superconducting properties

Resistance of thin Nb films was measured from room temperature to about 4 K in order to observe the transition to the superconducting state (T_c ~ 9.5 K) and to determine the residual resistance ratio (RRR) between 300 K and 10 K (i.e., just above T_c).

Both parameters are related with superconducting properties and are very sensitive to impurities. For these measurements, the standard four-lead method was applied with a dc current changing from 2 mA to 200 mA, depending on the resistance and thus on temperature. Four Cu leads were attached to the Nb film with a silver paint. Attention was paid to keep dimensions of the voltage contacts at least 10 times smaller than the distance between the Cu leads. This allowed one to measure the RRR with the precision better than 1% and to calculate the resistivity with the accuracy better than 10%, if the thickness of the film was known. RRR values, measured for 1.5 μm-thick Nb films under typical UHV conditions described above, ranged from 30 to 50.

3.3. Film structure

The crystalline structure of niobium films grown on the grounded and biased single-crystal sapphire (001) substrate has been studied in order to identify the parameters determining the resulting film structure. The application of –70 V bias potential makes the ion impact energy almost twice higher as compared to the case of the grounded substrate. It enhances the surface and in-depth diffusion.

X-ray diffraction measurements in the (θ–2θ) mode have been performed with the monochromatised $CuK_{\alpha 1}$ radiation. Obtained diffraction patterns show broadened reflections originating from the deposited Nb layer, accompanied by strong and narrow reflections associated with the substrate. For both samples, the Nb 110 reflections have been found 10^3 times stronger than intensities expected for the powdered niobium. That indicates the dominating out of plane orientation of the niobium <110> crystalline axis. This orientation results from the intrinsic properties of Nb the films which are enhanced by the interaction with the substrate. An epitaxial relation between sapphire and Nb has been studied in [7, 8].

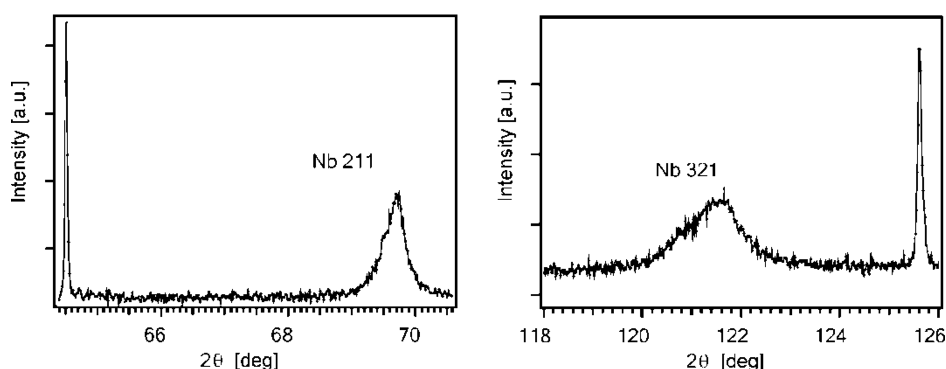

Fig. 2. Distinctive peak profiles observed for Nb 211 and 321 reflections

A comparison of the Nb reflections in diffraction patterns, as measured for two samples, reveals shifts in the angular position and different shapes of the peak profiles. The most pronounced differences occur for 211 and 321 reflections and which are asymmetric. The other ones are symmetric and differ slightly in FWHM. The most

distinctive features of diffraction patterns as measured for polarized and grounded samples are shown in Fig. 2.

The out of plane lattice parameters have been evaluated based on angular positions of the Nb reflections. They are 3.3032±0.003 Å and 3.3017±0.003 Å for the sample grown on the biased- and grounded-substrates, respectively. The obtained values are higher than 3.3004 Å reported for Nb bcc bulk. The structural distortions are different for the two investigated Nb/sapphire films. The observed differences in peak profiles point out that the lattice expansion is not uniform in the whole depth of the layer. The region affected by changes is in both cases wider than the Nb/sapphire interface. The diffraction pattern was measured for the Nb film deposited upon the electropolished copper substrate. None of the profile shape modifications observed for the Nb/sapphire diffraction pattern can be identified in that case. All niobium reflections are symmetric, much wider and shifted comparing to those observed for the Nb/sapphire.

The performed studies showed that the interaction of a sapphire single crystal substrate with the growing Nb layer modifies the resulting film structure. It leads to a strong texture and lattice distortion. On the other hand, the structure of the Nb film grown on the electropolished copper polycrystalline substrate is relaxed and closer to that of Nb bulk. Evidences for a weak influence of ion impact energy on the film structure have been found. The XRD analysis of thin Pb films deposited by means of the UHV arc technique is under preparation.

3.4. Surface morphology

Scanning electron microscopy (SEM) and atomic force microscopy (AFM) were applied for the surface quality inspection in search of small-scale defects and for the observation of the surface structure. Figure 3a shows a SEM picture of the deposited Nb layer. One can easily see a lack of micro-droplets upon the surface what confirms the effective plasma filtering. Moreover, the longitudinal shape of surface grains is clearly visible. The roughness of the Nb films deposited upon sapphire substrate was found to be of the order of few tens nanometers. A SEM picture of the Pb film surface is shown on Fig. 3b. The surface is also a very homogeneous and dense one.

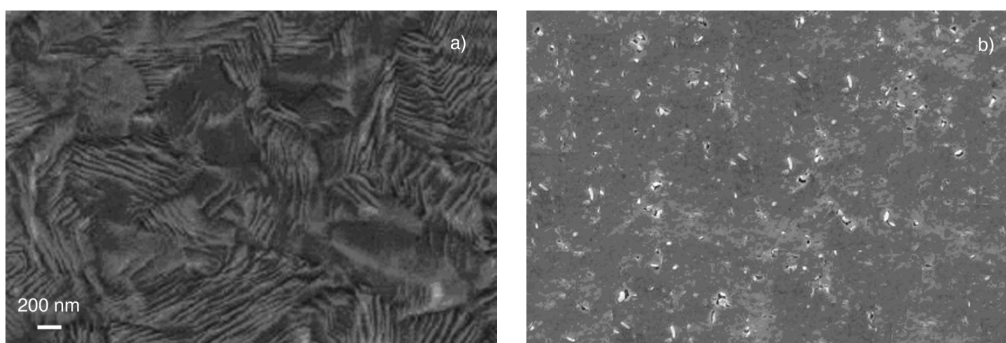

Fig. 3. SEM pictures of the surface of Nb (a) and Pb (b) films

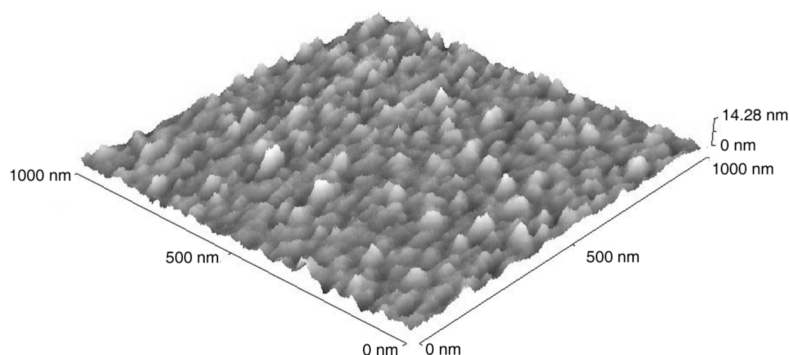

Fig. 4. AFM image of the thin Nb film

Additional data on the quality of the deposited thin Nb films has been obtained using the atomic force microscopy (AFM) technique. The AFM image of such a film is shown in Fig. 4. The measured values of the roughness of the deposited Nb film were below 20 nm. Moreover, a good quality of the film as well as good plasma filtering were confirmed.

3.5. Film purity

Information about the surface chemical composition and depth profiles of Nb and Pb layers were obtained by means of a time-of-flight (ToF) SIMS mass-spectrometer. Secondary ions emitted from the bombarded surface were mass-separated and counted with the ToF analyzer. Results of the depth profiles measurement are presented in Fig. 5.

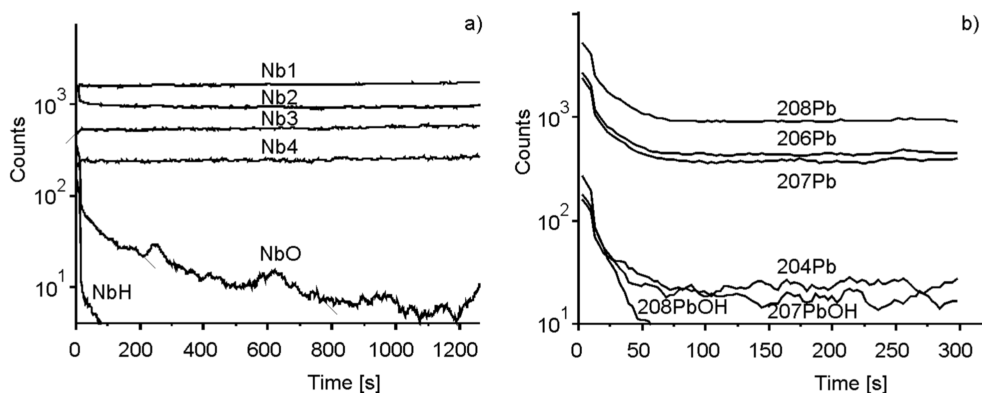

Fig. 5. Results of SIMS measurements of the deposited Nb (a) and Pb (b) layers

One can easily see that the deposited layers consisted mainly of the pure metals. The presence of some heavy impurities (like Na and K species) has also been observed but their amounts were very low (not shown in this scale). A characteristic feature of

the deposited layers is a relatively high level of oxidation in the near-surface region which probably originates from the atmospheric oxygen diffusion.

4. Conclusions

The UHV cathodic arc deposition technique has been successfully applied to obtain high purity superconducting layers of niobium and lead. The deposition of micro-droplets from vacuum-arc plasma has been avoided by the application of the especially designed and tested filters.

The reported XRD, SEM, AFM and SIMS studies showed unanimously that the impurities concentration in the obtained Nb and Pb films is satisfactorily low. The achieved cleanness goes together with outstanding superconducting properties. It opens a new road to many applications where dense, high-quality and very pure metallic films are needed, e.g. in micro-electronics, nanotechnology, medicine etc.

Acknowledgement

We acknowledge a support of the European Community-Research Infrastructure Activity under the FP6 *Structuring of the European Research Area* program (CARE, contract number RII3-CT-2003-506395) and a grant of the Ministry of Science and Informatics of Poland (Decision No. 621/E-78/SPB/6.PR UE/DIE 296/2004-2007).

References

[1] BOXMAN R.L., SANDERS D., MARTIN P.J., *Handbook of Vacuum Science and Technology*, Wiliam Andrew Publ., Noyes, Park Ridge, NJ, USA, 1995.
[2] LANGNER J., CATANI L., RUSSO R., TAZZARI S., CIRILLO M., MERLO V., TAZZIOLI F., Czech. J. Phys. Suppl. D, 52 (2002), D829.
[3] STRZYZEWSKI P., CATANI L., CIANCHI A., LANGNER J., MIROWSKI R., RUSSO R., SADOWSKI M.J., TAZZARI S., WITKOWSKI J., Am. Inst. Phys. Conf. Proc., 812 (2006), 485.
[4] SADOWSKI M.J., LANGNER J., STRZYZEWSKI P., MIROWSKI R., WITKOWSKI J., TAZZARI S., CATANI L., CIANCHI A., LOREKIEWICZ J., RUSSO R., Proc. Workshop on Thin Films, INFN-Legnaro, Italy, Oct. 9–12, 2006, p. 51.
[5] STRZYZEWSKI P., LANGNER J., MIROWSKI R., SADOWSKI M.J., TAZZARI S., WITKOWSKI J., Phys. Scripta, T123 (2006), 135.
[6] LANGNER J., MIROWSKI R., SADOWSKI M.J., STRZYZEWSKI P., WITKOWSKI J., TAZZARI S., CATANI L., CIANCHI A., LORKIEWICZ J., RUSSO R., Vacuum, 80 (2006),1288.
[7] SONG G., REMHOF K., THEIS-BROEHL K., ZABEL H., Phys. Rev. Lett., 79 (1997), 6962.
[8] REIMER P.M., ZABEL H., FLYN C.P., DURA J.A., Phys. Rev. B, 5 (1992),1142.

Received 28 April 2007
Revised 16 February 2008

Materials Science-Poland, Vol. 26, No. 1, 2008

Influence of the columnar structure of heteroepitaxial nitride layers on the transport of electrons

A. SZYSZKA*, B. PASZKIEWICZ, R. PASZKIEWICZ, M. TŁACZAŁA

Faculty of Microsystem Electronics and Photonics, Wrocław University of Technology,
ul. Janiszewskiego 11/17, 50-372 Wrocław, Poland

The influence of the columnar structure of heteroepitaxial nitride layers on electronic transport has been described within the model of thermionic emission of carriers through potential barriers formed at grain boundaries. Dependence of the potential barrier height on the material properties and applied external voltage has been calculated. Potential barriers heights for gallium nitride layers grown by the metalorganic vapour phase epitaxy method has been estimated to be in the range of 20–60 meV and 10–40 meV in the dark and under illumination, respectively.

Key words: *gallium nitride; columnar structure; electronic transport*

1. Introduction

Gallium nitride and its alloys are applied for fabrication of UV light detectors and emitters and for high frequency, high power field effect transistors. Despite a great progress in device technology, the highest predicted and calculated parameters of fabricated structures have not been obtained. Discrepancies between the theoretical and obtained parameters of the devices are mainly caused by an assumption that heteroepitaxial layers of A(III)N compounds have singlecrystalline structure. This assumption neglects the fact that epitaxial layers of nitrides always have columnar structure with low angle boundaries. Distribution of sizes of crystallites in heteroepitaxial layers grown by metal-organic chemical vapour deposition (MOCVD) method was examined by high resolution X-ray diffractometry [1]. It was shown that sizes of crystallites in a layer depend on conditions of the growth process and that GaN layers grown on sapphire substrates consist of crystallites of various sizes.

Dangling bonds and atoms of impurities existing in disordered boundary area introduce deep trap levels in the forbidden band of the material. Negatively charged

*E-mail: adam.szyszka@pwr.wroc.pl

acceptor traps, in n-type material, form potential barriers for a majority of carriers. Influence of these barriers on the surface potential in GaN layers was examined by the scanning Kelvin probe microscopy [2]. Nonuniformity of photocurrent flow in AlGaN MSM detectors, caused by columnar structure of the layer, was observed by the light beam induced current technique [3].

2. Calculations

One-dimensional model which allowed the analysis of the formation of potential barrier at the grain boundary was evaluated (cf. [4–7]) in order to describe electronic properties of polycrystalline silicon.

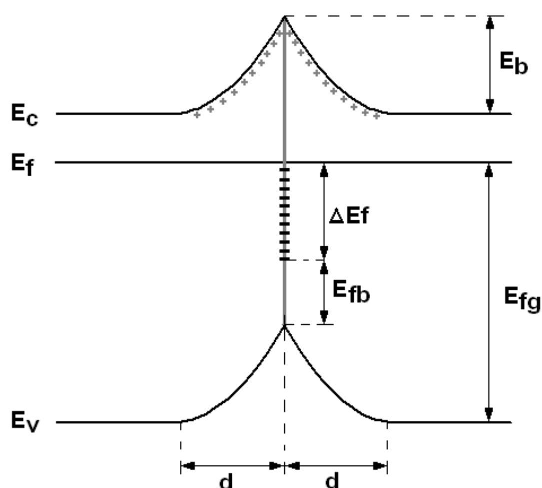

Fig. 1. Scheme of the energy band diagram of a potential barrier formed at the boundary of two grains: E_f – Fermi energy level, E_b – potential barrier height, E_{fg} – Fermi energy level in the volume of a grain, E_{fb} – Fermi energy level in grain boundary in neutral conditions, ΔE_f – shift of the Fermi level at the grain boundary caused by the excess charge ($\Delta E_f = E_{fg} - E_{fb}$), d – width of the space charge region

The energy band diagram of two adjacent grains in a semiconductor is presented in Fig. 1. The model assumes a constant distribution of densities of deep trap states at the grain interface. The negative charge associated with interface trap states is balanced by the positive net charge of uncompensated ionized shallow donor states. Donor states occur in GaN layers mainly due to the presence of N vacancies. Non-compensated donor states are localized in space charge regions created on both sides of the grain boundary. The height of the potential barrier depends on the relation between density of the interface states and concentration of donor states in the grains. It could be concluded (Fig. 2) that for higher values of the concentration of shallow donors in the volume of a grain (N_d), a higher density of acceptor trap states at the grain boundary (N_T) is needed to form the potential barrier. We have also found that for very

high values of trap densities at the grain boundary, the potential of the barrier was pinned and was dependent only on E_{fb}.

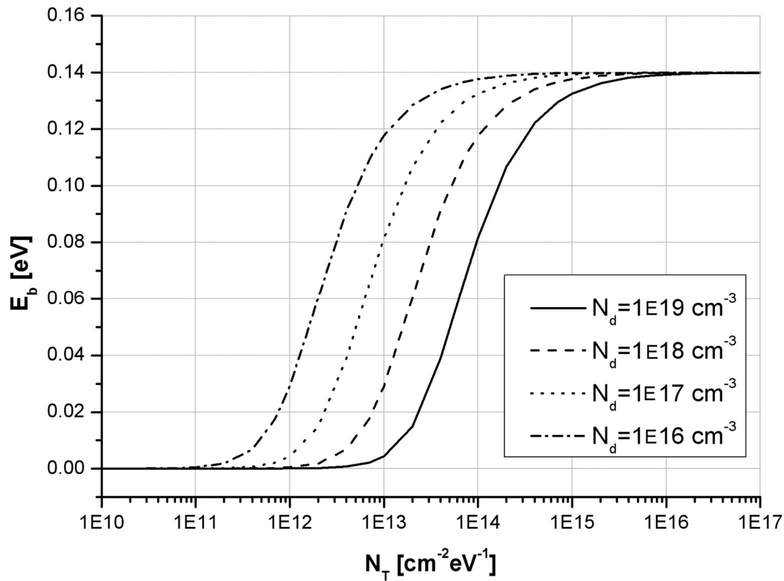

Fig. 2. Dependence of the calculated height of the potential barrier on the trap states density at grains boundary for various concentrations of donors in the grains (the calculation was carried out for E_{fb} = 3.1 eV)

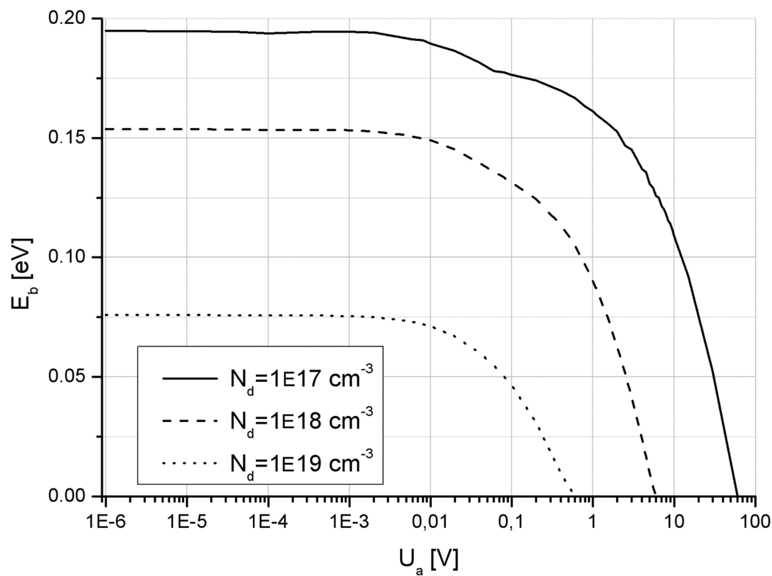

Fig. 3. Dependence of the calculated height of the potential barrier on the applied voltage at grains boundary for various concentrations of donors in the grains (the calculation was carried out for E_{fb} = 3.02 eV)

The calculated dependence of the height of the potential barrier on the external voltage is presented in Fig. 3. The N_T value at the grain boundary was assumed to be 4×10^{17} $cm^{-2}\cdot eV^{-1}$ based on Refs. [8] and [9]. For small values of the applied voltage the barrier height remained constant. Further, with subsequent increase of the voltage, the barrier height started to decrease to the point where it vanished for a defined value of voltage. The breakdown voltage of the potential barrier was higher for the higher initial barrier height. After reaching the breakdown voltage, the conductivity of the layer was controlled only by bulk conductivity of grains. This effect could explain the observed phenomenon that despite small mobility of electrons in heteroepitaxial layers of nitrides, the measured drift velocity of electrons in high electric fields is very high [10].

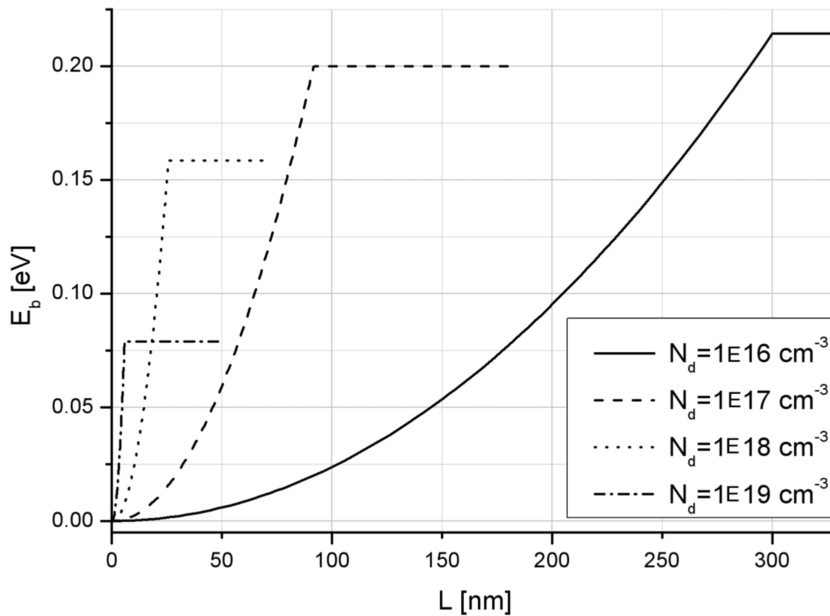

Fig. 4. Influence of the size of grains on the potential barrier height for various concentrations of donors in the grains

The dependence of the potential barrier height on the sizes of grains is presented in Fig. 4. It was observed that decrease of grain sizes did not influence the potential barrier height till the point when it reached the value equal to the double width of the space charge region. This occurs when the space charge regions occupy the whole grain. Further decreasing of the grain sizes caused the decrease of the barrier height due to overlapping of the depletion regions. These phenomena could be responsible for spatial non-uniformities in photo-response of AlGaN MSM detectors [3].

The dependence of the barrier height on the concentration of donors in grains is presented in Fig. 5. In the area of small donor concentration, its increase caused the increase of the barrier height due to an increase of the number of electrons trapped at the grain boundary. When all interface states were completely filled, the potential

barrier height reaches its maximum. Further, any increase of the concentration of donors results in a decrease of the barrier height due the increase of the compensating positive charge of ionized donors in the depletion layer.

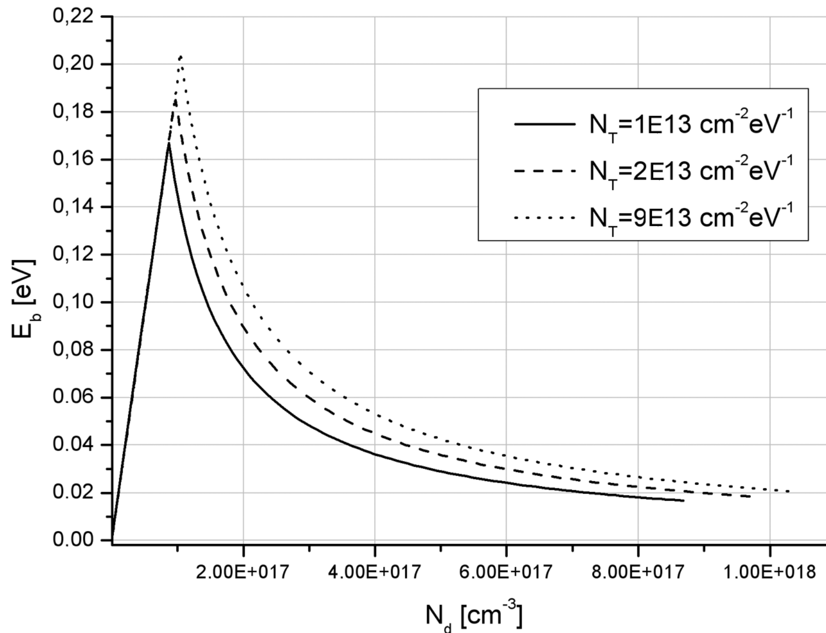

Fig. 5. Dependence of the calculated potential barrier height on the concentration of donors in the grains (calculation was carried out for E_{fb} = 3.02 eV)

3. Experiments

The potential barrier heights in MOVPE gallium nitride layer have been estimated based on the measurements of the temperature dependence of conductivity of the epitaxial layer (Fig. 6). Assuming a thermionic character of emission through potential barriers, their heights could be evaluated from the slope of the Arrhenius plot of the conductivity vs. temperature. Two values of barrier heights of the GaN heteroepitaxial layer were measured: one for dark conditions, the other for an illuminated sample. Potential barrier heights have been estimated to be in the range of 20–60 meV for the former case and 10–40 meV for the latter one. The decrease of the potential barrier heights for an illuminated sample could be explained by a release of electrons from the trap states caused by the incident photons. That also could explain another specific behaviour of nitride layers, namely the persistent photoconductivity. Presumably, photo-generated electrons could not re-occupy deep states because of the existence of residual negative charge at grain boundaries repelling electrons. Thus grain boundaries remain lowered for a long time after switching off the illumination.

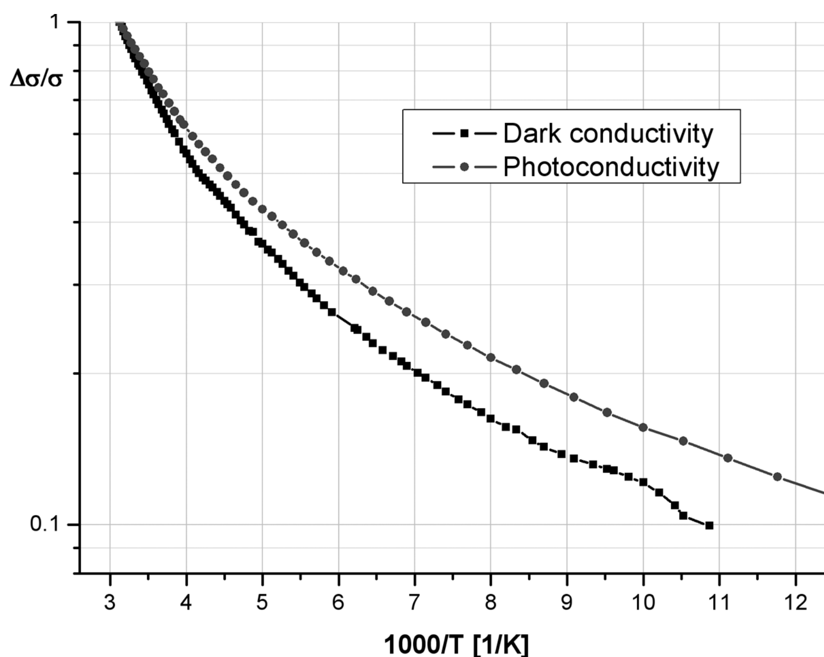

Fig. 6. Temperature dependence of conductivity of GaN heteroepitaxial layer

The nonlinearity of the Arrhenius plot observed in the low temperature region could indicate the occurrence of other conduction phenomena in nitride layers such as tunneling effect and/or impurity band conduction.

4. Conclusions

The model of formation of potential barriers at the grain boundaries of heteroepitaxial layers of nitrides has been put forward. The dependence of the barrier height on the layer parameters such as the density of deep traps, concentration of shallow donors, energy of Fermi level at grain boundary in neutral conditions and the size of grains has been calculated. The presence of potential barriers at grain boundaries allowed us to explain some characteristic properties of nitride heteroepitaxial layers. Potential barrier heights of MOVPE GaN layers were calculated based on the dependence of conductivity vs. temperature with an assumption of the thermionic character of the emission.

Acknowledgements

This work was partially supported by Polish Ministry of Science and Higher Education under Grant PBZ/100/1/1/2004, R0201802, PBZ-MEiN-6/2/2006, Wrocław University of Technology statutory grant and EU Structural Funds in Poland – Ph.D scholarschip under contract No. 49.

References

[1] PASZKIEWICZ R., PASZKIEWICZ B., KOZŁOWSKI J., PIASECKI T., KOŚNIKOWSKI W., TŁACZALA M., J. Crystal Growth, 248 (2003), 487.
[2] SIMPKINS B.S., YU E.T., WALTEREIT P., SPECK J.S., J. Appl. Phys., 94 (2003), 1448.
[3] PASZKIEWICZ B., SZYSZKA A., WOŚKO M., MACHERZYŃSKI W., PASZKIEWICZ R., TŁACZAŁA M., Phys. Stat. Sol. (c), 3 (2006), 602.
[4] SETO J.Y.W., J. Appl. Phys., 46 (1975), 5247.
[5] SEAGER C.H., CASTNER T.G., J. Appl. Phys., 49 (1978), 3879.
[6] PIKE G.E., SEAGER C.H., J. Appl. Phys., 50 (1979), 3414.
[7] BLATTER G., GREUTER F., Phys. Rev. B, 33(1986), 3952.
[8] SIMPKINS B., YU E., CHOWDHURY U., WONG M., ZHU T., YOO D., DUPUIS R., J. Appl. Phys., 95 (2004), 6225.
[9] SHALISH I., KRONIK L., SEGAL G., SHAPIRA Y., Phys. Rev. B, 61 (2000), 15573.
[10] ALBRECHT J.D., WANG R.P., RUDEN P.P., FARAHMAND M., BRENNAN K.F., J. Appl. Phys., 83 (1998), 4777.

Received 28 April 2007
Revised 16 February 2008

Materials Science-Poland, Vol. 26, No. 1, 2008

Novel nanoporous organic-inorganic hybrid materials containing niobium

K. WALCZAK, I. NOWAK*

Faculty of Chemistry, Adam Mickiewicz University, ul. Grunwaldzka 6, 60-780 Poznań, Poland

A synthetic protocol with the versatility to make high-quality periodic mesoporous organosilicas containing niobium and bridging carbon functional groups has been presented. This flexibility is discussed in terms of organic precursor structures. Niobium-containing silica-bridged periodic mesoporous organosilicas (Nb-PMOs) were synthesized by self-assembly of the nonionic surfactant P123, $EO_{20}PO_{70}EO_{20}$, and trimethoxysilyl functionalized organic compounds, namely silica precursors containing two different organic bridging groups ($(C_2H_5O)_3Si–R–Si(OC_2H_5)_3$, R – ethylene or octylene) under acidic conditions. The obtained bifunctionalized Nb-PMOs have been characterized by X-ray diffraction, transmission electron microscopy, and nitrogen physical sorption. Experiments show that the Nb-PMOs exhibit hexagonal mesoscopic structures. Increasing the amount of the organic chain length functionality in the precursors results in significant worsening of the mesostructural ordering of the product. It is shown that the organic monomer can act as a template in making nanoporous silica materials.

Key words: *Nb-PMOs; inorganic/organic hybrid; bimodal mesopores distribution*

1. Introduction

Since the advent of high surface area mesoporous molecular sieves (e.g., MCM-41 type silica materials) via a surfactant-templated synthesis route by Mobil in 1992 [1], organic modification schemes imparting various functionalities to the inorganic silica surface have received much attention. By using a bistrialkoxysilyl precursor in which bonding between silicon and carbon is established with the assured stoichiometry, periodic ordered mesoporous organosilicas (PMOs) in which organic groups were directly integrated into the silica framework, were synthesized in 1999 by three independently working groups [2–4]. These new materials have been expected to lead to advanced materials due to the possibility of controlling the kind of functional groups in the bridged organosilane precursors $(R'O)_3–Si–R–Si–(OR')_3$ (e.g., [5]). To date, PMOs with simple bridging groups derived from methane, ethane, ethylene, acetylene,

*Corresponding author, e-mail: nowakiza@amu.edu.pl

phenyl and its derivatives, thiophene, and ferrocene have been developed (e.g., review paper [6]). The pore diameters of the PMOs prepared by structure-directing agents with ionic alkyl ammonium surfactants (with chain lengths from C12 to C20) were restricted to the range between 2 nm and 5 nm. This limitation was finally overcome by using nonionic triblock copolymers such as P123 ($EO_{20}PO_{70}EO_{20}$) used previously as a structure directing agent in the synthesis of large-pore mesoporous SBA-15 pure silica phase. This kind of material with a hexagonal *p6mm* type structure is a representative of 2D mesostructure and possesses wall thicknesses between 3.1 nm and 6.4 nm with pore sizes in the range of 4.6–30 nm [7].

The PMOs materials have gained a general expectation that their efficient uses can be dimensionally expanded to a number of versatile applications as catalysts. Hence, intellectual efforts have been devoted to extend their unique properties in the area of heterogeneous catalysis, by the substitution of active metal sites in the wall positions so that they can be used as catalysts for various hydrophobic reactions, e.g. epoxidation processes, in order to improve the contact at the water (oxidant)–organic (cyclohexene) interface. Since the Nb-containing silicas were found to be active in oxidation processes, in this work we synthesized and optimized the synthesis condition of a new Nb-PMOs catalyst that is expected to find applications as a water-tolerant solid acid catalyst for the reactions requiring weak acidic sites and low temperatures.

2. Experimental

The nanostructured hybrid nioboorganosilicates have been synthesized by the hydrolysis and condensation of bridged silsesquioxane precursors containing two different organic bridging groups $((C_2H_5O)_3Si–R–Si(OC_2H_5)_3$, R – ethylene or octylene. The triblock copolymer Pluronic P123 ($(EO)_{20}(PO)_{70}(EO)_{20}$) was obtained from BASF, while 1,2-bis(triethoxysilyl)ethane (BTEE) and 1,2-bis(triethoxysilyl)octane (BTEO) were kindly provided by ABCR GmbH & Co. In a typical synthesis, the P123–H_2O solution was slowly added to the BTEE (or BTEO)–Nb source–H_2O–HCl mixture that was stirred for 24 h at 313 K. Ammonium trisoxalate complex of niobium(V) was used as a source of niobium, furthermore the TEOS/surfactant and the Si/Nb molar ratios were kept as 60 and 64 in all the syntheses, respectively. The slurry was then transferred into a polypropylene bottle and hydrothermally treated at 373 K for 20 h. White solids were recovered by filtration, washed with deionized water and ethanol, and dried under ambient conditions. For all as-synthesized materials, the surfactant molecules (occluded inside the pores of the hybrid material) were removed by solvent extraction (mixture of ethanol and HCl). The samples will be denoted as Nb-PMO-E in the case of using BTEE and Nb-PMO-O for BTEO, respectively, as the bistrialkoxysilyl precursors. The materials were then calcined at 773 K for 4 h to remove ethane or octane fragments chemically bonded in the framework. For comparison, an Nb-SBA-15 sample with Si/Nb ratio of 64 was also prepared and the details of the synthesis procedures have been reported elsewhere [8].

Various physicochemical studies (viz., X-ray diffraction (XRD), transition electron microscopy (TEM), N_2 physisorption) and XRF spectroscopy were used to check the mesoporosity and to find the location of niobium ions in the NbPMO.

X-Ray diffraction patterns were recorded with a TUR-62 diffractometer using CuK_α radiation and operating voltage of 40 kV. The samples were disc shaped pressed powders. The diffractograms were recorded at room temperature in two 2Θ ranges: 1.2–10° and 4–60° with the step size of 0.02° or 0.05°, respectively. Adsorption/desorption experiments using N_2 were carried out at 77 K on a Micromeritics ASAP 2010. Before each measurement, the samples were first outgassed at 573 K for 3 h in vacuum. The N_2 isotherms were used to determine the specific surface areas using the standard BET equation in the relative pressure (p/p_0) from 0.05 to 0.2 and the cross-sectional area of nitrogen molecule of 0.162 nm^2. Pore sizes were obtained from the N_2 adsorption branch, using the Barret–Joyner–Halenda (BJH) method with the corrected Kelvin equation, i.e. KJS–BJH method at the maximum of pore size distribution [9]. Moreover, the α_s-plot analysis [10] was performed for all obtained samples for the evaluation of the micropore volume. The single-point total pore volume was obtained from the amount adsorbed at $p/p_0 = 0.98$. Transmission electron microscopy (TEM) images were obtained using a JEOL-2000 transmission electronic microscope with an accelerating voltage of 80 kV. The samples were dispersed in ethanol under ultrasonic conditions and deposited on a copper grid before examination. The metal content in the calcined samples was determined by X-ray fluorescence spectroscopy (XRF, MiniPal, Philips) using calibration curves prepared from mixtures of mesoporous pure silica and Nb_2O_5.

3. Results and discussion

Highly ordered mesoporous nioboorganosilicates with large pores were synthesized under acidic conditions using a nonionic surfactant as a supramolecular structure directing agent. The mesostructural ordering of the as-synthesized and extracted Nb-PMOs was confirmed by powder XRD. Similarly to pure niobosilicate analogues, Nb-PMOs without extraction exhibit XRD patterns dominated by low-angle peaks, typically with a prominent peak with a *d* spacing of ca. 13 nm (Fig. 1, line a). The XRD pattern indicates a significant level of mesostructural ordering [12]; however, there is a lack of higher order peaks. This is a known feature of XRD patterns of template-containing mesophases. The XRD pattern of the extracted nioboorganosilicate Nb-PMO-E exhibits a high intensity prominent (100) peak along with (110) and (200) peaks, therefore confirming that the mesophase has a hexagonal (*P*6*mm* symmetry group) pore channel ordering. The material obtained from the silica source containing longer bridging carbon chain (Nb-PMO-O; not shown here) showed characteristic peaks at a low angle; they were, however, less resolved. Similarly to pure niobosilicate counterparts, Nb-PMOs exhibit XRD patterns dominated by low-angle peaks, typically with a prominent peak at $2\theta < 1.6°$. After calcination, a decrease in d_{100} peak

intensity, long-range ordering and lattice contraction is observed (Fig. 1, line c), showing the cross-linking of the framework silanols and/or the lack of ordering between the structures of adjacent pores. In addition to the structural ordering, XRF analysis showed that the hydrophobic nature of surfactant also plays a vital role in the amount of metal incorporation (Table 1). Even though there is no stoichiometric incorporation of niobium under the present synthesis conditions, it is likely that a large part of the metal remains in the gel solution.

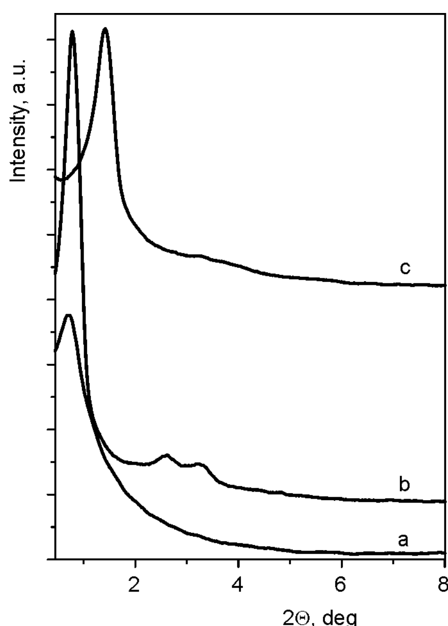

Fig. 1. XRD patterns for the Nb-PMO-E samples: a) as-synthesized; b) after extraction with HCl/EtOH mixture; c) after extraction and calcination at 773 K for 4 h

Table 1. Textural and structural properties of Nb-PMOs materials and their niobosilicate analogues

Material	Si/Nb	a_0[a] [nm]	Surface area [$m^2 \cdot g^{-1}$]	Pore width [nm]	Pore volume [$cm^3 \cdot g^{-1}$]			Wall thickness [nm]
					Total	Meso	Micro	
Nb-PMO-E	248	13.6	720	10.6	1.05	0.93	0.06	3.0
Nb-PMO-O	238	9.5	230	~6.0	0.51	0.37	0.05	3.5
Nb-SBA-15[b]	158	10.6	730	8.6	0.78	0.46	0.17	2.0

[a]a_0 – wall thickness ($a_0 = 2d_{100} \times 3^{-1/2}$, d – pore width).
[b]Synthesized with TEOS as a Si source.

To further elucidate the mesoporous characteristics of the obtained samples, their detailed pore structures were studied by the TEM technique. The TEM images of the extracted sample Nb-PMO-E observed from different orientations are shown in Fig. 2. They confirmed the 2D hexagonal pore structure with *P6mm* symmetry. For octane-

functionalized nioboorganosilicate two dimensional channels has been undoubtedly seen, however some areas with a lower order are also noticeable (not shown here).

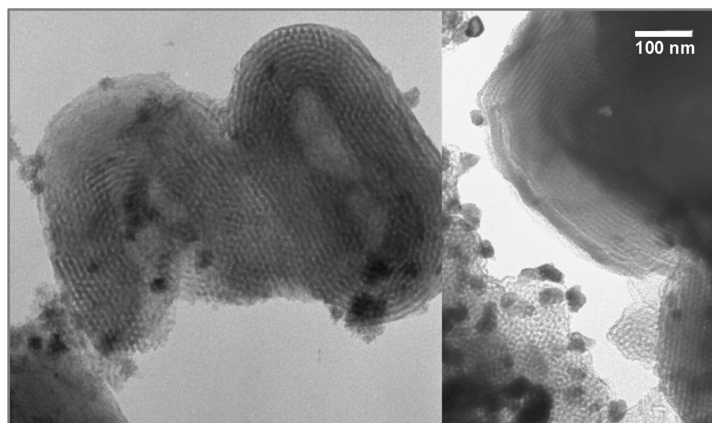

Fig. 2. Transmission electron micrographs for Nb-PMO-E

Surface areas, pore sizes, and pore volumes of the Nb-PMO materials are given in Table 1. The synthesis yielded Nb-PMO-E materials with the pore size of 10.6 nm and the specific surface area of 700 $m^2 \cdot g^{-1}$. The isotherm of PMO-E sample is of type IV with a pronounced uptake in the relative pressure (p/p_0) range of 0.7–0.9 due to capillary condensation in the mesopores, indicating the presence of relatively uniform mesopores (Fig. 3).

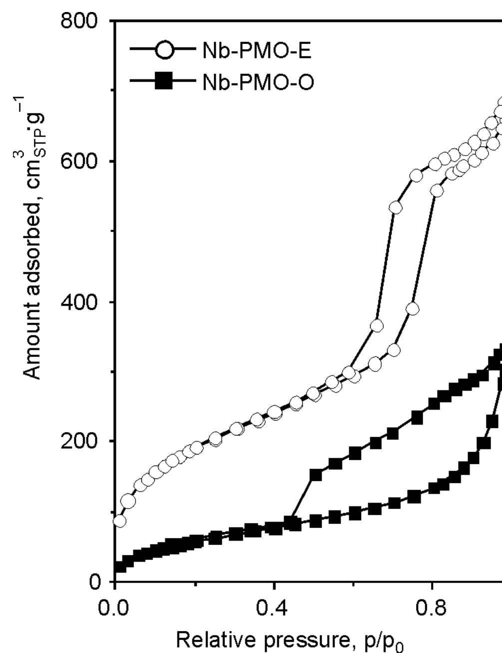

Fig. 3. Nitrogen adsorption-desorption isotherms at 77 K for Nb-PMOs materials

It is known that the inflection position depends on the width of the mesopores and that the sharpness usually indicates the uniformity of the mesopores, due to capillary condensation of N_2 within the mesopores. H1-type hysteresis loop displayed at a high relative pressure is characteristic of large-pore mesoporous materials with uniform cylindrical channels [7]. A visible increase in the adsorption at $p/p_0 > 0.9$ associated with the hysteresis for Nb-PMOs could be attributed to the existence of interparticle pores. The isotherm of the Nb-PMO-O sample is between type I and IV and thus can be regarded as supermicroporous (pores ranging between 1.5 and 2.0 nm [14]) which is further evidenced by a small contribution of typical mesopores (pore width ~6.0 nm) in the pore size distribution (Fig. 4). A decrease in the micropore volume is observed after introduction of silica source with bridging organic groups into the synthesis gel. This is also accompanied by a decrease in the primary mesopore volumes for longer organic chain in bridging positions, while an increase is visible for ethane group (Table 1). The wall thickness increases upon incorporation of organic groups. It is clearly visible from Table 1 that the sample prepared with the PO number equal to 7 possesses a lower wall thickness than the sample with $y = 14$. Moreover, the calcined samples lost the sharpness in the capillary condensation step, suggesting a partial collapse of the mesostructure, as observed from the XRD measurements (figure not shown) and a decrease of ~10–20% in the surface area in comparison to the extracted materials.

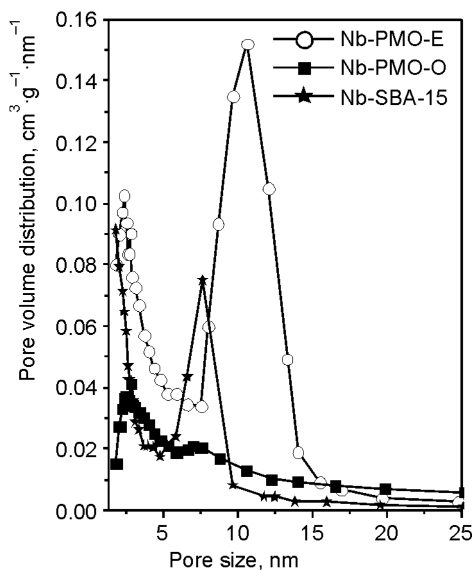

Fig. 4. Pore size distributions for the Nb-PMOs materials and their niobosilicate analogue

The pore size distribution (PSD) curves of the Nb-PMO-E and Nb-PMO-O are shown in Fig. 4. The KJS-BJH pore size distributions describe obvious existence of the bimodal pore structure, including some super micropores with widths lower than 2 nm and primary mesopores above 6 nm. It can be seen that Nb-PMO-E has a broader pore

size distribution, however with increased intensity compared to the pure Nb-SBA-15, indicating a lower degree of mesoorder obtained for the functionalized Nb-PMOs. As can also be seen, the pore size distribution for Nb-PMO-O material reveals only a very small mesopore volume in the typical mesoporous range (besides the supermicropores with pore widths lower than 2 nm). This feature is due to the nature of different sizes and molecular configurations of employed organic bistrialkoxysilyl precursors which causes different pore size distribution curves and ultimately different degrees of pore blockage/wall thickness.

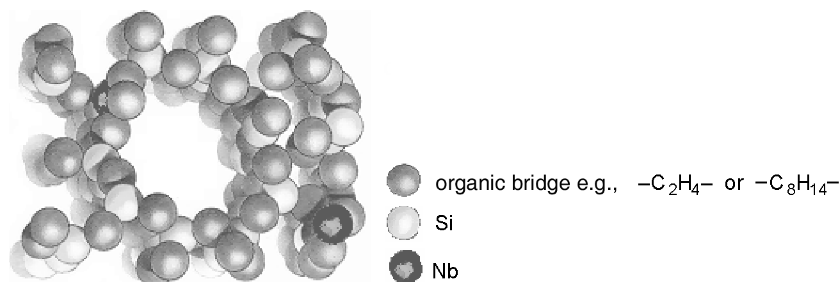

Fig. 5. General idea of the structure of Nb-PMOs materials synthesized from bissilylated organic bridging units and niobium species. Oxygen atoms have not been shown to make the picture clearer

FTIR and Raman data (not shown here) proved that the organic bridges are intact within the framework. Furthermore, these data provided evidence that the template was completely removed via extraction and there was no Si–C bonds cleaved during synthesis and extraction stages. The band at 225 nm on the UV-Vis patterns for Nb-PMOs (not shown here) clearly indicated a successful incorporation of Nb into the framework. Thus the framework clearly consists of both, organic groups and niobium species counterparts as shown in Fig. 5.

4. Conclusions

The nanostructured bridged nioboorganosilicates have been synthesized by the acid catalyzed hydrolysis and condensation of bridged silsesquioxane precursors containing two different organic bridging groups ($(C_2H_5O)_3Si–R–Si(OC_2H_5)_3$, R – ethylene or octylene) in the presence of nonionic template P123. The retention of niobium in the organosilica framework was ensured by a slow template removal. A successful synthesis of Nb-PMOs was confirmed by powder XRD (high periodicity), N_2 adsorption (surface area above 700 $m^2 \cdot g^{-1}$ and pore sizes with the maximum at about 8–11 nm), diffuse reflectance UV-vis spectroscopy (characteristic absorption band for Nb in the framework), and FTIR and Raman spectroscopies (presence of $CH_2–Si(OSi\equiv)_3$ groups).

Acknowledgements

The authors express their gratitude the Polish Ministry of Science and Higher Education for the financial support (N204 084 31/1965; 2006-09). BASF (Poland), ABCR GmbH & Co (Germany) and

Companhia Brasileira de Metalurgia e Mineração (Brazil) are acknowledged for donating surfactant, organosilica precursors and source of niobium used in this study.

References

[1] KRESGE C.T., LEONOWICZ M.E., ROTH W.J., VARTULI J.C., BECK J.S., Nature, 359 (1992), 710.
[2] INAGAKI S., GUAN S., FUKUSHIMA Y., OHSUNA T., TERASAKI O., J. Am. Chem. Soc., 121 (1999), 9611.
[3] ASEFA T., MACLACHAN M.J., COOMBS N., OZIN G.A., Nature, 402 (1999), 867.
[4] MELDE B.J., HOLLAND B.T., BLANFORD F., STEIN A., Chem. Mater., 11 (1999), 3302.
[5] ASEFA T., KRUK M., MACLACHAN M.J., COOMBS N., GRONDEY H., JARONIEC M., OZIN G.A., J. Am. Chem. Soc., 123 (2001), 8520.
[6] HOFFMANN F., CORNELIUS M., MORELL J., FROBA M., Angew. Chem. Int. Ed., 45 (2006), 3216.
[7] ZHAO D., HUO Q., FENG J., CHMELKA B.F., STUCKY G.D., J. Am. Chem. Soc., 120 (1998), 6024.
[8] NOWAK I., ZIOLEK M., JARONIEC M., J. Phys. Chem. B, 108 (2004), 3722.
[9] NOWAK I., ZIOLEK M., Microp. Mesop. Mater., 78 (2005), 281.
[10] KRUK M., JARONIEC M., SAYARI A., Langmuir, 13 (1997), 6267.
[11] JARONIEC M., KRUK M., OLIVIER J.P., Langmuir, 15 (1999), 5410.
[12] COUTINHO D., GORMAN B., FERRARIS J.P., YANG D.J., BALKUS K., Micropor. Mesopor. Mater., 91 (2006), 276.
[13] BOISSIERE C., LARBOT A., VAN DER LEE A., KOOYMAN P.J., PROUZET E., Chem. Mater., 12 (2000), 2902.

Received 28 April 2007
Revised 16 February 2008

Materials Science-Poland, Vol. 26, No. 1, 2008

Rational design of NbMSU-X type nanoporous materials with desired textural properties

A. FELICZAK, I. NOWAK*

Faculty of Chemistry, Adam Mickiewicz University, ul. Grunwaldzka 6, 60-780 Poznań, Poland

The so-called rational design principle – synthesis of materials with predictable structures and textures – has been explored using appropriate organic molecular structure directing agent, i.e. *p*-nonyl phenyl polyoxyethylene (PEO) polyoxypropylene (PPO) ether and tetraethyl orthosilicate (source of silicone) as a linker agent connecting to metal nodes via oxygen to control pore size and functionality of open coordination lattices. To rationally design new nanoporous materials based on niobosilicate, a small library of NbMSU-X nanoporous materials has been collected and its composites have been investigated by X-ray diffraction (XRD), transmission electron microscopy (TEM) and by nitrogen adsorption/desorption study. Design of structure directing agents and their composites with niobosilicates can lead to a rational synthesis of molecular sieves. We approach this strategy by using different pH and surfactant chain length.

Key words: *NbMSU-X synthesis; porous worm-like structure; characterization*

1. Introduction

Framework materials, three-dimensional (3D) solid-state assemblies, represent one of the most fascinating areas of current materials science. The significance of such constructions lays in their functional properties and applications as porous hosts for guest molecular species and as materials with interesting magnetic, electronic, optical and/or catalytic properties. A key topic of interest within the area of framework materials contains rational design and synthesis of such species allowing targeting properties of materials such as pore size, surface area, morphology, etc.

Nonionic alkyl poly(ethylene oxide) compounds are an important family of surfactants widely used as emulsifying, defoaming/antifoaming, coating, solubilizing, cleaning, lubricating and wetting agents. Pinnavaia et al. [1–3] used them to synthesize mesoporous silica and alumina in neutral aqueous solutions. The pore architecture of

---

*Corresponding author, e-mail: nowakiza@amu.edu.pl

the MSU-X molecular sieve materials is described as 3D interconnecting networks of worm-like channels. Although this class of mesoporous molecular sieves shows 'poor ordering', potential advantages of so-called MSU-X synthesis are lower surfactant toxicity and cost, high biodegradability, effortlessness for removal and regeneration [4]. Among various mesoporous molecular sieves, MSU-X materials possess regular pore diameters and wall thicknesses similar to MCM-41-type materials but generally they do not exhibit a long-range periodicity. On the other hand, a more disordered structure could have an immense impact on the catalytic activity and thus the incorporation of niobium into MSU-X framework is in the frame of our interest, as NbMCM-41 appeared to be highly active in the reaction of epoxidation [5]. Recently, these imperfectly ordered mesoporous materials were claimed to be more active in diffusion-limited reactions due to a faster effective diffusion in comparison to MCM-41 and SBA-15 materials [6]. Various strategies of synthesis for MSU-X materials have been applied since the first report [1–4]. Usually, alkyl-polyoxyethylene (PEO), alkyl aryl-PEO, polyoxypropylene(PPO)-PEO block copolymers or Tween-type nonionic ethoxylated sorbitan esters are used as the structure directing agents under neutral or acidic conditions.

Here, we report the formation of mesoporous silicas using low-cost commercially available nonionic surfactants, namely *p*-nonyl phenyl polyethylene polypropylene ether. The aim of this work was to find the synthesis conditions that would lead to the formation of materials with various textural properties, which after incorporation of niobium, would gain catalytic activity for the liquid phase oxidation of substrates with various sizes.

2. Experimental

The NbMSU-X samples were prepared at room temperature (RT) by using two different nonionic surfactants Rokafenol N8P7 and N8P14: *p*-nonyl phenyl polyoxyethylene(PEO) polyoxypropylene(PPO) ethers of general formula: 2-[(4-nonylphenoxy)(ethoxy)$_8$(propoxy)$_y$]ethanol: with different polyoxyethylene (PO) group numbers, i.e., 7 or 14. Tetraethyl orthosilicate (TEOS, Fluka) and ammonium trisoxalate complex of niobium(V) were used as silicon and niobium sources, correspondingly. The TEOS/surfactant and Si/Nb molar ratios were kept as 7 and 32 in all syntheses, respectively. After mixing all the ingredients, pH of the synthesis gel was adjusted to 0.1, 2 or 6. The synthesis system was stirred at moderate speed for 20 h at RT. The solids were then recovered by filtration, washed with distilled water, and air-dried at RT overnight. The template was then removed by calcination in air at 873 K for 4 h. The samples used in this work will be denoted as follows: NbMSU-X-*y*-*z*, where *y* is the amount of PO groups in the surfactant and *z* – rounded pH of the synthesis gel.

Various physicochemical studies, viz., X-ray diffraction (XRD), transition electron microscopy (TEM), N_2 physisorption, X-ray fluorescence spectroscopy (XRF),

H_2-temperature programmed reduction (H_2-TPR) were used to find the location of niobium ions in the MSU matrix and to check the mesoporosity of the samples with an emphasis on verification how the pH may affect the property of the NbMSU-X materials. XRD patterns were measured with a TUR-62 diffractometer (CuK_α radiation, 40 kV) in two 2Θ ranges: 1.2–10° and 4–60° with the step size of 0.02° or 0.05°, respectively.

Adsorption/desorption experiments using N_2 were carried out at 77 K on a Micromeritics ASAP 2010. Before each measurement, the samples were first outgassed at 573 K for 3 h in vacuum. The N_2 isotherms were used to determine the specific surface areas using the standard BET equation at the relative pressure (p/p_0) from 0.05 to 0.2. Pore sizes were obtained from the N_2 adsorption branch, by the Barret –Joyner–Halenda (BJH) method with the corrected Kelvin equation, i.e. the KJS–BJH method at the maximum of pore size distribution [7]. Moreover, the α_s-plot analysis [8] was performed for all obtained samples for the evaluation of the micropore volume. The single-point total pore volume was obtained from the amount adsorbed at p/p_0 = 0.98. Transmission electron microscopy images were obtained using a JEOL-2000 transmission electronic microscope with an accelerating voltage of 80 kV. The metal content in the calcined NbMSU-X samples was determined by X-ray fluorescence spectroscopy (MiniPal, Philips) using calibration curves. The H_2-TPR of the samples was carried out using 10 vol. % H_2 in Ar as reducing agent (flow rate 10 $cm^3\cdot min^{-1}$). The sample (0.1 g) was filled in a quartz tube, treated in a flow of helium at 623 K for 1 h and cooled down to room temperature. Then it was heated at the rate of 10 $K\cdot min^{-1}$ to 1373 K under the reducing mixture. Hydrogen consumption was measured by a thermal conductivity detector in the Micromeritics AutoChemII apparatus.

3. Results and discussion

The possibility of the isomorphous substitution of silicon with niobium in MSU-X mesoporous molecular sieves is dependent on the conditions of synthesis. The evolutions of Si/Nb ratio as a function of pH for NbMSU-X materials prepared with *p*-nonyl

Table 1. Structural and textural properties for NbMSU-X materials

Material	Si/Nb ratio	d [nm]	Surface area [$m^2\cdot g^{-1}$]	Pore volume [$cm^3\cdot g^{-1}$]				Pore width [nm]	t^a [nm]
				Total	Meso1st	Text.	Micro		
NbMSU-X-7-0	162	3.9	860	0.38	0.24	0.09	0.05	2.2	1.7
NbMSU-X-7-2	26	5.1	650	0.61	0.50	0.10	0.01	3.1	2.0
NbMSU-X-7-6	13	6.8	470	0.71	0.58	0.13	0.00	4.0	2.8
NbMSU-X-14-0	104	4.9	1020	0.47	0.35	0.08	0.04	2.6	2.3
NbMSU-X-14-2	24	6.0	860	0.65	0.55	0.10	0.01	3.6	2.4
NbMSU-X-14-6	12	7.6	640	0.80	0.69	0.11	0.00	5.2	2.4

[a]t – wall thickness calculated as the difference between d and a pore width.

phenyl polyoxyethylene polyoxypropylene ether with different (PO) group numbers, (7 or 14) are presented in Table 1. The Si/Nb ratios of the calcined products were four times higher than those of the initial gel mixtures at pH = 0.1 in the gel, indicating that not all niobium was incorporated to the final product. The Si/Nb ratio decreases with the increase of pH. At pH=6, the Si/Nb ratios are equal to 13, suggesting that a part of Si from the reactant mixture was not incorporated in the final product.

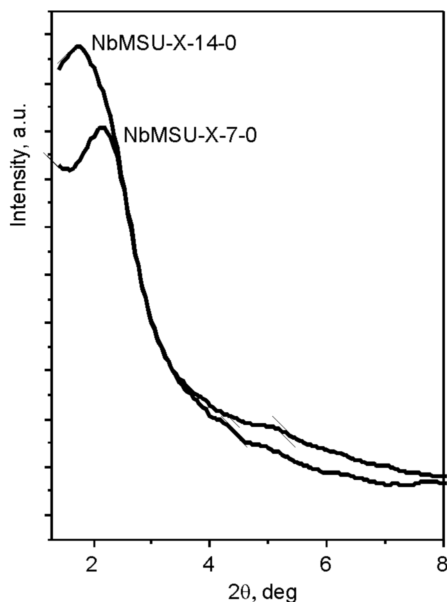

Fig. 1. XRD patterns for the NbMSU-X samples prepared at pH = 0.1

The powder XRD patterns of calcined NbMSU-X materials (representative low-angle diffraction patterns are shown in Fig. 1) showed single, rather broad peaks arising from the average pore–pore separation in the disordered worm-hole framework, characteristic of MSU-type materials. The mesoporous niobosilicates exhibit a single peak at low 2θ values in the X-ray diffraction patterns corresponding to a large d spacing whose intensity, position and width depend on the synthesis conditions. The basal distance (d) changed from 3.9 for pH = 0 to 6 for pH = 6 showing a gradual increase of the average pore-to-pore separation. The positions of the main diffraction line are correlated with the size of the surfactant. They moved to a lower 2Θ value upon increase of the PO group number (e.g., the d spacing increases from 3.9 to 4.9 for samples prepared at pH = 0.1 with the use of N8P7 and N8P14 types surfactants, respectively (Table 1)) thus suggesting the growth of the distance between two nearest pore centres. Additionally, X-ray diffraction data at high angles (2θ in the range of 10–60°) do not show any peaks of niobium(V) oxide phase.

The existence of the worm-like channel array was further confirmed by the transmission electron microscopy. Figure 2 shows the TEM micrograph of one representative of the NbMSU-X family. The disks of light contrast correspond to pores, while

the dark networks represent silica walls. One can clearly see that this sample presents a worm-like structure which has commonly been observed for MSU-type materials. Both XRD patterns and TEM micrographs suggest that NbMSU-X samples belong to the MSU-type materials.

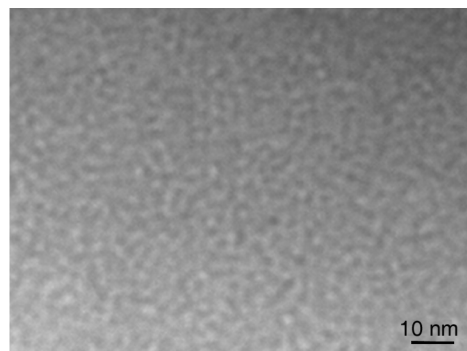

Fig. 2. Transmission electron micrograph for NbMSU-X-14-0

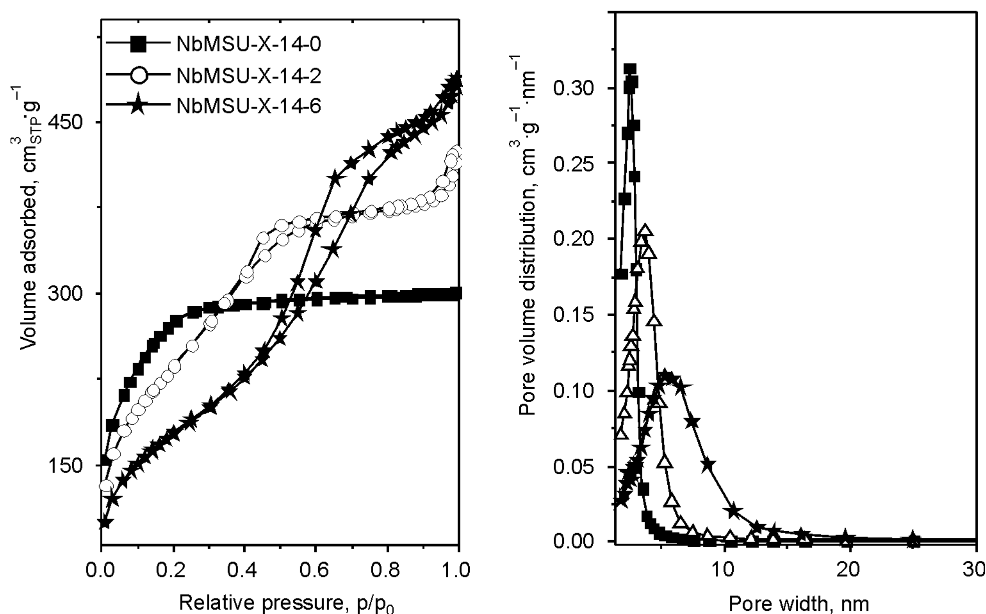

Fig. 3. Nitrogen adsorption-desorption isotherms at 77 K (left) and pore size distributions (right) for the NbMSU-X-14-z materials

Almost all N_2 isotherms for NbMSU-X samples (Fig. 3 shows nitrogen adsorption isotherms for a series of NbMSU-X-14-*z*) were of type IV, indicating that all materials belong to the mesoporous family. It should be noted that, with increasing pH value of the micellar solution from ~0.1 to 6.0, a sharp increase in the adsorbed volume (due to capillary condensation) shifts towards higher relative pressures. At pH = 6, the adsorbed volume still increases instead of reaching a plateau at high relative pressures. This explains the appearance of secondary porosity (compare textural pore volume in

Table 1). The N_2 isotherms for the NbMSU-X-14-0 (Fig. 3) and NbMSU-X-7-0 (not shown here) can be classified as intermediate Type I (characteristic of a microporous adsorbent) and IV isotherm in the IUPAC classification, which is characteristic of supermicroporous compounds, i.e., porous material with pores ranging between 1.5 and 2.0 nm [9, 10].

Narrow pore size distributions (PSDs) for mesoporous materials were characteristic of NbMSU-X prepared at pH = 0.1. The FWHM (full width at a half maximum) of about 1 nm measured for the pore size distribution curve (Fig. 3, right side) indicates that the NbMSU-X sample prepared via nonionic templating at very low pH has well-defined uniform pore dimensions. This behaviour is similar to that observed for mesoporous silicas prepared using ionic alkyl ammonium surfactants. The PSD became broader as the initial pH value increased and their maximum shifted from values below 2.6 nm for pH = 0.1 to 5.2 nm for pH = 6. It is worthy to stress that the NbMSU-X materials showed narrower PSD than the corresponding pure siliceous materials. The average pore widths estimated from the TEM images agree well with the results obtained from nitrogen adsorption data.

Table 1 summarizes all the textural characteristics of the niobium-containing MSU materials. The NbMSU-X samples hold the classical advantages of high surface area (~500–1000 $m^2 \cdot g^{-1}$), large porosity (total pore volume up to 0.8 $cm^3 \cdot g^{-1}$) and uniform pore size (pore width range: 2.4–5 nm) as typical mesoporous silicas. The evolutions of specific surface area vs. pH of micellar solution (Table 1) show that its value decreases between pH = 0.1 and 6. Despite incorporating large amount of niobium, the textural properties of NbMSU-X are better or similar to those of pure siliceous MSU-X (not shown here). The BET surface area for all niobium-containing materials studied was higher than that for corresponding pure siliceous materials. The total pore volume of Nb-containing materials was between 0.4 and 0.8 $cm^3 \cdot g^{-1}$ with the highest value for pH = 6 and also higher than for siliceous ones. The existence of micropores in NbMSU-X is obvious from Table 1. The pore width increases with increasing number of PO groups. Notably, the pore-wall thickness, as obtained from the difference between the pore–pore correlation distance and pore width, increases from 1.6 to 3.0 nm with increasing acid concentration and was higher for NbMSU-X than for MSU-X. Such an effect was more pronounced for samples made with the assistance of N8P7 surfactant. Apparently, these results of the analysis of N_2 adsorption were consistent with the XRD and TEM observations.

H_2-TPR profiles of the series of materials prepared at pH = 0.1 are presented in Fig. 4. The materials show a main reduction peak starting at 1200 K assigned to the stepwise reduction of framework niobium [11]. The same profiles were also observed for samples prepared at higher pH values. The TPR studies indicate that for all materials, a strong interaction of niobium with the siliceous framework is evidenced and the reduction of framework niobium is difficult and observed at temperatures higher than 1200 K. Also the DR UV-Vis spectra (not shown here) of the NbMSU-X materials displayed similar features, consisting of the main absorption band at 220 nm that can be mainly ascribed to

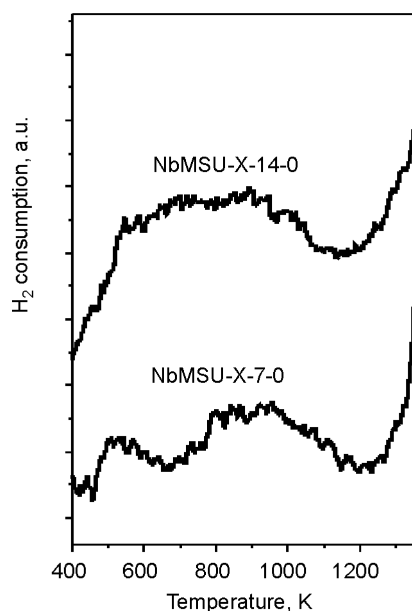

Fig. 4. H_2-TPR profiles for the NbMSU-X materials at pH = 0.1

Nb^{5+} in tetrahedral coordination [12]. No bands typical of five and six-coordinated Nb species (~250 nm) in small niobia nanodomains species [12] or of bulk niobia were observed in the spectra. Based on H_2-TPR and UV-Vis studies it is believed that niobium was incorporated into the framework of all samples studied.

4. Conclusions

The template properties have quite pronounced effect on the structural characteristics of mesoporous NbMSU-X molecular sieves prepared by using nonionic surfactant templates under acidic conditions. The ability of the *p*-nonyl phenyl polyoxyethylene polyoxypropylene ether/water micellar system to act as a template for the synthesis of mesoporous niobium-containing MSU-type materials was proved. As a result, supermicroporous and/or mesoporous molecular sieves of the NbMSU-X type have been synthesized by templating in strong acidic, acidic or almost neutral medium. Thus, the nanostructure of these materials can be monitored by the accurate control of the parameters of synthesis. Due to the simplicity of preparation and adjustable textural parameters, Nb-MSU-X materials can be expected to provide potentially high catalytic activity for a number of catalytic processes.

Acknowledgements

The authors would like to thank the Polish Ministry of Science and Higher Education for the financial support (N204 084 31/1965). PCC Rokita SA (Poland) and Companhia Brasileira de Metalurgia e Mineração (Brazil) are acknowledged for donating the surfactants and the source of niobium used in this study.

References

[1] BAGSHAW S.A., PROUZET E., PINNAVAIA T.J., Science, 269 (1995), 1242.
[2] BAGSHAW S.A., PINNAVAIA T.J., Angew. Chem., Int. Ed. Engl., 35 (1996), 1102.
[3] PROUZET E., PINNAVAIA T.J., Angew. Chem., Int. Ed. Engl., 36 (1997), 516.
[4] BAGSHAW S.A., Chem. Commun., (1999), 271.
[5] NOWAK I., KILOS B., ZIOLEK M., LEWANDOWSKA A., Catal. Today, 78 (2003), 487.
[6] LIU J., FENG X.D., FRYXELL G.E., WANG L.Q., KIM A.Y., GONG M.L., Adv. Mater., 10 (1998), 161.
[7] KRUK M., JARONIEC M., SAYARI A., Langmuir, 13 (1997), 6267.
[8] JARONIEC M., KRUK M., OLIVIER J.P., Langmuir, 15 (1999), 5410.
[9] INFANTES-MOLINA A., MERIDA-ROBLES J., MAIRELES-TORRES P., FINOCCHIO E., BUSCA G., RODRIGUEZ-CASTELLON E., FIERRO J.L.G., JIMENEZ-LOPEZ A., Microp. Mesop. Mater., 75 (2004), 23.
[10] BOISSIERE C., LARBOT A., VAN DER LEE A., KOOYMAN P.J., PROUZET E., Chem. Mater., 12 (2000), 2902.
[11] ZIOLEK M., SOBCZAK I., LEWANDOWSKA A., NOWAK I., DECYK P., RENN M., JANKOWSKA B., Catal. Today, 70 (2001), 169.
[12] GAO X.T., WACHS I.E., WONG M.S., YING J.Y., J. Catal., 203 (2001), 18.

Received 28 April 2007
Revised 16 February 2008

Materials Science-Poland, Vol. 26, No. 1, 2008

Application of phase imaging and force modulation mode for description of dispersion of carbon nanotubes in polyol matrix

M. J. WOŹNIAK[1, 2*], J. RYSZKOWSKA[1], T. SZYMBORSKI[1],
G. CHEN[2], T. TATEISHI[2], K. J. KURZYDŁOWSKI[1]

[1]Faculty of Materials Science and Engineering, Warsaw University of Technology,
ul. Wołoska 141, 02-507 Warsaw, Poland

[2]Biomaterials Centre, National Institute for Materials Science,
Namiki Site:1-1, Namiki, 305-0044 Tsukuba, Japan

Application of the phase imaging and force modulation SPM techniques for description of the dispersion of multiwalled carbon nanotubes (MWCNTs) in polyol (polyester diol- PED) matrix is presented. The MWCNTs-PED mixture is used to prepare polyurethane (PUR) nanocomposites. Dispersion of MWCNTs in PUR depends on the dispersion of carbon nanotubes in polyol. It is very important to evaluate the degree of homogeneity of the investigated materials. The phase imaging and force modulation microscopy connected with tapping mode allow collecting not only topography images but also images of mechanical properties of a material (hardness, adhesion, friction). By using these SPM modes, it is possible to distinguish structural elements of the mixture and hence to obtain direct information about the distribution of MWCNTs in PED matrix.

Key words: *AFM; phase imaging; force modulation; composite*

1. Introduction

Dynamic scanning probe microscopy (DSPM) includes techniques such as intermittent contact (IC) and non contact (NC) atomic force microscopy (AFM) modes in which an external source causes a cantilever oscillation [1]. Intermittent contact AFM (called also tapping mode – TM) works in a similar way as NC AFM with exception that the cantilever oscillates in relatively large amplitude, 10–100 nm. This results in a short-time contact of the tip with the sample surface during each cycle of the oscillation [2]. In a tapping mode, a stiff cantilever is set to oscillate near or at its resonant

*Corresponding author, e-mail: mwozniak@inmat.pw.edu.pl

frequency, with an amplitude A_0 (called a free oscillation amplitude) before a tip is brought in contact with the sample surface. As the tip is brought close to the sample surface, the characteristics of the cantilever vibration (amplitude, resonance frequency, phase angle of vibration) change due to tip-sample interaction [3, 4]. Important experimental parameter of TM is the set-point r, defined as

$$r = \frac{A_{sp}}{A_0}$$

where A_0 is the cantilever free oscillation amplitude, A_{sp} – set-point amplitude (cantilever oscillation amplitude during scanning) [2–5].

The oscillation amplitude during scanning, smaller than the free amplitude, is used as the feedback signal for the electronic controller [6]. The topographical contrast is generated by the vertical movement of the piezoelectric scanner which moves to maintain the set-point oscillation amplitude [6–8]. In TM SPM, a region of the surface of large amplitude damping is recorded as high in a topographic image and hence bright in a height image [4].

1.1. Phase imaging

In the tapping mode, material property variations can be additionally mapped by recording the phase lag (df) of the cantilever oscillation relative to the signal sent to the cantilever's piezoelectric driver (Fig. 1) [5, 7]. The phase image can be generated as a consequence of variations in properties of materials such as adhesion, friction, viscoelasticity [3, 5], hardness as well as a difference in electrical or magnetic properties

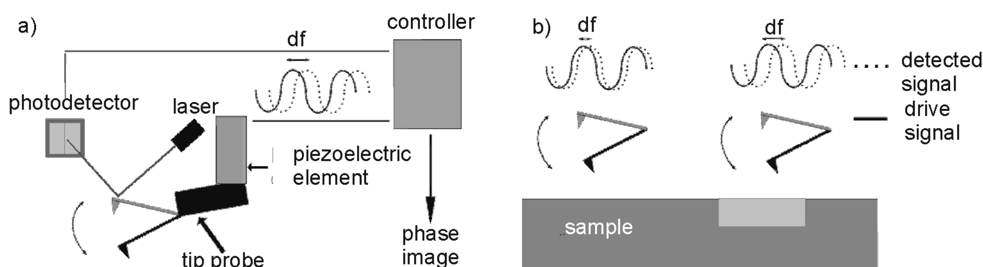

Fig. 1. Scheme of the phase imaging microscopy

[6, 8]. Under favourable conditions, the phase contrast imaging shows details of the surface roughness, which is not easily detected by topographical imaging [6]. Phase image (PI) is produced by monitoring the phase difference (df) between the oscillations of the cantilever and the standard signal, recorded by the piezoelectric element (Fig. 1) [6]. The phase contrast may not be generated if the surface is highly uniform [6]. It arises from variations in the composition of the sample surface as well as due to

variations in topography caused by changes in adhesion between the tip and specimen surface [6]. The phase contrast can be attributed to enhanced adhesion of the tip in a region of increased tip-surface contact area [6]. Due to a higher adhesion, the lateral forces on the tip increase. The effect is not only connected with the change of the chemical or mechanical material properties, as it could be related to nanoscopic topography that increases surface-tip contact area [6]. In the topographic contrast mode, small features of a rough surface are often hardly visible because the contrast of the image corresponds to variations in the topography. Image processing, e.g. highpass (edge detection filter), can normally enhance the resolution of an image which remains unsatisfactory anyway [6].

1.2. Force modulation microscopy

Another method of determining elastic and viscoelastic properties of surfaces is the force modulation microscopy (FMM) [9, 10]; local sample elasticity is measured by oscillating a probe in such a way that its tip slightly indents into a sample. It is an imaging mode derived from the contact mode (CM) AFM that measures relative elasticity/stiffness of surface features. It is commonly used to map the distribution of elements in composite systems [6, 8].

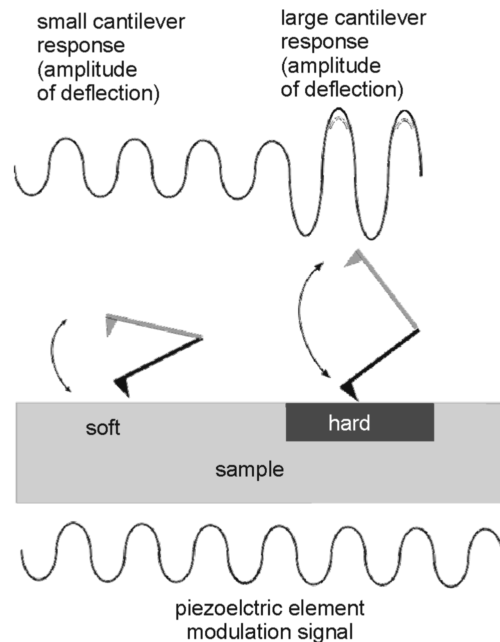

Fig. 2. Scheme of the force modulation microscopy

The measurement is performed in CM by applying an oscillation to the z-piezo and measuring the resulting cantilever amplitude (Fig. 2) [6]. Because of the periodic motion, a tip probe indents slightly into the sample during scanning across the surface.

The tip will be able to indent a soft material more easily than a harder material. The value of the cantilever deflection is inversely related to the value of indentation. In the case of an extremely soft material, the tip indents deeply into the surface, resulting in a very small deflection of the cantilever. A very hard sample allows less indentation, with the cantilever deflected by a larger value. The relative elasticity of the sample is measured by recording the amplitude of the tip deflection versus tip position over the sample [11]. When the tip encounters a hard site (dark area) surrounded by a soft medium, the hard material absorbs less energy of the cantilever, causing an increase in the cantilever response and signal amplitude. Softer sites absorb more cantilever energy, causing a reduced cantilever response and lower amplitudes, and these sites are recorded as light areas of the image [8].

2. Experimental

Materials studied were composites with PED matrix of poly(ethylene adipate) 2000 Da Alfaster T620 (Alfa Systems Poland) and multiwall carbon nanotubes (MWCNTs) obtained from Sun Nanotech Co Ltd, China. The diameter of a CNT was 10–30 nm, length 1–10 μm. Purity of the MWCNTs was over 90%. The mixture of MWCNTs and poly(ethylene adipate) was prepared by a two step process [12]. In the first stage, MWCNTs and acetone were mixed for 10 min using a mechanical stirrer. Afterwards carbon nanotubes with solvent were mixed in an ultrasonically assisted mixer VCX-750 (Sonics and Materials Inc.) at 50 °C in an ultrasonic bath under 40 kHz for 0.5 h. In the second stage, PED was added and the mixture was stirred under the same conditions as nanotubes with acetone. The MWCNT weight fraction was 0.05%. After the mixing process, acetone was evaporated.

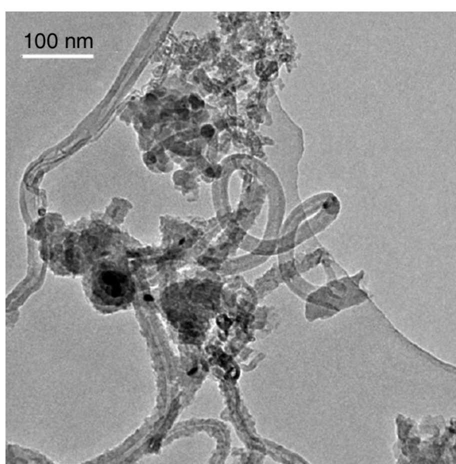

Fig. 3. TEM photograph of the carbon nanotubes

Measurements were performed using MultiMode SPM with NanoScope IIIa controller and Phase Extender Box, from Veeco Company. The microscope was equipped

with a TS 150 dynamic vibration isolation system, and worked in the tapping mode with phase imaging and in the tapping mode with a force modulation mode. For the phase imaging, tip probes, model RTESP (Veeco), made of P doped (*n*) Si were used. Nominal parameters were the following: radius of curvature < 10 nm, rectangular cantilever with the length of 125 μm, width – 35 μm, resonant frequency 300 kHz, spring constant 40 N/m. In the case of the force modulation, tip probes, model LTESP (Veeco), made of (*n*) doped Si were used. Nominal parameters were the following: radius of curvature < 10 nm, rectangular cantilever with the length of 225 μm, width 38 μm, resonant frequency 190 kHz, spring constant 48 N/m. All experiments were performed under ambient conditions at room temperature.

3. Results and discussion

3.1. Phase imaging

The phase imaging experiment was performed at a moderate tapping condition (set-point, $r = 0.6$) [2, 3]. This value of set-point was selected according to literature [2, 4, 5] because it was believed to provide the best phase contrast conditions, without the risk of contrast reversion [3–5] and damaging the sample surface [5]. In the case of moderate tapping, the cantilever behaviour is largely dominated by the indentation forces and hence tip-sample stiffness [3]. In the case of light tapping, the motion of the cantilever can be dominated by attractive forces and finally tip can be trapped on the sample surface [2, 3]. Hard tapping condition can make TM AFM more similar to force modulation microscopy [2, 3].

Figure 4a shows the topographic image (collected using the tapping mode) of the MWCNTs-polyol mixture after dimethylketone etching. Figure 4b is the topographic image after highpass filtering. Phase contrast image of the same area is shown in Fig. 4c. Highpass filtering replaces each data point in the image with the weighted difference between that data point and each of its eight neighbours. This filtering is useful in highlighting edges or areas with rapid changes of height in the image [13]. In the topographic image, long objects are visible with the average diameter of 180 nm covered with a droplet-like layer. The 180 nm diameter corresponds to the diameter of the bundle of nanotubes seen in the TEM photographs (Fig. 3). Slight differences may be due to the tip shape effect [8, 14] and thin polyol layer covering the nanotubes filler. Data processing (highpass filtering) allowed one to easily detect the edges of the filler and one can see that the filler was partly covered with the PED layer. The phase contrast image distinctly showed details hardly visible in topographic and processed images. From the phase image one could clearly recognize grain structure of the PED matrix and a droplet-like film of PED covered MWCNTs. This matrix grains and droplet-like structure could be an effect of chemical eching during the sample preparation. The results discussed above are clearly shown in Figs. 5a–c (magnified pictures

of the right bottom corner of Figs. 4a–c, respectively). Furthermore, in Fig. 5c fibres are visible (indicated with white arrows) with diameters about 40 nm that is in very good agreement with the average diameter of single MWCNTs (shown in the TEM photograph, Fig. 3). These details are invisible in topographic, even filtered, images. For the set-point value of 0.6, the stiff (harder) region of the sample causes a positive phase shift [3, 5] because the carbon nanotubes were brighter in the phase contrast image (a tip probe is more sensitive to stiff nanotubes than to thin and relatively soft polyol layer covered nanotubes).

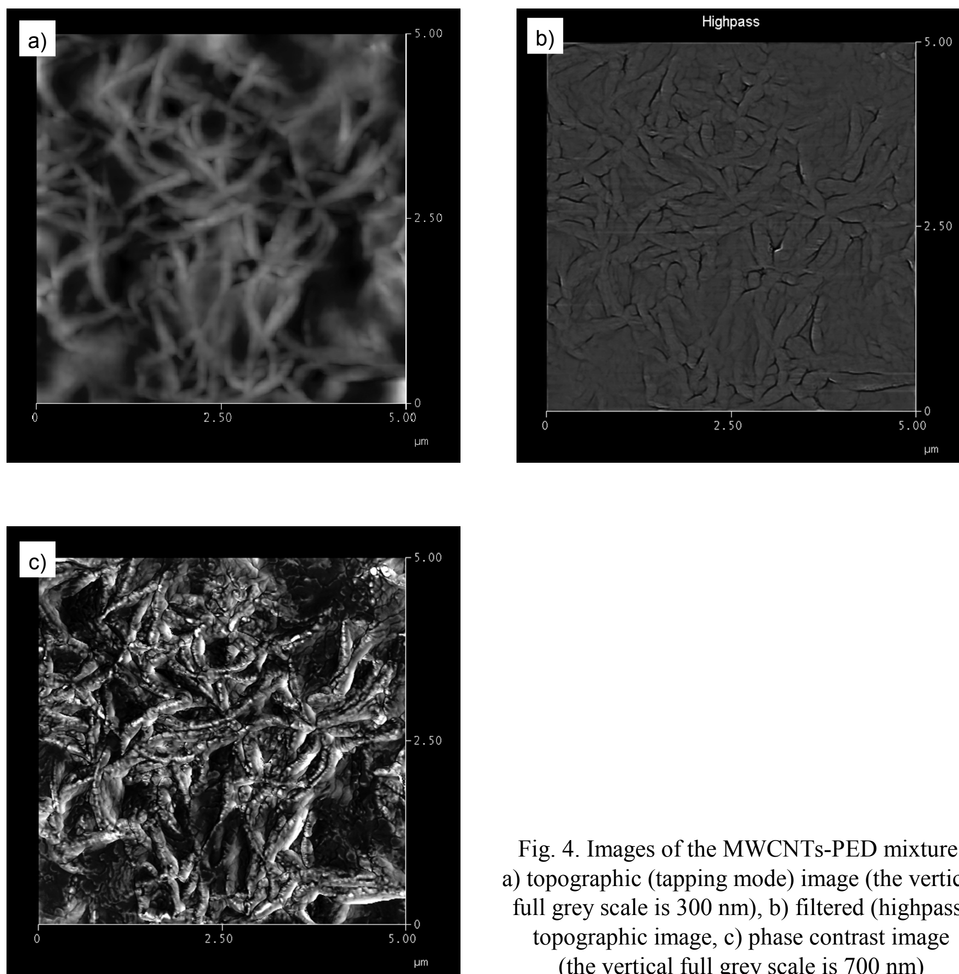

Fig. 4. Images of the MWCNTs-PED mixture: a) topographic (tapping mode) image (the vertical full grey scale is 300 nm), b) filtered (highpass) topographic image, c) phase contrast image (the vertical full grey scale is 700 nm)

Another effect visible in the phase contrast images is a difference in hydrophilicity. Hydrophilic elements of the structure cause positive phase shift (light parts of the image), and hydrophobic ones cause negative phase shift (darker parts) [4]. In this way, MWCNTs not covered with polyol droplets are visible in dark contrast (MWCNTs indicated with arrows in Fig. 5c).

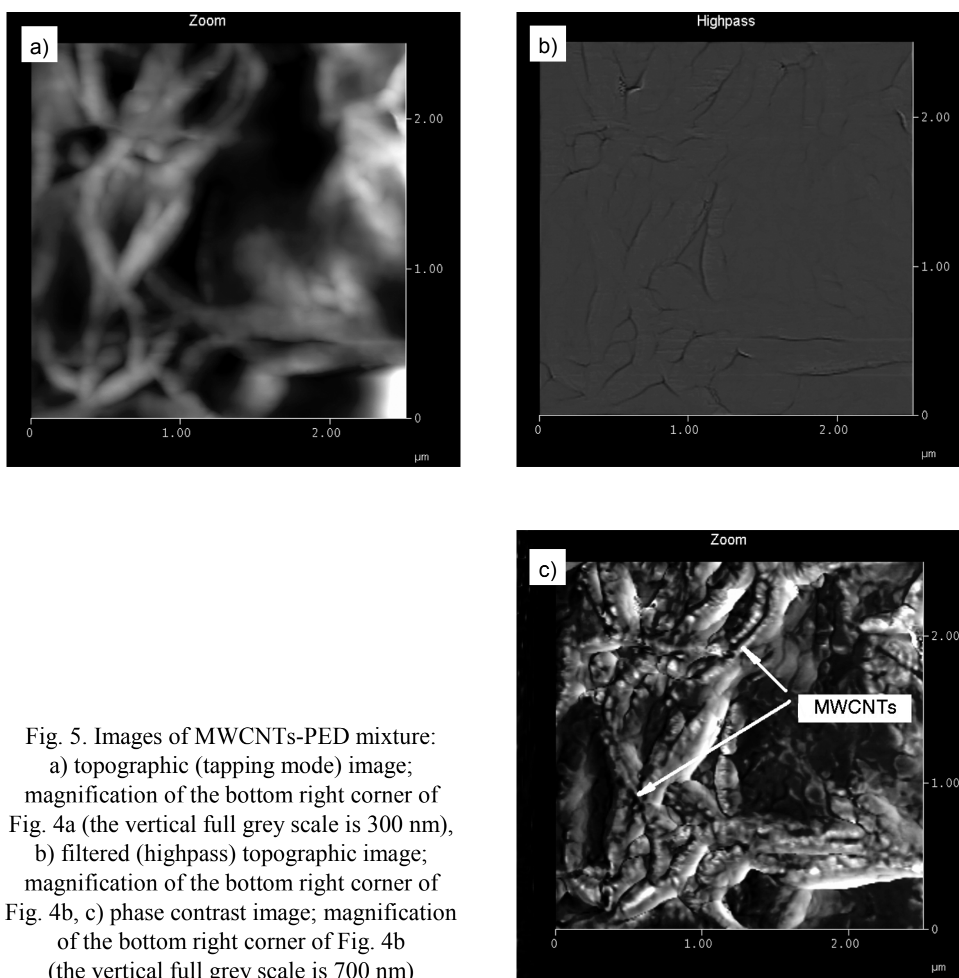

Fig. 5. Images of MWCNTs-PED mixture:
a) topographic (tapping mode) image;
magnification of the bottom right corner of
Fig. 4a (the vertical full grey scale is 300 nm),
b) filtered (highpass) topographic image;
magnification of the bottom right corner of
Fig. 4b, c) phase contrast image; magnification
of the bottom right corner of Fig. 4b
(the vertical full grey scale is 700 nm)

3.2. Force modulation microscopy

Figure 6 shows the topographic (collected in tapping mode), highpass processed topographic and force modulation images. In Figure 6a, large variations in topography can be seen. There were no clearly resolved structural elements of the MWCNTs-polyol mixture. Even image processing (highpass filtering, partly successful as discussed above) could not improve the quality of the image (Fig. 6b). Dark, long objects can be clearly distinguished (indicated with arrows) in Fig. 6c which is the force modulation image. In the case of the force modulation contrast, a dark contrast means that these objects are harder than the surrounding matrix. An average diameter of these elements was 170 nm which was in good agreement with the diameter of the bundle of nanotubes, as shown in TEM photographs. Objects of similar diameters were visible in phase images (described in Sect. 3.1). The diameter coincidence and high hardness indicate that the

object shown in the force modulation image was the carbon nanotube filler. Using the force modulation microscopy, it is possible to distinguish in an easy way structural elements of the hybrid material even if there is no differences in sample topography.

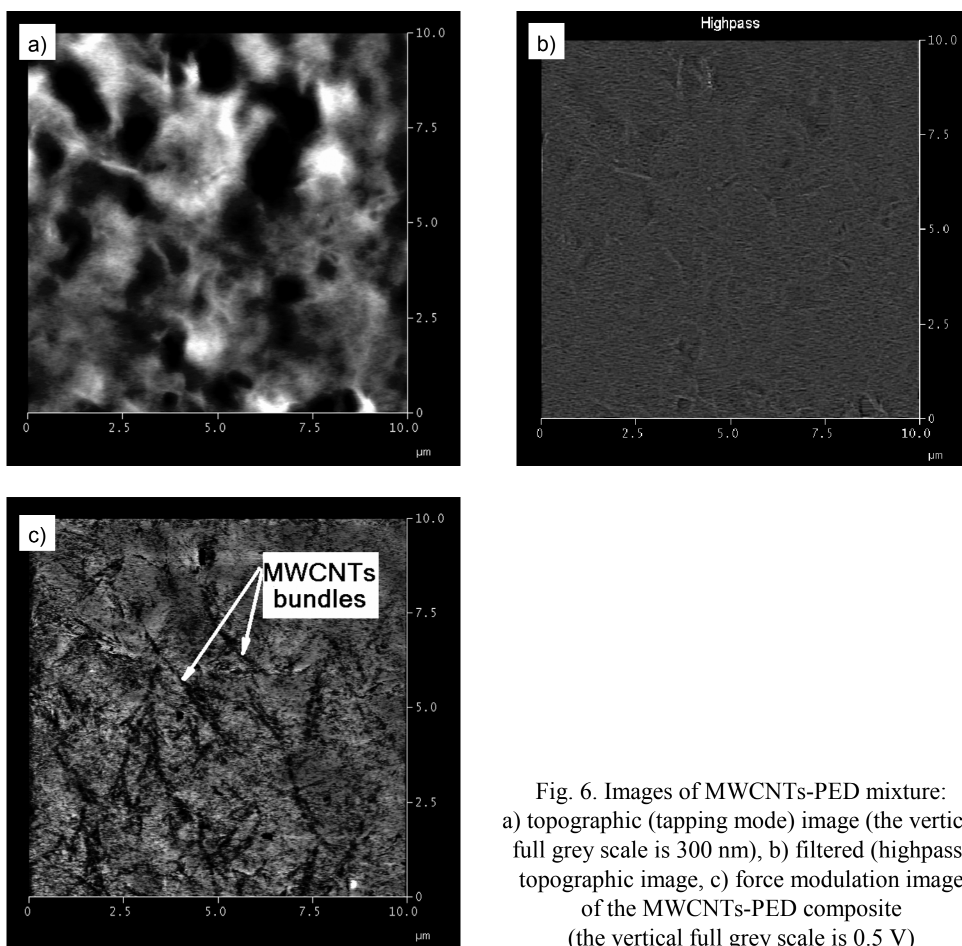

Fig. 6. Images of MWCNTs-PED mixture: a) topographic (tapping mode) image (the vertical full grey scale is 300 nm), b) filtered (highpass) topographic image, c) force modulation image of the MWCNTs-PED composite (the vertical full grey scale is 0.5 V)

4. Concluding remarks

Phase imaging and force modulation microscopy in connection with the tapping mode allow simultaneous acquisition of both topographic and material properties of images. A phase contrast image is generated as a consequence of variations in properties of materials such as adhesion, friction viscoelasticity, hardness as well as local differences in electrical or magnetic properties. The force modulation microscopy can serve as a convenient method of investigation of elastic and viscoelastic properties of the material surface.

These SPM methods may be especially useful for imaging hybrid nanomaterials where it is possible to obtain not only a topographic contrast, but also the contrast between regions of different properties. This usefulness was proved by the case of the multiwalled carbon nanotubes (MWCNTs) in polyol (polyester diol) matrix. The above mentioned techniques allow one to distinguish structural elements of a composite material even if differences in sample topography are small or none. Moreover, using phase imaging it is possible to analyse very fine details of sample morphology. Thus a combined study of the topography and material properties leads to a better understanding of the material in question.

Acknowledgements

M. J. Woźniak is awarded Domestic Grants for Young Scientists by Foundation for Polish Science (FNP) in 2006. This work was financially supported by Polish Committee for Scientific Research during 2005-2008 as a research project 3T08A07428.

References

[1] GREENE M.E., KINSER C.R., KRAMER D.E., PINGREE L.S.C., HERSAM M.C., Microscopy Res. Techn., 64 (2004), 415.
[2] CHEN X., DAVIES M.C., ROBERTS C.J., TENDLER S.J.B., WILLIAMS P.M., DAVIES J., DAWKES A.C., EDWARDS J.C., Ultramicroscopy 75 (1998), 171.
[3] BAR G., THOMANN Y., BRANDSCH R., CANTOW H.J., WHANGBO M.H., Langmuir, 13 (1997), 3807.
[4] BRANDSCH R., BAR G., WHANGBO M.H., Langmuir, 13 (1997), 6349.
[5] NAGAO E., DVORAK J.A., Biophys. J., 76 (1999), 3289.
[6] PANG G.K.H., BABA-KISHI K.Z., PATEL A., Ultramicroscopy, 81 (2000), 35.
[7] GARCIA R., PEREZ R., Surf. Sci. Rep., 47 (2002), 197.
[8] *A Practical Guide to Scanning Probe Microscopy SPM*, Veeco Instruments Inc., 2005, pp. 5, 6, 9, 12, 15, 26.
[9] MAIVALD P., BUTT H.J., GOULD S.A.C., PRATER C.B., DRAKE B., GURLEY J.A., ELINGS V.B., HANSMA P.K., Nanotechn., 2 (1991),103.
[10] RADMACHER M., TILMANN R .W., GAUB H.E., Biophys. J., 64 (1993), 735.
[11] *MultiMode™ SPM Instruction Manual Version 4.31ce*, Digital Instruments Veeco Metrology Group, 1996–1999, pp. 11.25–11.28.
[12] RYSZKOWSKA J., JURCZYK–KOWALSKA M., SZYMBORSKI T., KURZYDŁOWSKI K.J., Physica E, 39 (2007), 124.
[13] *NanoScope Command Reference Manual Version 5.12 Revision B*, Digital Instruments/Veeco Metrology Group, Inc, 2001, p. 15.42
[14] MIRONOV V.L., *Fundamentals of Scanning Probe Microscopy*, Russian Academy of Sciences, Institute for Physics of Microstructures, 2004, pp. 31–35.

Received 28 April 2007
Revised 16 February 2008